UNIVERSITY OF BERGAMO

DOCTORAL PROGRAM IN ENGINEERING AND APPLIED SCIENCE

XXXVIII Cycle

Improving structural assessment through large-scale monitoring and Finite Element Model Updating

LUCA ROTA

Supervisor:

Prof. Andrea BELLERI

UNIVERSITÀ DEGLI STUDI DI BERGAMO
Dottorato di ricerca in Ingegneria e Scienze Applicate – Tecnologie per la conservazione, la protezione, il recupero e la sostenibilità ambientale
XXXVIII Ciclo

UNIVERSITY OF BERGAMO
PhD Program in Engineering and Applied Science – Technologies for conservation, protection, restoration and environmental sustainability
XXXVIII Cycle

Coordinator: Prof. Alessandra MARINI
Supervisor: Prof. Andrea BELLERI
Author: Luca ROTA

Title: IMPROVING STRUCTURAL ASSESSMENT THROUGH LARGE-SCALE MONITORING AND FINITE ELEMENT MODEL UPDATING

Abstract

This thesis presents a multidisciplinary framework for structural health assessment and model updating of infrastructures, integrating satellite-based monitoring, in situ measurements, operational modal analysis, and finite element model updating. The research addresses the need for reliable, multi-scale methodologies to support modern infrastructure management by combining global deformation monitoring with local structural identification techniques.

At the territorial and building scale, satellite radar data are employed to detect and interpret slow ground and structural movements. The study discusses the potential and limitations of satellite-derived displacement measurements, particularly regarding temporal coverage and measurement uncertainty. At the infrastructure scale, the thesis focuses on integrating static and dynamic experimental data into finite element model updating procedures.

While the inclusion of static information in hybrid model updating is well established in the literature, this work systematically investigates its stabilizing role within the objective function and quantifies its influence on the robustness and reliability of the optimization process. Through synthetic benchmark examples and a real bridge case study, the research demonstrates that the combined use of static and dynamic data reduces parameter uncertainty, mitigates non-uniqueness issues, and improves model calibration stability compared to purely dynamic-based updating.

The proposed framework offers a structured workflow that links large-scale monitoring data to detailed structural modelling, contributing to a more comprehensive and scalable approach to infrastructure assessment. The thesis also critically examines methodological assumptions, sensitivity to data weighting, and applicability conditions, outlining the limitations and potential extensions of the approach.

Overall, the work advances the integration of multi-source monitoring data into model updating strategies and supports more reliable decision-making in structural health monitoring of infrastructures.

Index

List of Figure

List of Tables

Acronyms

AR – Autoregressive

ARMA – Autoregressive Moving Average

ARX – Autoregressive with Exogenous Input

DInSAR – Differential Interferometric Synthetic Aperture Radar

EFDD – Enhanced Frequency Domain Decomposition

EMA – Experimental Modal Analysis

FE – Finite Element

FEMU – Finite Element Model Update

FFT – Fast Fourier Transform

FDD – Frequency Domain Decomposition

MAC – Modal Assurance Criterion

MDOF – Multi Degree of Freedom

MEMS – Micro-Electro-Mechanical Systems

MPC – Modal Phase Collinearity

MPD – Mean Phase Deviation

OMA – Operational Modal Analysis

PP – Peak Picking

PSD – Power Spectral Density

PS – Persistent Scatterer

SAR – Synthetic Aperture Radar

SDOF – Single Degree of Freedom

SHM – Structural Health Monitoring

SSI-Cov – Covariance-driven Stochastic Subspace Identification

Introduction

The assessment and long-term management of existing civil infrastructure has become one of the most pressing challenges for researchers and practitioners in structural engineering. Bridges, viaducts, and buildings worldwide are increasingly exposed to natural hazards, ageing processes, and demands that often exceed those assumed in their original design. The collapse of individual structures, even when limited in number, has dramatic social and economic consequences, highlighting that systematic, large-scale monitoring is now a necessity rather than an option. In this context, advances in remote sensing and numerical modelling have opened new avenues for integrating large-scale observations with detailed structural analysis.

This doctoral research focuses on structural assessment and monitoring, combining general risk classification tools with advanced, model-based techniques applied to a specific case study. The overall goal is to explore how both standard procedures and innovative technologies, such as satellite data and model updating, can be used to better understand and manage infrastructure assets. In particular, the aim is to establish a framework for conducting large-scale analyses and more refined single-structure analyses to rank the structures and reduce uncertainties between reality and numerical models.

In the early stages of this research, the potential of remote sensing technologies, particularly Synthetic Aperture Radar (SAR), was explored as a tool for large-scale infrastructure monitoring. Owing to its ability to detect millimetric ground and structural displacements over time, SAR provides a powerful means to observe changes across extensive areas, even before visible damage occurs. This satellite-based approach serves as a screening tool: it does not replace in-situ inspection or detailed evaluation, but it helps identify areas or assets showing signs of potential instability or deformation trends. It is especially useful in mountainous or hard-to-access regions, such as the Aosta Valley, where systematic ground surveys are logistically challenging and economically costly. The use of SAR data in this research was therefore intended as a preliminary layer of information, supporting the prioritisation of further analyses and complementing traditional engineering judgement.

Following the SAR-based analysis, a network-scale structural risk assessment was conducted on a selected road section in the Aosta Valley, based on the Italian Ministry Guidelines for the Classification and Management of Risk in Existing Bridges (MIT, 2020). These guidelines provide a structured method to classify bridges and to evaluate and rank their structural condition based on

vulnerability, exposure, and potential consequences of failure. Now established in law in Italy, these guidelines offer a systematic approach to prioritising inspections and interventions.While the SAR data highlighted potentially critical zones, the guideline-based assessment provided a formalized risk score and supported the definition of intervention priorities across the network. Integrating these two approaches offers a more comprehensive picture of the condition of existing infrastructure, promoting more effective maintenance planning. Although SAR interferometry provides a data-driven indication of potential structural movement, it lacks the structured, risk-based classification provided by national guidelines. The use of satellite data alongside risk classification guidelines is a contribution of this work, demonstrating how traditional and modern tools can be combined to improve infrastructure monitoring on a regional scale. Combining both methods ensures a more robust and multi-perspective assessment.

While the first part of the work examines the problem from a general, large-scale perspective, the second part shifts the focus to a specific structure. It explores how experimental data and numerical models can be combined to better understand the behaviour of an existing structure and reduce discrepancies between reality and numerical models, thereby contributing to more reliable models for risk analysis and other applications. A case study of a bridge was conducted using ambient vibration measurements, a non-invasive technique that captures how a structure naturally responds to environmental loads such as wind or traffic. From these measurements, dynamic properties such as natural frequencies and mode shapes were extracted. These experimental results were then used in a model updating process, in which a finite element model of the bridge was calibrated to better match the real structure. Traditionally, model updating relies solely on dynamic data, but this approach can sometimes lead to ambiguous or unstable results, especially when multiple parameters influence the same frequency. To improve the quality of the updating process, a new approach was proposed in this thesis: the introduction of a residual based on displacement into the objective function. This involves adding information from static measurements (e.g., displacements or strains under known loads) to the optimization process. This addition helps make the model more accurate and reduces the gap between simulation and reality, thereby reducing uncertainties and making the model more realistic. In particular, adding a specific term that is not influenced by certain parameters can reduce ambiguity in the solution. This part of the research complements large-scale assessment strategies.

The first chapter introduces the use of satellite SAR data as a tool for monitoring the built environment. It focuses on the development of processing procedures for interferometric data, the extraction and interpolation of displacement time series, and the implementation of simplified methods for evaluating the effects of differential settlements on buildings. Using examples from real

case studies, the chapter demonstrates the potential of combining satellite observations with simplified structural indicators to detect early signs of vulnerability in buildings and bridges.

The second chapter moves from this methodological framework to the regulatory domain, focusing on the Italian Ministry of Infrastructure and Transport guidelines for the classification and risk management of existing bridges. The multi-level approach proposed by the guidelines is described and then applied to the road network of the T2 route in Valle d'Aosta. This application demonstrates how risk classification procedures can be used in practice to prioritise maintenance and intervention needs, and how satellite-based monitoring can complement traditional inspection data to support decision-making processes at the territorial scale.

The third chapter shifts focus to the theoretical foundations of dynamic analysis and model updating. It presents the main techniques of operational modal analysis, including frequency and stochastic subspace methods, and discusses the principles of signal processing and spectral analysis. The mathematical formulation of the model updating problem is also described, laying the groundwork for calibrating finite element models against experimental results. This chapter provides the essential background for the subsequent development of the proposed methodology.

In the fourth chapter, the thesis presents its most innovative contribution: the integration of static response data into the model updating process. Whereas traditional approaches typically rely solely on residuals based on modal properties such as natural frequencies and mode shapes, and very few studies consider this possibility, this research demonstrates how static load test results can be incorporated into the objective function. Simplified examples show that including static information increases the stability of the optimisation procedure, reduces uncertainties, and improves the overall reliability of the calibrated numerical models.

The fifth chapter presents the application of the proposed methodology to a real structure, the Canonica d'Adda bridge. This case study combines data from material investigations, static load tests, and ambient vibration measurements, both before and after the replacement of the hangers. The information collected was used to perform manual and automatic model updating, allowing direct comparison between experimental evidence and numerical predictions. The results confirm that the combined use of static and dynamic terms in the updating process provides more accurate and robust models, capable of reproducing the actual behaviour of the structure with greater fidelity.

Research Objectives

This research is motivated by the growing need to improve the way we manage existing structures. In particular, the following goals were defined:

- Support risk-based decisions at a territorial level using structured guidelines and quantitative methods.
- Reduce uncertainty between models and real data that reflect the actual behaviour of existing structures
- Promote a multi-scale approach, where network-wide analysis and local detailed studies are part of the same assessment process.

By addressing the problem from both a wide-area and a structure-specific perspective, this thesis aims to contribute to a more efficient and modern approach to managing infrastructure.

Chapter 1

Structural Monitoring with Satellite Data

Throughout their lifespan, structures undergo damage and degradation caused by various factors. These causes may include material deterioration due to loading and unloading cycles, exposure to external environmental agents (e.g., carbonation), or structural displacements due to differential settlement of foundation soil. Major damage can also result from exceptional events such as earthquakes, landslides, or floods. These forms of deterioration can lead to a reduction in the performance of the original structure. Hence, there arises the need and interest to keep structures and areas of land under observation and control. Monitoring a structure means implementing operational procedures capable of estimating/measuring the damage or degradation state of the structure and its components. The implementation of such strategies for damage detection and characterization is known as Structural Health Monitoring (SHM) [1] [2] [3]. Structural monitoring applies to various fields such as aerospace and mechanical engineering, civil and infrastructure engineering, including both historical and new constructions, bridges, tunnels, industrial buildings, production facilities, offshore platforms, port structures, foundations, and excavations [4] [5], [6] [7] [8], [9] [10], [11] . The most common monitoring techniques are generally classified into static, dynamic, and geomatic monitoring. Static monitoring involves measuring absolute and relative displacements of the structure or its parts. By using sensors such as inclinometers, strain gauges, etc., readings are taken at regular time intervals, allowing the reconstruction and ongoing observation of the evolution of displacements and crack patterns. Dynamic monitoring, on the other hand, analyses signals generated by natural or induced vibrations, which are measured and recorded by dedicated sensors placed on the structure. A classic example of dynamic monitoring is the Italian seismic network. Geomatic monitoring takes its name from the various techniques used to implement it. These include photogrammetry, laser scanning, total stations, and GPS, which enable the identification and measurement of many control points, allowing for the measurement of both absolute and relative displacements.

There are many tools and methods for structural monitoring, from traditional instruments to the most advanced technologies. It begins with devices like plumb lines and inverted pendulums, which are used to measure vertical displacements in structures such as towers, dams, and bell towers. These

systems rely on a suspended weight or float to detect movements with sub-millimetric precision. When such setups are impractical, zenith levels are used as an alternative to monitor horizontal displacements, while optical collimators allow the precise detection of movements in large structures by aligning visual reference points.

Instruments such as inclinometers and clinometers are employed to measure angular rotations of structural elements, often used in dams, viaducts, or for monitoring landslides through inclinometric probes embedded in the soil [6]. Displacement meters, including extensometers and deformometers, are used to monitor cracks, joints, and faults, offering high accuracy over varying measurement ranges. Accelerometers are crucial for recording vibrations either natural or induced across three axes and are extensively used in infrastructure monitoring and national seismic networks. Load and pressure cells measure internal forces within materials and structural components, while piezometers monitor water pressure within the soil. Thermocouples, though primarily used for temperature measurement, also help distinguish structural deformations caused by thermal variations from those indicating actual damage. Total stations and laser scanners represent more advanced techniques: the former track positional shifts of predefined points, while the latter generates 3D point clouds of entire structures, allowing for comprehensive deformation analysis over time. Optical fiber sensors represent a cutting-edge solution for long-term, high-precision structural health monitoring, taking advantage of light-based measurements and offering immunity to electromagnetic interference. Finally, MEMS (Micro-Electro-Mechanical Systems) sensors offer a compact, low-cost, and wireless solution for structural monitoring. Thanks to their small size and integration capabilities, MEMS devices can collect, process, and transmit data in real-time. They have been applied successfully in monitoring buildings, historical structures, slopes, and infrastructures, and are particularly suitable for dynamic identification methods using accelerometers [12], [13] [14] [15].

Satellite Systems

Satellite technology is used across a wide range of sectors, from military applications to broadcasting, meteorology and land observation. In recent decades, techniques leveraging this technology have been developed for monitoring buildings and infrastructure. One of the main satellite-based techniques is GNSS (Global Navigation Satellite Systems), which allows for continuous positioning checks of reference points over time. This makes it possible to measure the absolute displacements of a structure, even across large areas. GNSS can be used in both static and dynamic modes, allowing

spatial positioning data to be collected at temporal intervals ranging from hours or days down to just a few seconds. Another widely studied and applied technique is SAR (Synthetic Aperture Radar) Interferometry (InSAR), and the technique can be divided into satellite-based SAR interferometry (S-InSAR) and ground-based SAR interferometry (T-InSAR). Satellite SAR Interferometry (S-InSAR) uses pairs of images captured from orbiting satellites to detect changes that occurred between the acquisition times. It relies on the phase of the electromagnetic signal emitted by the satellite sensors and reflected by ground features. The satellite travel along trajectories that are slightly inclined with respect to the meridians (by only a few degrees), covering half of their orbit from the North Pole to the South Pole (descending orbit) and the other half from the South Pole to the North Pole (ascending orbit), as shown in Figure 1.

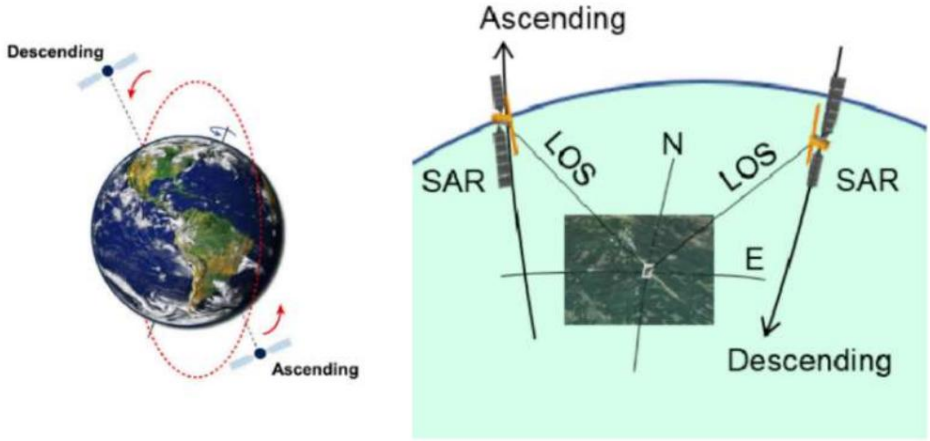

Figure 1: Ascending and Descending orbit [16].

During their flight along the orbital path, the radar sensors mounted on the satellite emit electromagnetic signals in a direction known as the *Line of Sight* (LOS), within a specific frequency band, and record the backscattered echoes. These echoes are stored as time delays, which correspond to the distances between the ground targets and the sensor. The collected information is then processed through algorithms that elaborate the ensemble of recorded digital echoes to produce a radar image of the observed area. Each image is composed of complex-valued pixels, defined by two coordinate axes: the *azimuth*, corresponding to the direction of the satellite's flight, and the ground *range*, which represents the distance between the sensor and the target on the ground. Because the radar operates in a side-looking configuration, the resulting images are affected by geometric distortions such as foreshortening, layover, and shadowing. This method processes radar satellite data to detect slow ground movements caused by subsidence, volcanic activity, landslides, or seismic events [17] and allows for the monitoring of deformations caused by earthquakes, subsidence, landslides, and other processes over very large areas [18] [19]. In addition, InSAR has been applied successfully for the assessment of cultural heritage sites, demonstrating its potential for non-invasive

monitoring [20] [21]. Also, long-term SAR analyses, such as those at Beijing Capital Airport, demonstrate the value of persistent monitoring for infrastructure resilience [22]. In essence, it involves calculating the phase difference between two SAR images of the same scene, acquired under similar geometric conditions at different times. The resulting interferogram reflects the pixel-by-pixel phase shifts between the two acquisitions. SAR interferometry enables the reconstruction of surface deformations by comparing two radar images that contain the necessary information for the process. This enables the reconstruction of deformation histories and the assessment of their temporal evolution.

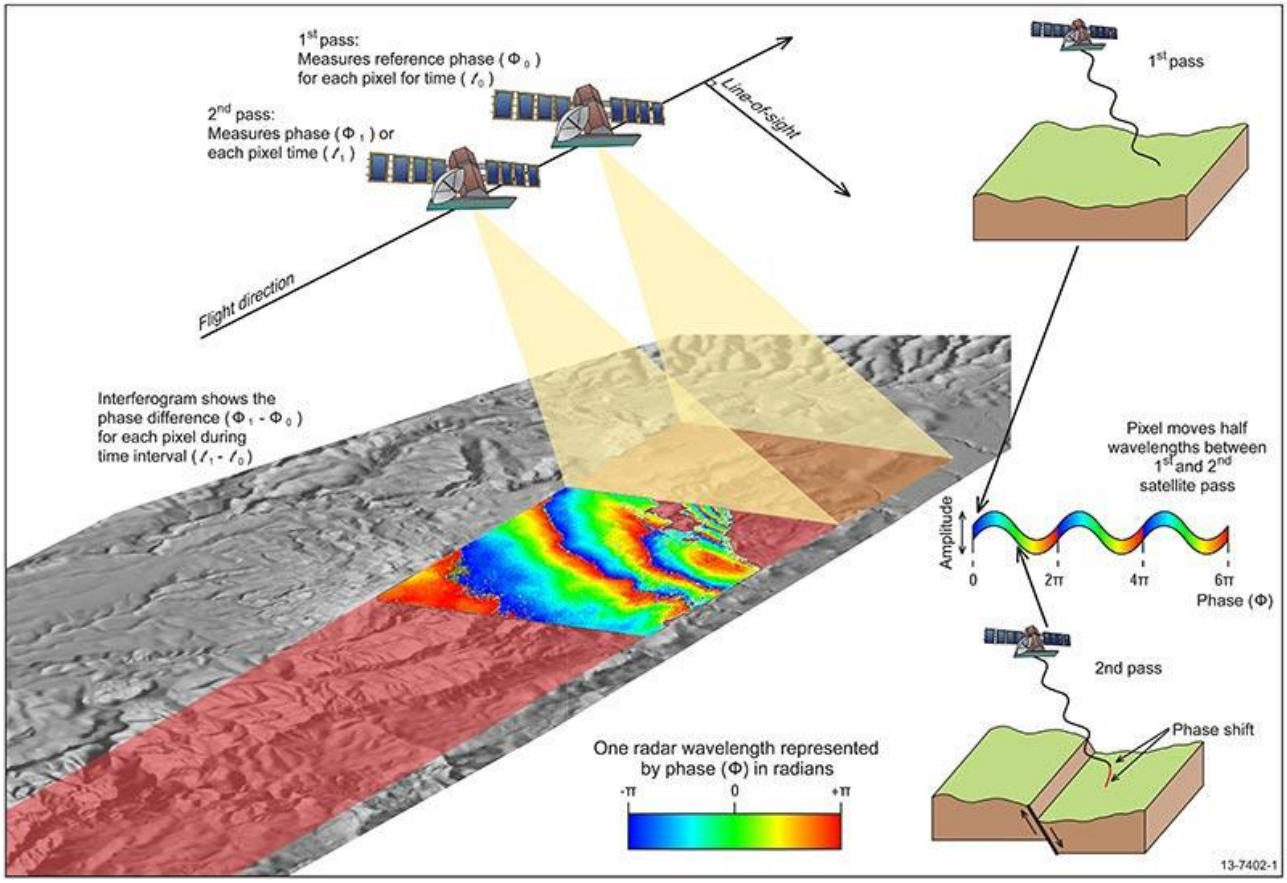

Figure 2: lnSAR technology description.

The displacement measured by a radar satellite represents the projection of the real three-dimensional displacement vector d $= [d_E, d_N, d_U]$ onto the radar Line of Sight (LOS), according to:

$$d_{LOS} = \ell_E \cdot d_E + \ell_N \cdot d_N + \ell_U \cdot d_U$$

where ℓ_E, ℓ_N, ℓ_U are the LOS direction cosines defined by the satellite geometry (incidence and heading angles). Sentinel-1, for example, has an incidence angle of about 39–43° and a heading of approximately −13° for ascending and +13° for descending passes, resulting in a sensitivity mainly

to vertical and East–West motions, while the North–South component remains practically undetectable.

To overcome limitations of basic differential InSAR such as atmospheric interference, advanced methods have been developed, known as A-DInSAR (Advanced Differential InSAR). Among these, PS-InSAR (Persistent Scatterers Interferometry) analyses specific ground targets with stable and high radar reflectivity over time, often including buildings, roads, metallic structures, and outcropping rocks [23]. Urban PS-InSAR mapping, as in Srinagar City, illustrates how persistent scatterers reveal subtle long-term subsidence providing insights that can be directly transferred to the monitoring of structure or infrastructure [24]. Multi-track approaches improve displacement retrieval along multiple directions, enhancing bridge and urban infrastructure monitoring [25]. A-DInSAR techniques make it possible to monitor surface and structural deformations over time with high precision by using multiple satellite images of the same area. Co-analysis of long-term DInSAR with geology helps distinguish bridge and building settlements from broader city-wide subsidence patterns [26]. Since the first SAR satellite missions in the early 1990s, a vast archive of imagery has been collected with revisit times ranging from 35 days (e.g., Envisat-ASAR) to as short as 6 days (e.g., Sentinel-1 constellation). Modern radar satellites, such as those of the COSMO-SkyMed constellation managed by the Italian Space Agency, now offer ground pixel resolutions as fine as 1 meter. Similar performance is provided by the German TerraSAR-X. Earlier satellites like ERS-1/2 and Envisat, launched by the European Space Agency between 1991 and 2002 for scientific purposes, provided coarser resolutions around 30 meters. Second-generation SAR constellations, with shorter revisit times and higher spatial resolution, enable near-operational tracking of urban or infrastructure-related motions [27]. Although originally developed for large-scale monitoring of slow terrain movements, SAR technology is now being explored for its potential in building-scale deformation detection.

Ground-Based SAR Interferometry (T-InSAR) is the second major application of SAR systems. In this method, a radar sensor moves along a rail to acquire high-resolution images of a target area or structure. Data is captured at high temporal frequency, without the need for artificial reflectors, enabling comprehensive coverage of the illuminated scene. Each pixel in the radar image provides information about displacement using the same interferometric principles as in satellite-based SAR. This makes it possible to generate deformation maps for both natural and man-made elements, and if the system is active long enough build temporal displacement series to assess ongoing deformation.

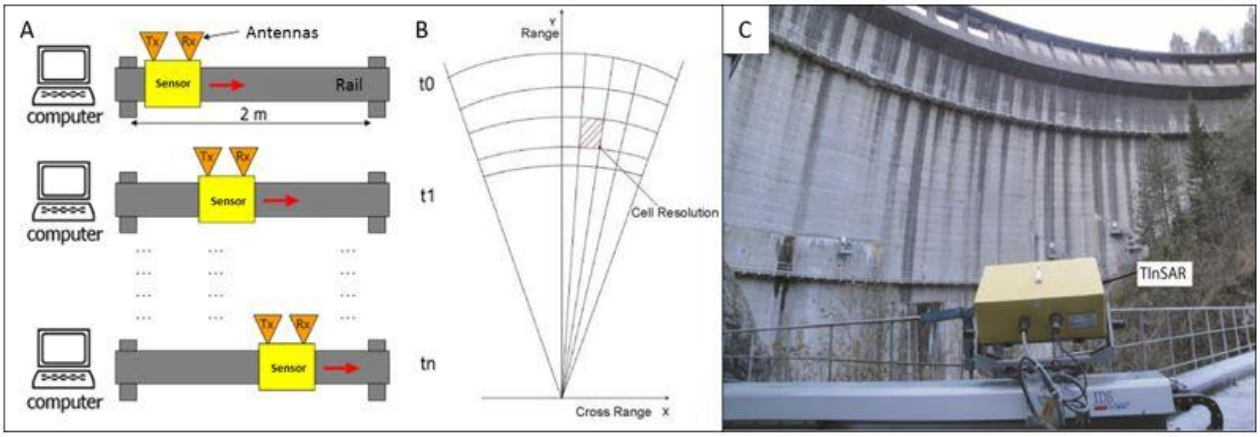

Figure 3: Ground-Based SAR Interferometry on a dam.

One key advantage of this approach is its ability to monitor large areas remotely, without physical access and regardless of weather conditions. Interferometric radar has also been used to extract dynamic features, such as modal frequencies, from civil structures, offering a complementary perspective to quasi-static satellite InSAR [28].

During this work, following a literature review, the initial objective was to become familiar with this type of data in order to later investigate which information may be useful in identifying potential signs of structural damage in buildings and offer a large-scale approach to evaluate potential damage. The data was available due to a collaboration in the Reluis Project DPC_ReLUIS 2019_2021, specifically '*ReluisWP6-Monitoraggio e Dati Satellitari',* where SAR data was studied for possible use at a building scale to detect deformations and possible damages. The satellite data is processed using the Small BAseline Subset (SBAS) - DInSAR algorithm, resulting in text files containing information about the points detected by the satellite. The SBAS algorithm allows retrieving long-term deformation histories from dense stacks while reducing decorrelation and atmospheric noise [29] [30] [31] and [32] demonstrated the potential of the small-baseline (SBAS) and extended SBAS approaches for deformation monitoring at full spatial resolution, showing how these techniques can effectively reduce decorrelation effects, improve phase unwrapping, and generate long-term displacement time series. A two-scale SBAS-DInSAR analysis, combining urban context and asset-level focus, helps isolate structure-related signals from broader deformation fields [33]. Building-scale SBAS-DInSAR time series can also be combined with semi-empirical indicators to prioritize assets and screen for damage, as demonstrated for buildings in Rome [34]. Others case studies illustrate practical applications of SAR for infrastructure, [35] integrated DInSAR with in-situ geological data to investigate slow-moving landslides, highlighting the benefit of combining satellite and field observations, [36] evaluated post-tunnelling settlements, providing insights relevant for

bridges affected by underground works, [37] demonstrated an integrated approach for the "Ponte della Musica," combining satellite SAR with on-site vibration acquisitions.

The first dataset, processed and supplied by the CNR (National Research Council of Italy) processed with the SBAS algorithm, refers to an urban area in the city of Naples. An example of the file content is shown below.

DDSS_ID: LOS_DISPLACEMENT_TIMESERIES
Product_ID: N/A
Product_format: ASCII
Product_size:
Preview_url: N/A
Product_url: N/A
Bounding_box: 44.910267, 8.5472437, 45.766685, 10.058197
Bounding_box_wkt: POLYGON((9.8595880 45.766685,10.058197 45.109584,8.7622088 44.910267,8.5472437 45.566341,9.8595880 45.766685))
License: https://creativecommons.org/licenses/by/4.0
User_ID: CNR-IREA
Software_version: CNR-IREA P-SBAS 25
Applied_algorithm_description: Parallel SBAS Interferometry Chain
Main_reference: 10.1109/TGRS.2002.803792, 10.1109/JSTARS.2014.2322671
Date_of_measurement_start: 1995-06-18T21:33:01.0998520Z
Date_of_measurement_end: 2010-10-17T21:02:33.079696Z
Date_of_production: 2018-06-15T13:36:55Z
Date_of_publication:
Service_used_for_generation: EPOSAR
Geographic_CS_type_code: EPSG4326
Used_DEM: SRTM_1arcsec
Super_master_SAR_image_ID: SAR_IM__0PWDSI19990627_213159_00000362A043_00487_21884_0000.E2
Spatial_resolution: 80
Sensor: ERS
Mode: STRIPMAP
Antenna_side: Right
Relative_orbit_number: 487
Orbit_direction: ASCENDING
Wavelenght: 0.0565646
Value_unit: N/A, deg, deg, m, cm/yr, N/A, N/A, N/A, N/A, cm
Number_of_looks_azimuth: 20
Number_of_looks_range: 4
Applied_filter: Goldstein_0.50
Number_of_dates: 76
Reference_date: 1995-06-18T21:33:01Z
Reference_point: 9.1507690 45.187567
Applied_corrections: No_Corrections
Time_Years: 1995.46844, 1995.84949, 1995.94652, 1996.32643, 1996.32917, 1996.52164, 1997.28808, 1997.47940, 1997.67072, 1998.34401, 1998.53534, 1998.72392, 1999.20474, ...
List_of_dates: 1995-06-18T21:33:01Z, 1995-11-05T21:33:01Z, 1995-12-10T21:33:15Z, 1996-04-27T21:33:01Z, 1996-04-28T21:33:01Z, 1996-07-07T21:33:00Z, 1997-04-13T21:32:53Z, ...

Figure 4: Example of data from a satellite file.

```
ID,    Lat,     Lon,   Topo,    Vel,    Coer,    cosN,    cosE,    cosU, TS

  0, 45.43292,   8.59931, 147.43, -0.0901, 0.7513005,-0.0700857,-0.3161337, 0.9461223, -0.0000,   0.2047,
0.5086,   0.4411,   0.4871,   0.0201,  -0.5830,  -0.5434, ……

  1, 45.43375,   8.59903, 146.89, -0.0011, 0.7507089,-0.0700843,-0.3161245, 0.9461255, -0.0000,  -0.0511,
0.0183,  -0.3773,  -0.2634,  -0.4669,  -0.5700,  -0.5117,……..

  2, 45.43431,   8.59875, 147.50,  0.0498, 0.7348265,-0.0700839,-0.3161202, 0.9461270, -0.0000,  -0.3551,
-0.2971,  -0.7358,  -0.6270,  -0.7423,  -0.2663,  -0.3302, ……..

  3, 45.43514,   8.59875, 148.36, -0.0912, 0.8078599,-0.0700837,-0.3161169, 0.9461281, -0.0000,  -0.2180,
-0.1503,  -0.5823,  -0.5135,  -0.6380,  -0.4939,  -0.4527,……..

  4, 45.43569,   8.59819, 145.91, -0.1100, 0.7460570,-0.0700830,-0.3161115, 0.9461300, -0.0000,  -0.1834,
-0.1740,  -0.8636,  -0.8206,  -0.9444,  -0.5035,  -0.5658,……..
```

Figure 5: Example of data from a satellite file.

In Figure 4, the first part of the file is shown, containing general information about the analysed area, the list of temporal acquisition dates, and the processing parameters. Following the header lines, the file includes a list of points with their corresponding data, as shown in Figure 5. The available information includes:

- ID: Numerical identifier of the pixel.
- Lat: Latitude of the point, in the WGS84 reference system.
- Lon: Longitude of the point, in the WGS84 reference system.
- Topo: Elevation of the point.
- Vel: Average deformation velocity in cm/year, calculated as the linear regression of the displacement time series (TS).
- Coer: Interferometric coherence, a value between 0 and 1 that indicates the reliability of the measurement.
- cosN, cosE, cosU: Directional cosines of the Line-of-Sight (LOS) vector components in the North, East, and vertical directions.
- TS: Time series of displacements along the satellite's Line-of-Sight (LOS), corresponding to the temporal acquisitions listed in the first rows of the file.

In the initial phase, the data was processed using Matlab software. The points were plotted over a georeferenced image. The result is shown in the following Figure 6.

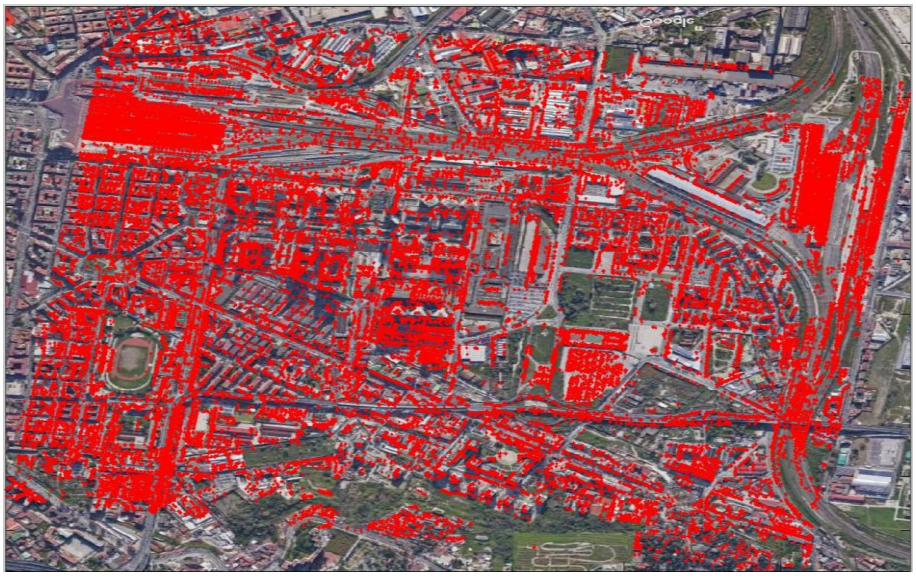

Figure 6: Georeferenced distribution of measurement points in the Naples area, derived from SAR processing.

Given the large area covered, and in order to focus on building-scale analysis, a script was developed to extract specific sections of the dataset. It is also possible to apply filters, such as coherence or spatial distance, to refine the selection. This is particularly useful for producing lighter, more manageable files for further processing. An example of data selection over the train station area and a smaller portion including buildings is shown in the following figures. The next step was to generate an image in which the points are color-coded according to the maximum displacement detected in the vertical direction. This approach helps to visually highlight areas undergoing more significant deformation. The result, obtained by assigning different colours to defined displacement intervals, is presented below (Figure 7).

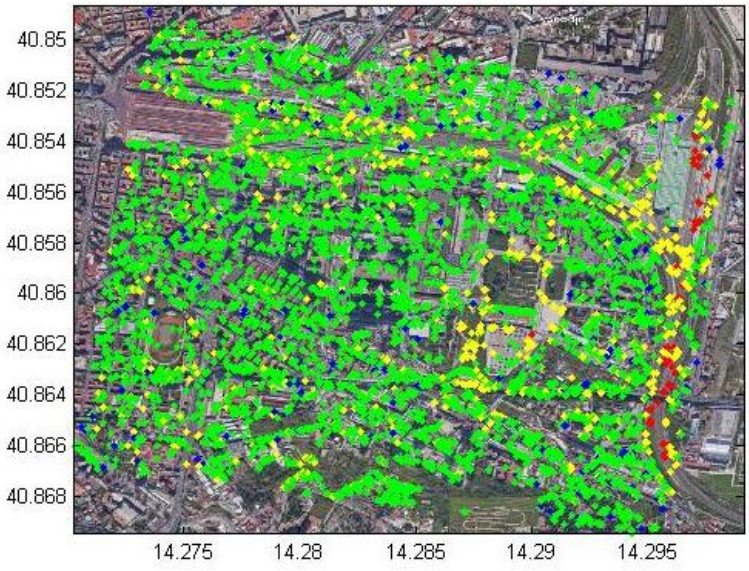

Figure 7: Representation of station area points graduated based on displacements velocities.

Following the initial processing in Matlab, a decision was made to switch to a more specialized software for handling geospatial data specifically, a GIS application. In this case, the open-source software QGIS was used. The program allows for the direct import of the text file and the plotting of georeferenced points within the WGS84 reference system. When overlaid with a satellite map, the result appears as shown below. Using QGIS makes it significantly easier to visualize specific areas, as simply zooming into the desired region provides immediate visual feedback. Moreover, it is possible to apply filters directly to the data fields, allowing the user to perform the same operations that were previously implemented in Matlab.

SAR Data – Rome

Following the analysis of the file related to the Naples area, other analyses were conducted on the SAR data for the Rome area, that are more extended. As mentioned in the previous, the files were processed using both Matlab and GIS software. The main purpose of using Matlab was to automate repeated operations across all files related to the Rome area. The area covered is significantly larger than that of Naples and is shown in Figure 8 below.

Figure 8: Overview of the Rome area analysed in the SAR dataset.

The dataset for the entire area (approximately 40x40 km) consists of 309 files, each corresponding to a smaller sub-area (approximately 2x2 km). Due to the significant computational resources required to process all the files in a single GIS project, a specific algorithm was developed to access only the files corresponding to areas or buildings of interest. The output of this algorithm is illustrated in Figure 9.

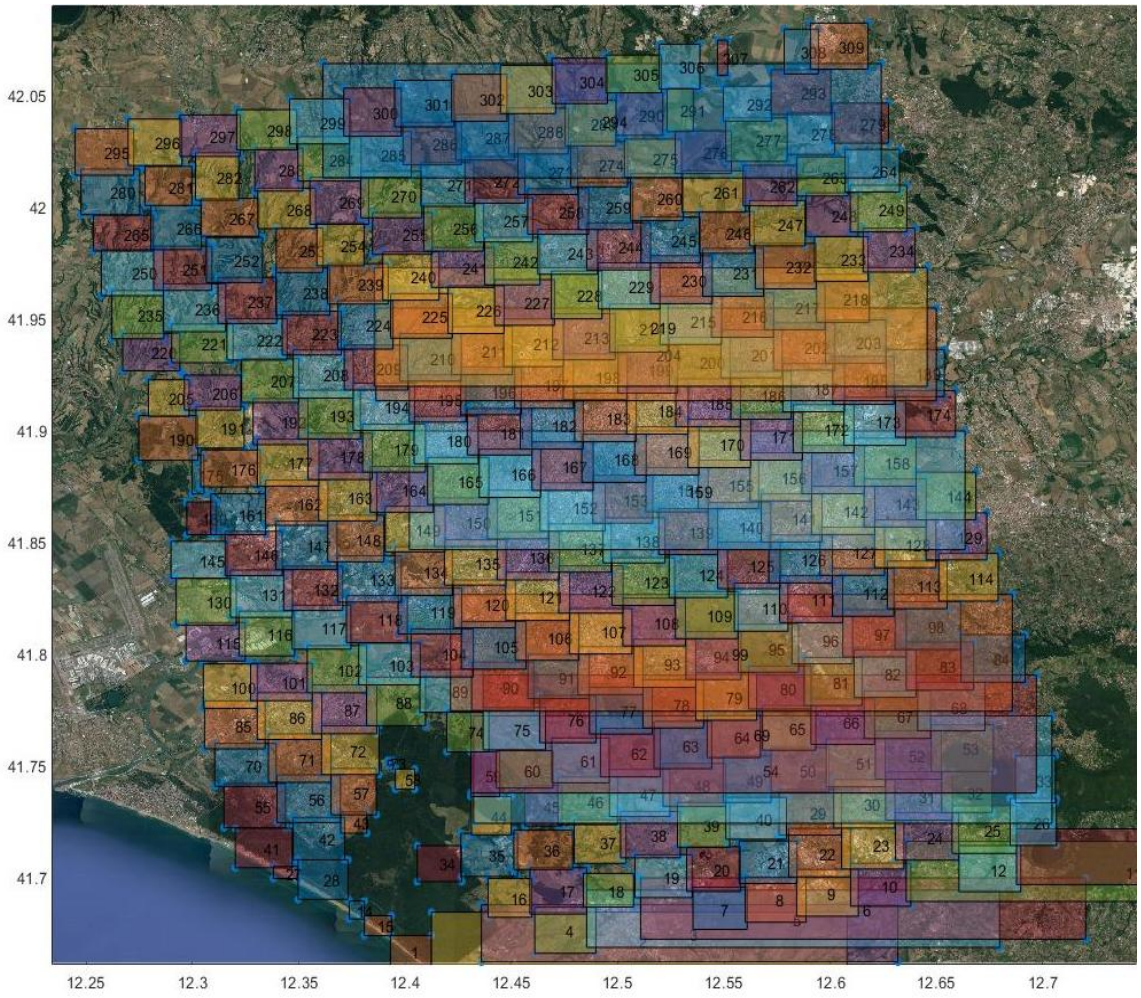

Figure 9: Representation of the areas resulting from file subdivision.

Each number corresponds to a specific file, which can then be loaded by selecting the appropriate ID, making the data readily available for further analysis. For instance, if one wishes to analyse the Civil Protection headquarters building on Via Ulpiano - Rome, selecting area n. 182 will load the corresponding data.

Figure 10: Images showing the selection of the building and corresponding file.

The code was later refined to operate at the building scale, allowing users to select points within a defined area based on a user-defined centre. By entering the coordinates of the building (or area) of interest, it becomes possible to analyse all points within the specified radius. In the previous example of the Via Ulpiano building, entering coordinates 41.904108, 12.472073 yields the following result:

Figure 11: Representation of selected points in Matlab.

Once the points within the selected area are identified, further analyses can be performed on average deformation velocities, displacements, and more. Plotting the time series of displacements in centimetres for the selected points results in the graph in Figure 12:

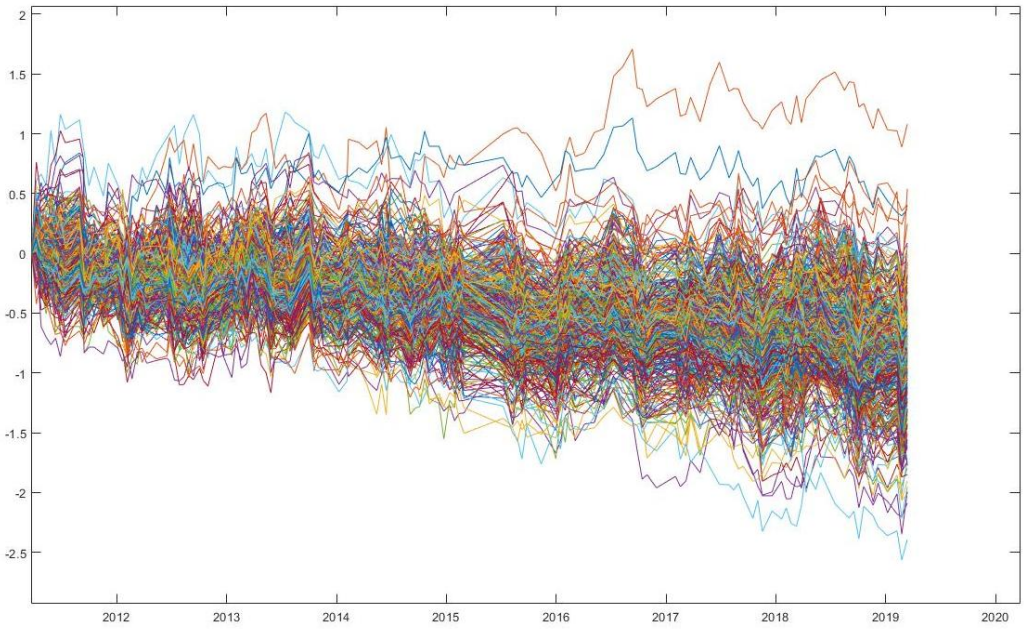

Figure 12: Time series of displacements for a selected area (cm).

The graph suggests that the points move uniformly and exhibit relatively small displacements (maximum displacement ~2 cm).

Parallel to the Matlab implementation, the same data was processed in the GIS environment. Using the previously described algorithm, specific areas of interest were selected, loaded, and analysed. For example, areas near Roma Tre University also studied in [34]. The Figure 13 below shows points color-coded based on deformation velocity. Notably, in certain zones (shown in red), higher velocities indicate ongoing displacement phenomena.

Figure 13: Representation of deformation velocities for an urban area in Rome (QGIS).

By analysing specific buildings and plotting the displacement time series in Matlab, the following results were obtained:

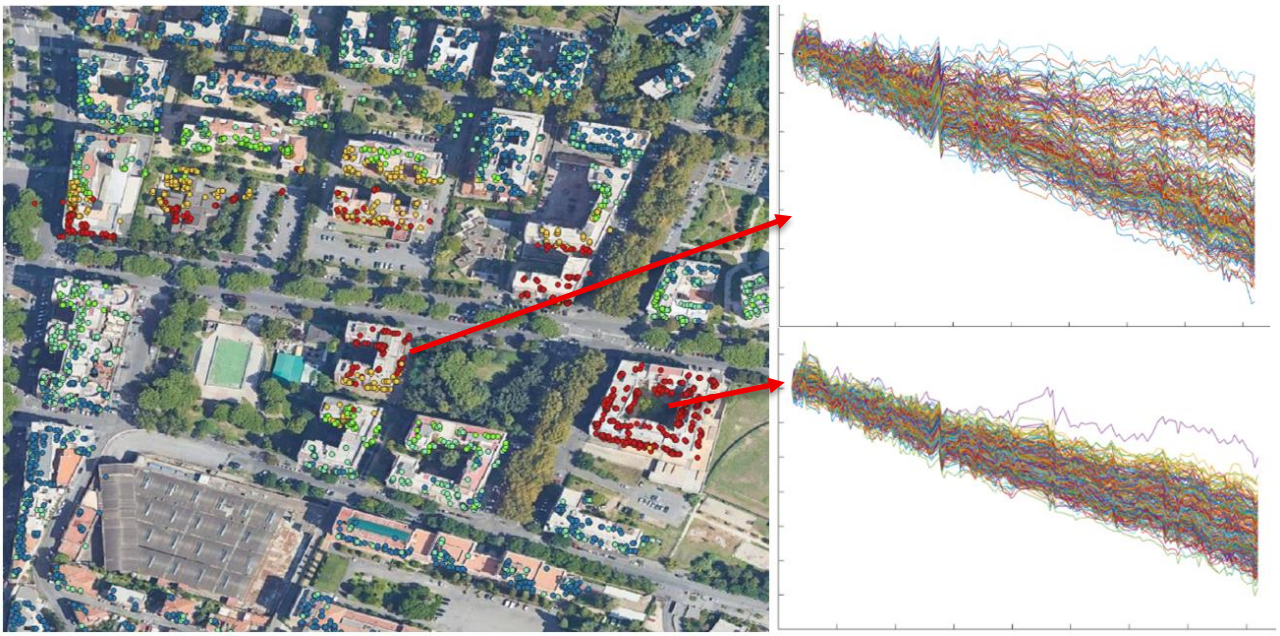

Figure 14: Time series of displacements for two buildings.

The top-right graph in Figure 14 suggests that the building is experiencing differential displacement among its monitored points, while the bottom graph in Figure 14 shows large displacements occurring uniformly. These analyses aim to assess the potential of satellite-derived data for both displacement monitoring and deformation velocity evaluation.

After conducting a thorough literature review on both satellite systems and traditional monitoring methodologies and instrumentation, analyses and processing of satellite data were carried out. The studies were performed using two different software platforms, Matlab and QGIS, in order to leverage their respective strengths. The main goal is to investigate which types of information can effectively help determine the damage state of a building. Following this, the research will focus on assessing to what extent satellite data can be useful in evaluating building conditions, particularly by analysing ground deformation detected through SAR data.

Study of the Single Building Using SAR Data, QGIS, and Matlab

Regarding the study of the single building, the focus move on the analysis of displacements and velocities. Initially, a procedure was developed to extract data related to a building and its surrounding area, allowing investigation into which displacements can be obtained and applied to a single building. Based on previous tests and given the enormous versatility of a GIS program, it was decided to use QGIS for visualization and data extraction, and then Matlab for analyses. For the GIS part, a set of files containing only the first columns of the original files was created to have lightweight files enabling complete visualization of the analysed area in terms of average deformation velocity. The result of this file set is shown in Figure 15.

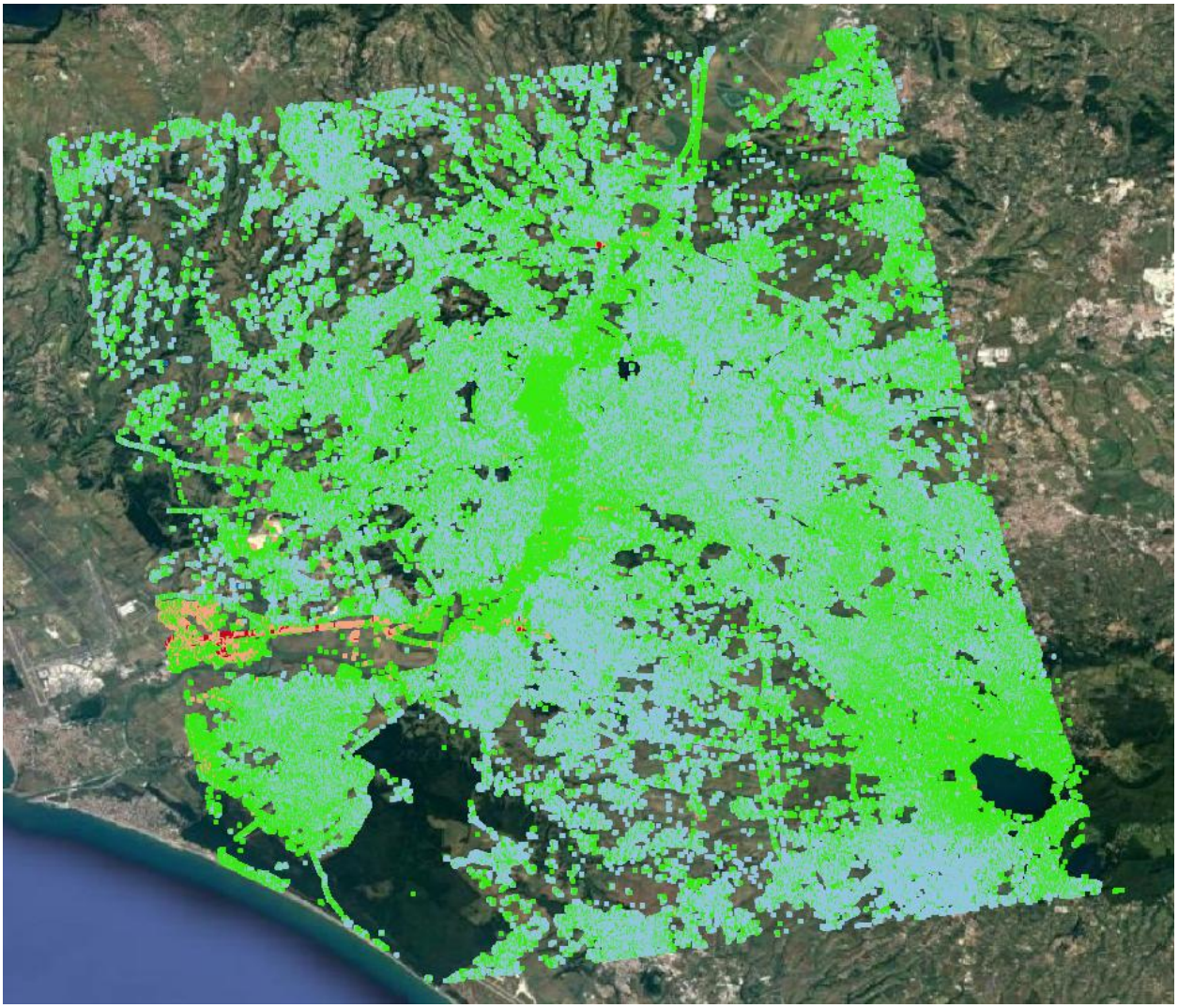

Figure 15: Average deformation velocities for the entire area of Rome (ascending orbit).

During filtering of the data for individual points, information regarding the file number of origin was added. This was done for having the necessary information to load the specific file for further processing and extraction once an area or building of interest is identified. This file can be used to easily identify areas with high velocities and thus potentially affected by subsidence. Once the area of interest is chosen and the files containing all the information are loaded in the GIS environment, it is possible to extract data relating to a building and the points around it. The image below (Figure 16) shows a QGIS screenshot related to a file used for loading single original text files and extracting the aforementioned data.

Figure 16: QGIS project screenshot used for extracting building data

Like observable in Figure 16, the QGIS project include multiple layers. Among them were layers representing the administrative subdivisions of the Rome area, as well as a shapefile (*.shp*) containing the geometries of individual buildings. The integration of the shapefile was particularly important, as it enabled the precise identification of buildings and the association of SAR-derived points with specific structures. Through QGIS, it was possible to select a single building geometry and directly extract the corresponding points and related attributes. These data could then be saved and exported for further numerical analysis in Matlab. The following Figure 17 illustrates the selection of a building within the QGIS environment and the outcome of the implemented algorithm, which was developed using the graphical modeler available in QGIS.

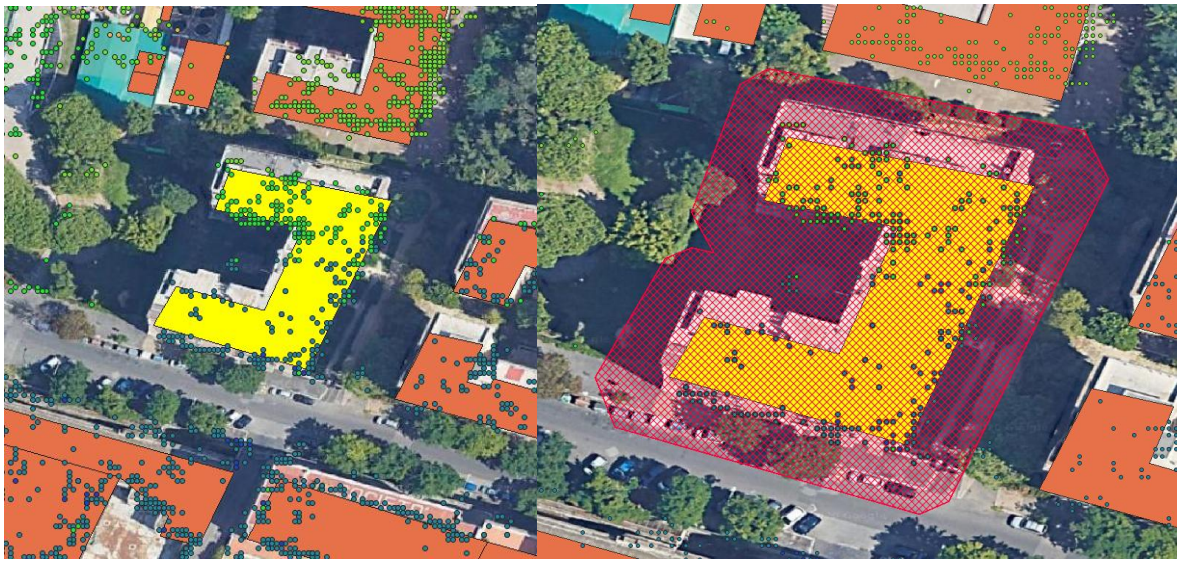

Figure 17: QGIS project screenshot used for extracting building data, particular building and surrounding area.

Once the building data are extracted, the process continues in Matlab, where an algorithm has been written for further analyses. The main objective is to understand how the data can be used together with a finite element model developed in parallel with these studies; this aspect will be explored further later. Regarding Matlab, some analyses were carried out on the points. To visualize the points on the building, a code was developed to plot the building outline in three dimensions. The data needed are extracted from QGIS during the previous phase. Figure 18 shows the result.

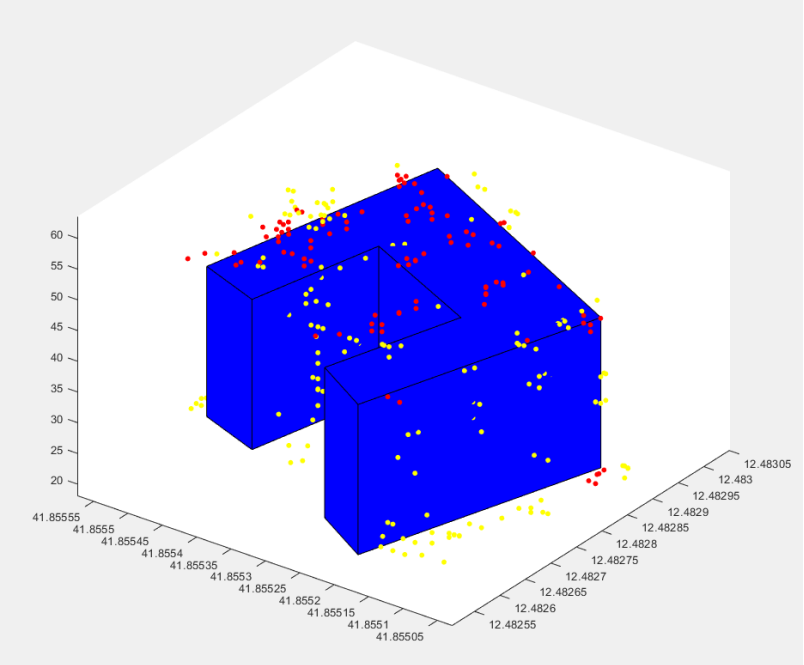

Figure 18: Three-dimensional model of the building in Matlab.

In Figure 18, SAR points from both ascending and descending orbits are visible. The base elevation and building height were estimated using SAR data, with the intention to later insert the actual base and height elevations obtained from DEM models. At this stage, the 3D model helps to understand where the points are located around the building. During these tests, the issue of a height offset between ascending and descending orbits was noticed and confirmed, with a difference of about 5 meters. After this, attention was given to the displacements, specifically questioning how and whether it is possible to easily identify a building subject to differential subsidence. To this end, the statistical distribution of average velocities on the building was investigated. It was found that buildings with possible differential displacement problems show a much higher variance in the distribution of average velocities than buildings without issues. See for example the following image.

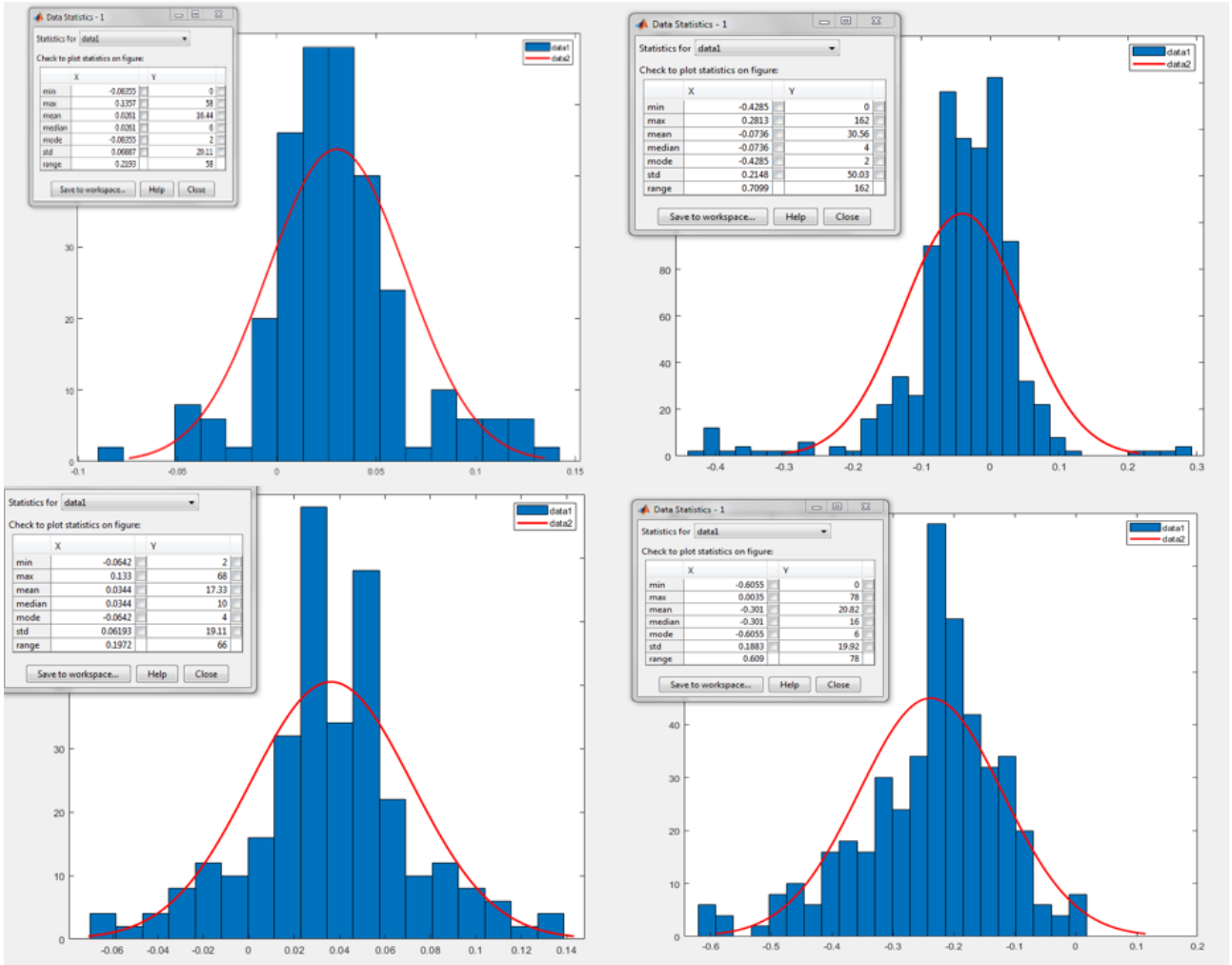

Figure 19: Velocity distributions (cm/year) with basic statistics indicated for four different buildings.
Top left: warehouse,
Bottom right: non-problematic building C,
Top right: problematic building ED_E,
Bottom left: problematic residential building.

It could therefore be interesting to establish a threshold above which to investigate a building. This could also be useful for potential guidelines as it is easy to apply. The effect of excluding points with low coherence values on the results was then considered. By filtering data according to different coherence thresholds, the following Figure 20 was obtained:

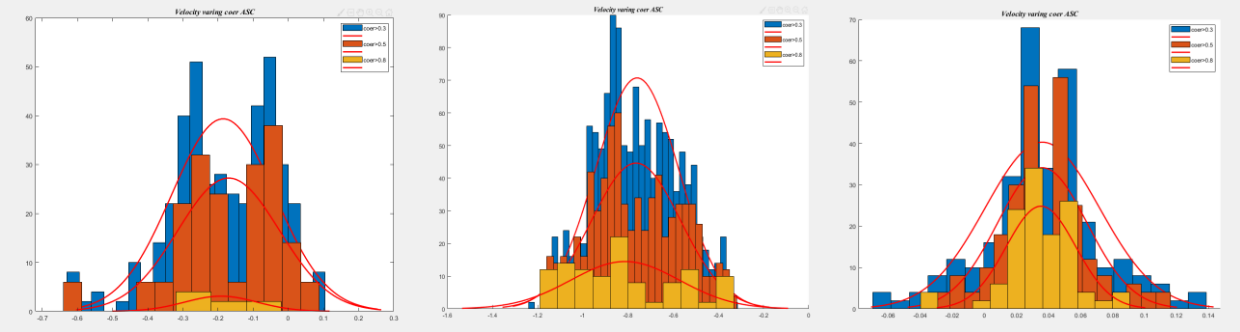

Figure 20: Distributions of average velocities in cm/year for three different buildings at varying coherence levels.

As shown, using different coherence thresholds yields different average velocity results; high coherence values do not necessarily mean better results, as points with low coherence could be excluded precisely because they moved over time, indicating a building problem. More analyses would be needed to investigate how coherence affects estimates extractable from satellite data. Since these issues require studies on many buildings, a sort of "standard sheet" for each building was created, providing a summary easily comparable across buildings. The result is Figure 21:

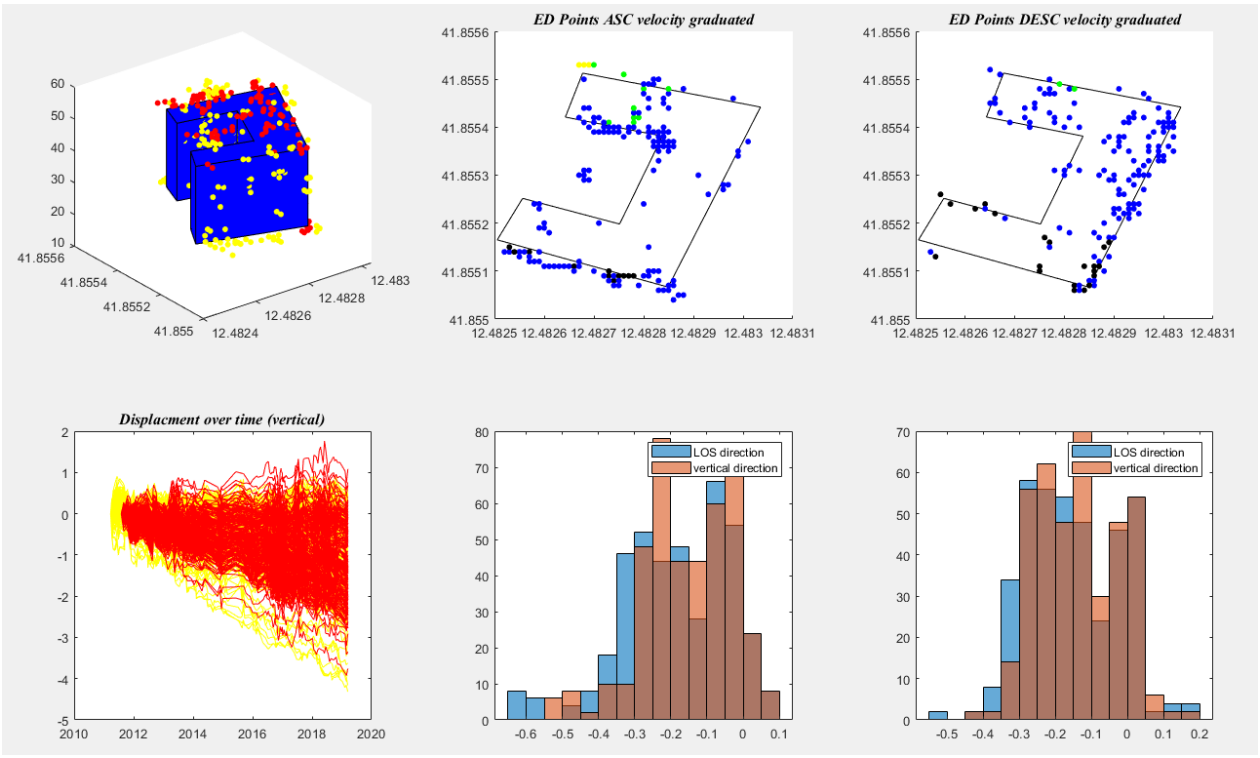

Figure 21: Standard analysis sheet for buildings using Matlab.

The next phase was to search for a "displacement surface" derivable from SAR data. The underlying idea is to define displacements applicable to a building based on the "average" displacements detected by SAR data. To do this, both maximum displacements obtained from time series and average displacements derived from the average velocity provided by CNR analyses were considered. In both cases, only the vertical component was taken into account. By linearly interpolating selected points on the building, it is possible to obtain a surface as shown in Figure 22. The idea is to create a mean displacement to apply to a simplified model in order not to have a precise estimation but a simple calculation that can be applied to a large area to select which building or infrastructure are subject to possible damage.

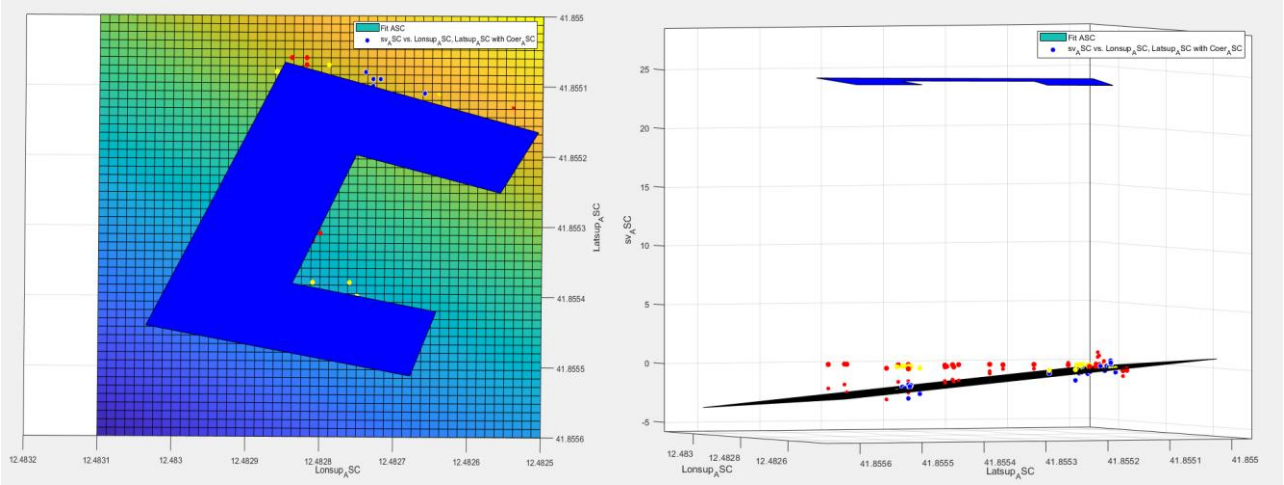

Figure 22: Displacement surface.

The developed code allows interpolation of higher degree polynomials weighted by the SAR data coherence; the case with higher polynomials term will be investigated in the later. Since the goal is to estimate an average displacement surface, it was obtained by averaging points from both ascending and descending orbits to reduce SAR data uncertainty relative to the real position.

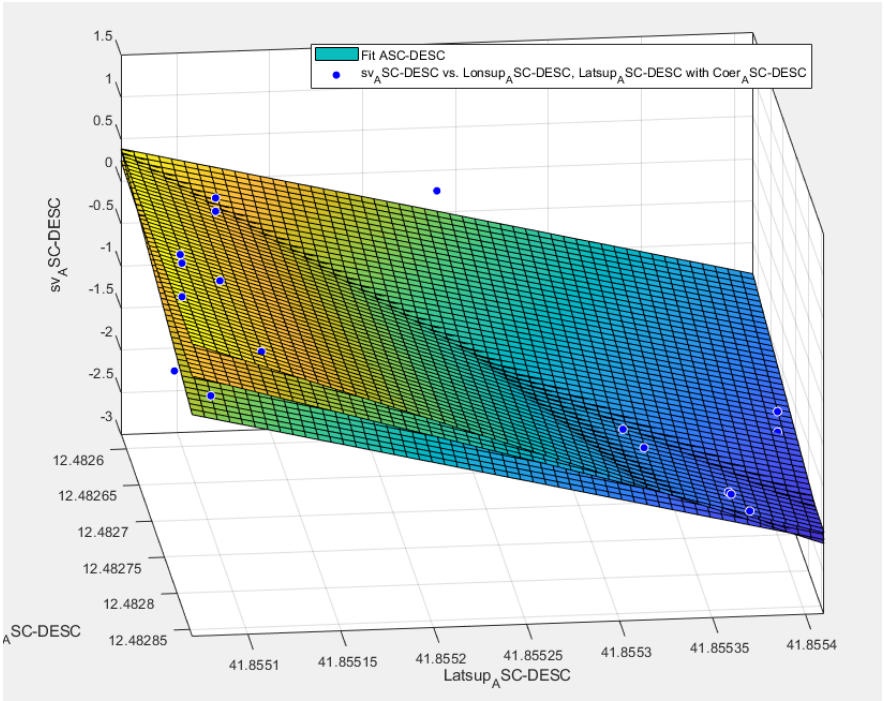

Figure 23: Surfaces derived from ascending orbit, descending orbit, and their average.

It remains to investigate the sensitivity of SAR data parameters (coherence, intrinsic error, number of points used, etc.) regarding this surface and the precision with which displacements can be estimated comparing in situ measurements. The following Figure 24 shows surfaces derived from the maximum displacement of points.

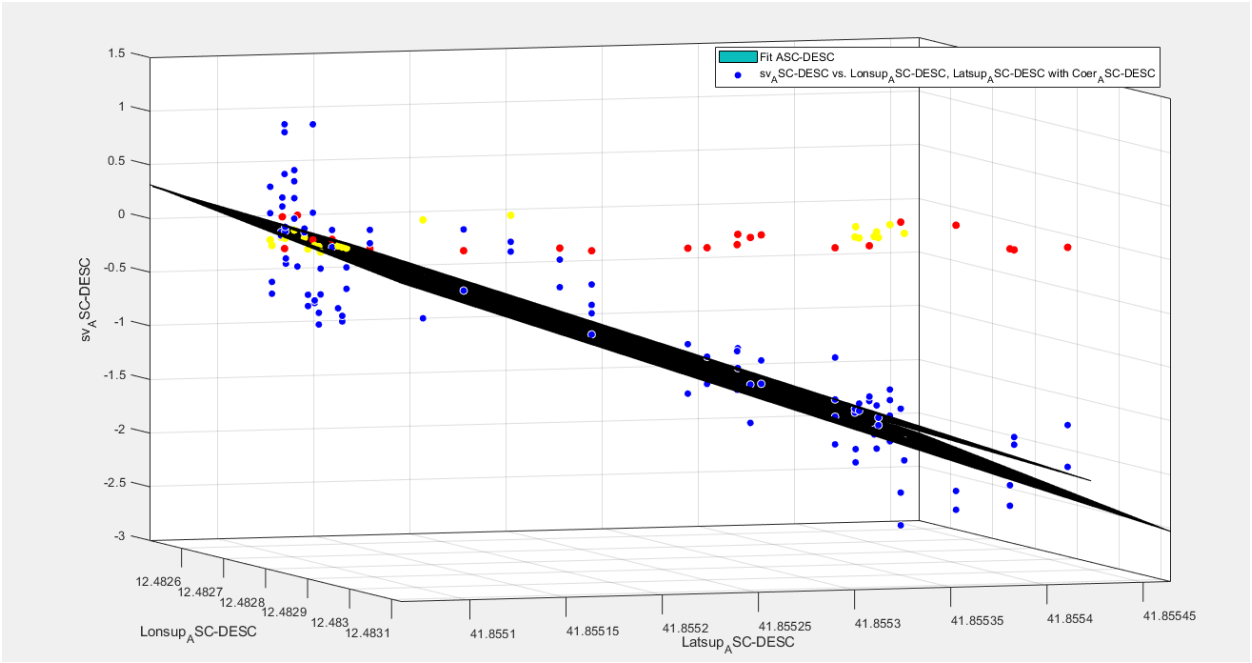

Figure 24: Surfaces derived from ascending orbit, descending orbit, and their average.

Linear interpolation works well for buildings showing homogeneous displacements or those that increase linearly over the building dimensions; however, it cannot reliably represent subsidence affecting only a portion of the building. In such cases, a higher-degree interpolation might better capture these aspects. Nonetheless, for diagnosis purposes, it is also necessary to consider the time series of displacements, as it provides information on the evolution of the ongoing phenomenon. While the literature describes more advanced methods for interpolating spatial points, such as TIN or kriging [38], these techniques are often complex for practical use by engineers. In this study, a simpler interpolation approach was deliberately chosen, with the aim of providing a method that is both accessible and practical for engineers, while still being effective for analysing SAR data.

Case Studies

After analysing the data, the next phase involved investigating some case studies represented in Figure 25. Two of them was chosen with the probability of having differential settlement and one without in order to see if the procedure could work. Building in this area has already been studied in several works [34].

Figure 25: Area of the case studies.

Case A: Residential Building

The first building considered is located in the Rome VIII area, coordinates 12.482153 41.857200. It is situated in an area characterized by high deformation velocities affecting multiple buildings. Using the procedure described previously, the following building sheet can be derived Figure 26.

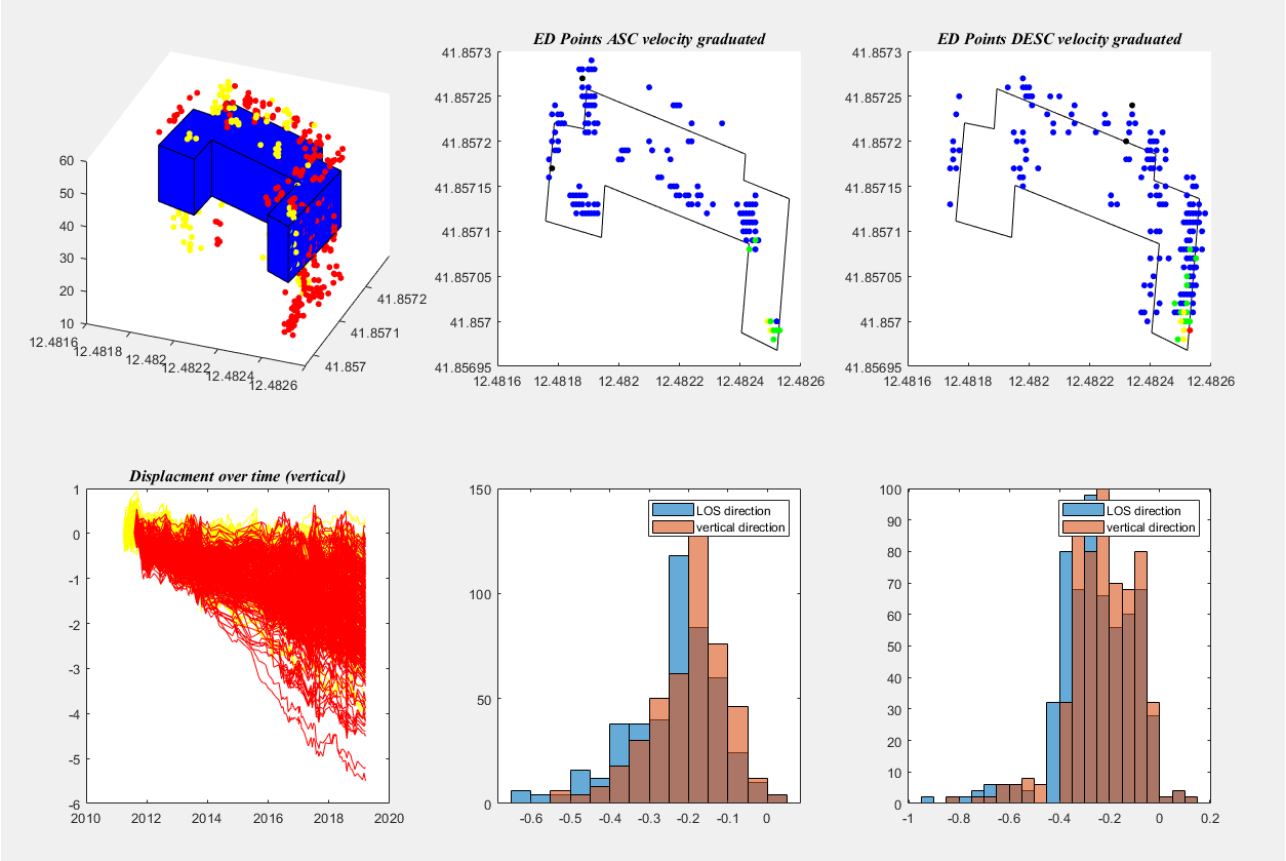

Figure 26: Building sheet for the residential building.

It can be observed that the building experiences differential settlements that vary differently over time. When creating the building model, the estimate of the minimum height appears incorrect because there is no point accumulations detected at the base; this is probably due to the building's base being hidden by territorial obstacles. This issue was improved by considering both satellite orbits for defining the height and accounting for the 5-meter offset between them. The corrected result is shown in Figure 27.

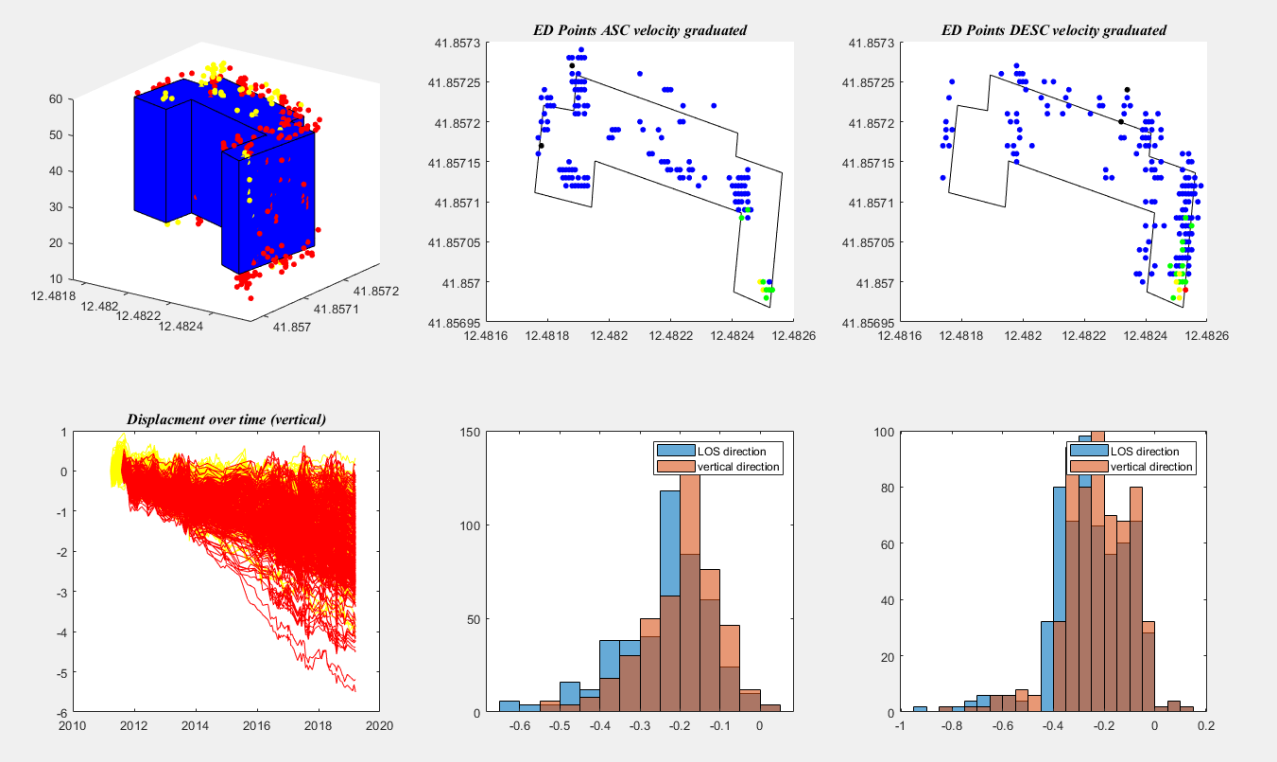

Figure 27: Building sheet for the residential building with modified estimated height.

The image also shows points with higher deformation velocities concentrated at one corner. To analyse displacements, the surface described earlier was created, obtaining the following results Figure 28.

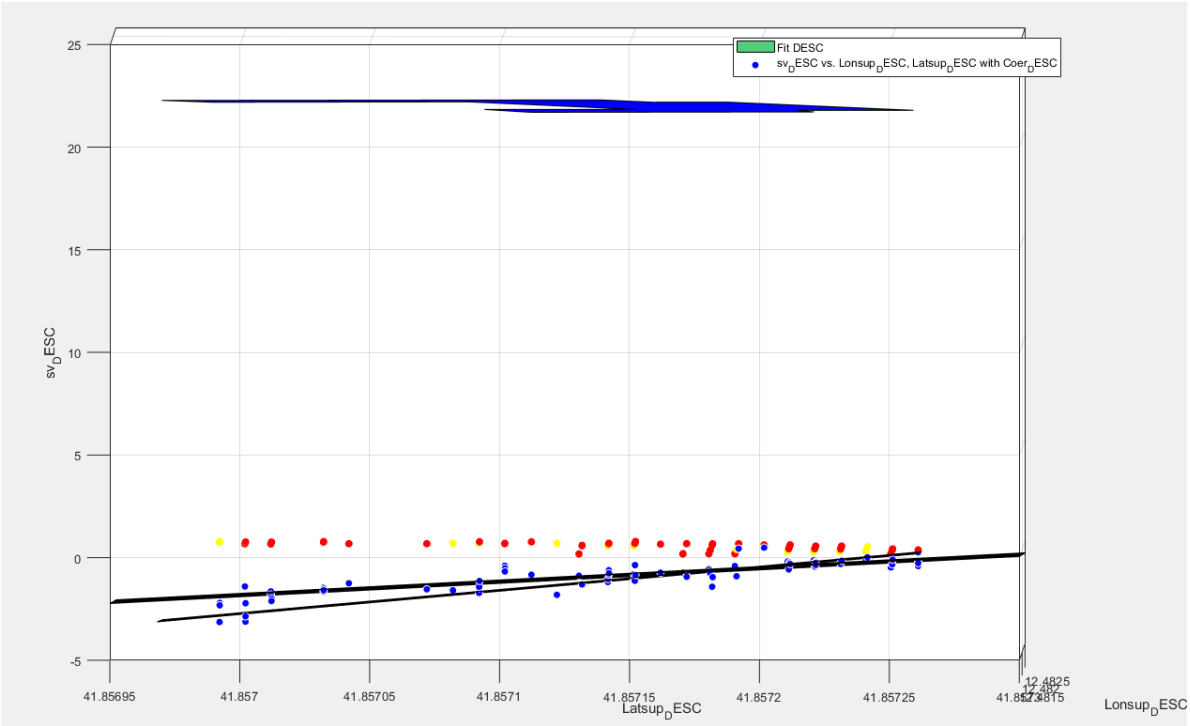

Figure 28: Displacement surfaces derived from ascending and descending orbits.

In this case, the surfaces differ from each other, likely due to the points with higher velocity on the corner not being visible in one of the orbits. Additionally, analysing the two orbits separately shows that a linear surface is a good estimate for displacements over the building except at the corner. In such cases, it is considered appropriate to investigate whether surfaces obtained through higher-degree interpolations could provide more accurate estimates. Cases like this suggest, as mentioned before, the importance of investigating the nature of displacement evolution over time to understand if the displacements are stable or if the settlement progresses, and at what speed.

Case B: Courtyard Building

The second building studied is located in the same area as the previous one, coordinates 12.484765 41.855483. It is a courtyard building experiencing high displacement velocities, which motivated its selection.

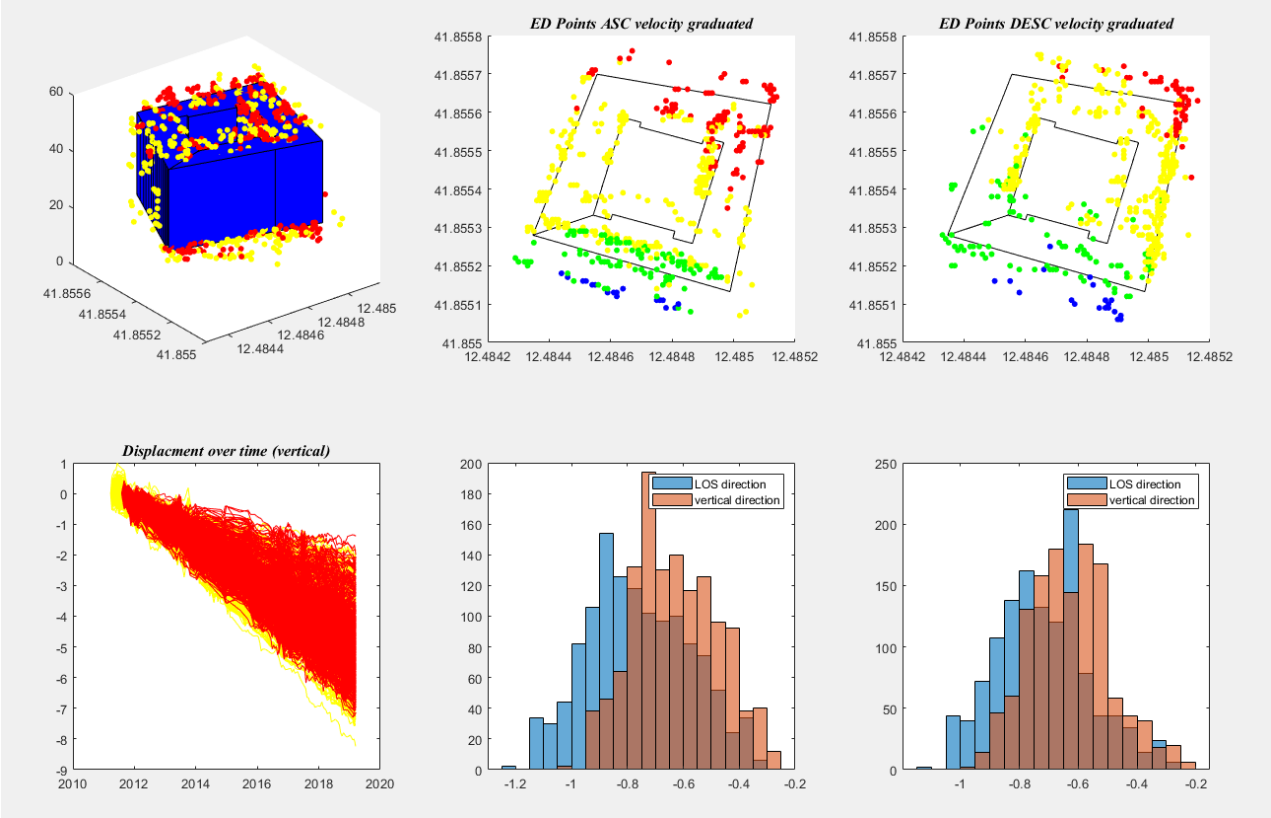

Figure 29: Building sheet for the courtyard building.

As shown in Figure 29, the building is subject to different average deformation velocities, implying differential settlements of the points, as can also be seen in the displacement graph. The displacement surface was then created, yielding the following results (Figure 30).

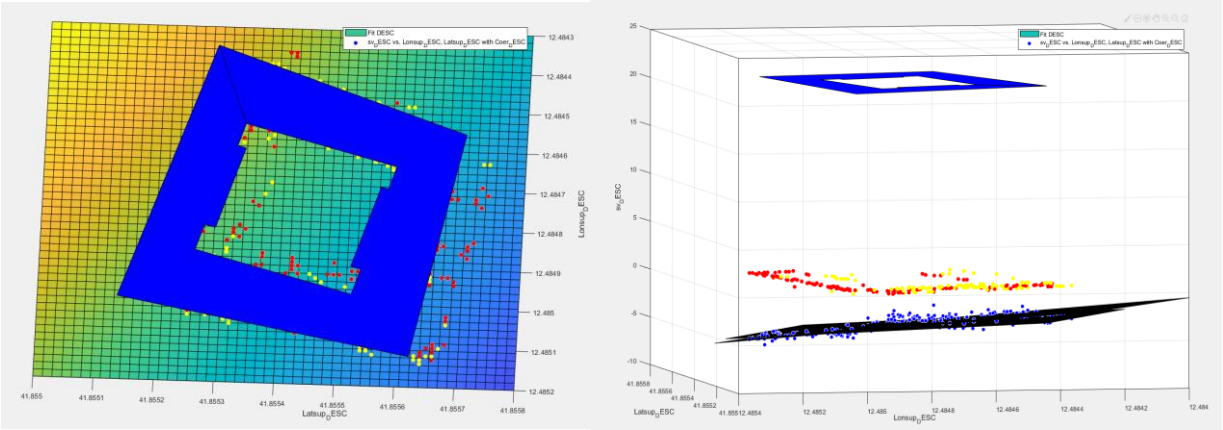

Figure 30: Displacement surface for the courtyard building.

The two orbits provide practically the same result; the values obtained from the average surface could therefore be verified on-site to assess their accuracy. In this case, creating the surface by interpolating points with coherence greater than 0.3 and points with coherence greater than 0.7 does not produce significant differences between the two resulting surfaces.

Case C: Warehouse

For the third case, a very simple building was chosen, not subject to significant displacement velocities and without surrounding obstacles. The selected case is an industrial warehouse with coordinates 12.471990 41.844468, not far from the previous cases but outside areas with significant settlements. The building sheet is represented in Figure 31.

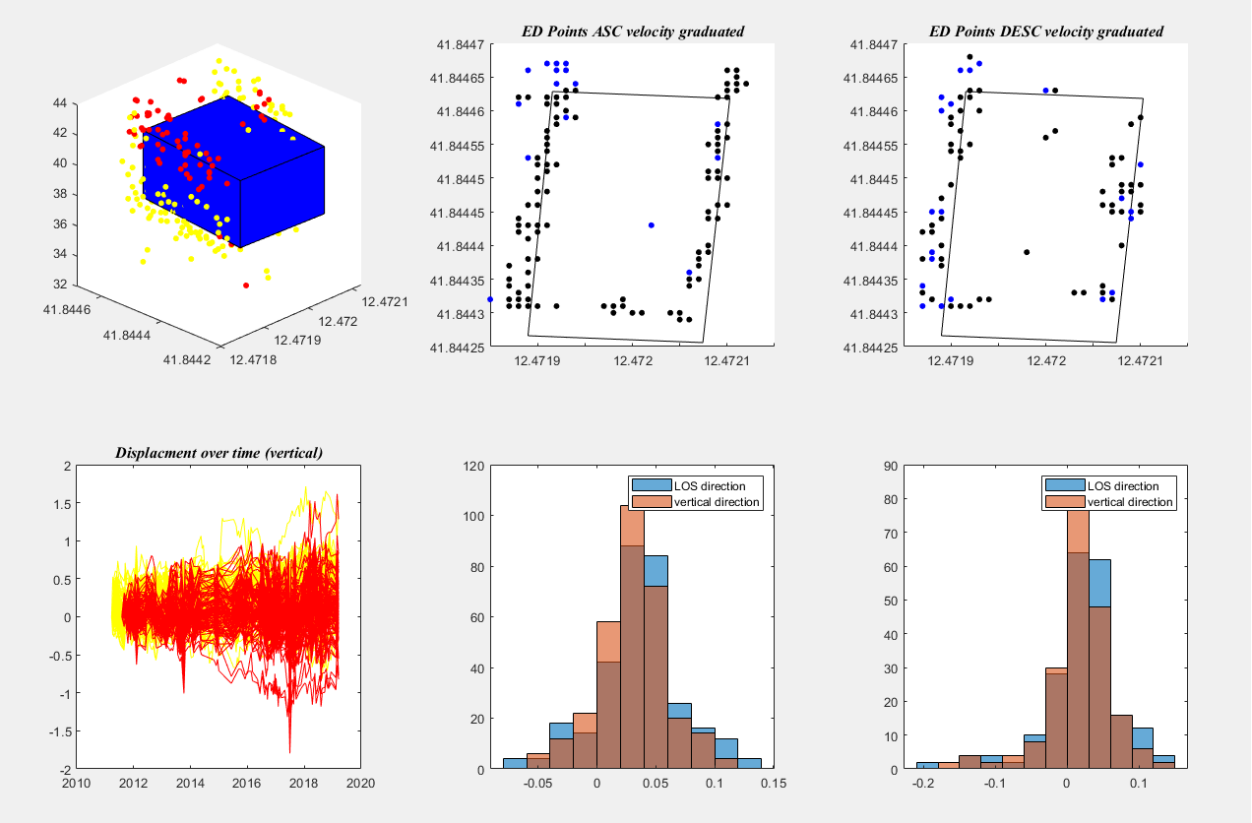

Figure 31: Building sheet for the warehouse case study.

As seen in the image, in this case the velocity distributions are little variable among themselves, as confirmed by the displacements which are both very low and homogeneous across the points. Here, higher coherence values were also compared to the previous cases, as expected since the satellite does not detect large displacements. The displacement surface created is show in Figure 32 where the surfaces are practically overlapping, horizontal, and without downward displacements.

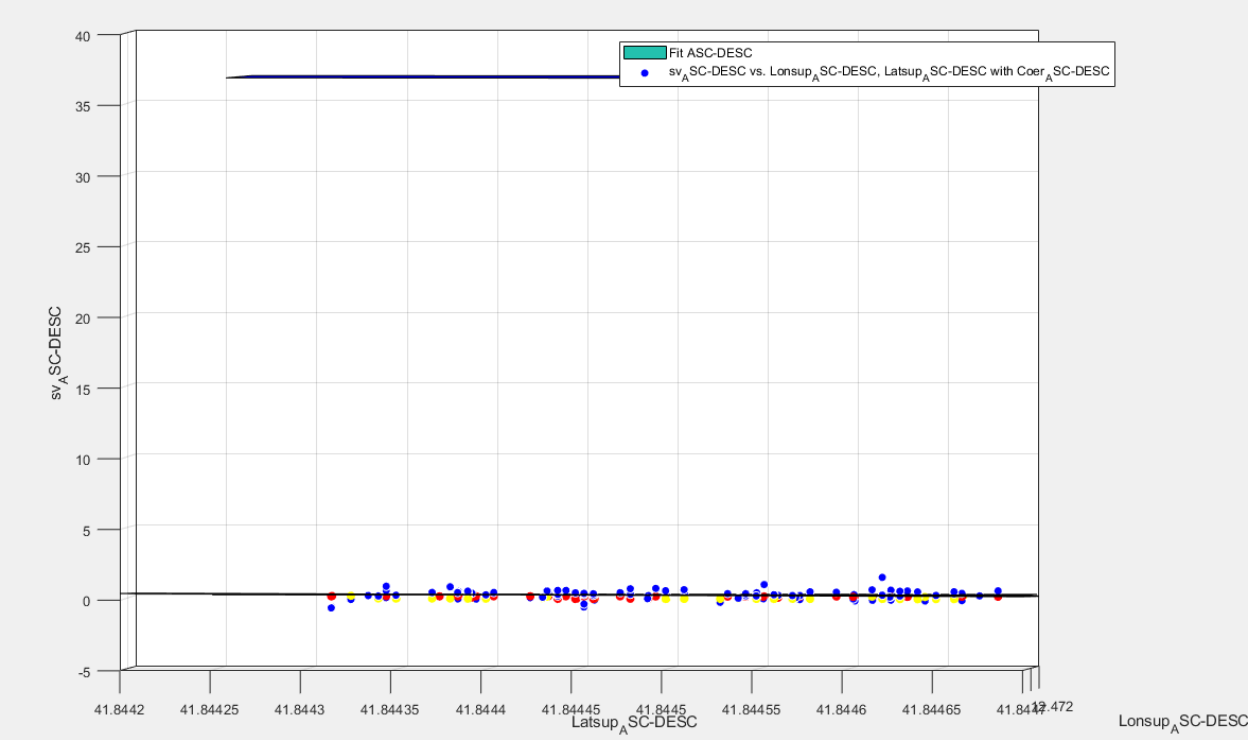

Figure 32: Displacement surface for the warehouse case study.

The case studies presented above primarily served to validate the extraction and analysis procedure for buildings; this procedure proves to be a valid tool for quickly investigating buildings potentially affected by differential settlements and, subsequently, for exploring some aspects of the SAR data.

Surface Development and Time Series

As mentioned earlier, depending on the building under analysis, the surface interpolated with a linear method might not adequately capture displacements affecting only a portion of the building. An example is the case study of the "long" building, where some points on a corner have higher displacement values than others. In such cases, higher-degree interpolation or other methods might provide better results. In this case, after some trials, a piecewise linear interpolation method was chosen, which can adequately capture isolated displacements and gives good results for the studied cases. This method was applied to the previously considered case studies, and the results are shown in the following Figure 33 and Figure 34.

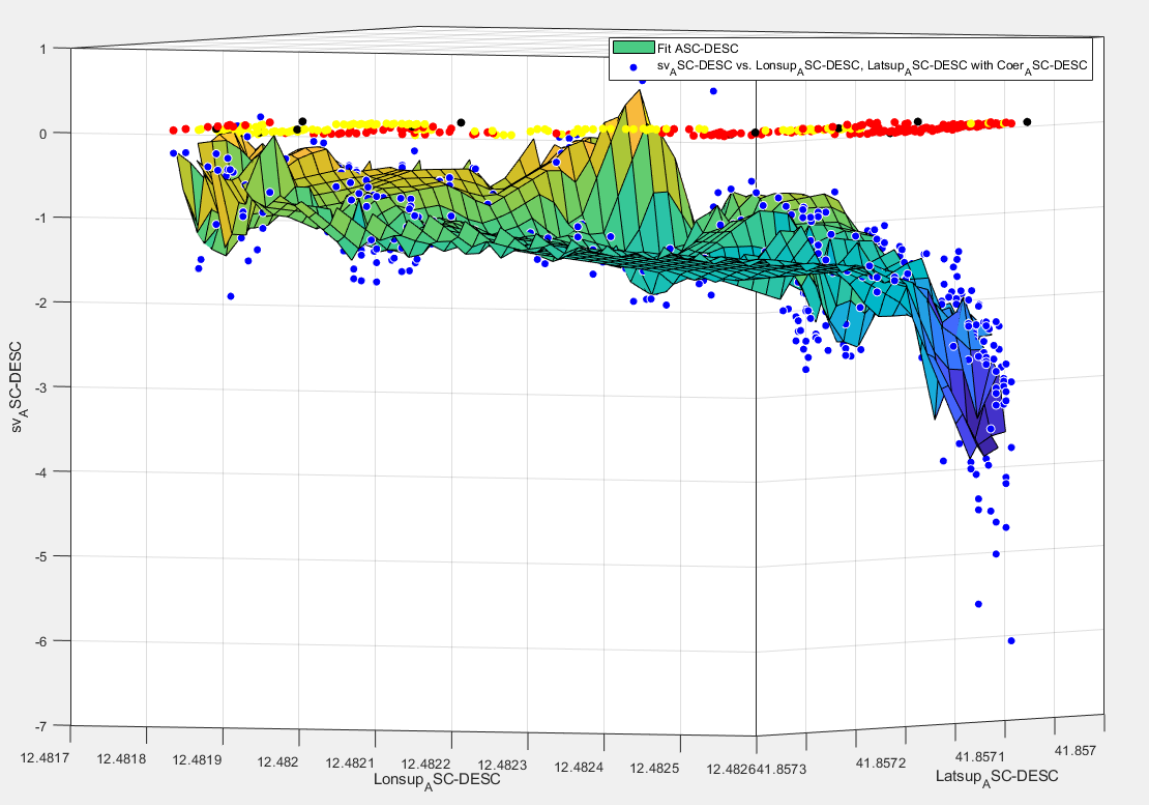

Figure 33: Piecewise linear surface interpolation.

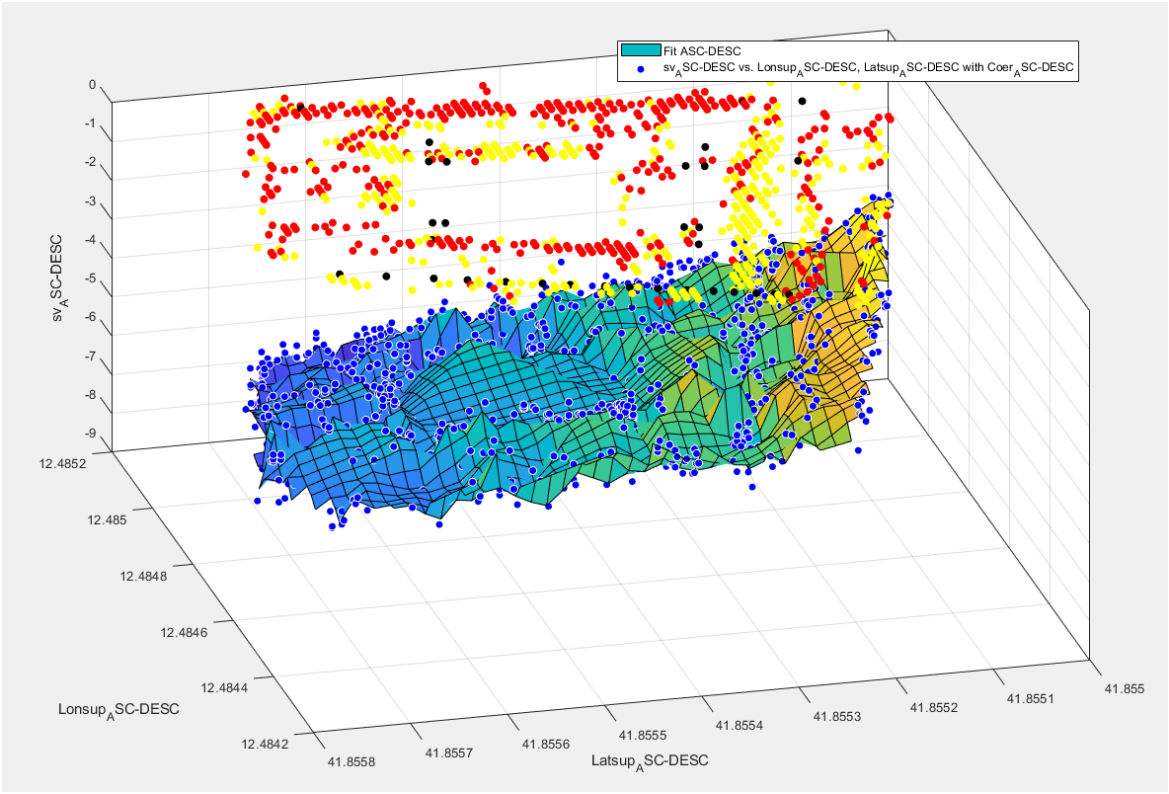

Figure 34: Piecewise linear surface interpolation.

For the warehouse, no further surface studies were carried out with other methods since it would not produce any result, as the surface is practically a plane due to the lack of settlements. From the above, it was seen that different methods can be used to estimate point displacements, to be evaluated case by case. Furthermore, a dedicated method could be studied specifically for this type of data. During the study of surface generation, another methodology was hypothesized to evaluate the presence of differential settlements affecting the building. The idea is to subdivide the building into small areas and perform statistics on the points belonging to them to better capture the fundamental aspect of the problem: vertical displacements. This procedure was also conceived to develop a method that uses simple calculations to determine the presence or absence of potential problems in the building and to develop code capable of analysing large areas and selecting problematic buildings. However, this method was not explored further because of two complications: one related to how to subdivide the building and the other concerning how to best estimate "average" settlements. This can be also useful in order to better consider the uncertainties of the SAR data. The note is left in case this topic is considered interesting for future development. The following Figure 35 schematically illustrates this idea.

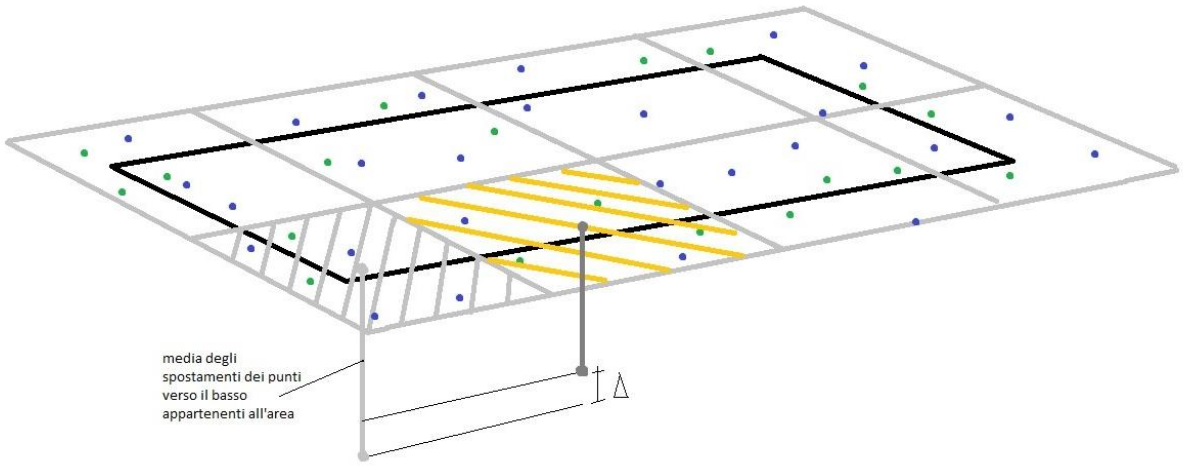

Figure 35: Hypothetical subdivision into areas to verify differential settlements through simple statistical parameters.

Displacement Velocities

Another issue investigated concerns the evaluation of displacement trends over time. Considering again the "long" building, it is possible to see from the time series of displacements that some points appear to increase their rate of settlement.

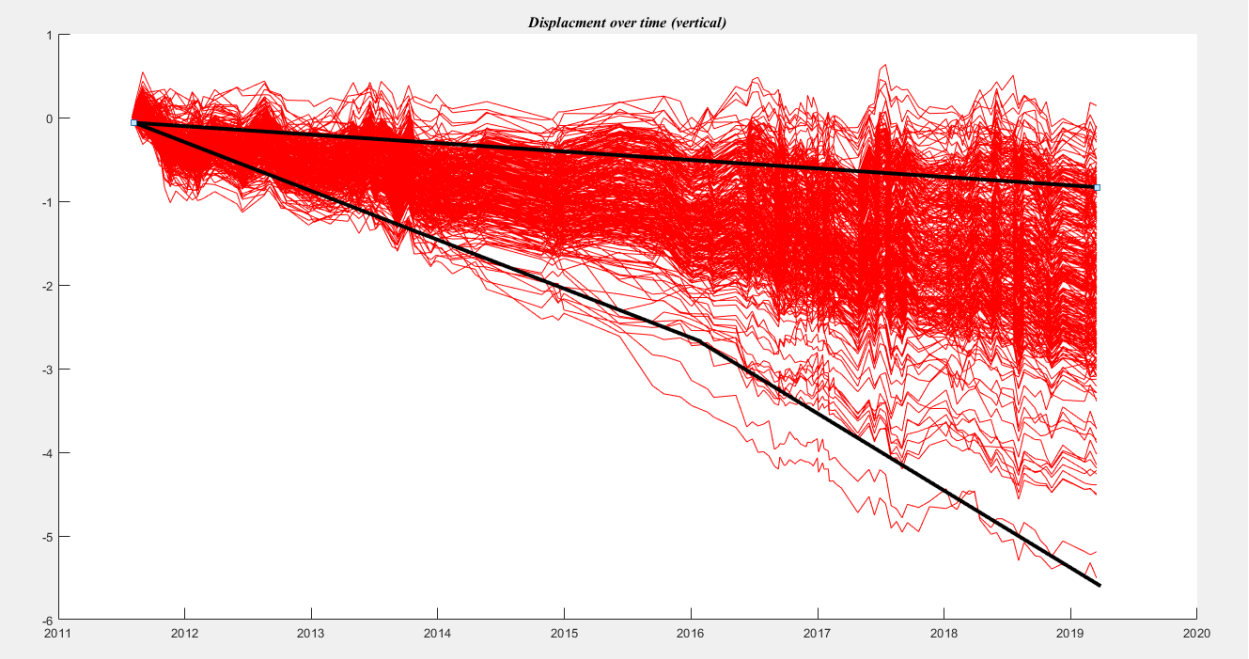

Figure 36: Time series analysis to verify displacement trends.

This may suggest a possible worsening of the building's conditions in the future. More generally, knowing the temporal history of displacements allows evaluating the advancement stage of the displacements, identifying phenomena that may have stabilized or those continuing their evolution. For example, considering the time series represented in Figure 37, it is possible to hypothesize that the points shown in the right figure have likely exhausted the displacement phase, while those in the left figure appear to have started the deformation phenomenon and then increased the propagation velocity.

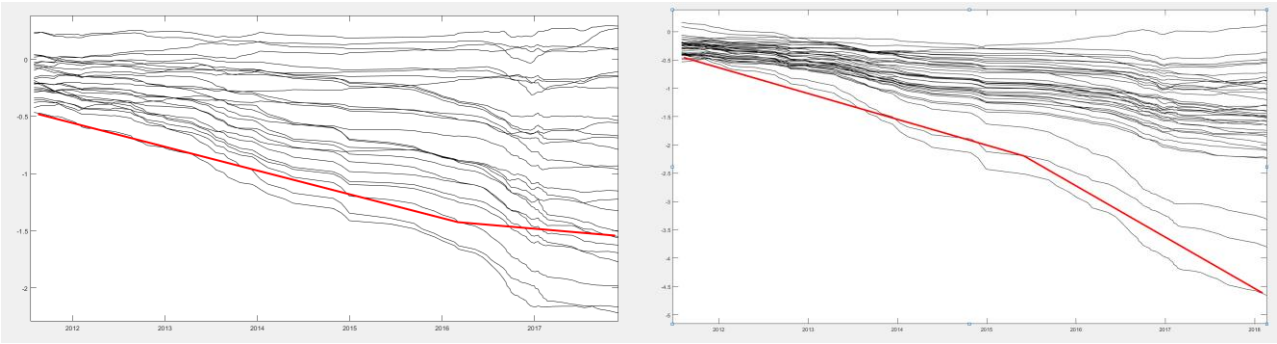

Figure 37: Difference between two possible types of displacement trend behaviour.

It must be considered that time series start from zero displacement at the beginning of the time series; in reality, this could correspond to a point already having displacements greater than zero from years before the start of satellite data recording. While analysing the time series, it was noticed that data filtering is necessary to obtain a clearer visualization of the ongoing trend. Applying a 24-period

moving average (which corresponds to the number of measurements in a year), the following Figure 38 is obtained. Using the clean data, changes in trends can be better identified.

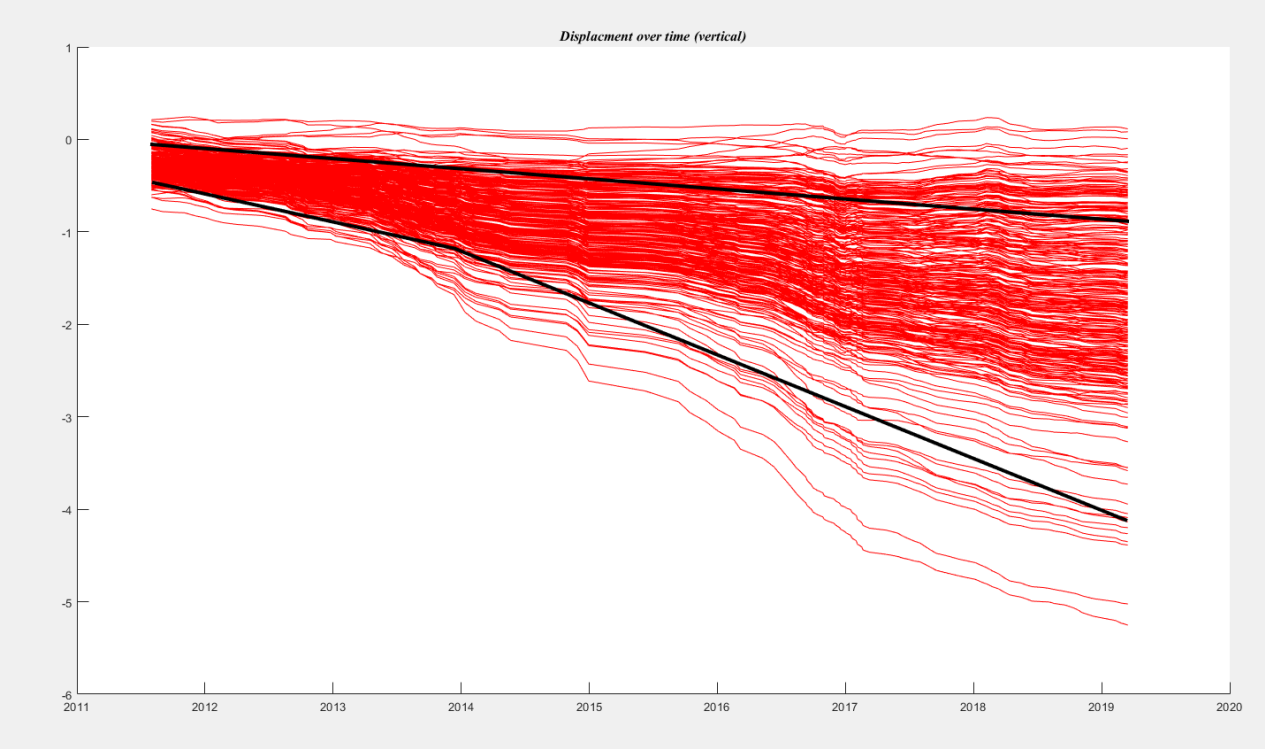

Figure 38: Trend identification using filtered points (24-period moving average).

Use of SAR for building structural assessment - Combining SAR and Simplified Method

Simplified Estimation

Alongside the investigations on the SAR points, the question arose whether it is possible to estimate the damage using simplified methods. To do this, reference was made to the classical theory of shallow foundations. The settlements of shallow foundations are vertical displacements, the integral of the vertical deformations of the soil beneath the foundation. There exist simplified methods based only on the building's geometric parameters that allow damage estimation. Considering Figure 39, it is possible to relate different damage classes with the geometric parameters θmax, βmax, δmax.

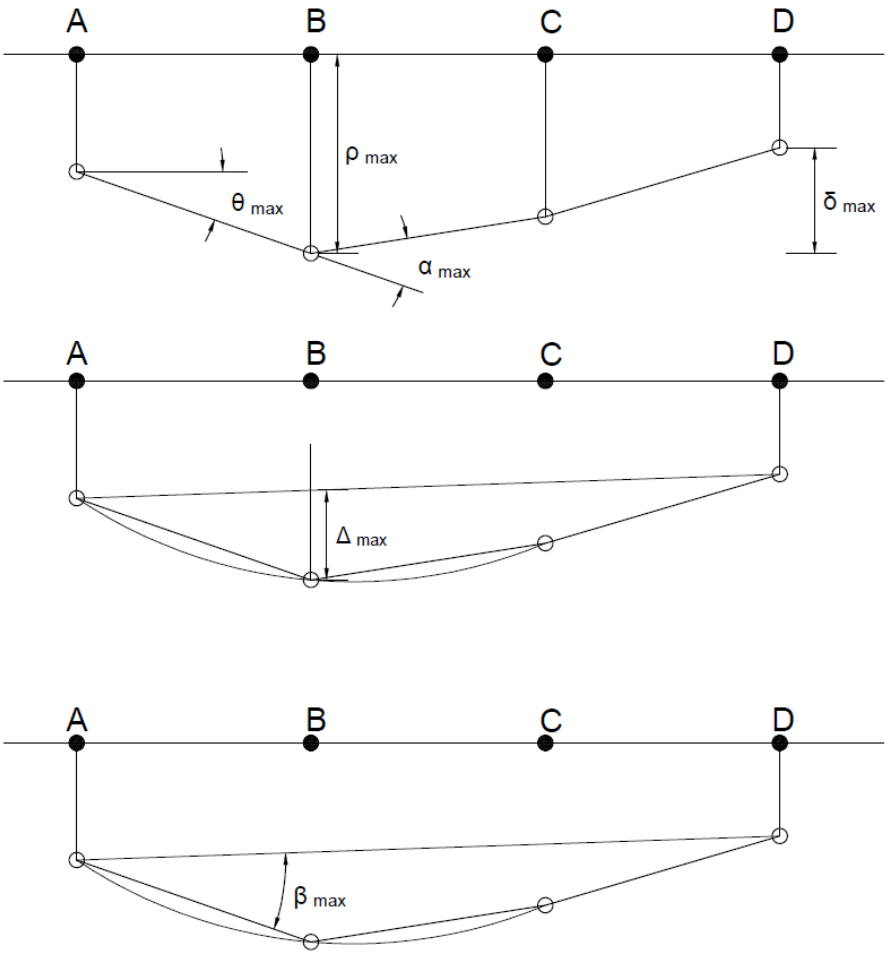

Figure 39: Geometric parameters considered by the simplified estimation.

By comparing displacement values derived from SAR data with tables and graphs from various authors, it is possible to estimate the damage of the building under consideration. These graphs were created statistically, and in our case, the following Table 1 was taken into account [39]:

Potential Damage	tan β
Limit beyond which problems may arise in machinery sensitive to deformations	1/750
Limit for truss structures	1/600
Safety limit for buildings where cracking is not allowed	1/500
Limit beyond which the first cracks may appear in infill walls	1/300
Limit beyond which inclinations in tall buildings can be observed	1/250
Large cracks in masonry	
Limit for infill walls with h/L<1/4	1/150
Limit for evident damage in buildings	

Table 1: Limits for possible damage in buildings in relation to parameter β.

Choosing a building with a simple structural scheme (hypothesis), this method could be tested on them to compare results with reality, which would be useful to validate this simplified method for use combined with satellite data. To use a simplified method to estimate a building's health status, a methodology using the proposed estimation is done. Taking a building in an area affected by settlements, displacements were derived by generating a surface as described earlier, and the deformation status was evaluated by comparing with the simplified method tables seen before. In particular, in Figure 40 below shows the building's outline considered in QGIS; thanks to the procedure described in previous section, data related to this building were extracted and subsequently analysed.

Figure 40: Image of the building used as example (QGIS).

The extracted data were then processed using Matlab, with the summary sheets described earlier and show in Figure 41, Figure 42 and Figure 43, obtaining the displacement surface shown in Figure 44.

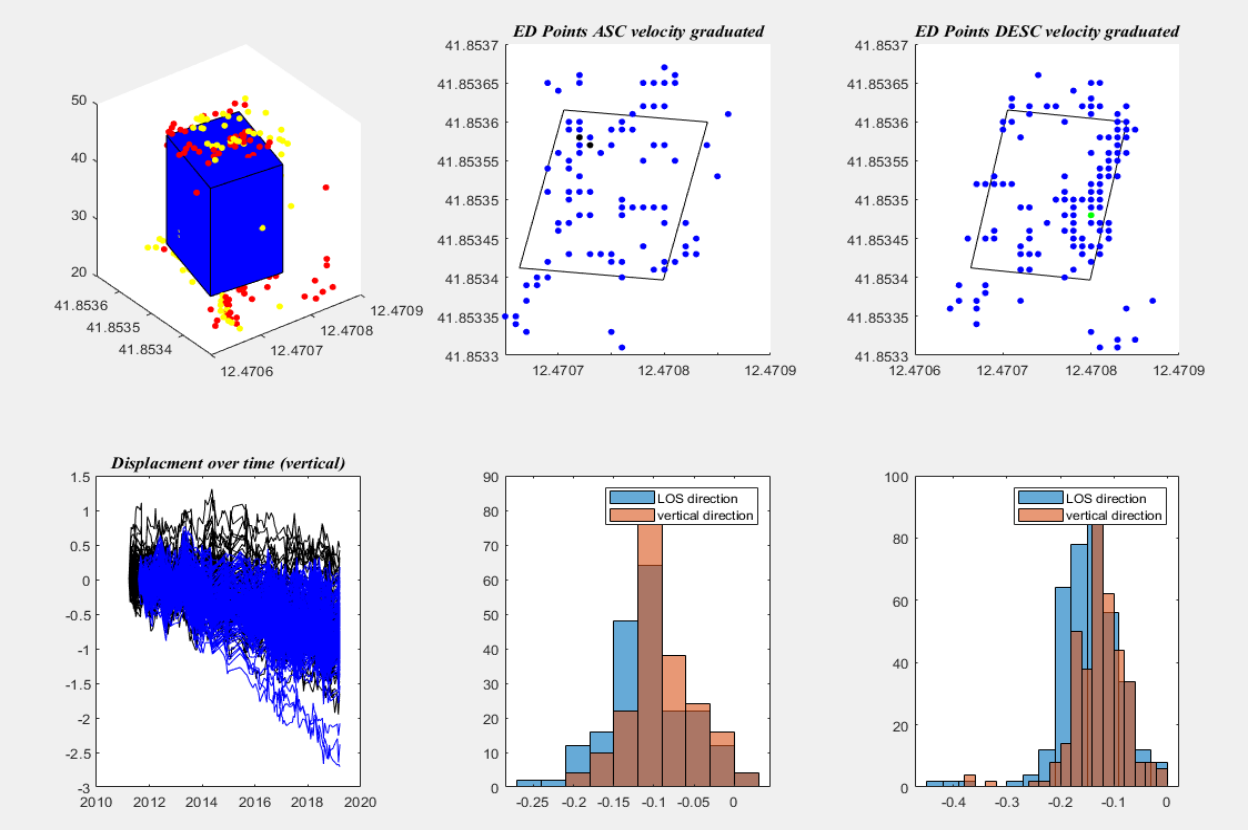

Figure 41: Summary sheet of main data for building analysis.

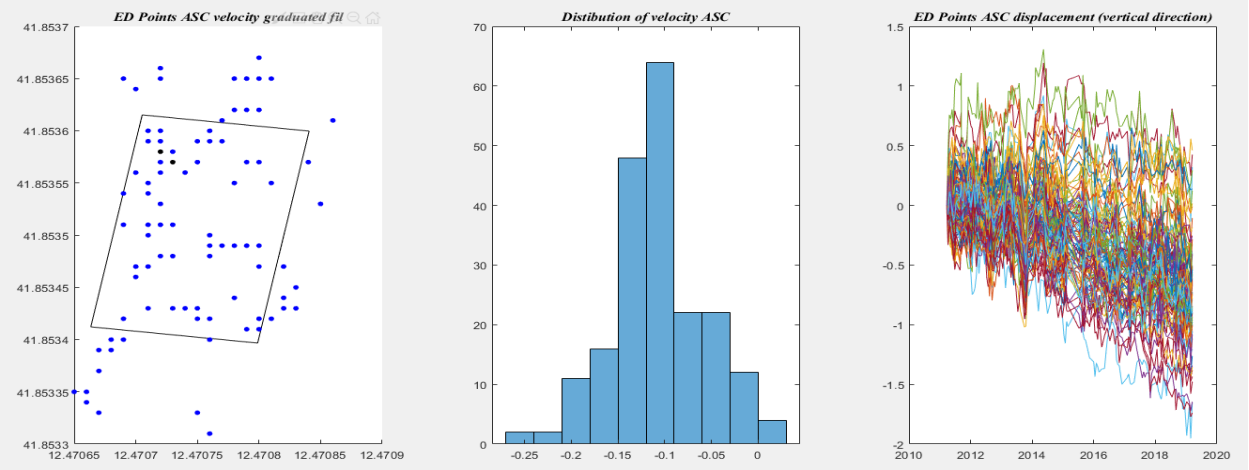

Figure 42: Building data relative to ascending orbit.

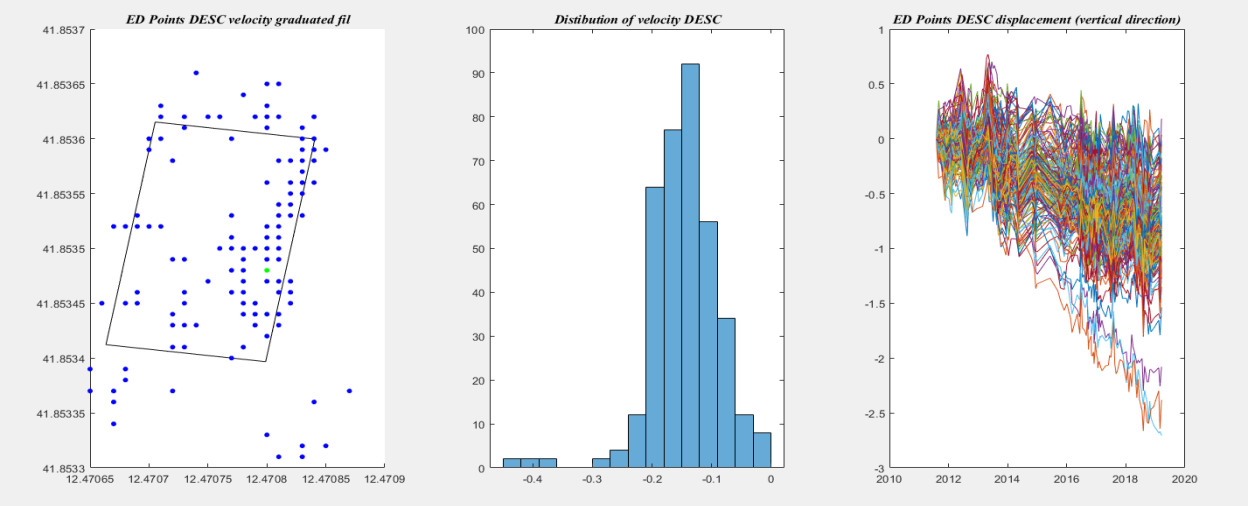

Figure 43: Building data relative to descending orbit.

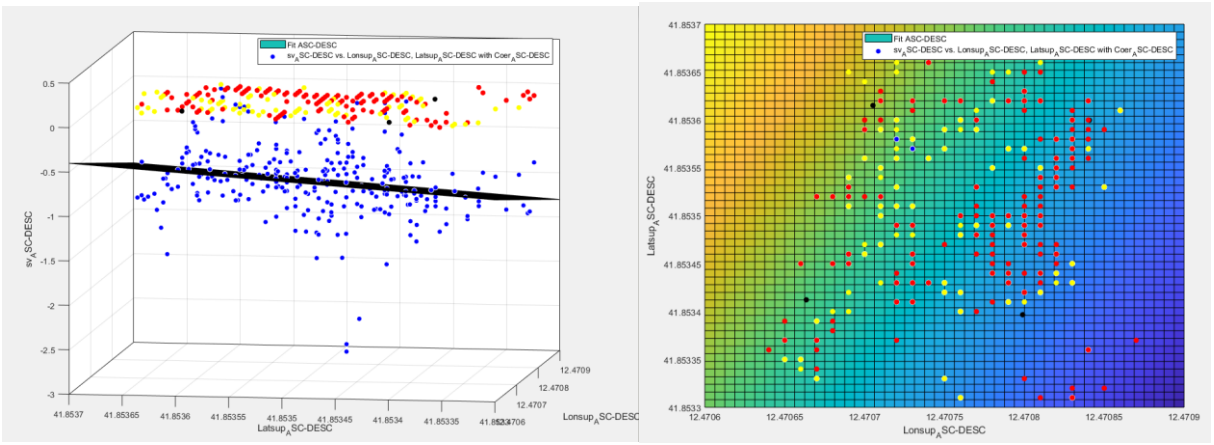

Figure 44: Displacement surface.

In this case, linear interpolation provides a good result. Displacements to be applied to various pillars were then evaluated, and through them, the simplified procedure was applied. Considering both directions, a maximum tangent beta value (reference Table 1) of 0.0012 was found, a value close to the limit beyond which machinery problems may arise. There are no problems regarding cracks or building stability.

A further step was investigating the nature of displacements over time, to establish or better hypothesize a possible future damage state and plan interventions.

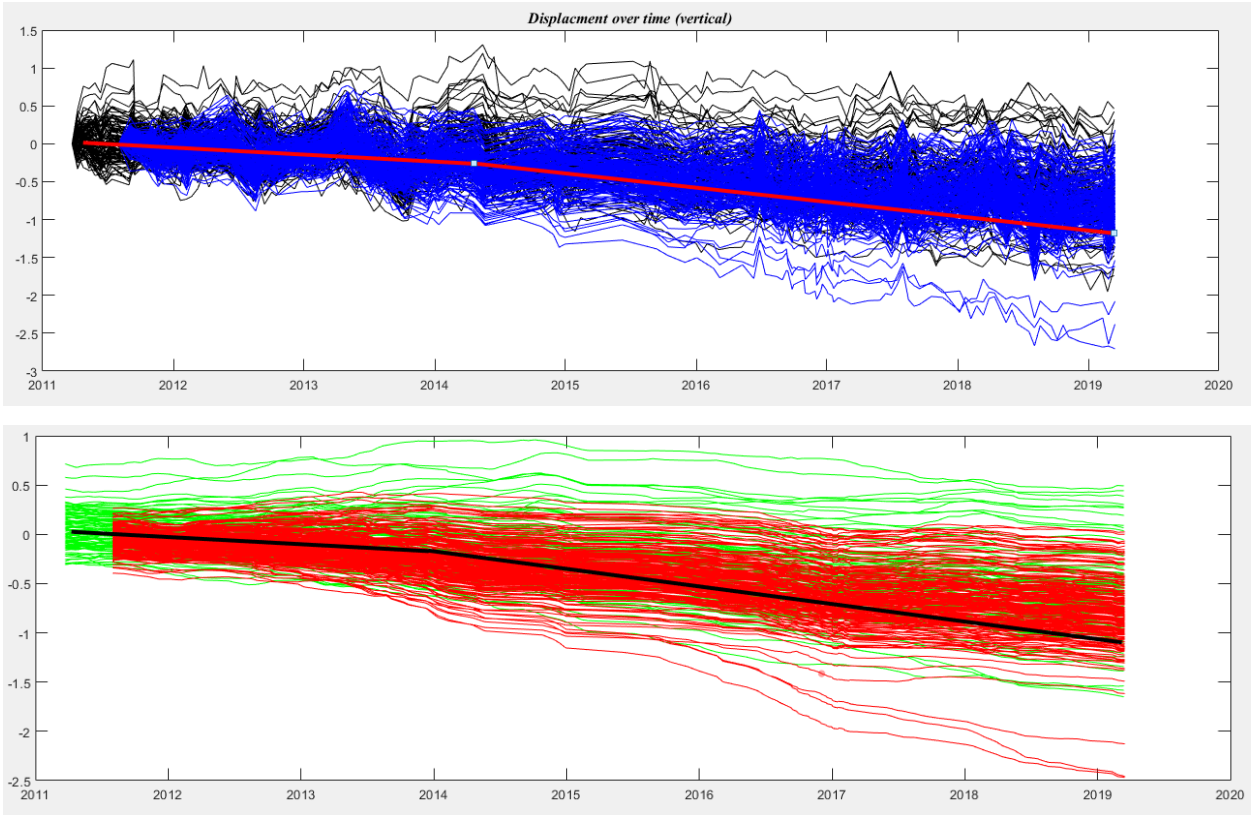

Figure 45: Time series analysis. Unfiltered series (above) and series filtered with 24-period moving average (below).

From Figure 45, it is seen how the phenomenon seems to have intensified starting around 2014. Hypothesizing that displacements continue maintaining the slope of the second straight segment shown, the following hypotheses can be made:

- Displacements will be uniform over the building area; in this case, there will be no differential settlements as the building will continue to settle uniformly, keeping relative rotations between spans unchanged.
- Displacements of one corner/side of the building will settle faster than the rest; in this case, relative rotations between spans may eventually create problems.

Analysing time series of some points on building corners, it appears that the first hypothesis applies here, see Figure 46.

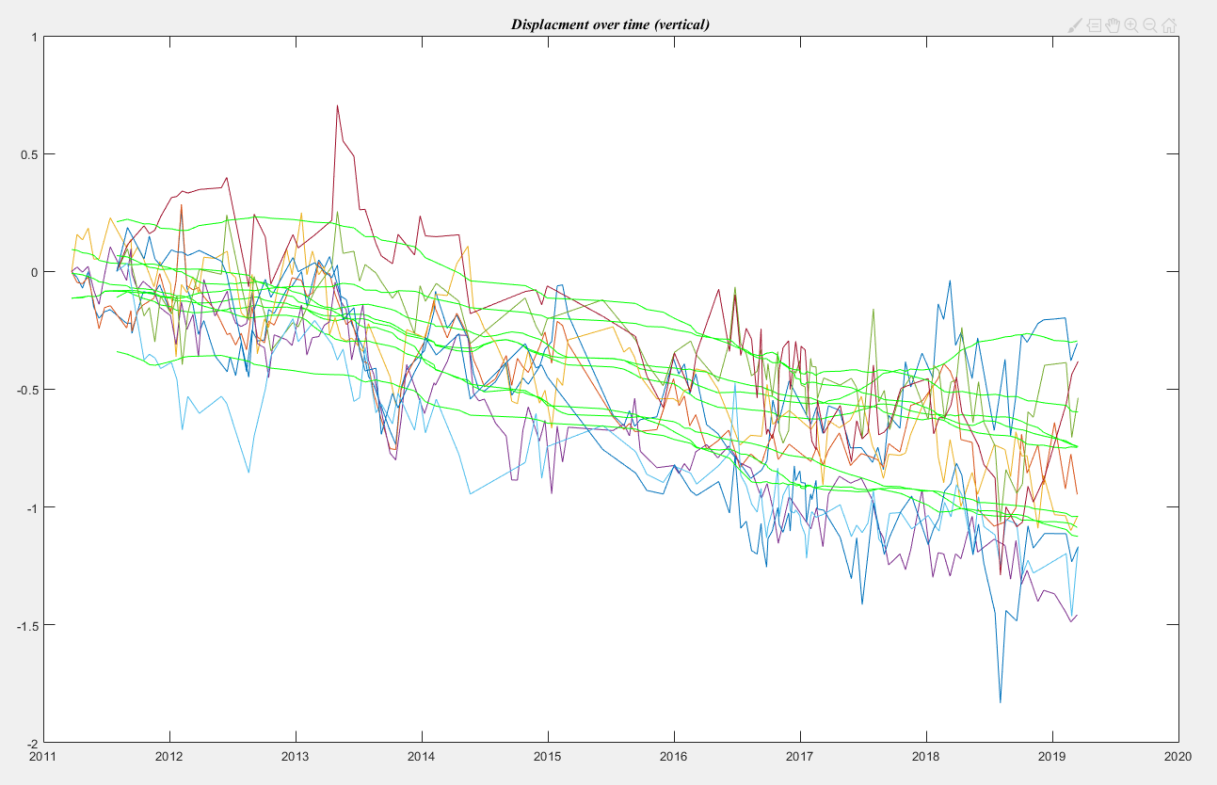

Figure 46: Time series of some significant points on the building (cm).

Supposing, for explanation, the second hypothesis applies, it is possible to estimate when differential settlements causing problems might occur by extrapolating from the displacement time series a possible future displacement trend. Considering, for example, the displacements in the Figure 47 below, the simplified procedure can be applied at a future time and conditions verified.

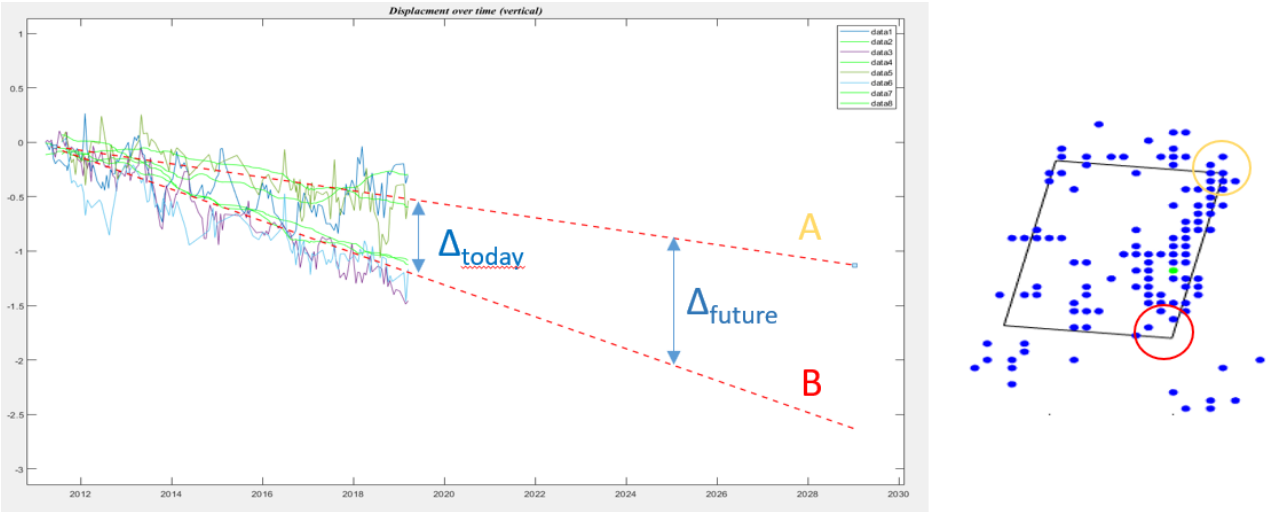

Figure 47: Hypothesis of differential settlements over time.

In this specific case, considering the situation in the year 2028, a tangent beta value (referencing Table 1) of 0.002 would be obtained, a value at which first cracks could appear.

At the conclusion, a summary diagram is proposed that schematically illustrates the procedure described in the previous sections. The purpose is to provide clear guidance on the various aspects to consider during the study of satellite data and a possible investigation method using such data. This diagram serves as a useful tool to guide subsequent study and intervention phases, promoting an integrated approach between simplified methods and detailed analyses, with the aim of promptly identifying potential risk situations and effectively planning corrective actions.

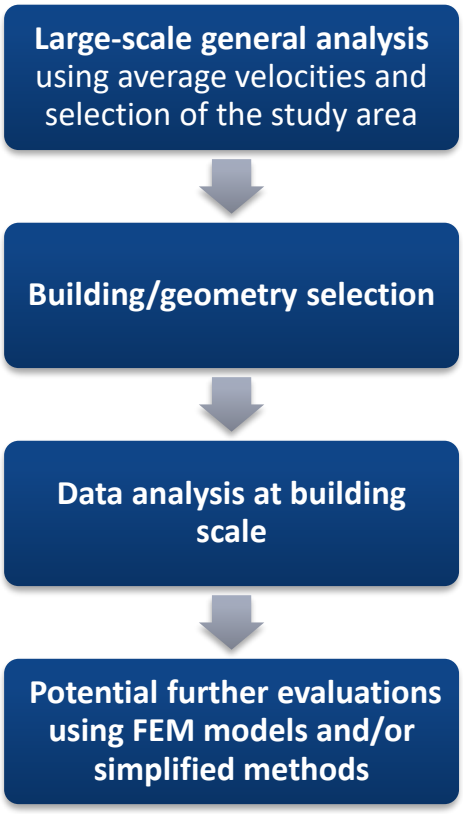

Use of SAR for bridge assessment - Apply SAR to Bridge case study

In this section, the application of satellite data to a civil infrastructure is presented, with specific reference to a bridge belonging to the T2 highway segment, that will be under study in the next chapter. The case study was selected not only because project documentation was available from the material analysis, but also because it represents a typical example of strategic infrastructure where satellite data can be helpful for monitoring. The selected structure is in the Aosta Valley, a region characterized by complex geomorphological conditions and subject to potential landslides and slope instabilities. In such contexts, the integration of satellite data into the monitoring process becomes particularly valuable, as it allows early detection of deformations that could compromise the safety of infrastructures. In continuity with what has been discussed in the previous chapter where satellite data were applied to buildings, this section aims to extend the approach to infrastructures, thereby exploring the potential of such data for large scale analysis.

To extend the contribution related to satellite data, beyond the datasets provided by CNR, the possibility of employing open-source data from regional geoportals was also investigated. These open data initiatives can significantly increase the accessibility and scalability of monitoring procedures. In this specific case, access was requested to the satellite datasets available on the Valle d'Aosta regional portal, which were then employed for the analyses now presented. To explore this potential, a simplified procedure was developed to assess the risk associated with differential settlements in bridge structures. The procedure provides a conceptual framework to understand how displacement data can be transformed into useful indicators for infrastructure performance.
In particular, a finite element model of the structure under study, Chantelle 2, was developed using the dimensional information extracted from the original design documents provided. The finite element model allows the simulation of the bridge's behaviour under settlement scenario. The model was subjected to differential settlement, and the resulting variations in internal forces were evaluated. Although the procedure is simplified and not intended as a fully calibrated structural assessment, it effectively illustrates the type of analyses that can be carried out on a larger scale once satellite-derived deformation data are available.

The broader objective is to show how the methodology can be generalized. By applying the same workflow to other bridges or infrastructures, satellite monitoring could serve as a first-level screening tool, capable of highlighting critical areas where detailed on-site investigations should be prioritized.

This vision aligns with the growing interest in combining remote sensing with structural engineering models to support risk-informed asset management strategies.

The first step consisted in comparing and analysing the landslide maps available on the regional geoportals, overlaying them with the infrastructure map and with the map of satellite data points corresponding to PS (Persistent Scatterers). As recalled from the previous chapter, PS are radar targets that maintain a stable reflective behaviour over time, thus allowing consistent displacement measurements across long temporal series.

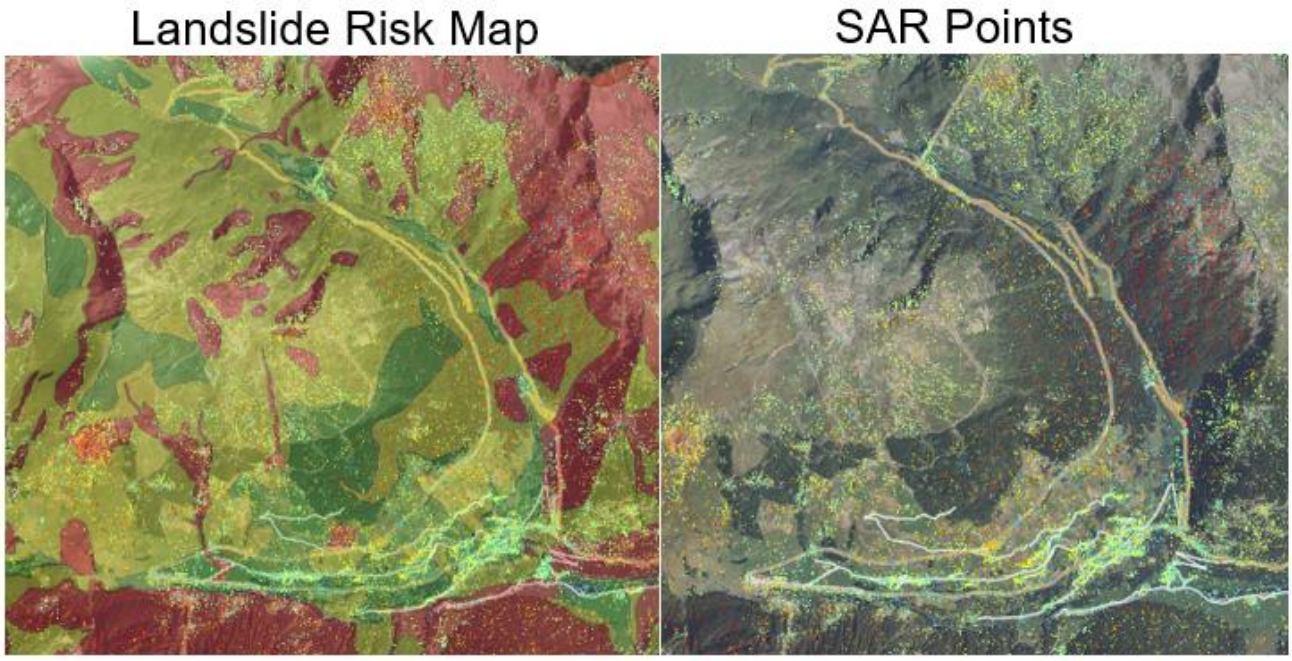

Figure 48: Landslide risk map and PS SAR points.

Through this combined analysis, visible in Figure 48, a specific structure, like said before, the Chantelle 2 viaduct, was selected as a case study where differential settlements appeared possible, as indicated by the temporal histories of the satellite data. The identification of the structure was carried out using its coordinates, which were available in the project documentation analysed.

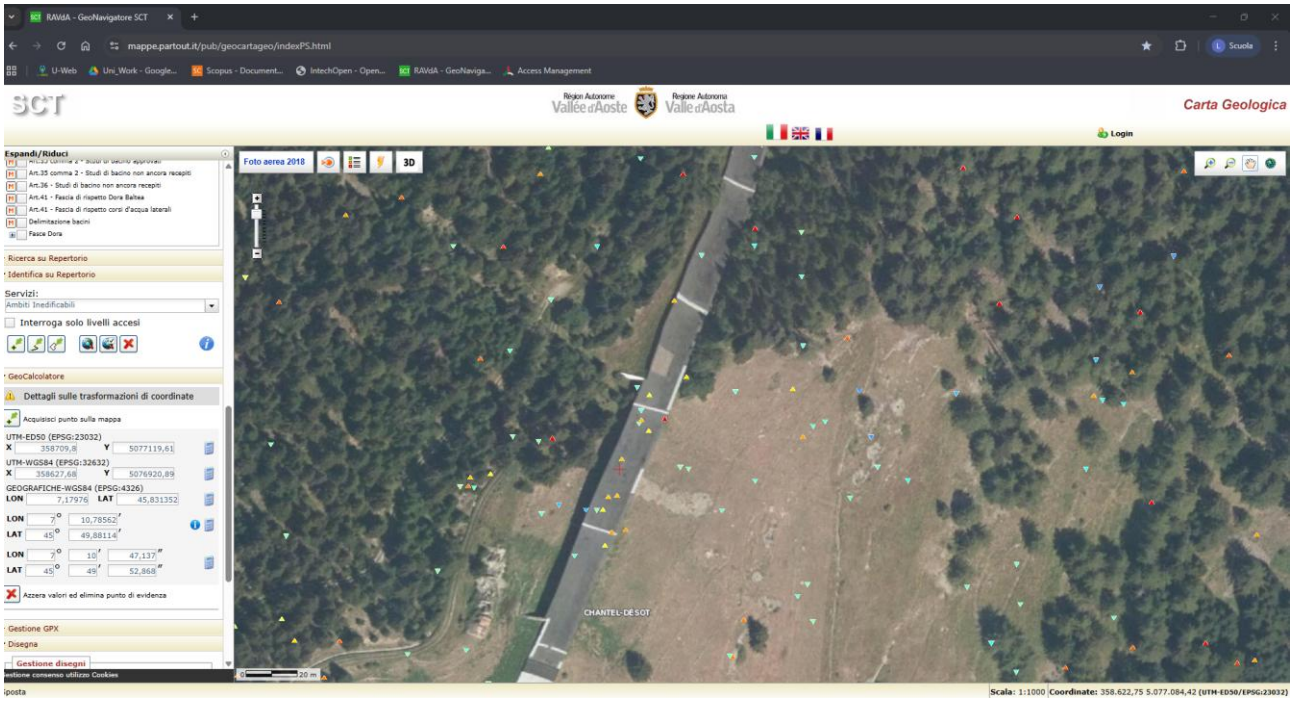

Figure 49: Valle d'Aosta geoportal.

Once the structure had been identified, the displacement values and displacement histories were extracted. In addition to simple visualization, the Valle d'Aosta geoportal provides a straightforward analysis dashboard, illustrated in the following Figure 50. This tool allows the temporal series of each point to be quickly examined, including the possibility of fitting trends or highlighting variations, thereby offering an immediate overview and rapid insight into local ground movements at the selected location.

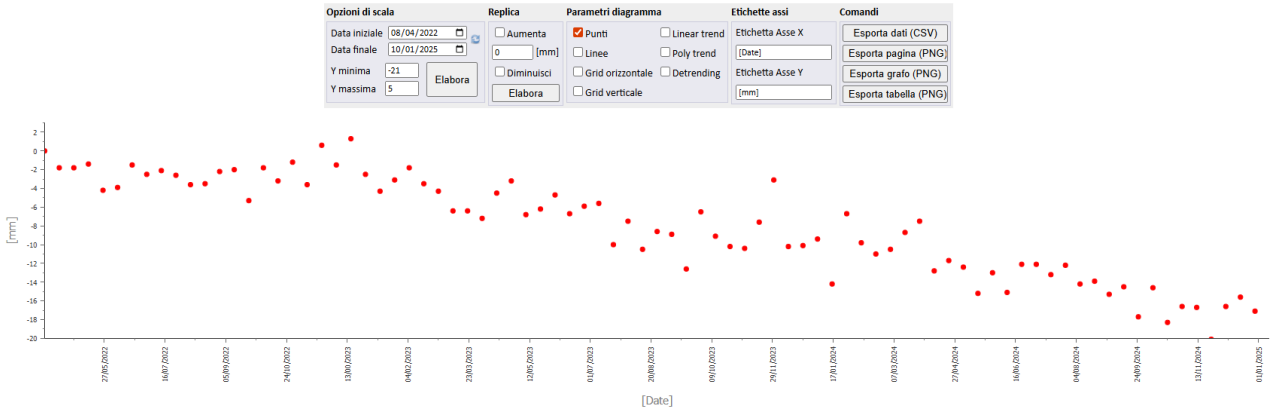

Figure 50: Valle d'Aosta geoportal analysis tool.

Using the analysis dashboard available on the Valle d'Aosta geoportal, several points indicated in the Figure 49 were examined. As also noted in the regional guidelines, it was observed that, for these points, the ascending and descending satellite orbits show different behaviours: in the first case, a negative trend indicates displacement opposite of the line of sight (Figure 51-bottom), while in the second case, a positive trend indicates displacement along to the line of sight (Figure 51-up). This condition is consistent with the presence of a possible landslide.

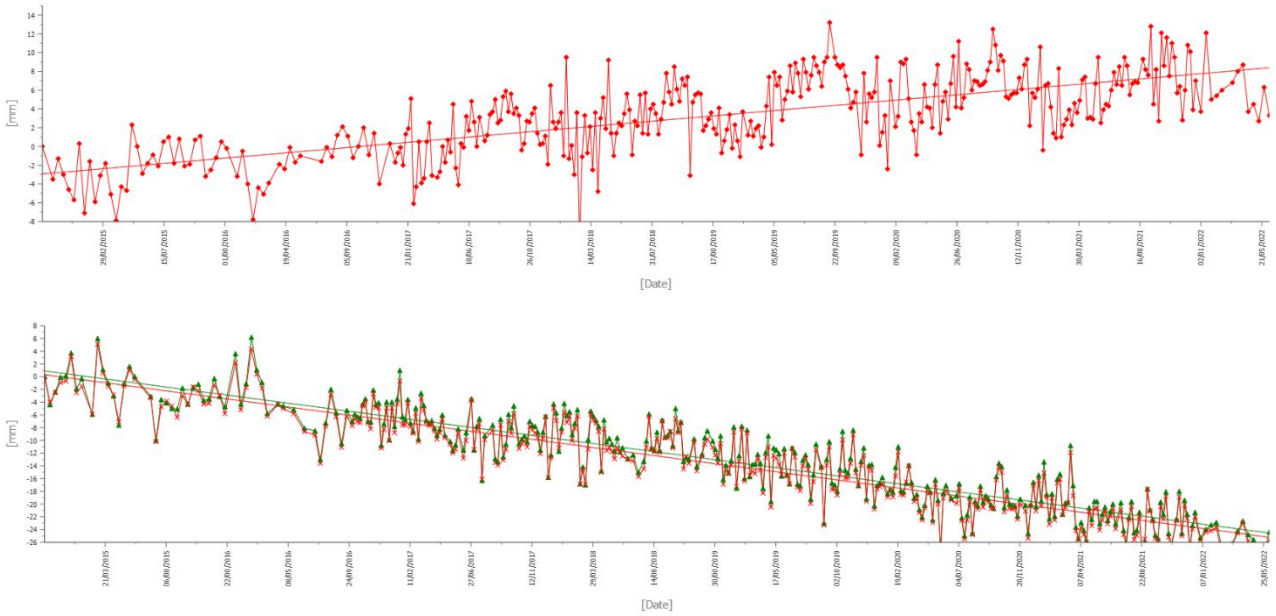

Figure 51: Displacement time series for some points along the selected bridge.

Since the direction cosines were not available, the SAR data could only provide a rough estimate of the displacements, which was then applied to the FEM model as an imposed settlement. Therefore, this analysis should be considered a preliminary demonstration of the methodology, while more refined and accurate investigations can be conducted once the complete geometric parameters are available. For instance, a surface like the one described earlier can be derived from the data, and the mean displacement applied to the bridge piles. Although more complex spatial analyses could also be performed, the primary goal is to maintain the approach as simple and practical as possible. When both ascending and descending orbits are available, it is possible to decompose the measured Line of Sight (LOS) displacements into their vertical (d_U) and East–West (d_E) components. In practice, the combination of ascending and descending geometries to retrieve the vertical and horizontal components of motion is often limited by the spatial mismatch between the two datasets. Each orbit observes the ground from opposite viewing directions eastward for ascending and westward for descending passes resulting in distinct sets of coherent points that rarely correspond to the same

physical target on the ground. As a result, the LOS measurements from the two orbits are generally not collocated, and a direct pixel-by-pixel decomposition is not feasible. To address this limitation, a spatial aggregation or interpolation approach is typically adopted. Over wide areas, the territory can be discretized into regular cells and average LOS velocities from both orbits are computed within each cell before applying the decomposition equations.

The model was created using the Midas Civil software (Figure 52). The structure was developed using beam elements (grillage model), which facilitates the extraction of results in terms of internal forces.

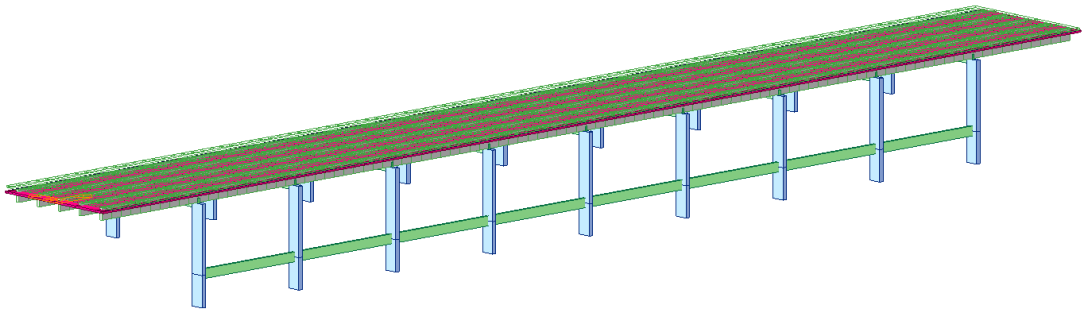

Figure 52: Finite Element Model of Chantel 2 viaduct.

The bridge deck consists of five continuous beams spanning eight spans of 10 meters each. The beams are illustrated in the following Figure 53, derived from the original design documentation. The piers are framed and composed of two rectangular columns connected by a cap beam on which the five continuous beams fixed. All made in reinforced concrete also the slab that act compositely with the beams, with a thickness of 15 cm. Some photos of the bridge structure are in Figure 53.

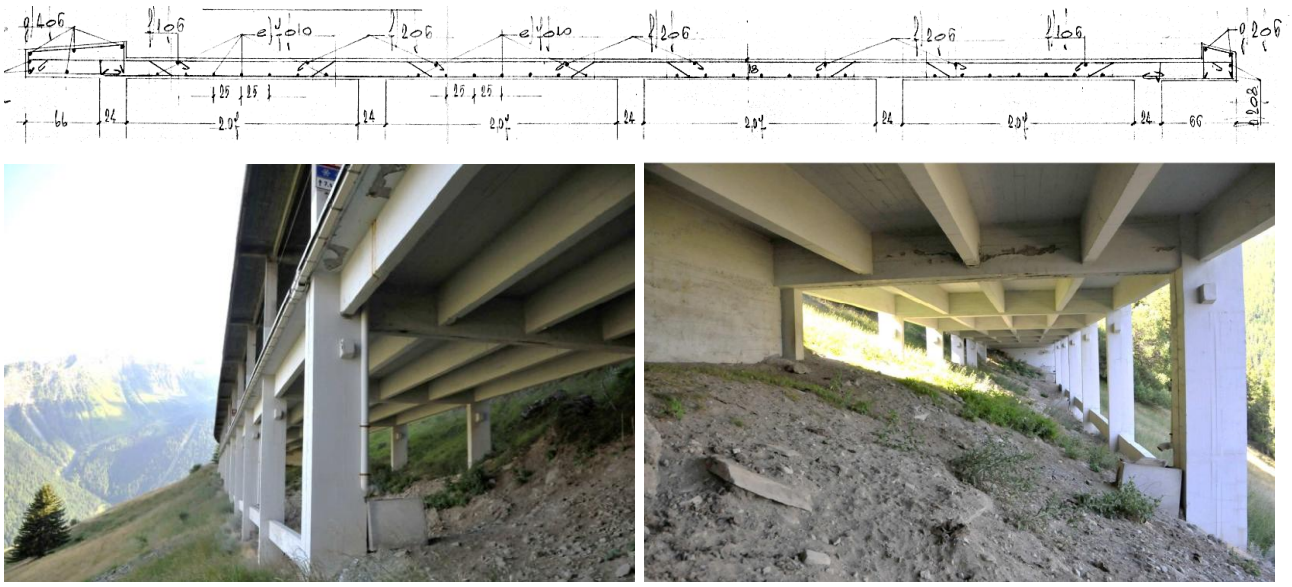

Figure 53: Chantel 2 Viaduct, original design of deck section and nowadays photo of the structure.

The FE model was subjected to a static analysis that accounted for both the self-weight of the structure and the permanent loads. In order to simulate a potential displacement of the piers an imposed displacement of the piers was applied Figure 54. Such displacement can be introduced in different ways, depending on the type of scenario considered. In practice, the choice of the imposed displacement may be refined based on the outcomes of SAR data analyses, which can provide alternative patterns of movement to be investigated.

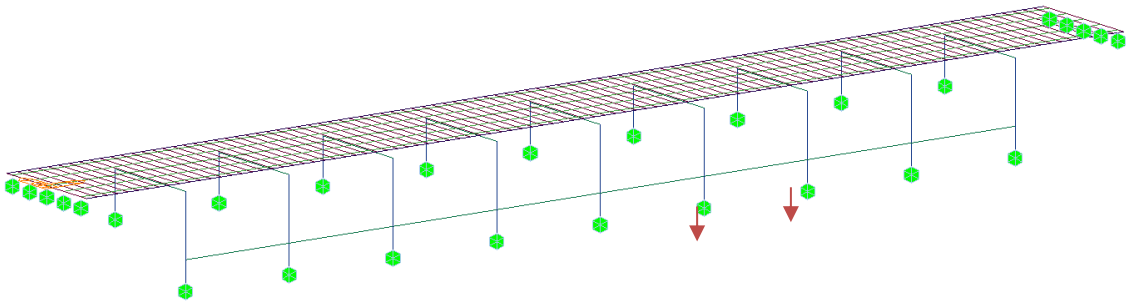

Figure 54: Imposed displacement simulating landslide interesting two piers.

The outcome of this procedure allowed for the evaluation of the variations in internal forces, providing insights into how settlements inferred from satellite monitoring could be meaningfully integrated into structural analysis. In particular, the analysis enabled the identification of changes in internal forces, offering a preliminary way to assess how differential settlements may influence the structural response. Such an approach, despite its simplified nature, can provide a methodological basis for investigating the potential impact of ground deformations such as those induced by active landslides on infrastructure, supporting preliminary assessments of structural vulnerability.

For example, by comparing the bending moment diagrams shown in Figure 55 and Figure 56, it is possible to observe a substantial change both in the overall shape of the curves and in the magnitude of the maxima and minima due to the load combination considering the imposed displacement. Focusing on the highlighted beam in red in Figure 56, it becomes evident that not only do the bending moments in the spans increase significantly, but also areas originally designed and reinforced to resist negative moments are now subjected to positive ones. This inversion has important implications in concrete structures leading to cracking and possible failure mechanisms. Such observations highlight the sensitivity of structural response to imposed settlements and illustrate how the redistribution of internal forces may critically affect both serviceability and ultimate limit states.

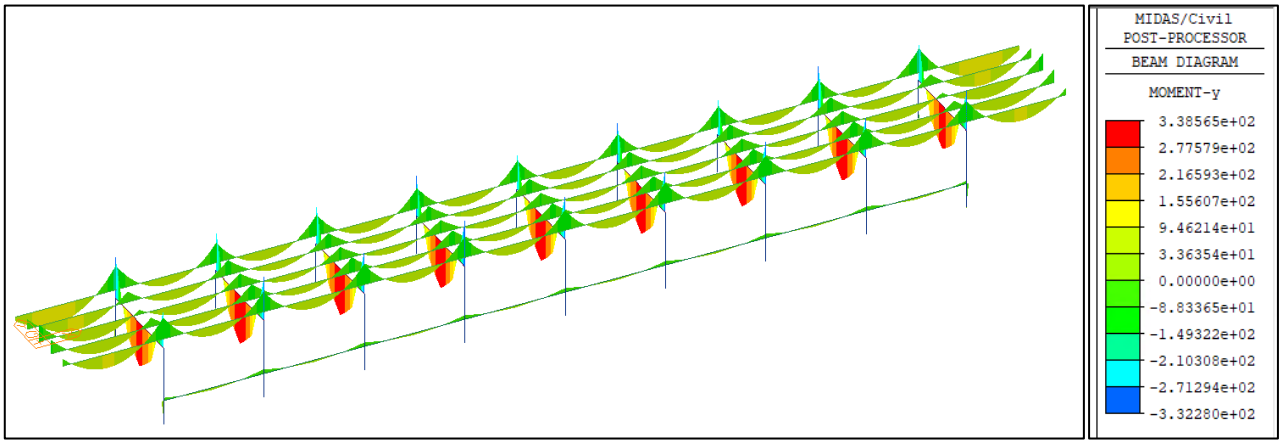

Figure 55: Bending moments due to self-weight.

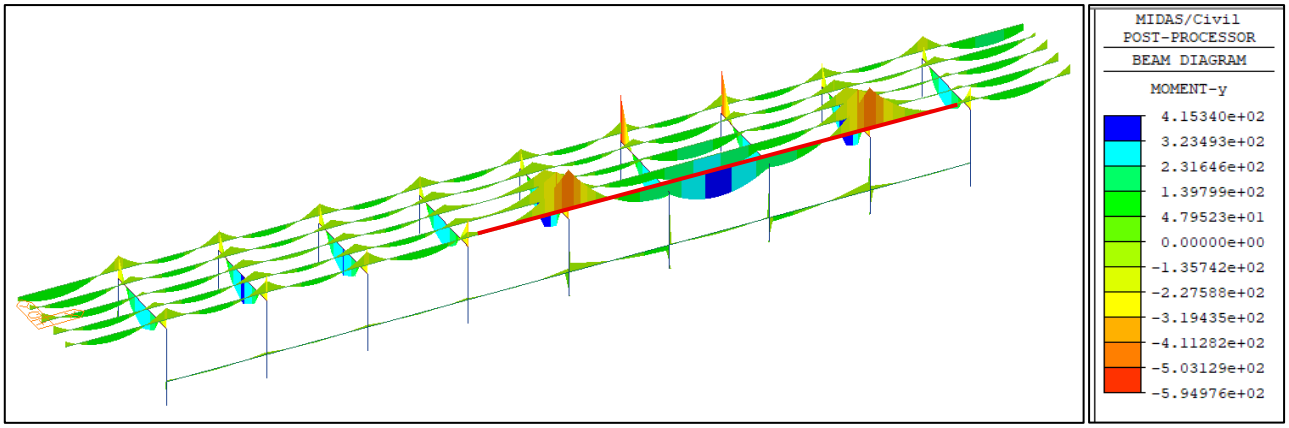

Figure 56: Bending moment due to self-weight and imposed displacement.

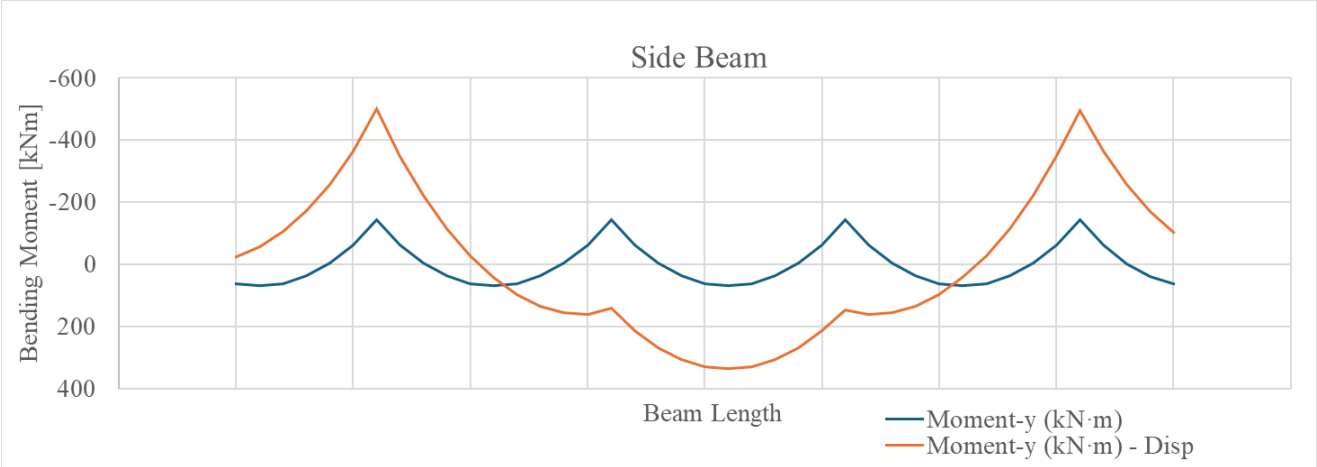

Figure 57: Bending Moment on side beam.

A similar consideration can be made about shear forces illustrated in Figure 58. For instance, when examining the shear demand on the pier caps supporting the main girders beams, the analysis shows that the maximum value increases from approximately 400 kN to 600 kN. This represents a significant

rise, which may in turn lead to cracking, shear-related damage, or even brittle failure if not adequately accounted for in the design.

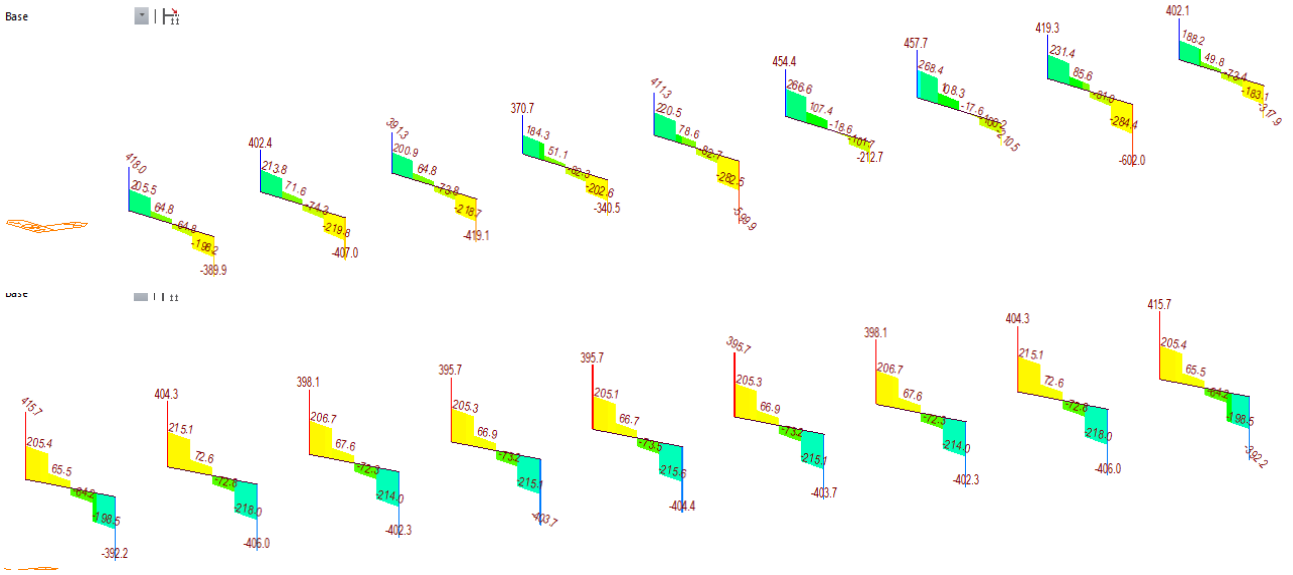

Figure 58: Shear on transverse beams.

It should be emphasized that the finite element analysis presented here is also a simplified approach. A more refined strategy could be adopted by, for example, introducing spring elements to represent the stiffness of the supporting soil and applying displacements at the base of those springs. This would make it possible to more realistically capture the interaction between ground settlements and the superstructure. Furthermore, the elastic analysis carried out in this study could be extended by performing nonlinear simulations, thereby accounting for redistribution of bending moments and other behaviours that cannot be fully captured within an elastic model.

The use of satellite data made available through the geoportal, together with the adoption of an elastic modelling approach, reflects the deliberate choice to keep the overall procedure simple. The objective was not to reproduce all the structural complexities, but rather to demonstrate how such a methodology can be employed to identify potentially critical structures on a large scale, providing a basis for subsequent, more detailed analyses. In this specific case, given the similarity among the structures along the route, a more comprehensive procedure for the assessment of the entire section could be developed. In such a context, it would be possible to design a parametric nonlinear model capable of deriving capacity curves for representative structures and comparing them with differential displacements obtained from satellite data. This approach would enable large-scale assessments while ensuring that the numerical model represent the real behaviour capturing the nonlinear effects and redistribution of internal actions that may occur under varying loads or boundary conditions.

Conclusion

In this chapter, the use and application of SAR data have been analysed, initially focusing on their potential for large-scale assessment of building settlements. The study then extended this approach to the evaluation of infrastructure, demonstrating how satellite-derived measurements can provide valuable insights into the behaviour of larger structural systems under differential displacement.

It is important to emphasize the need to integrate SAR-derived data with other information sources, such as GNSS measurements, topographic surveys, and in-situ monitoring, to improve the accuracy and reliability of deformation estimates. In the specific case study considered here, the presence of a continuous deck covering the viaducts could facilitate the installation of artificial radar reflectors, creating stable and well-defined targets for the satellite. Such reflectors would improve the coherence and precision of the measurements, allowing more accurate displacement estimation and better comparison with other monitoring data.

Building on this preliminary work, the focus now shifts from monitoring to risk assessment, while maintaining a large-scale perspective. In the next chapter, Italian guidelines for the assessment of structural vulnerability and hazard are introduced and applied.

This approach enables the prioritization of interventions by ranking structures according to various risk factors, ensuring that those most susceptible to potential hazards are identified for further detailed investigation and resource allocation.

Chapter 2

Classification and Risk Management of Existing Bridges

In recent years, in response to the growing need for a structured and repeatable method to assess the condition of existing bridges, the Italian Ministry of Infrastructure and Transport and the Higher Council of Public Works, has promoted the development of systematic tools for managing the risk associated with existing bridges. The result is the "Guidelines for the Classification and Risk Management of Existing Bridges" (MIT, 2020), a reference document intended to support road operators, owners and infrastructure managers in the identification of structural priorities across national and local networks [40] [41]. The Guidelines do not aim to provide detailed structural analysis methods, but rather to define a risk-based framework for classifying existing bridges, enabling authorities to plan inspections, maintenance, and retrofitting more effectively.

Figure 59: Example of degrading on bridges.

Figure 60: Example of collapsed bridges.

A uniform methodology is required for all asset-managing authorities, since defect analysis alone is not sufficient for effective risk management.

The guidelines define a multi-level framework for the management of bridge assets spans from the basic inventory to the full structural safety verifications and aiming to support structural risks management in a rational and data-informed way. The guidelines focus on bridges and viaducts and are based on the principle of determining a Class of Attention (CoA) for each structure. This class reflects the urgency and priority for further investigations or interventions. The Class of Attention assigned to each bridge is determined by evaluating a set of different risks, which are: Structural risk, Seismic risk, Hydraulic risk, Landslide risk and is inspired by the risk assessment framework and is the result of the combination of three main factors: hazard, vulnerability, and exposure. Each of these factors is determined by evaluating a set of influencing parameters, which are categorized as primary and secondary. Primary parameters are considered to have greater weight in the classification process, while secondary parameters serve as modifiers. The evaluation of these factors and consequently of the overall CoA is carried out through a class-based approach using logical operators, in which each parameter (primary or secondary) is assigned to a predefined class, and the resulting classes are combined through structured decision rules.
Primary and secondary parameters are derived from the data collected during the inventory phase and visual inspections.

Based on the values of the primary parameters, five classes are defined:

- Low
- Medium-Low
- Medium
- Medium-High
- High

These initial classes are then adjusted based on the secondary parameters, which are themselves grouped into two or more classes depending on the parameter type. The final Class of Attention is then derived by combining these three intermediate classes using the logical framework defined in the Guidelines. This full process is summarized in Figure 61, which illustrates the logical flow underlying the classification method.

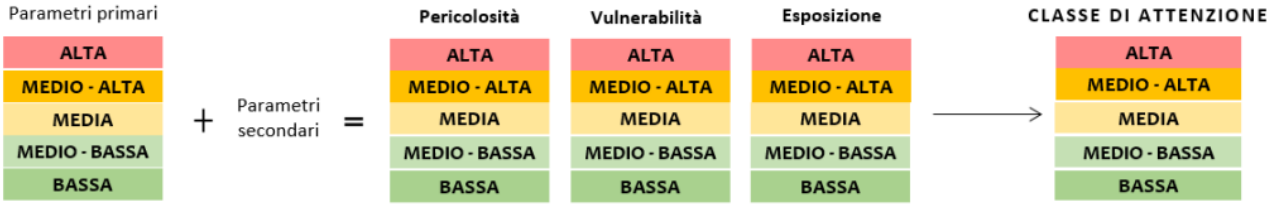

Figure 61: Logical flow for the determination of the Class of Attention.

The process led to a set of risk-specific Class of Attention:

- Structural Class of Attention
- Seismic Class of Attention
- Hydrogeological Class of Attention
- Hydraulic Class of Attention

The overall Class of Attention for the structure is then determined by aggregating the highest or most critical among the specific risk classes, following the logic defined in the Guidelines. This final classification supports decision-making on whether deeper evaluations, inspections, or monitoring actions are required. The distinction between “risk” and “attention” is crucial. A risk class typically implies an in-depth, probabilistically sound analysis based on objective numerical data and validated models. However, such a rigorous process is not feasible when attempting to rapidly assess a large number of bridges across the national territory. The term “attention”, therefore, refers to a classification that is logic-driven, multi-level, and applicable directly in the field, allowing operators to produce a first-level risk estimate quickly and efficiently.

The classification process is progressive, moving from broad screening to more detailed and specific evaluations depending on the initial findings and available information. To this end, the methodology is articulated into six levels of increasing complexity:

- Level 0: Inventory and documentation of all bridges, collecting basic geometrical, administrative, and contextual data.
- Level 1: Visual inspections and damage surveys to assess the structural condition, supported by standardized defect sheets.
- Level 2: Territorial-scale classification of each structure into a Class of Attention based on the calculated risk from hazard, vulnerability, and exposure indicators.
- Level 3: Preliminary assessments for bridges in medium or higher risk classes, often including more detailed inspections or measurements.
- Level 4: Full structural safety evaluation in accordance with national technical codes (NTC), including numerical modelling, testing, and material characterization.
- Level 5: Strategic relevance analysis of the bridge within the transportation network, including socioeconomic impact studies and resilience evaluation.

This classification determines whether further actions such as advanced analysis (Level 3 or 4) or installation of monitoring systems are required.

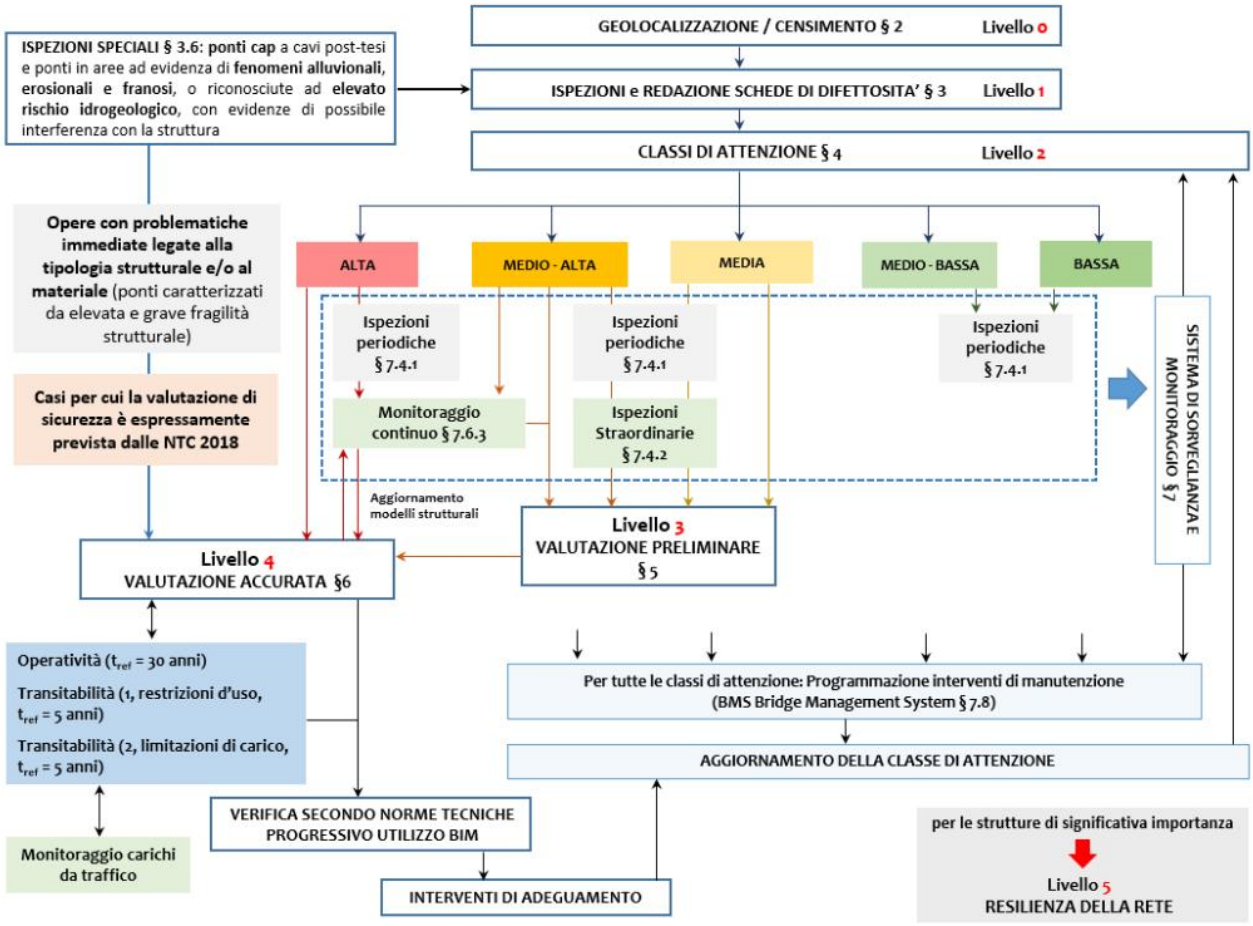

Figure 62: Multilevel approach and relationships among the different levels of analysis time.

A key strength of this system is its scalability: it can be applied to thousands of bridges using initial qualitative assessments and then refined only where needed. This makes it suitable for national and regional road operators dealing with extensive infrastructure networks and limited resources.

Overall, the Guidelines represent a comprehensive, pragmatic tool for asset management that connects administrative duties with technical risk assessment, allowing decision-makers to prioritize maintenance and inspection efforts based on transparent criteria. Here is a brief description of the Levels.

Level 0 - Inventory of Existing Structures

Level 0 represents the starting point of the multi-level assessment process. It consists of a systematic inventory of existing bridge structures, aimed at organizing them into a standardized and digital registry. This activity is essential for enabling subsequent risk classification procedures. The inventory includes all bridges and viaducts with a span greater than 6 meters, regardless of their structural typology or construction age.

The main goal of Level 0 is to collect a dataset of information on each structure, such as:

- Location and identification numbers.
- Year of construction and rehabilitation.
- Road category and functional classification.
- Structural type (e.g., arch, frame, prestressed girder, etc.).
- Geometrical characteristics (span length, width, clearance).
- Traffic etc.

The collected data is entered into a standardized Level 0 Inventory Sheet illustrated in Figure 63.

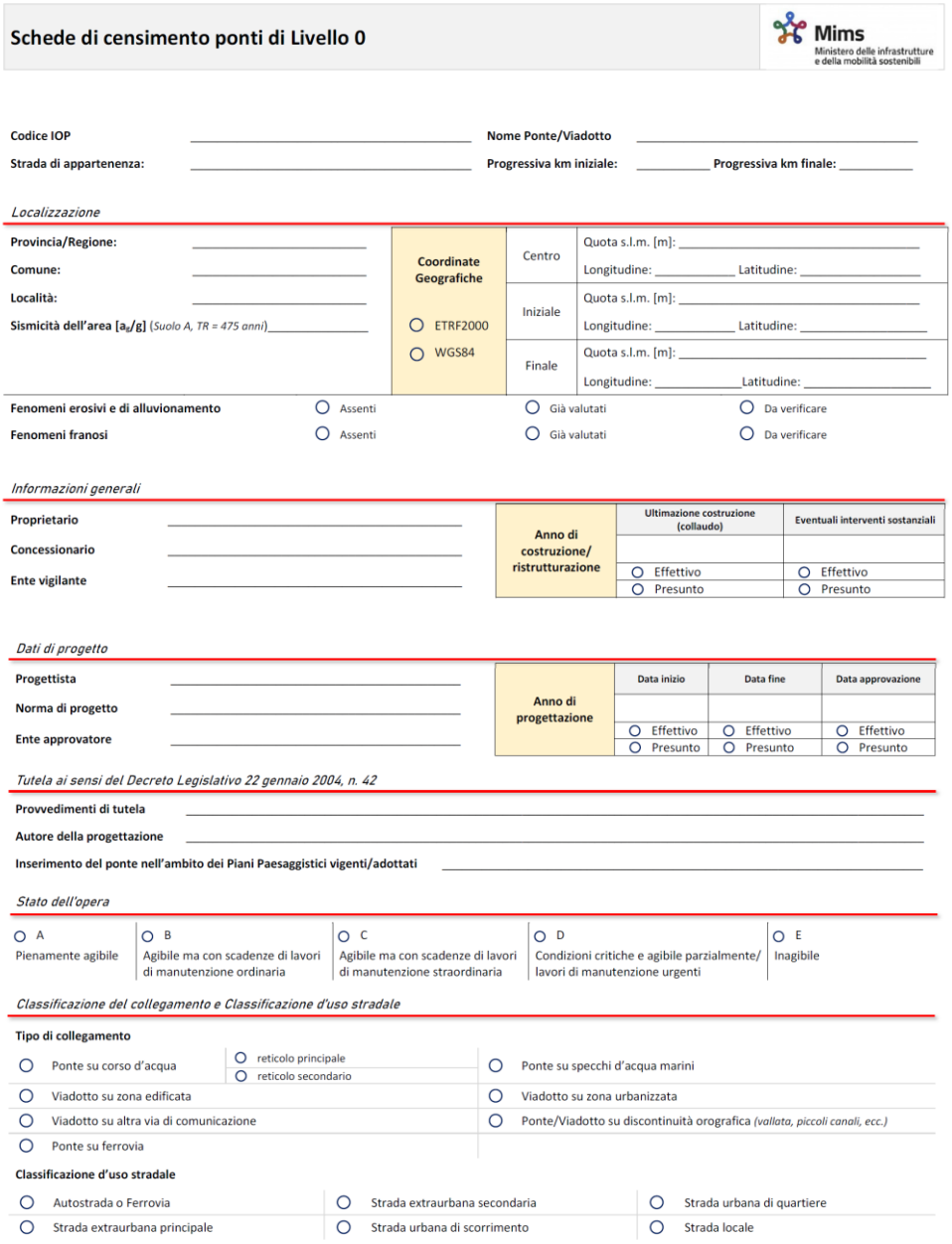

Schede di censimento ponti di Livello 0

Mims
Ministero delle infrastrutture e della mobilità sostenibili

Codice IOP _____ **Nome Ponte/Viadotto** _____

Strada di appartenenza: _____ **Progressiva km iniziale:** _____ **Progressiva km finale:** _____

Localizzazione

Provincia/Regione: _____
Comune: _____
Località: _____
Sismicità dell'area [a_g/g] (*Suolo A, TR = 475 anni*)_____

Coordinate Geografiche
○ ETRF2000
○ WGS84

Centro	Quota s.l.m. [m]: _____ Longitudine: _____ Latitudine: _____
Iniziale	Quota s.l.m. [m]: _____ Longitudine: _____ Latitudine: _____
Finale	Quota s.l.m. [m]: _____ Longitudine: _____ Latitudine: _____

Fenomeni erosivi e di alluvionamento	○ Assenti	○ Già valutati	○ Da verificare
Fenomeni franosi	○ Assenti	○ Già valutati	○ Da verificare

Informazioni generali

Proprietario _____
Concessionario _____
Ente vigilante _____

Anno di costruzione/ ristrutturazione	**Ultimazione costruzione (collaudo)**	**Eventuali interventi sostanziali**
	○ Effettivo	○ Effettivo
	○ Presunto	○ Presunto

Dati di progetto

Progettista _____
Norma di progetto _____
Ente approvatore _____

Anno di progettazione	**Data inizio**	**Data fine**	**Data approvazione**
	○ Effettivo	○ Effettivo	○ Effettivo
	○ Presunto	○ Presunto	○ Presunto

Tutela ai sensi del Decreto Legislativo 22 gennaio 2004, n. 42

Provvedimenti di tutela _____
Autore della progettazione _____
Inserimento del ponte nell'ambito dei Piani Paesaggistici vigenti/adottati _____

Stato dell'opera

○ A	○ B	○ C	○ D	○ E
Pienamente agibile	Agibile ma con scadenze di lavori di manutenzione ordinaria	Agibile ma con scadenze di lavori di manutenzione straordinaria	Condizioni critiche e agibile parzialmente/ lavori di manutenzione urgenti	Inagibile

Classificazione del collegamento e Classificazione d'uso stradale

Tipo di collegamento

○ Ponte su corso d'acqua	○ reticolo principale ○ reticolo secondario	○ Ponte su specchi d'acqua marini
○ Viadotto su zona edificata		○ Viadotto su zona urbanizzata
○ Viadotto su altra via di comunicazione		○ Ponte/Viadotto su discontinuità orografica *(vallata, piccoli canali, ecc.)*
○ Ponte su ferrovia		

Classificazione d'uso stradale

○ Autostrada o Ferrovia	○ Strada extraurbana secondaria	○ Strada urbana di quartiere
○ Strada extraurbana principale	○ Strada urbana di scorrimento	○ Strada locale

Figure 63: Level 0 inventory sheets.

The structure of the form and the type of data it contains are consistent with the provisions of by the Italian Ministry of Infrastructure and Transport, and it will be useful to create the National Digital Archive of Public Works (AINOP), which can be progressively updated as new inspections or assessments are performed. The inventory does not include performance evaluations or damage assessments. However, it allows for a first-level sorting of structures, helping identify those for which further investigation is urgent due to missing documentation, outdated construction methods, or potential exposure to specific hazards.

Level 1 - Visual Inspections and Defect Mapping

Level 1 introduces on-site visual inspections as a follow-up to the census in Level 0. These inspections are intended to provide a preliminary qualitative assessment of each bridge's current state, identifying visible signs of deterioration and possible structural or functional concerns with a uniform methodology. Visual inspections are intended to verify the reliability of the data collected during the Level 0 inventory, to gather additional information on the actual geometric and structural characteristics of the structure and its construction site, and to perform a preliminary and approximate assessment of the structure's state of preservation. These inspections provide a "snapshot" and an objective description as accurate as possible of the actual condition of the structure and its surrounding environment.

Each inspected bridge is associated with one or more defect sheets, where all anomalies are recorded following a structured system. The guidelines define:

- Types of elements to inspect (deck, piers, abutments, joints, bearings, etc.).
- Categories of defects, such as corrosion, cracks, loss of section, delamination, joint failures.
- Severity levels of damage (based on geometry, location, and impact).
- Extent indicators (local, widespread, systemic).

These sheets are completed by qualified personnel using a uniform coding system, allowing consistent comparisons across bridges and over time (Figure 64).

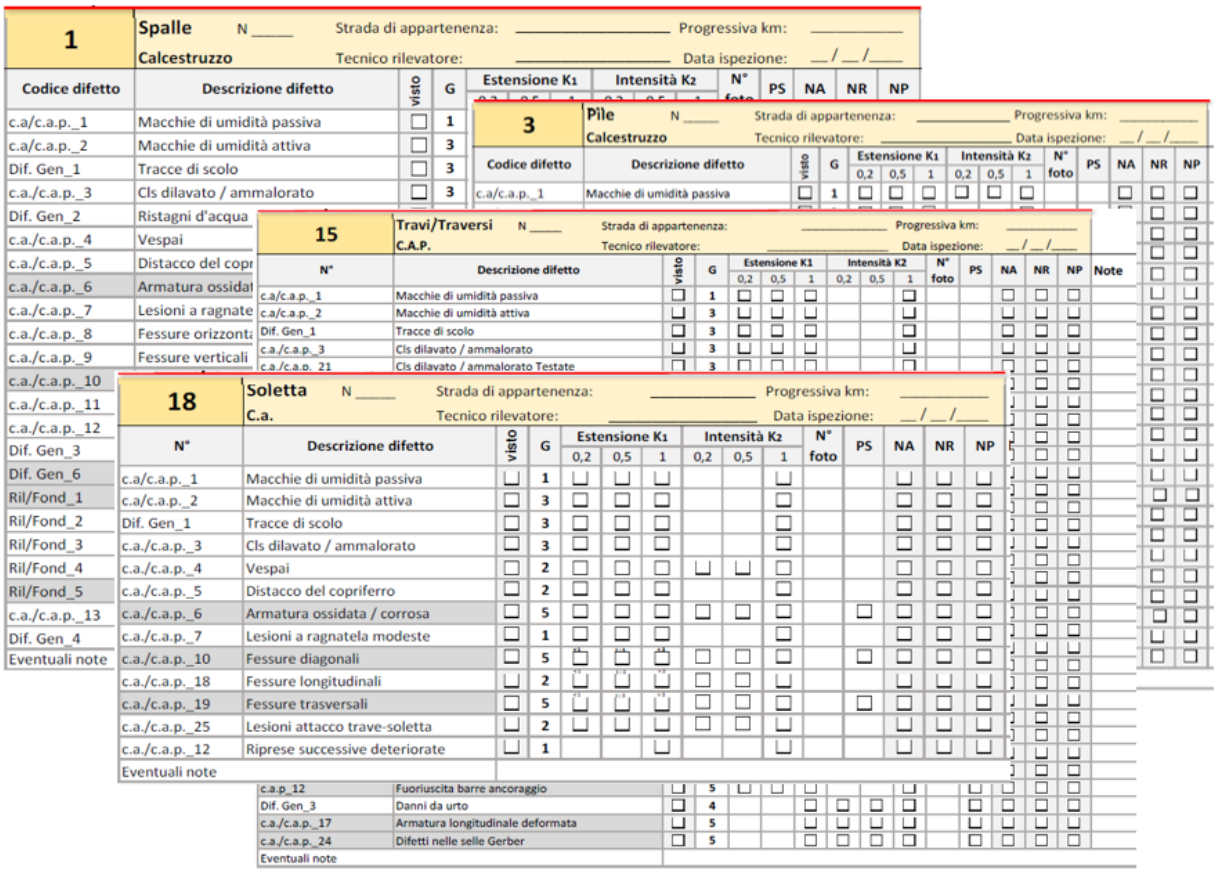

Figure 64: Level 1 defect sheets.

The outcome of Level 1 is not yet a structural safety index, but rather a condition assessment based on observed damage. This serves as input for Level 2 (risk classification), especially for the vulnerability component of the risk model.

Level 2 - Risk Classification on a Territorial Scale

Level 2 can represent the core phase of the risk-based approach proposed by the Guidelines. It is designed to provide a territorial-scale classification of existing bridges, and the outcome of this phase is the assignment of a Class of Attention (CoA) to each structure, which expresses the urgency for further analysis, monitoring, or intervention. The risk model adopted in Level 2 is multi-hazard and includes five main risk types:

1. Structural risk, related to the intrinsic characteristics and state of conservation of the bridge.
2. Seismic risk, based on the seismic hazard of the area and the vulnerability of the structural system.
3. Hydraulic risk, considering the potential for flooding, river erosion, or scour at foundations.

4. Landslide risk, involving landslides or slope instability in the vicinity of the structure.

Each of these risks is assessed using dedicated indicators, often based on simplified models or expert judgment. The indicators are combined into a Risk Index that reflects the likelihood and consequence of failure for each hazard.

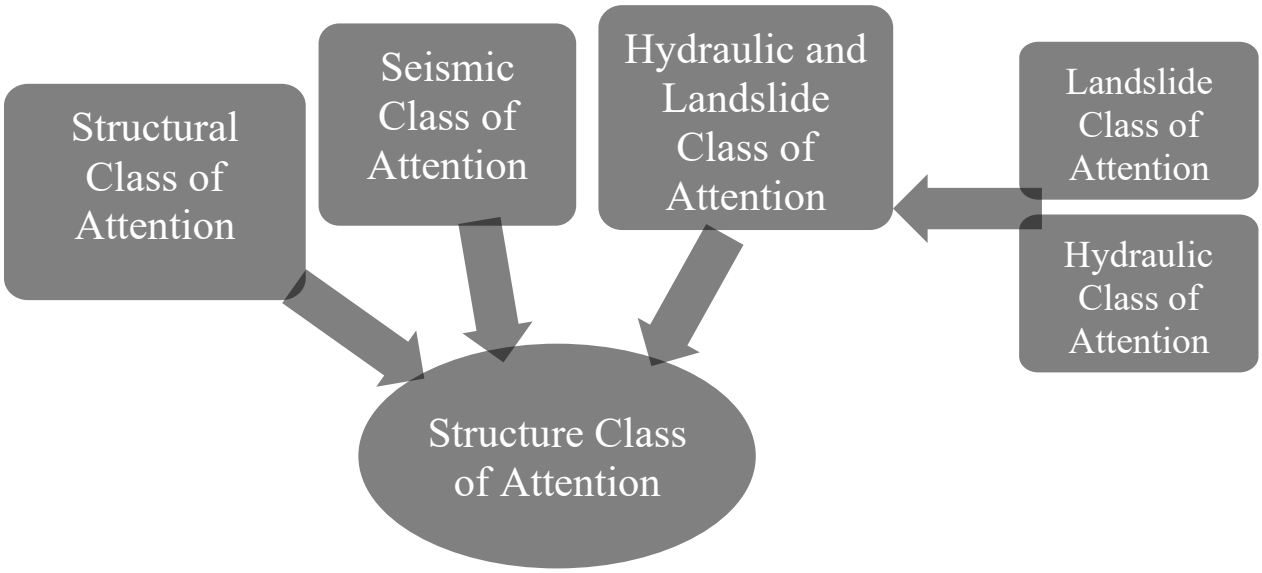

Figure 65: Chart of Class of Attention.

The Level 2 assessment is based on the aggregation of three components:

- Hazard, which describes the external actions or threats acting on the bridge.
- Vulnerability, which expresses how susceptible the structure is to those threats, given its geometry, materials, construction type, and current condition.
- Exposure, which reflects the consequences of a potential failure, both in terms of safety and socio-economic impact (e.g., service interruption, emergency access, traffic volume).

These three components are used to compute a Class of Attention, ranked on a scale Very-Low, Low, Medium, Medium-Hight, Hight. Like it said before for every type of risk primary and secondary parameters are defined.

For the structural

	Primary Parameters	Secondary Parameters
Hazard	Entity of present loads with particular reference to the transit of exceptional transport	-
Vulnerability	Level of defect. Static scheme, span, material, and number of spans	Speed of degradation evolution. Design standard
Exposure	Level of DMT (Daily Mean Traffic) and average span length	Road alternatives. Type of crossed entity. Transport of dangerous goods

For seismic

	Primary Parameters	Secondary Parameters
Hazard	Peak ground acceleration and topographic category	Subsoil category
Vulnerability	Structural scheme, span length, material. Level of defect	Design criteria
Exposure	Level of DMT (Daily Mean Traffic) and average span length	Road alternatives Type of underpass entity Transport of hazardous goods Strategic importance of the structure

For landslide

	Primary Parameters	Secondary Parameters
Susceptibility	Slope instability (Magnitude, Velocity, State of activity)	Model uncertainty Mitigation measures
Vulnerability	Bridge type/robustness and foundation type	Extent of interference
Exposure	Level of DMT (Daily Mean Traffic) and average span length	Road alternatives Type of underpass entity Strategic importance of the structure

For hydraulic

	Primary Parameters	Secondary Parameters
Hazard/Susceptibility	Probability of occurrence and event consistency	Model uncertainty Mitigation measures
Vulnerability	Resilience to the natural event	Type, magnitude, and frequency of event Type and efficiency of mitigation works
Exposure	Potential damage	Type of crossed entity Strategic importance of the work Extent of damage

Each component is processed through a logical flow. The overall CoA is then assigned as the most critical among these, unless otherwise justified. In Figure 66 is show an example for the calculation of overall Class of Attention for Medium-Low structural class of attention.

Classe di attenzione strutturale/fondazionale ***MEDIO-BASSA***

		Classe di attenzione idraulica e frane				
		Alta	Medio-Alta	Media	Medio-Bassa	Bassa
Classe di attenzione sismica	Alta	Medio-Alta	Media			
	Medio-Alta	Media				Medio-Bassa
	Media	Media			Medio-Bassa	
	Medio-Bassa	Media		Medio-Bassa		
	Bassa	Media	Medio-Bassa			

Figure 66: Example of table for global Class of Attention.

The assigned Class of Attention defines the next steps in the assessment or monitoring process and based on the resulting CoA the Guidelines outline differentiated follow-up procedures:

- For bridges classified as High CoA: Immediate and detailed evaluations are mandatory, including full structural safety assessments (Level 4) and, if needed, deeper investigations of geotechnical or structural characteristics. Periodic ordinary and extraordinary inspections are mandatory, and the installation of periodic or continuous monitoring systems is advised. Structural models should be developed and continuously updated using monitoring data.
- For Medium-High CoA bridges: Preliminary evaluations (Level 3) and periodic inspections are required. Extraordinary inspections and monitoring may be necessary based on the outcome of Level 3. If defects or deterioration are confirmed, a Level 4 analysis may also be required, potentially upgrading the bridge to High CoA.
- For Medium CoA bridges: Level 3 evaluations are also needed, along with ordinary inspections. If inspections detect rapidly evolving deterioration, extraordinary inspections must be carried out. Depending on the results, installation of monitoring systems and/or transition to a Medium-High or High CoA may be required.
- For Medium-Low CoA bridges: No further assessments are required beyond those already completed. However, frequent periodic inspections must be conducted.
- For Low CoA bridges: Only standard periodic inspections are expected. No additional evaluations are necessary.

These procedures allow for a progressive refinement of knowledge about each structure, supporting decision-making regarding maintenance, rehabilitation, or monitoring, based on the actual risk and importance of each bridge within the network.

Level 3 - Preliminary In-Depth Investigations

Level 3 represents the next step after the classification obtained in Level 2. If a bridge has been assigned a Medium-High or Medium Class of Attention (CoA), or when specific issues identified during inspections warrant further study, level 3 is mandatory, and the objective is to carry out preliminary evaluations to better understand the structure's condition and to determine whether a full structural safety assessment (Level 4) is necessary. The assessment starts from the assumption that the bridge was designed according to the standards of its time and dimensioned for the traffic loads then in effect. A comparison is made between the demand induced on the various components of the bridge (slabs, crossbeams, main girders and/or principal structures, piers, abutments, bearings, and foundations) by the traffic loads prescribed in the original design standards (considered as the minimum capacity guaranteed by the original design code), and the demand obtained using the traffic load models specified in the current technical standards. The demand can be computed using simplified static schemes and assumption based on the bridge design teory (e.g. Corbon method for the transversal load distribution) to estimate the actions. This analysis allows for a preliminary estimate of the minimum capacities guaranteed by different historical standards, taking into account the evolution of traffic load models over time. It also provides the managing authority with the basis to assess, on a case-by-case basis, the need to perform a full Level 4 safety assessment, considering the type and severity of defects identified through the various inspection levels (and whether these may have been caused by vertical traffic loads), as well as the results of the preliminary Level 3 analyses. Additional information obtained from monitoring systems, where available, can further support Level 3 preliminary evaluations.

Level 4 - Structural Safety Assessment

Level 4 represents the most in-depth stage of the multi-level methodology proposed by the Guidelines. At this stage, the goal is to carry out a comprehensive structural safety verification of an existing bridge, aligned with the requirements of the *Norme Tecniche per le Costruzioni* (NTC 2018) and its explanatory Circular. Unlike the preliminary evaluations of Levels 2 and 3, which aim to prioritise and filter the structures requiring further analysis, Level 4 is dedicated to producing a quantitative safety assessment. This type of assessment is required for bridges that have been assigned a High Class of Attention in Level 2, or in cases where Level 3 investigations reveal defects or vulnerabilities of such severity that a deeper evaluation is justified. It may also be applied proactively to structures with known intrinsic fragility such as certain pre and post-tensioned concrete bridges or in the presence of specific hazards like high hydrogeological or seismic risk.

The process usually begins with the knowledge phase, where all available information about the bridge is collected and verified. This includes historical and design documentation, detailed geometric surveys, and a thorough characterisation of materials. Field activities can range from non-destructive tests (e.g., ultrasonic or radar surveys) to semi-destructive sampling (e.g., core extraction) and, where necessary, destructive tests carried out by accredited laboratories. Special inspections may also be required for structural types known to present particular vulnerabilities. The Guidelines adopt the concept of Levels of Knowledge, each associated with a Confidence Factor that influences the safety margins applied in the verification. Simply, the more complete and reliable the information collected, the lower the uncertainty and the more precise the assessment. Once the knowledge base is established, the next step is modelling and analysis. A numerical model of the bridge often a finite element model is created to simulate its behaviour under the loads (permanent load, seismic load, traffic load, etc.). The model must accurately reflect the bridge's geometry, material properties, load conditions, and boundary constraints. Safety verifications are then performed using partial factors and load combinations specified by the NTC, with adjustments depending on the level of knowledge achieved.

The Guidelines identify different verification outcomes:

- Adequate, meaning it fully complies with current safety standards and no restrictions are needed.
- Operable, meaning that the bridge meets safety verifications performed according to the principles of the *NTC* but where the partial factors for loads and materials are determined with reference to a reduced design working life. In the Guidelines, the indicative reference period, tref, is conventionally set at 30 years.
- Transit-only means that the bridge meets safety verifications for a short reference period, within which upgrading or operational works are planned and executed, accompanied by safety measures such as Load restrictions on the bridge. A detailed schedule for these interventions must be defined and entered into regional and national institutional databases. For the calculation of partial factors Guidelines is set at no more than 5 years.

The results of the Level 4 assessment directly inform the choice of corrective actions whether strengthening, rehabilitation, or replacement and can also justify intermediate safety measures such as load restrictions or the installation of continuous monitoring systems. Ultimately, the accuracy and reliability of a Level 4 verification depend on the depth and quality of the knowledge acquired in the preliminary phases. Investing in thorough investigations at this stage not only reduces uncertainty but

also ensures that the proposed interventions are targeted, effective, and proportionate to the actual condition and importance of the bridge.

Surveillance and Monitoring System

The final part of the Guidelines describes how bridge safety should be managed over time through coordinated activities of surveillance, inspection, and monitoring. Surveillance consists of routine visual observations by trained personnel to detect early signs of defects or unusual behaviour, with anomalies reported to the managing authority. Each bridge must be uniquely identified and recorded in a centralised database consistent with the AINOP system, ensuring full traceability of inspection and maintenance data. For structures with High or Medium-High Class of Attention, or of strategic importance, the Guidelines recommend installing structural health monitoring systems, either periodic or continuous, to record key parameters such as displacement, strain, acceleration, or temperature. Also, in some cases especially when structural doubts remain static load tests or dynamic identification campaigns may be necessary to evaluate the behaviour of the bridge under controlled conditions. The combined use of surveillance, inspections, and monitoring provides an updated and objective picture of the bridge's condition, supports both preliminary (Level 3) and detailed (Level 4) evaluations, and informs timely maintenance or strengthening decisions.

Large Scale risk assessment on T2 Road

The T2 road is part of the regional road network of the Aosta Valley, a mountainous region in north-western Italy characterised by complex orography, steep slopes, and a dense hydrographic system. The demanding terrain has required the construction of numerous bridges and viaducts to maintain road continuity across valleys, rivers, and unstable slopes. Strategically, the T2 section connects key urban centres within the valley to cross-border routes leading to France and Switzerland with the Gran San Bernardo tunnel. This makes it a crucial link for local mobility, regional logistics, and international transit. However, the mountainous setting also exposes the structures to multiple hazards, including hydrogeological instability, hydraulic actions from river floods, and seasonal freeze thaw cycles, all of which can accelerate structural deterioration. These characteristics make the T2 section particularly well-suited for testing the *Guidelines for the Classification and Risk Management of Existing Bridges*. Its environmental complexity and strategic importance also make it a relevant case for exploring the integration of Synthetic Aperture Radar (SAR) displacement monitoring, like explained in the previous chapter. SAR data can efficiently cover the entire section, detect millimetric structural or ground movements, and complement on-site inspections especially in locations that are difficult to access thus offering a valuable layer of information to support the risk classification process in a large scale. Within the RELUIS WP2 project, this section was selected as one of the experimental road stretches for the application of the Guidelines. A total of 20 bridge structures were assigned to the research team: 8 located in Lombardy and 12 in the Aosta Valley. After the first contact with the managing authorities for both sections, documentation prepared according to the Guidelines was received. For the T2 section, joint on-site inspections were conducted by SINA in collaboration with the research group, focusing on verifying the possible issues in application of the procedures. For most structures in the T2 section, documentation was available for Levels 1, 2, and 3, and was generally compliant with the Guidelines, although Level 3 data was missing for some bridges. Additional material included monitoring system records, original design drawings, and rehabilitation project documentation. One notable observation concerned the Level 1 defect sheets, which were compiled for groups of elements per span (e.g., “girders – span 1”, “deck slab – span 1”) rather than for each individual element. This application of the Guidelines provided an opportunity to assess their practical feasibility in a real network context and to explore the potential benefits of combining traditional inspection and classification methods with SAR-based large-scale monitoring. In the following table the structures analysed by the University of Bergamo are listed, the remaining was studied by the Politecnico di Milano.

Group	Society	Route	AINOP Code	Name
AISCAT	SITRASB	T2	STAU00T2PNGJUORVBU	Viadotto Chantel 1
AISCAT	SITRASB	T2	STAU00T2PNVYJXDI8D	Viadotto Chantel 2
AISCAT	SITRASB	T2	STAU00T2PN1MSBWLCW	Viadotto Closette
AISCAT	SITRASB	T2	STAU00T2PNPOXKDSWJ	Viadotto Curvone
AISCAT	SITRASB	T2	STAU00T2PNCTFOQA2S	Viadotto Dardanelli
AISCAT	SITRASB	T2	STAU00T2PNWIRE4TRP	Viadotto Devie
AISCAT	SITRASB	T2	STAU00T2PNLTTNAQ0R	Viadotto Envy 1
AISCAT	SITRASB	T2	STAU00T2PNLVWYFMG7	Viadotto Envy 2
AISCAT	SITRASB	T2	STAU00T2PNU8ZRYLZD	Viadotto Envy 3
AISCAT	SITRASB	T2	STAU00T2PNA9GMMTCJ	Viadotto Fortino
AISCAT	SITRASB	T2	STAU00T2PNG3QSNWPY	Viadotto Gorres
AISCAT	SITRASB	T2	STAU00T2PN70SJMJEV	Viadotto Imbocco

Table 2: List of T2 bridges and viaduct.

Figure 67: T2 road.

All the structures are located in the Valle d'Aosta region, in the municipality of Saint-Rhèmy-en-Bosses, a hamlet of Aosta, and were constructed around the 1963. The main engineers who designed these works are A. Vaudetti and Giorgio Binelli. From the point of view of materials and typology, the structures are made of reinforced concrete, with a prevalence of continuous beams, with the exception of the "Viadotto Curvone" and the "Viadotto Dardanelli," which have supported beams. In most of the cases the pillars have a rectangular section and the foundations are almost all direct on isolated footing type. Among the structures, there are differences particularly in the length, that varies considerably: the longest viaduct is the "Viadotto Curvone" at 1,010 meters, while the shortest, the "Viadotto Chantel 1" and the "Viadotto Envy 1," measure 80 meters. Regarding maintenance, all the viaducts have undergone extraordinary interventions, mainly to rehabilitate deteriorated parts and

replace joints. Finally, only the "Viadotto Curvone" is equipped with a system that includes a control unit, inclinometers, and displacement sensors, acting as monitoring system.

The following table resume the material analysed during the work.

Structure	Level 0	Level 1	Level 2	Level 3	Other Material
STAU00T2PNGJUORVBU	x	x	x		Projects and inspections, material related to recovery interventions
STAU00T2PNVYJXDI8D	x	x	x		Projects and inspections, material related to recovery interventions
STAU00T2PN1MSBWLCW	x	x	x	x	Projects and inspections, material related to recovery interventions
STAU00T2PNPOXKDSWJ	x	x	x		Projects and inspections, material related to recovery interventions and monitoring activities
STAU00T2PNCTFOQA2S	x	x	x	x	Projects and inspections, material related to recovery interventions
STAU00T2PNWIRE4TRP	x	x	x		Projects and inspections, material related to recovery interventions
STAU00T2PNLTTNAQ0R	x	x	x		Projects and inspections, material related to recovery interventions
STAU00T2PNLVWYFMG7	x	x	x	x	Projects and inspections, material related to recovery interventions
STAU00T2PNU8ZRYLZD	x	x	x		Projects and inspections, material related to recovery interventions
STAU00T2PNA9GMMTCJ	x	x	x	x	Projects and inspections, material related to recovery interventions
STAU00T2PNG3QSNWPY	x	x	x	x	Projects and inspections, material related to recovery interventions
STAU00T2PN70SJMJEV	x	x	x	x	Projects and inspections, material related to recovery interventions

Table 3: Provided and analysed material from T2 owners.

Name	Typology	Year	Spans	Length	Abutments	Piers (hmax)	Interventions	Defect Index* (2021–2022)
Chantel 123	Continuous girders	1963	8	80	r.c. gravity wall	Solid r.c. with footing (12)	2008	1.9–2.2
Chantel 224	Continuous girders	1963	10	100	r.c. gravity wall	Solid r.c. with footing (7)	2010	1.4–1.4
Closette 15	Continuous girders	1963	12	120	r.c. gravity wall	Solid r.c. with footing (17)	2012	0.9–1.3
Curvone 12	Simply supported girders	1963	100	1010	r.c. gravity wall (piles)	Solid r.c. with footing (+piles) (15)	2003–2022	1.5–1.8
Dardanelli 01	Simply supported girders	1963	17	305	r.c. gravity wall	Solid r.c. + hollow with footing (70)	1996 and 2005	1.3–1.9
Devie 13	Continuous girders	1963	16	160	r.c. gravity wall	Solid r.c. with footing (10)	2006 and 2016	3.6–4.0
Envy 120	Continuous girders	1963	8	80	r.c. gravity wall	Solid r.c. with footing (8)	2022	5.6–5.5
Envy 221	Continuous girders	1963	9	90	r.c. gravity wall	Solid r.c. with footing (16)	–	1.6–2.2
Envy 322	Continuous girders	1963	20	200	r.c. gravity wall	Solid r.c. with footing (17)	2010	1.3–1.6
Fortino 28	Continuous girders	1963	11	110	r.c. gravity wall	Solid r.c. with footing (12)	2022	2.5–3.9
Gorres 10	Continuous girders	1963	13	130	r.c. gravity wall	Solid r.c. with footing (8)	1997, 2005, 2014	2.5–3.3
Imbocco 31	Continuous girders	1963	8	164	r.c. gravity wall	Solid r.c. with footing (34)	-	3.5-3.8

Table 4: Summary of main information from analysed material. Note: the defect index reported is not based on the Italian Guidelines but is an index calculated by the inspections company.

Class of Attention

After analysing the material the class of attention using the guidelines was done for the bridges and the result are in the table.

Name	Structural class of attention	Seismic class of attention	Hydraulic and landslide class of attention	Total class of attention
Viadotto Chantel 1	Medium	Medium	Medium	Medium
Viadotto Chantel 2	Medium	Medium	Medium	Medium
Viadotto Closette	Medium	Medium	Medium-high	Medium
Viadotto Curvone	Medium-high	Medium-high	Medium	Medium-high
Viadotto Dardanelli	Medium	Medium	Medium-high	Medium
Viadotto Devie	Medium	Medium	Medium	Medium
Viadotto Envy 1	Medium	Medium	Medium	Medium
Viadotto Envy 2	Medium	Medium	Medium-high	Medium
Viadotto Envy 3	Medium	Medium	Medium	Medium
Viadotto Fortino	Medium	Medium	Medium	Medium
Viadotto Gorres	Medium	Medium	Medium	Medium
Viadotto Imbocco	Medio-Alta	High	Medium-high	High

Table 5: Calculated Class of Attention.

For better explanation of the classification process, an example for one of the bridges are reported below. In the next pages the classification for the Curvone viaduct is presented.

Example of Analysis Sheet - Viadotto "Imbocco 31"

Viaduct on an extra-urban motorway (section T2, Valle d'Aosta) in reinforced concrete – 8 spans with an average length of about 21 m – continuous beams, 4 single girders and 2 box girders closed at the bottom by a slab forming a tunnel.

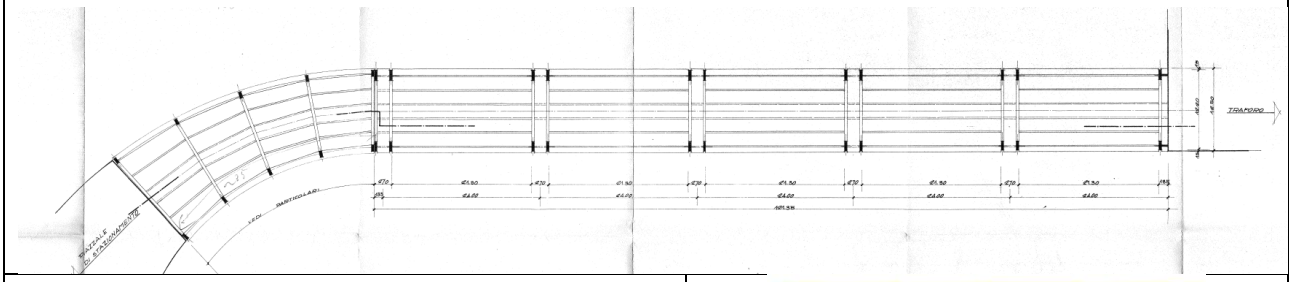

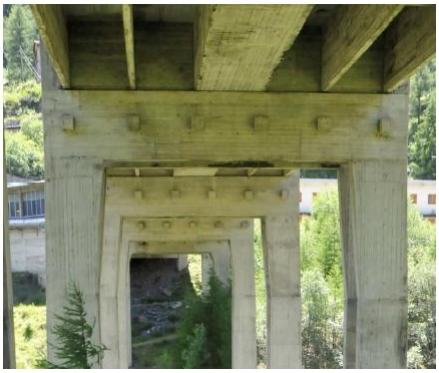

Structural and Foundation Class of Attention

Hazard	
Maximum admissible load: Class A	**Hazard Class: Medium-High**
Frequency of heavy vehicle traffic: Low	
Vulnerability	
Defect level: Medium-High	**Vulnerability Class: Medium-High**
Degradation rate: Construction: 1945–1980 (1963)	
Design standards: Class A	
Static scheme and materials: continuous girders – span length 15 < L < 25 – 8 spans – R.C.: Medium	
Exposure	
Average daily traffic: Low (< 10,000 vehicles/day)	**Exposure Class: Medium-Low**
Span length: Medium	
Road alternatives: None	
Type of crossed entity: Low	
Transport of dangerous goods: No	
Structural and Foundation Class of Attention: Medium-High	

Seismic Class of Attention

Hazard	
Peak ground acceleration on rigid soil (SLV): 0.10–0.15	**Hazard Class: Medium**
Topographic category: T2	
Subsoil category: B	
Vulnerability	
Structural scheme: Hyperstatic	**Vulnerability Class: High**
Materials: Reinforced concrete	
Span length: High	
Single/multi-span: Multi-span	
Additional seismic vulnerability elements: Yes	
Design criterion: Non-seismic	
Defect level: Medium-High	
Exposure	
Structural and foundation exposure: Medium-Low	**Exposure Class: Medium**
Strategic infrastructure: Yes	
Seismic Class of Attention: High	

Landslide risk class of attention

Susceptibility	
Slope instability: (3+5+15=23) High	**Susceptibility Class: High**
Reliability of the assessment: Good	
Mitigation measures: N/A	
Vulnerability	
Structural and foundation vulnerability (seismic – Table 4.13):	**Vulnerability Class: Medium-High**
Foundation type: Shallow	
Extension of interference (between landslide and structure): Partial	
Exposure	
Structural and foundation exposure: Medium-Low	**Exposure Class: Medium**
Strategic infrastructure: Yes	
Landslide risk class of attention: Medium-High	

Hydraulic risk class of attention

Overtopping			
Susceptibility: Low		**Overtopping Class: Medium-Low**	
Vulnerability: Medium-Low			
Exposure	Structural and foundation exposure: Medium-Low		
	Strategic infrastructure: Yes		
Generalized erosion			**Erosion Class: Medium-High**
Susceptibility: Medium-Low		**Generalized erosion Class: Medium**	
Vulnerability: Medium			
Exposure	Structural and foundation exposure: Medium-Low		
	Strategic infrastructure: Yes		
Localized erosion			
Susceptibility: Medium-Low		**Localized erosion: Medium**	
Vulnerability: Medium			
Exposure	Structural and foundation exposure: Medium-Low		
	Strategic infrastructure: Yes		
Hydraulic risk class of attention: Medium-High			

Final class of attention

Structural and foundation class of attention:	Medium-High
Seismic class of attention:	High
Landslide/hydraulic risk class of attention:	Medium-High
Overall bridge class of attention:	**High**

The final classification "high" is due to the presence of the high class for seismic risk and the concurrent presence of "medium–high" landslide and hydraulic risks. This classification is consistent with the actual condition of the structure.

Classe di attenzione strutturale/fondazionale ***MEDIO - ALTA***

Classe di attenzione sismica \ Classe di attenzione idraulica e frane	Alta	Medio-Alta	Media	Medio-Bassa	Bassa
Alta	Alta		Medio-Alta		
Medio-Alta	Alta	Medio-Alta			Media
Media	Medio-Alta			Media	
Medio-Bassa	Medio-Alta		Media		
Bassa	Medio-Alta	Media			

Figure 68: Final classification table.

Having established the Class of Attention (CoA) for the structures under investigation, the next step, following the Guidelines, is to proceed with the more detailed evaluations of Levels 3 and 4. Level 3 focuses on a preliminary assessment of the structure's resources and the nature of observed defects, while Level 4 requires a full and accurate safety verification. For this latter stage, the availability of reliable finite element (FEM) models is essential, as the accuracy of the safety assessment directly depends on the quality of the numerical representation of the structure. This necessity provided the motivation for the subsequent work presented in this thesis, which focuses on model updating procedures aimed at reducing the uncertainties between the FEM predictions and real structural behaviour.

In the following chapter, the theoretical background concerning model updating and modal analysis is presented. This section serves as a necessary foundation for the subsequent analyses, as it introduces the principles and methodologies that will later be applied to the case studies. While the practical applications presented later represent the core of the research, the forthcoming chapter illustrates the theoretical framework at the base.

Chapter 3

Modal Analysis and Model Update – Theoretical background

In applied sciences and engineering, modal dynamic identification provides a framework for determining the fundamental dynamic properties of structures namely natural frequencies, mode shapes, and modal damping ratios. Within civil engineering, these methods are particularly valuable for a broad range of objectives, including structural dynamics characterization, response prediction, Structural Health Monitoring (SHM), damage detection, and structural assessment [42] [3]. As modern civil structures grow increasingly complex in both geometry and material behaviour, and as existing constructions often present uncertain mechanical parameters, the accurate prediction of their dynamic response becomes a challenging task. This motivates the adoption of advanced analytical strategies, including finite element modelling, complemented by experimental and data-driven identification techniques. Modal identification techniques can be broadly classified into two categories. Experimental Modal Analysis (EMA) relies on measured responses to known excitations, providing input–output formulations that are fundamental for validation. Operational Modal Analysis (OMA), in contrast, uses only structural responses induced by unknown ambient or operational loads, and has become increasingly popular for civil infrastructure [43] [44] [45] [46].

Early studies on long-span bridges illustrated how ambient vibration testing can characterize modal properties without interrupting service, practical applications summarized by [47] demonstrate the effectiveness of output-only testing for bridge dynamic assessment. Case studies such as the Humber Bridge [48] the Guadiana Bridge [49], and the Millau Viaduct [50] exemplify the combination of field measurements with advanced processing or finite element models. Research has been done for study if human-induced excitations in lightweight footbridges [51] or traffic loads [52] affect dynamic behaviour. Wireless sensor networks have enabled flexible large-scale deployments, as in the output-only modal testing of cable-stayed bridges [53]. More recent reviews synthesize accumulated knowledge and best practices for OMA in bridges [54].

Beyond bridges, OMA has been successfully applied to tall buildings and towers. For instance, the Guangzhou New TV Tower was analysed through combined theoretical and experimental modal testing, revealing the challenges posed by super-tall structures [55]. More recently, ambient vibration tests of high-rise buildings in Shanghai highlighted how full-scale measurements support finite

element model updating [56]. In rotating machinery, operational modal identification has been extended to include the effect of frictional damping, improving estimates under real operating conditions [57]. Application to dams further illustrates the value of automated OMA algorithms for continuous monitoring of critical infrastructure [58]. Also historical structures have been subject of dedicated analysis campaigns emphasizing diagnostic methods and monitoring strategies adapted to heritage buildings [59]. These examples illustrate the versatility of modal identification methods across engineering domains.

The integration of OMA into structural health monitoring has been a major development. Automated pipelines capable of tracking modal parameters in real time enable vibration-based damage detection strategies [60] [61] [62] and hybrid approaches that account dynamic identification with high-quality measurements, robust algorithms, and increasingly automated pipelines that enable continuous monitoring, finite element modelling and mathematical methods are becoming a stone of structural assessment, with a wide range of successful applications. Its effectiveness relies on high-quality measurements, robust algorithms, and increasingly automated pipelines that enable continuous monitoring.

Fundamentally, modal identification can be interpreted as an inverse problem given the measured response of a system (and, where applicable, the applied excitation), the aim is to infer the underlying structural parameters. For the purposes of this dissertation, emphasis will be placed on the theoretical foundations of signal processing and on the basic operational frameworks for both domains, as a necessary prelude to the rest of the work [63] [64] [65] [66].

Signal Analysis

In engineering, some physical phenomena can be described by a mathematical relationship in a deterministic way, such as the free vibration response of a single degree of freedom (SDOF) system subjected to initial conditions, as it is governed by an explicit mathematical expression depending on the mass and stiffness properties of the system. From a physical perspective, structures exposed to operational excitations (e.g., wind, traffic, earth tremors) are subjected to inputs that are not only unknown but also intrinsically random. Therefore, the dynamic response must be modelled as a stochastic (or random) process $x(t)$, which is a set of time-indexed random variables. A random variable X describes an outcome or realization with an associated probability. For structural

monitoring, acceleration, velocity, or displacement signals measured over time are modelled as realizations of such processes. Due to the randomness, the process can be described by its Probability Density Function (pdf), denoted as $p(x)$, and its moments, for example, the first moment, the mean value μ_x (or expected value) is:

$$\mu_x = E[x(t)] = \int_{-\infty}^{+\infty} x\, p(x)\, dx$$

the variance is defined as:

$$\sigma_x{}^2 = E[(x(t) - \mu_x)^2] = \int_{-\infty}^{\infty} (x - \mu_x)^2\ p(x)\, dx$$

that is the second moment of the *pdf* and which the well-known standard deviation σ, calculated as the square root of $\sigma_x{}^2$, represents a measure of the width of the *pdf*. In the real application, the data is sampled in time in a discrete way, the mean and the variance became:

$$\mu_x \approx \sum_{i=1}^{n} x_i\ P(x_i)$$

$$\sigma_x^2 \approx \sum_{i=1}^{n} (x_i - \mu_x)^2\ P(x_i)$$

where $P(x_i)$ denotes the probability associated with the value x_i at a certain instant i.

Stationarity, ergodicity and Gaussian processes

A random process is said to be stationary (Strong-Sense Stationary (SSS)) if the *pdf* of the underlying stochastic variable *X* is not a function of time. This implies that its statistical properties of any order (mean, variance, skewness ecc.) are invariant under time shifts τ. Real data are always more or less nonstationary, but, if the signals have:

- constant mean: $\mu_x(t) = \mu_x$
- time-invariant autocorrelation: $R_{xx}(\mathrm{t}, \mathrm{t} + \tau) = R_{xx}(\tau)$

Then the process can be considered weakly-sense stationary (WSS), and this simplification is critical in practice, as many identification algorithms rely on stationarity to estimate spectral content or modal parameters. A stochastic process is defined as Gaussian if every finite-dimensional vector formed by

its values at any collection of time instants follows a multivariate normal distribution. This definition implies that a Gaussian process is completely characterized by its first two moments: mean and autocorrelation (or covariance), regardless of higher-order statistics. This property is especially valuable in output-only modal identification, as used in Operational Modal Analysis (OMA). Under the assumption of Gaussianity and stationarity, second-order statistics such as the autocorrelation function contain all the information necessary to extract modal parameters, including natural frequencies, damping ratios, and mode shapes. Moreover, when a process is both weakly-sense stationary (WSS) and Gaussian, it is also ergodic. This justifies the common practice in structural monitoring of estimating modal properties from a single realization of the response signal, provided the observation window is sufficiently long and the excitation is broadband. In real applications, excitation sources such as traffic, wind, or ambient vibrations are typically not strictly Gaussian, but empirical studies show that their statistical behaviour is often close enough to Gaussian to make this assumption a reasonable and effective approximation. When the input is only approximately white and Gaussian, the modal parameters extracted under these assumptions remain physically meaningful and reliable.

In practical applications, individual time history records are considered stationary if the properties computed over short time intervals do not vary significantly from one interval to the next. In other words, any variations are limited to statistical sampling variations. Since a sample record obtained from an ergodic process is stationary, verifying the stationarity of individual records justifies the assumption of stationarity and ergodicity for the random process from which the sample record is obtained. Tests for stationarity of data are advisable before processing [64]. Or in a practical way Mean and variance over sliding windows can be evaluated. Given a long record $x(t)$, the time series is segmented into windows $x_k(t)$ of length t. Only segments satisfying:

$$\frac{\Delta\sigma_k}{\bar{\sigma}} < \varepsilon \quad \text{and} \quad \frac{\Delta\mu_k}{\bar{\mu}} < \varepsilon$$

are retained, where μ_k and σ_k are the local mean and standard deviation, and ε is a tolerance threshold (e.g., 5%).

Autocorrelation, Cross-Correlation, and Covariance Functions

In the analysis of stochastic processes, the concepts of autocorrelation, cross-correlation, and covariance functions are fundamental tools for characterising the temporal structure and statistical dependencies within and between signals. Under the assumption of stationary and random response of the structure, the second-order statistics of the response contain all the physical information. The

autocorrelation function quantifies the similarity of a signal $x(t)$ with a time-shifted version of itself $x(t+\tau)$:

$$R_{xx}(\tau) = E[x(t)x(t+\tau)]$$

Where τ is the time shift. Physically, the autocorrelation captures how predictable the signal is over time: if the signal repeats patterns, the autocorrelation will exhibit peaks corresponding to those time intervals. In modal analysis, peaks and oscillations in the autocorrelation function are directly related to the natural frequencies and damping characteristics of the system. If two signals are considered, the quantity

$$R_{xy}(\tau) = E[x(t)y(t+\tau)]$$

take the name of cross-correlation function and indicates how the two signals are correlated in time. The covariance function is

$$C_{xx}(t_1, t_2) = E\big[\big(x(t_1) - \mu_x(t_1)\big) \cdot \big(x(t_2) - \mu_x(t_2)\big)\big]$$

Where t_1 and t_2 and two different time instants, if the process is stationary the mean does not depend on time and if the process is Gaussian is also equal to zero, that implies that the covariance function is equal to the correlation function. It can also be proved that at time shift $\tau = 0$

$$R_{xx}(0) = E[x^2(t)] \qquad C_{xx}(0) = {\sigma_x}^2$$

The formulations presented are written for time random processes, as indicated by the presence of E(). In the continuous time domain, the formulation could be written, for example, for the autocorrelation, as follows:

$$R_{xx}(\tau) = \int_{-\infty}^{+\infty} x(t) \cdot x(t+\tau)\, dt \qquad R_{xy}(\tau) = \int_{-\infty}^{+\infty} x(t) \cdot y(t+\tau)\, dt$$

Power Spectral Density (PSD)

The Power Spectral Density (PSD) function $S_{xx}(\omega)$ describes how signal power is distributed over frequency and is one the most important tools in OMA, it is defined:

$$S_{xx}(\omega) = \int_{-\infty}^{+\infty} R_{xx}(\tau)\ e^{-j\omega\tau}\, d\tau$$

If two signals are considered, the following function is called the cross-correlation function.

$$S_{xy}(\omega) = \int_{-\infty}^{+\infty} R_{xy}(\tau)\ e^{-j\omega\tau}\, d\tau$$

These are the Fourier transforms of the autocorrelation functions and are also called the Wiener-Khinchin relations. In real-world applications, PSDs are not computed from theoretical autocorrelation functions, but are estimated from measured time series using one of several methods:

- Periodogram: Based on the squared magnitude of the FFT.
- Welch's method: Averages multiple overlapping periodograms to reduce variance.
- Parametric methods: Fit a model (e.g., AR, ARMA) and derive the PSD analytically.

The PSD quantifies the amount of signal power present at each frequency component. For mechanical systems, peaks in the PSD correspond to resonant frequencies, that is, frequencies at which the system naturally tends to vibrate. In output-only modal analysis, the PSD of the response signal contains information about the underlying modal characteristics, provided the input excitation is broadband and has sufficient energy to excite all natural modes. If multiple outputs are considered, the cross-power spectral density matrix, $S_{yy}(\omega)$, is used:

$$S_{yy}(\omega) = E[Y(\omega)Y^H(\omega)]$$

where $Y(\omega)$ is the Fourier transform of the response vector, and apex H denotes the Hermitian (conjugate transpose). The auto-spectral density functions are real-valued functions, while the cross-spectral density functions are complex-valued

Fourier Transform

The Fourier transform is a fundamental mathematical tool in modal analysis. It enables the transition from the time domain, where signals are acquired, to the frequency domain, where modal characteristics are most easily interpreted.

Given a continuous signal $x(t)$, its Fourier transform $X(\omega)$ is defined as:

$$X(\omega) = \int_{-\infty}^{+\infty} x(t)\ e^{-j\omega t}\, dt$$

where:

- ω is the angular frequency (rad/s),
- j is the imaginary unit.

The inverse transform recovers the time-domain signal:

$$x(t) = \frac{1}{2\pi}\int_{-\infty}^{+\infty} X(\omega)\ e^{j\omega t}\, d$$

In operational modal analysis, the Fourier transform decomposes a response signal into its frequency components, revealing peaks at frequencies where the structure resonates, i.e., its natural frequencies. This is based on the principle of superposition: for linear time-invariant (LTI) systems, any input can be represented as a sum of harmonic functions. The structure's output will reflect these frequencies, filtered by the system's dynamics. Methods such as Frequency Domain Decomposition (FDD) and Enhanced FDD rely on the singular value decomposition (SVD) of the output cross-spectral density matrix, obtained using the Fourier transform. Peaks in the singular value spectra correspond to structural modes. Therefore, the Fourier domain reveals modal frequencies and enables mode shape estimation by extracting the spatial distribution of amplitudes across sensors at resonance.

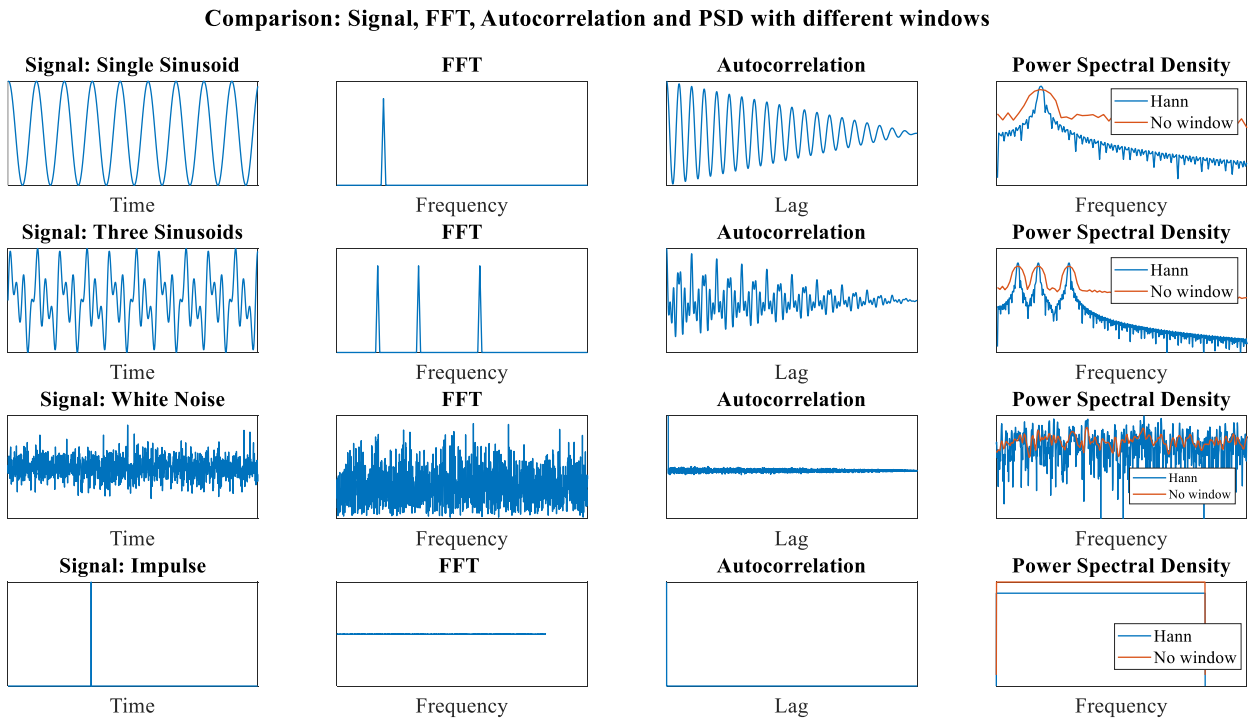

Figure 69: Example of FFT, Autocorrelation and PSD for different type of signals.

Mathematical Modelling and System Representations

Basic Concepts: SDOF and MDOF Systems

A structural system can be modelled dynamically by representing it as a set of masses, stiffness elements, and damping mechanisms. The simplest abstraction is the single degree of freedom (SDOF) system, which captures the essence of linear vibration behaviour. This model is physically interpreted as a mass-spring-damper system subjected to an external force. The corresponding equation of motion, derived from Newton's second law, relates inertia, damping, stiffness, and applied forces.

$$m\ddot{x}(t) + c\dot{x}(t) + kx(t) = f(t)$$

The solution to the homogeneous (free vibration) version of this equation reveals the system's natural dynamics, including its undamped natural frequency and damping ratio

$$\omega_n = \sqrt{\frac{k}{m}}\ \xi = \frac{c}{2\sqrt{km}} = \frac{c}{2m\omega_n}$$

For real structures, especially civil infrastructure such as bridges, a multiple degree of freedom (MDOF) system is necessary. In such models, each degree of freedom corresponds to an independent coordinate describing displacement. The equations of motion can be concisely expressed in matrix form

$$M\ddot{x}(t) + C\dot{x}(t) + Kx(t) = f(t)$$

Where:

- M, C, K are the mass, damping, and stiffness matrices,
- $x(t)$ is the displacement vector,
- $f(t)$ is the external force vector.

The modal properties (natural frequencies and mode shapes) are obtained by solving the eigenvalue problem:

$$(K - \omega^2 M)\phi = 0$$

Assuming linearity and time invariance, the system's response to any input can be analysed in the frequency domain, where the system can be decomposed into harmonic components. Using Fourier transforms, the relationship between input $F(\omega)$ and output $Y(\omega)$ becomes:

$$Y(\omega) = H(\omega)\, F(\omega)$$

The Frequency Response Function (FRF) $H(\omega)$ is defined as:

$$H(\omega) = \frac{Y(\omega)}{F(\omega)}$$

It encapsulates the system's dynamics in the frequency domain, including resonance, anti-resonance, and damping. This function encapsulates how the system amplifies or attenuates sinusoidal inputs at different frequencies. Peaks in the magnitude of $H(\omega)$ correspond to natural frequencies, and the shape of the peaks reflects the damping characteristics.
In the time domain, the relationship between input and output is described by the impulse response function $h(t)$. It represents the system's output when subjected to a unit impulse at $t = 0$. The output is given by the convolution:

$$y(t) = h(t) * f(t) = \int_0^t h(\tau) f(t-\tau)\, d$$

In the frequency domain, this convolution $*$ becomes a simple multiplication $Y(\omega) = H(\omega)F(\omega)$
Thus, the impulse response $h(t)$ and the FRF $H(\omega)$ form a Fourier transform pair:

$$H(\omega) = \int_{-\infty}^{+\infty} h(t)\; e^{-j\omega t}\, dt$$

These concepts are the foundation for Frequency Domain Decomposition (FDD) that is described in the follow.

Autoregressive Models and State-Space Representation

For system identification, particularly in the time domain, the system can be modelled using autoregressive models. These represent the output signal as a function of past outputs and, optionally,

past inputs and noise terms. An AR model uses only previous outputs; ARMA includes moving average (noise) terms; ARX includes known external inputs. These models are linear difference equations whose coefficients encode the system dynamics.

The state-space model offers a concise and general framework for modelling linear dynamic systems. It represents the system with a set of first-order differential equations involving state variables, inputs, and outputs.

The continuous-time state-space form is:

$$\begin{cases} \dot{x}(t) = Ax(t) + Bu(t) \\ y(t) = Cx(t) + Du(t) \end{cases}$$

The discrete-time counterpart (used in digital processing) is:

$$\begin{cases} x_{k+1} = A_d x_k + B_d u_k \\ y_k = C_d x_k + D_d u_k \end{cases}$$

Where:

- x_k : state vector
- y_k : output vector
- u_k : input vector
- A, B, C, D are the system matrices

This representation is central to modern OMA techniques such as Stochastic Subspace Identification (SSI). The modal parameters (frequencies, damping, modes) are extracted from the system matrices via eigen-decomposition. System identification is the process of deriving a mathematical model that describes the dynamic behaviour of the structure directly from measured data. Modal analysis is the subsequent step, in which the modal parameters (eigenfrequencies, damping ratios, mode shapes, modal scaling) are determined from the identified system model. In other words, system identification produces a model, while modal analysis extracts the modal characteristics from that model.

Fundamentals of Operational Modal Analysis (OMA)

Operational Modal Analysis aims to extract the modal properties of a structure (natural frequencies, damping ratios, and mode shapes) based on its response to ambient, uncontrolled excitation. Unlike traditional modal analysis, OMA requires measurement only of the output (usually acceleration or displacement), not the input. The fundamental assumption is that the input can be modelled as

stochastic broadband excitation, typically approximated as white noise. Consequently, each mode of the structure is expected to be sufficiently excited over time, allowing its dynamic signature to emerge in the output data. Physically, ambient forces (traffic, wind, microseismic motion) are considered spatially and temporally uncorrelated, although in practice some correlation may exist. This still allows reliable identification if the statistical assumptions are approximately valid. OMA relies on a set of core assumptions:

- Linearity: the structural system behaves linearly in the range of observed response.
- Time-invariance: the system's properties do not change during measurement.
- Stationarity: the excitation and the resulting response are statistically stationary.
- Broadband excitation: the input has sufficient energy across the frequency band of interest.

These assumptions may not always hold in real-world applications. For example, time-varying stiffness due to temperature or strongly correlated excitation (e.g., synchronized traffic) can violate OMA requirements. Nevertheless, many structures approximate these conditions sufficiently, and accurate modal identification can be achieved if preprocessing and validation techniques are applied correctly.

OMA algorithms are typically classified into two major families:

- Frequency-domain methods operate on the spectral representation of signals. They are intuitive, computationally efficient, and particularly suitable for structures with well-separated modes. Spectral peaks correspond to modal frequencies, and mode shapes are extracted from cross-spectral information. [67] [63]
- Time-domain methods model the system's impulse or correlation response, typically using state-space or autoregressive formulations. These methods are more robust when closely spaced modes or noise are present, and allow the use of stabilization diagrams for mode validation.

The choice depends on the structure’s dynamic complexity, noise levels, and the required level of automation. [68] [69]. Among frequency-domain methods, Frequency Domain Decomposition (FDD) remains a reference approach for output-only modal identification [70], while in the time domain stochastic subspace identification (SSI) has been established as a rigorous framework [71] [69].

Peak Picking (PP)

This is the simplest method. It relies on identifying peaks in the output power spectral density (PSD). If the input is truly white noise, these peaks correspond to the structure's natural frequencies. Mode shapes are obtained by evaluating the relative amplitudes of the output signals at each peak.

$$S_{yy}(\omega) = H(\omega)S_{ff}(\omega)H^H(\omega)$$

Limitations:

- No damping estimation
- Requires well-separated modes
- Sensitive to non-white excitation

Frequency Domain Decomposition (FDD)

FDD improves upon peak picking by considering the cross-spectral density matrix $S_{yy}(\omega)$ and performing Singular Value Decomposition (SVD):

$$S_{yy}(\omega) = U(\omega)\Sigma(\omega)U^H(\omega)$$

The first singular value shows a peak at each modal frequency, and the corresponding singular vector approximates the mode shape.

Advantages:

- Handles multiple outputs
- Allows mode shape estimation
- Easy to implement

Enhanced FDD (EFDD)

EFDD adds damping estimation by inverse-transforming a narrowband segment around each frequency peak back into the time domain. The logarithmic decrement of the resulting impulse-like response is used to estimate the damping ratio. $\xi = \frac{1}{2\pi N}\ln\left(\frac{x(t)}{x(t+NT_d)}\right)$

Stochastic Subspace Identification (SSI)

A time-domain method based on state-space modelling. SSI reconstructs system matrices from output-only data and estimates modal parameters via eigen-decomposition.

Variants:

- Covariance-driven (Cov-SSI): uses correlation matrices
- Data-driven (DD-SSI): works directly on raw data

This method provides high-quality estimates of all modal parameters and is robust in noisy conditions or for structures with closely spaced modes.

Stabilization Diagrams and Mode Validation

To distinguish true physical modes from numerical or noise-induced artifacts, stabilization diagrams are used. These diagrams display identified modal parameters (frequency, damping, mode shape) as a function of the model order.

A mode is considered stable if it appears repeatedly across increasing model orders with minimal variation.

Stabilization criteria:

- Frequency variation $\varepsilon_f < \Delta f < \varepsilon f$
- Damping variation $\varepsilon\xi < \Delta\xi < \varepsilon\xi$
- High Modal Assurance Criterion (MAC) between repeated shapes

The Modal Assurance Criterion (MAC) quantifies the correlation between two mode shapes

$$\mathrm{MAC}(\phi_i, \phi_j) = \frac{\left|\phi_i^H \phi_j\right|^2}{(\phi_i^H \phi_i)(\phi_j^H \phi_j)}$$

Values range from 0 (orthogonal) to 1 (identical), with values > 0.9 typically considered acceptable for identifying repeated or consistent modes [72].

Other modal indicators include the Modal Phase Collinearity (MPC) and the Modal Phase Deviation (MPD), which are used to assess the quality and reliability of identified modes. These indicators are implemented in the MACEC [136] code and were used during the selection of physically meaningful modes in the identification process. Their mathematical formulation is given below.

Modal Phase Collinearity (MPC)

When a structure is proportionally damped, the mode shape components of a single mode lie on a straight line in the complex plane. For double modes, that is, two modes with exactly the same eigenfrequency, this is not the case; however, such modes are very rare in practice, except in doubly symmetric structures. For nearly axisymmetric structures, valid mode shapes have been found to form a circle in the complex plane. Therefore, although mode shape collinearity is a very powerful single-mode validation criterion, it should be used with care.

The complexity of a mode shape ϕ can be measured with the modal phase collinearity (MPC):

$$MPC(\phi_j) = \frac{\left\|Re(\phi_{j0})\right\|_2^2 + \frac{1}{\epsilon_{MPC}} Re(\phi_{j0})^T Im(\phi_{j0})(2(\epsilon_{MPC}+1)\sin^2(\theta_{MPC}) - 1)}{||Re(\phi_{j0})||_2^2 + ||Im(\phi_{j0})||_2^2}$$

Where:

- $\mathrm{Re}(\phi_j)$ is the real part of the complex eigenvector ϕ_j
- $Im(\phi_j)$ is the imaginary part,
- ϕ_{j_0} is the centered eigenvector
- ϵ_{MPC} ,θ_{MPC} are auxiliary quantities defined as:
- Where n_y is the number of output degrees of freedom considered.

$$\phi_{j_0} = \phi_j - \frac{\sum_{i=1}^{n_y} \phi_j}{n_y}$$

$$\epsilon_{MPC} = \frac{||Im(\phi_j)||_2^2 - ||Re(\phi_j)||_2^2}{2Re(\phi_j)^T Im(\phi_j)}$$

$$\theta_{MPC} = \arctan\left(|\epsilon_{MPC}| + \mathrm{sign}(\epsilon_{MPC})\sqrt{1+\epsilon_{MPC}^2}\right)$$

A detailed motivation of this expression can be found in [30]. MPC values are dimensionless; they lie between 0 (not collinear at all) and 1 (perfect collinearity). [62]

Mean Phase Deviation (MPD):

Alternatively, one can compute the mean phase (MP) of the mode shape components, together with the mean phase deviation (MPD), defined as the (weighted) average deviation of these components

from the mean phase. Approximate formulas for MP and MPD exist, but they become unreliable when the mode shape has a large imaginary part and only a small real part. This situation may occur, for example, when a mode shape is well identified in an EMA or OMA test, but its mass normalisation is of poor quality. For this reason, new formulations are introduced here.

The mean phase can be obtained as the angle of the straight line that best fits the mode shape in the complex plane, determined such that the orthogonal regression error is minimized. This leads directly to the following total least squares problem:

$$MP(\phi_j) = argmin_\theta \frac{\left\| Im(\phi_j) - \tan(\theta)\, Re(\phi_j) \right\|_2^2}{1 + \tan(\theta)}$$

$$MP(\phi_j) = \arctan\left(\frac{-V_{12}}{V_{22}}\right) \qquad USV^T = \left[\mathrm{Re}(\phi_j) \quad \mathrm{Im}(\phi_j)\right]$$

where:

- $U \in R^{n_y \times 2}$, $S \in R^{2\times 2}$, $V \in R^{2\times 2}$ constitute a singular value decomposition, i.e., S is a diagonal matrix with decreasing entries along the diagonal, and U and V have orthonormal columns.
- V_{12} and V_{22} denote the elements (1,2) and (2,2) of matrix V, respectively.

The deviation of the phase of ϕ_{j0} from the mean phase can be computed from the scalar product between $\left[\mathrm{Re}(\phi_{j0}) \quad \mathrm{Im}(\phi_{j0})\right]^T$ and $[V_{22} \;\; -V_{12}]^T$

The mean phase deviation is subsequently obtained as:

$$MPD(\phi_j) = \frac{\sum_{o=1}^{n_y} w_o \arccos\left(\dfrac{\mathrm{Re}(\phi_{j_0})V_{22} - \mathrm{Im}(\phi_{j_0})V_{12}}{\sqrt{V_{12}^2 + V_{22}^2}|\phi_{j_0}|}\right)}{\sum_{o=1}^{n_y} w_o}$$

with the condition:

$$\sum_{o=1}^{n_y} w_o \neq 0$$

where wo are weighting factors, that may be chosen equal to $|\phi_{j_0}|$ in order to give mode shape components with a larger amplitude a larger weight. [62] or in other formulations [73]. These help detect spurious or poorly estimated modes, especially in automated workflows.

Practical Aspects of Signal Acquisition and Processing

To obtain a reliable estimate of the modal characteristics, it is essential to perform accurate data acquisition.

Sensors and Measurement Chain

The core of an OMA campaign is the measurement chain, comprising sensors, signal conditioning units, and data acquisition systems (DAQs). The most commonly used sensors in civil structures are piezoelectric accelerometers, which generate a charge in response to dynamic motion. Their sensitivity is expressed in mV/g or mV/(m/s²). Before digitization, analogue signals are passed through anti-aliasing filters to remove frequencies above half the sampling rate (the Nyquist frequency). Failure to do so causes aliasing, where high-frequency content folds back into the lower spectrum, corrupting spectral estimates.
To reliably estimate frequency content and modes, sampling and record length must follow physical and signal-processing constraints.

- Nyquist Criterion: sampling frequency f_s must be at least twice the highest frequency f_{max} of interest:

  $$f_s \geq 2f_{\max}$$

  Aliasing occurs when this condition is not met, leading to frequency overlap and distortion.
- Frequency resolution is inversely proportional to the observation time T:

  $$\Delta f = \frac{1}{T}$$

  Longer records improve frequency resolution, critical for identifying closely spaced modes.
- Anti-aliasing filters must be applied before sampling to avoid folding of high-frequency components into the baseband.

Effective modal identification requires observable and distinguishable modes, which is directly affected by sensor layout. Mode observability depends on:

- Number of sensors and their spatial distribution
- Direction of measurement (vertical, horizontal, torsional)
- Sensor location with respect to modal curvature; let $\phi i \in R$, denote the i-th mode shape vector across n sensor locations. If ϕi has zero or near-zero components at certain points, sensors placed there will contribute little or no information about that mode.

Sensor layout optimization often uses Modal Assurance Criterion (MAC) sensitivity or Effective Independence (EFI) algorithms to maximize modal observability. These methods are part of Optimal Sensor Placement (OSP), a useful tool in modal analysis to ensure that sensors efficiently capture all relevant modes. Methods such as Effective Independence (EFI) and the Fisher Information Matrix (FIM) optimize sensor locations to maximize independent information and reduce uncertainty in modal estimates. Other approaches, such as the Modal Kinetic Energy (MKE) method or information-theoretic techniques, focus on placing sensors where measurements are most sensitive to the modes of interest. More recently, machine learning algorithms have been used to find optimal layouts for complex structures.

Signal Preprocessing

Another important consideration is that raw structural signals are often affected by sensor drift, mechanical noise, and external interference. To obtain reliable results, signals must undergo preprocessing, which typically includes:

- Detrending removes DC bias or slow drift by polynomial subtraction or high-pass filtering.
- Windowing applies a tapering function (e.g., Hanning window) to minimize spectral leakage in the Fourier domain. There are many types of window, each applied based on the intended purpose.
- Filtering is a signal-processing tool that selectively allows certain frequency components to pass while attenuating others. Band-pass filters are used in modal analysis to focus on specific frequency regions associated with structural modes, reducing noise and improving the clarity of the dynamic response. They can be expressed as a transfer function such as:

$$H(f) = \frac{f^2}{\sqrt{(f^2 - f_0^2)^2 + (2\xi f f_0)^2}}$$

Data Quality Estimation

Quantitative evaluation of signal quality is crucial. A key metric is the Signal-to-Noise Ratio (SNR):

$$\mathrm{SNR}_{\mathrm{dB}} = 10 \log_{10} \left(\frac{\sigma^2_{\mathrm{signal}}}{\sigma^2_{\mathrm{noise}}} \right)$$

where $\sigma^2_{\mathrm{signal}}$ and $\sigma^2_{\mathrm{noise}}$ denotes the variance of the signal and the background noise, respectively.

Other commonly used metrics for assessing data quality include:

- Mean: the average value of the signal over a segment; large drifts may indicate sensor bias or low-frequency noise.
- Variance: measures the signal's power or spread; helps identify segments with unusually high or low activity.
- Noise floor: estimated from quiet periods (e.g., low traffic at night).
- Kurtosis: high values may indicate impulsive noise or outliers.
- Skewness: measures asymmetry in the signal distribution.
- Peak-to-RMS ratio: useful for assessing transient content.
- Total harmonic distortion (THD): quantifies the presence of harmonic components, revealing sensor or structural nonlinearities.
- Cross-correlation with reference channels detects inconsistencies or spurious signals in multi-sensor setups.

These metrics, combined with visual tools such as spectrograms, provide a comprehensive assessment of signal quality and help identify segments suitable for reliable modal analysis.

Concluding Remarks on Modal Analysis

Output-Only Modal Analysis enables continuous or periodic monitoring of bridges and other civil structures, allowing detection of changes in dynamic characteristics over time, identification of anomalies following extreme events such as earthquakes, and revealing signs of structural degradation, including corrosion or loosening of joints. It can also serve as a non-invasive diagnostic tool for maintenance.

The modal parameters extracted via OMA can be used to calibrate numerical models and that is the focus of this work. The model updating process seeks to minimize the error:

$$J(\boldsymbol{\theta}) = y^{\exp} - y^{model}(\boldsymbol{\theta})$$

Where $y^{\exp} and\ y^{model}$ are the response of the real structure and the respnce of the numeric model, θ is the set of model parameters (e.g., stiffness, mass). This optimization aligns model response with the identified modes, improving predictive capacity. Once updated, models can simulate extreme load conditions to evaluate safety margins. Additionally, trends in modal parameters can indicate:

- Localized damage (stiffness loss)
- Global weakening (mass or boundary changes)
- Nonlinear behaviour (change in damping patterns)

OMA thus informs risk-based decision-making regarding maintenance, restriction, or replacement. Although OMA is a well-established technique, several challenges remain. Temperature variations can cause shifts in modal frequencies that may be mistaken for structural damage, making temperature compensation an important consideration. Automated modal classification also remains complex, as distinguishing physical modes from spurious results often requires expert judgment. Integrating OMA with digital twins presents significant opportunities, allowing real-time data to continuously update numerical models for predictive analytics. Meanwhile, the development of low-cost structural health monitoring (SHM) technologies, such as MEMS sensors and wireless platforms, could enable dense, scalable sensing networks. The future of OMA is likely to focus on fully automated, cloud-connected monitoring systems capable of providing real-time diagnostics and predictive insights across large-scale structural networks. Having established the mathematical foundations for modal analysis, the discussion now turns to the fundamental principles of model updating.

Model Update

Introduction

Finite Element (FE) models are widely used in structural engineering to predict the dynamic and static responses of structures. However, discrepancies often occur between the predicted behaviour of a numerical model and the actual response observed in experimental testing. These differences arise from various sources of uncertainty, such as simplifications in the modelling process, inaccurate estimates of physical parameters, unknown boundary conditions, and unmodelled damage or degradation. Input parameters such as elastic modulus, mass density, and geometric dimensions are often uncertain or variable in practice, particularly in existing structures. Variability in construction quality, ageing effects, and material degradation (e.g., corrosion, fatigue) further contribute to parameter uncertainty. Such parameters are typically treated as variables θ in the model updating problem, and to address this mismatch, model updating techniques are employed. The aim is to adjust selected model parameters so that numerical predictions align more closely with experimental data. Model updating thus provides a systematic framework for improving the fidelity of numerical models by calibrating them against physical evidence. A well-updated model enables more reliable structural assessments, supports condition monitoring, and can enhance the accuracy of safety evaluations, especially for ageing or critical infrastructure. An updated model increases confidence in structural assessment results, particularly for ageing infrastructure or where code-based assumptions are insufficient.

Many authors have been applying FEMU since the early development of structural identification methods, dating back to the 1970s and 1980s, when early methods were developed to improve the correlation between analytical and experimental modal data. [74] proposed a foundational approach to modify the stiffness matrix using test data. [75] further advanced this by introducing systematic techniques for large model adjustments. The field was later consolidated by the pivotal review of [76] who offered a comprehensive taxonomy of FEMU strategies distinguishing between direct (non-iterative) and indirect (iterative) methods and addressing challenges such as parameter identifiability, model stability, and physical consistency. The direct methods directly update the elements of stiffness and mass matrices and are a one-step procedure [77]. These methods allow the updated analytical model to reproduce measured vibration modal data, but there is no guarantee that the updated model truly represents the physical properties of the actual structure concerned. On the other hand, the iterative parameter updating methods use different strategies to perform the calibration, for example it can adopt the sensitivity of the parameters to update the analytical model [78]. Such methods set

the errors between the analytical and measured data as an objective function, and attempt to minimise the chosen objective function by adjusting the preselected set of physical parameters of the analytical model in question [79].

Over the years, FEMU has evolved into a standard methodology in a wide range of engineering disciplines, including mechanical , aerospace, automotive, and civil engineering [80]. Its importance is particularly evident also in Structural Health Monitoring (SHM) and damage detection, where the comparison between measured and predicted modal parameters reveals degradation in stiffness or mass [81] A notable case study often cited in literature is the Z24 bridge experiment [81] which serves as a benchmark for model updating and damage identification under environmental variability. It demonstrates how FEMU can be applied to real-world SHM challenges involving temperature-induced frequency shifts and progressive structural degradation. [82]

The literature presents another classification of FEMU methods commonly categorized into manual and automatic approaches. Manual model updating relies on engineering judgment and trial-and-error procedures to refine the initial FEM based engineering judgment and helps to approximate the numerical model to the current structural behaviour. While this process can preserve physical insight and avoid unrealistic convergence, it is deterministic and cannot adequately represent uncertainty Moreover, manual methods become impractical as the number of parameters increases or when dealing with high-fidelity models. This combination of automated and manual methods is usually used to bring the initial numerical model as close as possible to the actual behaviour of the structure using manual updating, while automated model updating is performed to further reduce these differences and obtain a more reliable estimate of the unknown parameters. In addition, this combi nation can improve complete process of model updating and speed up computational time [83], [84] [85].

To address this, automatic updating techniques have been developed using optimization algorithms. These techniques aim to minimize an objective function that quantifies the dissimilarity between numerical predictions and experimental observation typically based on natural frequencies, modal damping, and mode shapes, implementing various type of objective function [86] [87] . Only a limited number of studies have explored the use of static or quasi-static measurements for finite element model updating. [88] developed one of the first systematic formulations for parameter estimation using static displacement and strain measurements, introducing weighting factors to reduce measurement uncertainty and demonstrating that static data can effectively identify stiffness parameters in small-scale frames. [89] extended this concept to bridge structures, showing that the combined use of static and dynamic measurements improves model reliability and allows better

calibration of boundary conditions and stiffness distribution. [90] applied a progressive model updating procedure to the Runyang Suspension Bridge, integrating both ambient vibration and static load test data in a two-phase calibration process, and highlighting the advantages of incorporating static responses to enhance model fidelity. [91] applied a similar approach to an existing T-girder bridge, proposing a quasi-static influence line methodology for calibrating finite element models under field loading conditions. Despite these advances, the integration of static information remains limited and not yet formalized. Previous studies have generally not considered the potential complementarity between static and dynamic data. In particular, they have not explored the idea that measurements influenced by different subsets of model parameters can provide independent information, helping to mitigate parameter correlation and improve the conditioning of the optimization problem. The present work develops this perspective by explicitly incorporating static response error terms within the updating process to assess their contribution to model robustness. The idea is that, when model updating is carried out using only dynamic quantities such as natural frequencies and mode shapes, multiple solutions may satisfy the objective function, leading to non-uniqueness of the identification problem. To address this issue, additional terms can be introduced into the objective function that are sensitive only to the stiffness of the system. For instance, including a displacement measurement, which is a direct function of the structural stiffness, helps to constrain the solution space and makes the updating problem better posed.

There are many algorithms to resolve the optimization problem, including derivative methods and derivative-free methods like Genetic Algorithms (GA), Particle Swarm Optimization (PSO), Simulated Annealing, Pattern search, each offering a trade-off between accuracy, robustness, and computational cost [92] [93] [94].

There is another type of model update implementation based on surrogate models. To improve computational efficiency in finite element model updating problems, the finite element model is replaced by a mathematical model that approximates the relationship between the preselected inputs and outputs of the FE model. The main objective in developing the surrogate-based model updating method is to replace the original finite element model with a surrogate that is analytically more practical and computationally more convenient, using methods such as response surfaces [95] [96].
Furthermore, in recent years, Bayesian approaches have gained traction for their ability to incorporate measurement uncertainty and prior knowledge. These probabilistic methods generate posterior distributions of model parameters [97] [98] [99]. Other works about Bayesian model updating in the

context of structural engineering was done by [100] [101], [102], work that compare deterministic and probabilistic approaches to model updating was realized by [103].

In civil engineering, Finite Element Model Updating (FEMU) has found critical applications in the analysis of bridges [98] [104] [81], tall towers [105] [106] and historical masonry monuments [107] [108] where direct inspection or destructive testing is not always feasible. There are in the recent decades interest in assenting condition of offshore wind turbine and model update using also machine learning features could improve the result [109], [110] These studies have proven instrumental in improving the accuracy of numerical simulations and enhancing the reliability of safety evaluations. Recent studies have performed an overview of the methods [111].

Fundamentals of optimization

To reduce discrepancies between predicted modal characteristics and those identified experimentally, such as through Operational Modal Analysis, numerical optimization techniques are employed. These methods aim to adjust model parameters so that numerical predictions align more closely with experimental observations. In essence, numerical optimization theory involves designing and implementing algorithms to find the best solution to a given problem. In the context of model updating, this means identifying the optimal set of parameters that minimize an objective function representing the deviation between simulated and measured properties.

Integrating optimization theory into the model updating process enables engineers and researchers to systematically calibrate numerical models, improving their ability to replicate the real-world dynamic behaviour of structures. The model parameters to be updated can be regarded as the set of input variables for the optimization problem. However, it is important to recognise that the complexity of such problems increases exponentially with the number of variables. Therefore, reducing the dimensionality of the problem by selecting only the most influential variables is advantageous. A preliminary sensitivity analysis can help identify the parameters that have the most significant impact on the system response. Constraints can also be imposed on the input variables; for example, in simple cases, this may involve assigning upper and lower bounds to each variable, corresponding to the physical range within which the parameters are expected to vary. When only one objective function is considered, the problem is referred to as single-objective optimization. Conversely, when multiple performance objectives such as frequencies, mode shapes, and displacements are considered, the problem extends into the domain of multi-objective optimization. The following sections present the

core concepts of optimization theory and problem formulation that underpin the methods adopted in this work [112] [113] [114] [115].

Mathematical formulation of the update problem

The model updating process is based on an inverse problem: determining the values of physical parameters so that the numerical model reproduces the experimental behaviour of the structure. This process is typically formulated as an optimization problem, where the updated model should minimize the discrepancy between predicted and measured structural responses. A general form of the model updating problem can be written as:

$$\min_{\theta} J(\theta) = |y^{\exp} - y^{model}(\theta)|^2$$

Where:

- θ is the vector of parameters to be updated (e.g., elastic moduli, mass densities, boundary conditions stiffnesses, etc.)
- $y^{\exp}$: vector of measured quantities (e.g., natural frequencies, mode shapes, frequency response functions)
- y^{model}: corresponding model predictions, dependent on the parameters θ
- $J(\theta)$: cost function quantifying the error between model and measurements

The cost function $J(\theta)$ can take various forms depending on the type of problem and the available data. For example, it can be formulated using least squares or norm-based approaches, and weighting factors can be introduced to emphasize certain quantities over others. If multiple types of responses are involved (e.g., frequencies, displacements, strains), a multi-term or composite objective function is constructed. The formulation is flexible, allowing different weights and normalizations depending on data reliability and the objectives to be achieved.

Residual minimization and objective functions

A residual vector can be defined as:

$$r(\theta) = z_n(\theta) - z_e$$

Where $z_n(\theta)$ is the model quantity (e.g. frequency) and z_e is the measured quantity. Those residuals can be expressed in different way, for example, a common way for frequency r_f and mode shapes r_ϕ is:

$$r_f = \frac{f_{exp,i} - f_{model,i}}{f_{exp,i}} \qquad r_\phi = 1 - MAC_i$$

Also the objective function J can take several forms:

- Absolute residual (J_1):

$$J_1 = |r(\theta)|^2 = \sum_{i=1}^{m} \left(z_{n,i} - z_{e,i}\right)^2$$

- Relative error (J_2):

$$J_2 = \sum_{i=1}^{m} \left(\frac{z_{n,i} - z_{e,i}}{z_{e,i}}\right)^2$$

- Weighted residual with uncertainty (J_3):

$$J_3 = \sum_{i=1}^{m} \frac{\left(z_{n,i} - z_{e,i}\right)^2}{\sigma_i^2}$$

Introduction to the Optimization Problem

The model updating process can be formally described as an optimization problem, where the goal is to determine the set of parameters θ that minimize a scalar-valued objective function $J(\theta)$. This function quantifies the discrepancy between numerical predictions and experimental measurements, and its minimum corresponds to the best-fit model. Optimization is a fundamental discipline in applied mathematics, engineering, economics, and computational science. At its core, optimization addresses the problem of selecting the best solution according to a specific criterion from a set of feasible alternatives. Mathematically, the general optimization problem can be expressed as:

$$\min_{x \in R^n} f\,(x)$$

where:

- $x = [x_1, x_2, \ldots, x_n]$ is the vector of variables
- $f(x)$ is the objective function (or cost function)
- R^n is the search space, i.e., the set of all possible solutions

The objective function represents a quantity to minimize (e.g., cost, error, energy) or to maximize (by minimizing its negative). Optimization seeks the point x^* at which $f(x)$ attains its minimum value. From a mathematical standpoint, finding a minimum of a differentiable function $f: R^n \to R^f$ involves identifying a point x^* such that the first-order optimality condition is satisfied:

$$\nabla f(x^*) = 0$$

This condition states that the gradient of the function, which generalizes the derivative to multiple dimensions, must be equal to zero at a local minimum or maximum or saddle point. In one-dimensional problems, this reduces to the familiar:

$$f'(x^*) = 0$$

To verify that x^* is indeed a minimum, a check the second-order condition, which requires the Hessian matrix $H(x) = \nabla^2 f(x)$ to be positive definite at x^*.
However, in most engineering applications, such theoretical conditions are impractical to verify directly, especially when the function is evaluated using finite element simulations or experimental data. In practical model updating, the objective function $J(\theta)$ often cannot be written in closed form and may be non-linear and multi-modal. For this reason, numerical optimization algorithms are used to approximate the solution. These methods iteratively explore the parameter space in search of an optimal solution, relying either on gradient-based information when derivatives of the objective function are available or on direct evaluations of the objective function. Depending on the nature of the problem, they may use local or global search strategies and can accommodate both smooth and non-smooth objective functions, making them suitable for a wide range of optimization scenarios in model updating. The nature of the objective function influences the choice of optimization strategy. In particular:

- If $J(\theta)$ is smooth and differentiable, gradient-based methods (e.g., Newton, quasi-Newton, Levenberg–Marquardt) are efficient and provide fast convergence.

- If $J(\theta)$ is noisy, discontinuous, or computed through black-box simulations (e.g., finite element models), derivative-free methods (e.g., Nelder–Mead, genetic algorithms) are preferred.

In the following sections an overview of optimization algorithms used in model updating is provide.

Unconstrained and Constrained optimization

Optimization problems can be broadly categorized according to whether the variables are subject to constraints.

Unconstrained Optimization

In unconstrained problems, the variables can vary freely in the entire space R^n. The optimization reduces to $\min_{x \in R^n} f(\boldsymbol{x})$. Such problems are typically simpler to solve and require fewer mathematical tools because the simple formulation of the problem. However, in many real-world scenarios, allowing unrestricted variable values may lead to unrealistic or infeasible solutions.

Constrained Optimization

In constrained optimization, the decision variables must satisfy a set of conditions, equalities, inequalities, or both. The general formulation becomes:

$$\min_{x \in R^n} f(x)$$

$$\text{subject to:}$$

$$g_i(x) \leq 0, \ = 1, \dots, m;$$

$$h_j(x) = 0, \ = 1, \dots, p$$

where:

- $g_i(x)$ are inequality constraints,
- $h_j(x)$ are equality constraints.

Constraints are essential for modelling realistic systems where physical, economic, safety, or regulatory limits must be respected. They add complexity to the problem and require specialized methods for enforcement, such as penalty functions, barrier methods, projection methods, or Karush-Kuhn-Tucker (KKT) conditions.

Optimization algorithms

In the context of model updating, optimization algorithms aim to minimize a cost function that represents the discrepancy between numerical simulations and experimental data. These algorithms can be broadly divided into two categories:

- Gradient-based algorithms require the computation of derivatives of the objective function, such as first derivatives (gradients) and second derivatives (Hessians). They are efficient and converge rapidly when the function is smooth and well-behaved, but may struggle in the presence of noise, non-differentiabilities, or multiple local minima.
- Derivative-free (or direct search) algorithms do not require gradient information and are therefore better suited to problems with discontinuities, numerical noise, or poorly conditioned functions. These methods generally explore the solution space using geometric or stochastic strategies.

Gradient-Based Methods

Newton (second order)

The Newton method is a second-order optimization algorithm designed for finding local minima (or maxima) of a continuously differentiable function f: $R^n \rightarrow R^f$. It is based on a second-order Taylor expansion of the objective function around the current point.

Given a current estimate x_k the function f is locally approximated as:

$$f(x_k + p) \approx f(x_k) + \nabla f(x_k)^T p + \frac{1}{2} p^T H(x_k) p$$

Where:

- $\nabla f(x_k)$ is the gradient vector,
- $H(x_k)$is the Hessian matrix, containing second-order partial derivatives.

To minimize the approximation, one solves the following Newton system:

$$H(x_k) p_k = -\nabla f(x_k)$$

The update rule is:

$$x_{k+1} = x_k - H^{-1}(x_k) \nabla f(x_k)$$

- Quadratic convergence near the minimum, provided the Hessian is positive definite and the starting point is sufficiently close to the solution.
- Can converge in very few steps for well-behaved functions.

- Requires computation and inversion of the Hessian matrix H(x), which has complexity O(n3) and becomes impractical for large n.
- If the Hessian is not positive definite, the update direction may not be a descent direction.
- Sensitive to the initial guess; poor initial points may lead to divergence or convergence to a saddle point.

Methods That Evaluate or Approximate Gradients (first order)

These are the most commonly used methods for large-scale or medium-sized problems. They can exploit structure and sparsity in the gradient, and often achieve a balance between efficiency and robustness.

Gradient Descent (Steepest Descent)

Updates in the direction of the negative gradient:

$$x_{k+1} = x_k - \alpha_k \nabla f(x_k)$$

Conjugate Gradient Methods

Efficient for large-scale unconstrained problems, particularly when the objective is (approximately) quadratic. Avoids full matrix storage and solves using successive directions that are conjugate with respect to the Hessian.

Coordinate Descent Methods

Update one variable at a time while keeping the others fixed. Especially useful for problems with separable structure or when gradient computation is expensive.

Quasi-Newton Methods (e.g., BFGS)

Approximate the Hessian using rank-one or rank-two updates based on gradient evaluations:

$$x_{k+1} = x_k - B_k^{-1} \nabla f(x_k)$$

Where B_k^{-1} is an approximation to the Hessian. These methods provide a good trade-off between accuracy and computational cost for problems with N<1000N < 1000N<1000.

Levenberg–Marquardt Algorithm

A hybrid between Gauss–Newton and gradient descent. It is particularly effective for nonlinear least-squares problems and widely used in structural parameter estimation. It adjusts the search direction based on curvature, improving convergence stability.

Derivative-Free Methods

These methods are used when gradients are unavailable, expensive, or unreliable. They are particularly relevant for black-box optimization and model updating.

Pattern Search Methods

Systematically explore the space by evaluating the function at points around the current iterate. This method can converge even when the objective is non-differentiable or noisy. In this thesis, Matlab's "patternsearch" function evaluates values along a positive spanning set and adjusts the mesh size dynamically.

Nelder–Mead Simplex Method

Maintains a geometric simplex and updates it iteratively using reflection, expansion, contraction, and shrinkage. It is heuristic and simple, but offers limited convergence guarantees.

Heuristic and Stochastic Methods

There are also families of algorithms inspired by natural processes or designed as heuristic and stochastic optimization approaches. These population-based or probabilistic algorithms are particularly useful for global optimization, especially when the objective function has many local minima or an irregular landscape. Below are some of the most widely used methods:

Genetic Algorithms (GA)

GA are population-based stochastic optimization methods inspired by the principles of natural selection. Each solution is represented as a *chromosome*, and evolution occurs through operators such as:

- Selection, where individuals are chosen based on their fitness.
- Crossover, which combines parts of two parent solutions.
- Mutation, introducing random variations to maintain diversity.

GA are robust and versatile, well suited for discrete or highly nonlinear problems. However, they often require careful parameter tuning to balance exploration and exploitation.

Particle Swarm Optimization (PSO)

PSO is inspired by the collective behaviour of bird flocks or fish schools. Each particle represents a candidate solution and moves through the search space with a velocity influenced by:

- its own best-known position, and

- the best position found by its neighbours or the entire swarm.

PSO is simple to implement, effective for continuous problems, and typically converges quickly in the early iterations.

Simulated Annealing (SA)

SA mimics the principle of thermal annealing. New solutions are generated and can be accepted even if they are worse than the current one, with a probability:

$$P = \exp\left(-\frac{\Delta f}{T}\right)$$

where:

- Δf = increase in the objective function,
- T = a temperature parameter that decreases over time.

This mechanism enables the algorithm to escape local minima in the early stages and focus on the global optimum as the temperature cools down. SA is particularly useful for problems with multiple local optima.

Stochastic Tunnelling

This method modifies the objective function to flatten the basins of local minima, improving global exploration. Instead of directly optimizing the initial function, a transformed function is considered, Depending by a control parameter gamma. This transformation could reduce the dominance of local minima and helps the algorithm escape function "traps."

Ant Colony Optimization (ACO)

ACO is based on the behaviour of ants, which deposit pheromones along paths leading to food sources. In optimization:

- Solutions are built step by step
- Component choices depend on pheromone intensity (historical memory) and heuristic desirability (local evaluation).

Pheromones are updated according to solution quality and decay over time, preventing premature convergence. ACO is particularly effective in combinatorial problems such as routing and scheduling. [116]

Regularization and ill-posedness

One of the main challenges in model updating problems, particularly in structural dynamics, is the inherently ill-posed nature of the inverse problem. When updating a finite element (FE) model based on experimental observations such as natural frequencies and mode shapes, the mathematical formulation of the optimization problem often violates one or more of the classical criteria for well-posedness defined by Hadamard: existence, uniqueness, and stability of the solution with respect to perturbations in the input data. This ill-posedness typically arises from a combination of insufficient or noisy measurements, limited sensitivity of the model outputs to certain parameters, and intrinsic redundancies in the model structure. For example, different combinations of stiffness or mass parameters may produce virtually indistinguishable dynamic responses. In such cases, the solution to the updating problem is not unique, and small changes in the input data, such as measurement noise, can lead to large variations in the estimated parameters. A particularly problematic manifestation of ill-posedness is malconditioning. This occurs when the cost function landscape exhibits flat or elongated regions in the parameter space, indicating directions in which the function is weakly sensitive to parameter variations. Numerically, this corresponds to an ill-conditioned or nearly singular Hessian matrix. Gradient-based methods may converge slowly or even fail in such regions, and the solutions obtained may be extremely sensitive to the initial guess or to numerical noise. From a physical standpoint, this reflects the ambiguity in identifying model parameters when the observable data are insufficient to constrain the solution.

To address these difficulties, regularization techniques are incorporated into the optimization framework. Regularization serves the dual purpose of stabilizing the numerical problem and embedding prior knowledge or assumptions about the physical system. One of the most widely used approaches is Tikhonov regularization, in which the original objective function is augmented with a penalty term that discourages deviations from a reference model. This results in a modified cost function of the form:

$$J_\lambda(\theta) = J(\theta) + \lambda|L(\theta - \theta_0)|^2$$

Here, $J(\theta)$ represents the original misfit function, typically based on the discrepancy between measured and simulated quantities, while the second term enforces proximity to a nominal parameter set θ. The matrix L defines the structure of the regularization often taken as the identity matrix or a finite-difference operator to impose smoothness and the scalar λ controls the balance between fidelity to data and adherence to prior assumptions. Choosing an appropriate value for the regularization parameter λ is crucial. If it is too small, the ill-posedness is not mitigated; if too large, the solution

becomes overly biased toward the prior model, potentially masking real structural changes. Several methods are available to address this issue.

Regularisation techniques offer useful tools to mitigate such instability, but they often do so by introducing external assumptions or constraints that may not fully reflect the actual physical behaviour of the structure. The purpose of this work is not to further refine the optimisation problem through purely mathematical techniques, but to modify the objective function itself by introducing a natural constraint. To address this, the approach proposed in the following work is to enrich the classical objective function with an additional term associated with static quantities, such as displacements obtained from controlled static tests. Unlike dynamic quantities, these displacements depend solely on stiffness and not on mass, thereby providing complementary and non-redundant information. The idea is that this static term can act as a natural constraint, improving the conditioning of the problem and making the optimization more stable and robust, without forcing the model towards a predefined set of parameters.

In the next chapter, this concept will be illustrated with simple numerical examples. The discussion will begin with a cantilever beam, intuitively showing how including static measurements in the objective function influences the updating process. The approach will then be extended to a more complex and realistic example involving a simple bridge structure.

Chapter 4

Integration of Static Response in Model Updating

In this chapter, numerical examples are provided to clarify the concept of enriching the objective function with an additional term to improve the optimization process. By including the static displacement response, the optimization process is expected to improve, as the following examples aim to demonstrate. The key idea is that quantities depending only on a subset of parameters, rather than simultaneously on several parameters, can provide complementary information that helps stabilize the optimization problem. In the case considered here, the additional quantity is a static displacement, which depends exclusively on stiffness, specifically an error term that expresses the difference between the measured displacement and the displacement obtained from a numerical model. In the literature, functions such as the following can be found:

$$res = \omega_i^f res\_f + \omega_i^{MAC} res\_modes$$

Where:

- f_i^{Num} are the frequencies obtained from the numerical model.
- ω_i^f are the weights on the frequencies.
- f_i^{Exp} are the experimental frequencies
- ω_i^{MAC} are the weights on the mode shapes.

In this work the function proposed is

$$res\_load = \omega_i^f res\_f + \omega_i^{MAC} res\_modes + \omega^d res\_disp$$

Where:

- res_disp is the residual on the displacement expressed as $\frac{|s^{Num} - s^{Exp}|}{s^{Exp}}$
- ω^d is the weight on displacement error

To clarify the idea, a simple initial example involves a cantilever beam with a lumped mass attached at its free end. In this configuration, the natural frequency of the system depends on both stiffness and

mass. When only the canonical objective function based on frequencies and mode shapes is considered, this dependence leads to an optimization problem with infinitely many solutions. (In this case, mode shapes are not considered, as they do not provide meaningful information for such a simple system.) To resolve this ambiguity, an additional error term is introduced into the objective function. This term is obtained by applying a static force at the free end of the beam and measuring the corresponding displacement, which depends only on the stiffness.

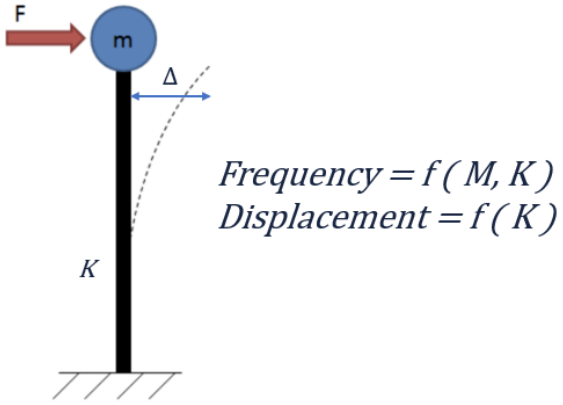

Figure 70: Cantilever beam.

To illustrate the hypothesis, a MidasGen model was built and treated as the "reference" or "experimental" system, in the same way as will later be done for the simplified bridge model and, in the final part of the thesis, replaced with a real case study using measurements from an existing bridge, replicating real practice. The same model was then replicated in OpenSees, and the updating procedure was performed using a Matlab-OpenSees process developed in this work, which will be described in detail in the following chapter. The objective function has been plotted both with and without the error on the static term, and their difference has been analyzed.

$$\sum_{i=1}^{n} \omega_i^f \frac{|f_{ID,i} - f_{FEM,i}|}{f_{ID,i}} + \omega^d \frac{|s^{Num} - s^{Exp}|}{s^{Exp}}$$

The results show that in the canonical case, the objective function presents a valley of minima, highlighting the ambiguity of the solution space. However, with the inclusion of the static term, the surface exhibits a single well-defined minimum, suggesting that the proposed formulation can lead to a more robust and stable optimization process.

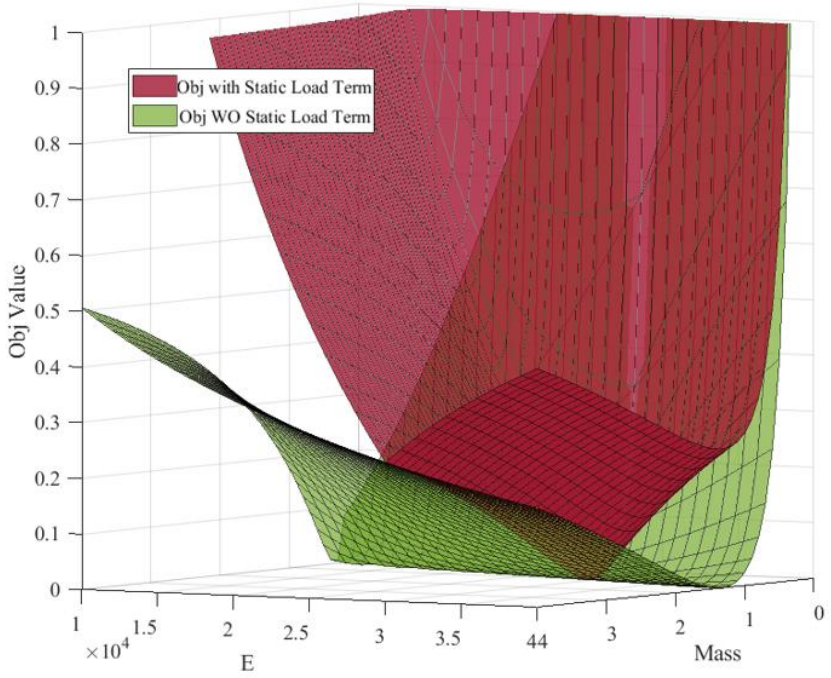

Figure 71: Objective functions of the cantilever beam.

In fact, running an algorithm for the optimization, in one case it results in solutions that depend on the starting point and in the other case the solution is always the same and the correct one.

NoLoad						Load					
Run	**E**	**Mass**	**Sol_E**	**Sol_Mass**	**ObjValue**	**Run**	**E**	**Mass**	**Sol_E**	**Sol_Mass**	**ObjValue**
1	24341	0.40	24342	0.81	0	1	10866	1.78	30000	1.00	0
2	50696	0.31	50712	1.69	0	2	57904	3.65	30000	1.00	0
3	37190	2.17	53574	1.79	0	3	5255	0.81	30000	1.00	0
4	35235	3.14	51623	1.72	0	4	47620	1.13	30000	1.00	0
5	55446	3.74	55442	1.85	0	5	49952	0.67	30000	1.00	0
6	20721	0.61	20722	0.69	0	6	52778	0.63	30000	1.00	0
7	46646	2.32	54846	1.83	0	7	9644	3.49	30000	1.00	0
8	46455	1.93	50567	1.69	0	8	26988	2.36	30000	1.00	0
9	25925	0.15	42309	1.41	0	9	19293	2.24	30000	1.00	0
10	36230	1.41	36230	1.21	0	10	49004	0.67	30000	1.00	0

Table 6: Solutions for the cantilever beam example using the load term and without.

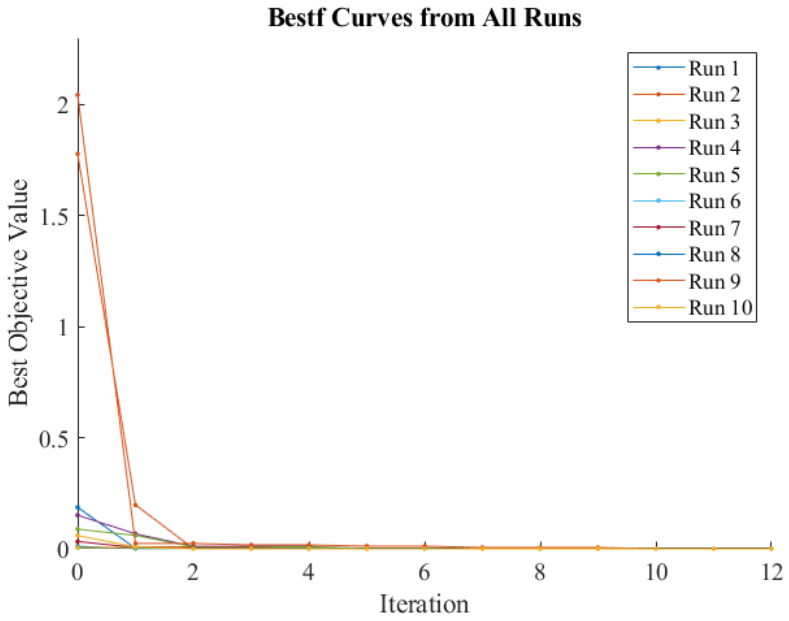

Figure 72: Function Value in the optimization process, for the ten starting point with No Load term.

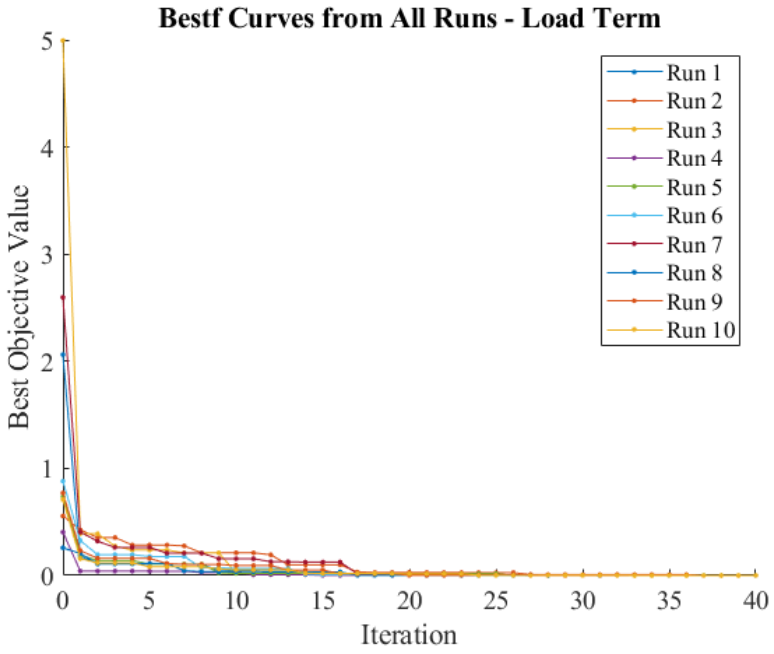

Figure 73: Function Value in the optimization process, for the ten starting point with Load term.

The figure show that with the load term is necessary more iteration but converge at the same result.

Bridge Model

To further investigate the hypothesis that introducing an error in static quantities into the objective function improves the results of the finite element model updating process, a model of a simple bridge structure was developed, inspired by typical highway bridges and viaducts found in Italy.

The bridge is a reinforced concrete bridge and consists in five beams on four supports, two on the piers and two on the side abutment. The structure is made of reinforced concrete, with rectangular beams and a collaborating concrete slab. The total span is about 56 meters, with shorter side spans of 15.5 m and a longer central one of 24.6 m. The beams are made of reinforced concrete with cross-sectional dimensions of 1.x0.25 m, and a 0.20 m thick slab. The structural layout is very similar to that of the Annone bridge, which collapsed in 2016 due to lack of maintenance [117], resulting in a brittle failure and loss of human life. This highlights the importance of structural health monitoring for bridges, viaducts, and civil structures in general. The goal was to understand how to develop a finite element model capable of realistically representing the structure after a proper calibration process. In particular, the aim was to explore how modifying the objective function by introducing static constraints could improve the accuracy of the solution.

Like explained before in the first example, the function is built similar, in this case the term on mode shapes is added

$$\sum_{i=1}^{n} \omega_i^f \frac{\left|f_{ID,i} - f_{FEM,i}\right|}{f_{ID,i}} + \omega_i^{MAC} \sum_{i=1}^{n} (1 - MAC(\Phi_i^{ID}, \Phi_i^{FEM})) + \omega^d \frac{|s^{Num} - s^{Exp}|}{s^{Exp}}$$

Here, $f_{ID,i}$ and $f_{FEM,i}$ represent the identified (in this case, obtained from the finite element model in MidasGen) and numerical frequencies (obtained from OpenSees Model), respectively, while MAC is the Modal Assurance Criterion comparing experimental and numerical mode shapes and s^{Num} is the displacement computed by the reference model and s^{Exp} is the numerical displacement calculated by the FE model.

As a first step, a model was created using the commercial finite element software MIDAS Gen, under the assumption that this model represents reality (i.e., the existing bridge). The model was built with beam elements for the reinforced concrete girders, which were connected to the composite deck slab, modelled with four-node plate elements, via rigid links. Beam elements were also used for the piers. Bearings at the piers and abutments were modelled as elastic springs with assigned stiffness. A more

simplified representation, such as a grillage model, was deliberately avoided at this stage to capture the structural response as accurately as possible.

Using this model, synthetic data were generated to simulate experimental tests and to evaluate the previously described method. Specifically, frequencies and mode shapes were extracted in the first phase, simulating a dynamic identification campaign. Static loads were then applied, and linear static analyses were performed to measure displacements at selected points. This step simulates, in real life, the effect of heavy vehicle traffic and the measurement of displacements, such as during a static load test. Once the model was created in MidasGen, the next step was to simulate what would be done in a real-world scenario by developing another finite element model using the STKO software, as shown in Figure 74. This second model serves as the numerical model representing the digital twin of the real structure – in this case, the structure initially modelled in MidasGen.

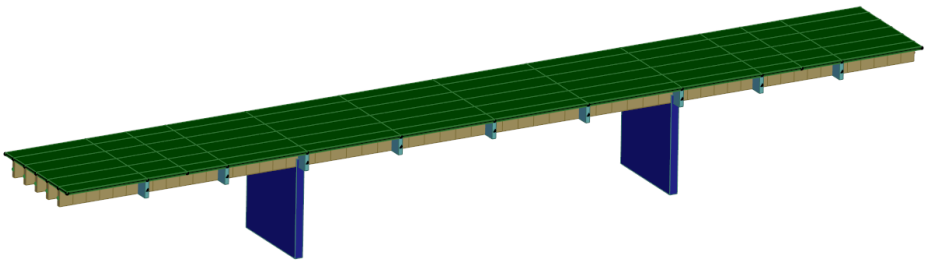

Figure 74: Simple bridge FE model.

Once the model was created using the same parameters – geometry, elastic modulus, and boundary condition properties – frequencies and mode shapes were extracted to obtain a model as close as possible to the one developed in MIDAS Gen. The goal was to eliminate potential uncertainties in subsequent phases. The following table shows the frequencies of the developed models. The differences are mainly due to the different types of finite elements used; in particular, for the quadrilateral element, the formulation of the shape functions for quadrilateral elements in MIDAS Gen differs from that used in STKO.

Midas	3.58	4.01	4.23	6.69	6.79	7.32	7.48	9.81	11.28	11.74
STKO	3.58	3.97	4.21	6.7	6.83	7.39	7.5	9.46	11.08	11.87
diff%	0.14	-1.15	-0.49	0.19	0.46	1.00	0.19	-3.66	-1.82	1.10
MAC	1.00	0.99	1.00	1.00	0.99	0.99	1.00	0.99	0.99	0.98

Table 7: Differences between Midas Gen and STKO model.

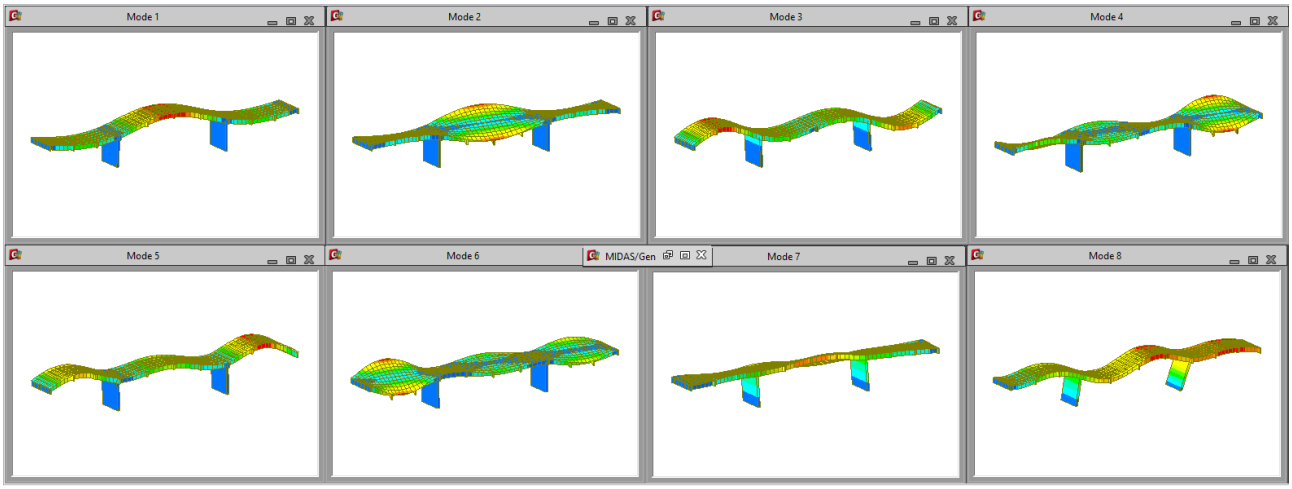

Figure 75: Midas Gen mode shapes.

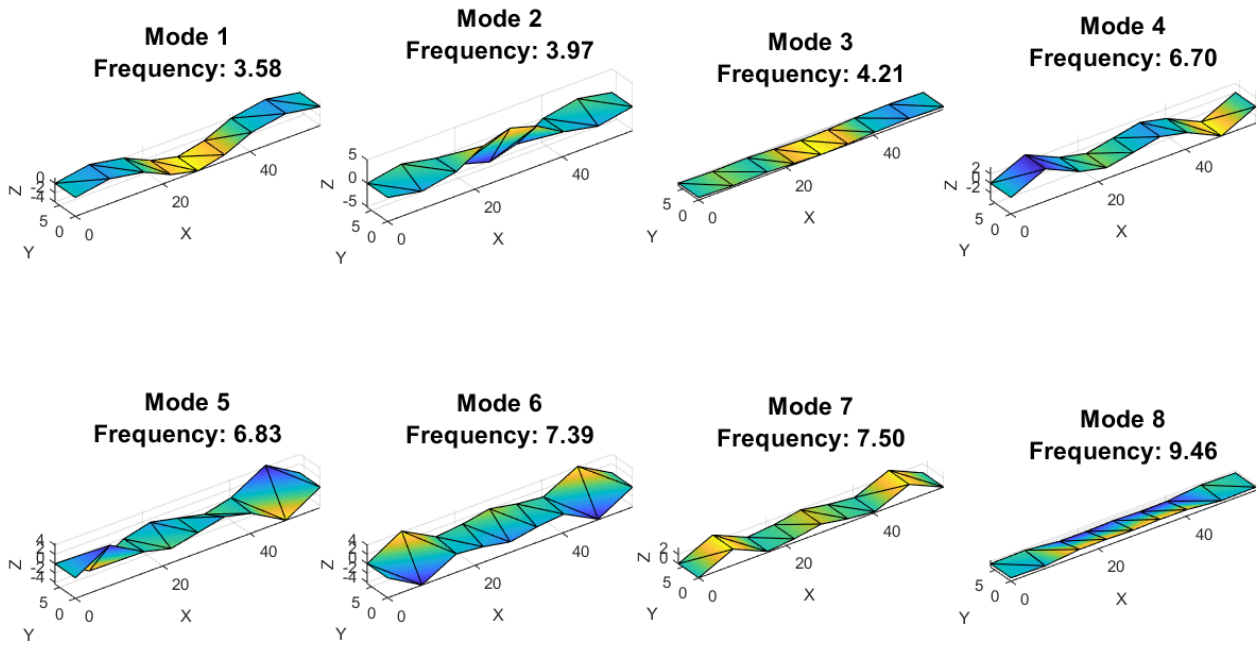

Figure 76: STKO mode shapes.

After the model was completed, the procedure for performing automatic model updating of the bridge was implemented. For a bridge like this, the model updating process could involve parameters such as the elastic modulus of the concrete, its density, and boundary conditions, for example, the stiffness of the neoprene bearings on the piers or the stiffness representing the soil at the abutment supports. To demonstrate this approach, an updating process was carried out first using only one parameter, the elastic modulus of the concrete, and then by including the density as well. The results are presented in the following sections.

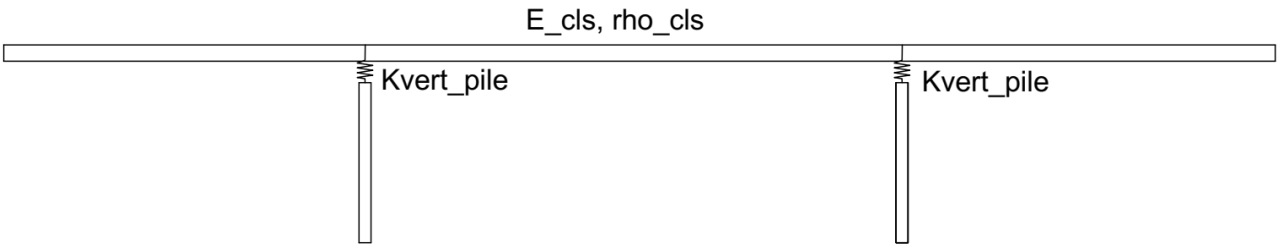

Figure 77: Parameters of Simple Bridge Model.

Update with Elastic Modulus

Running the update using the previously described procedure and using only the modulus of elasticity of the concrete as the calibration parameter, the result matched the correct value (the one entered in the MidasGen model). In this case, the objective function could also be plotted. For higher dimensions, where plotting the objective function is not possible, five starting points were used to demonstrate that the method works. These points were selected based on engineering knowledge and typical parameter values. The results of the updates are plotted, showing that the outcome is the same for every starting point.

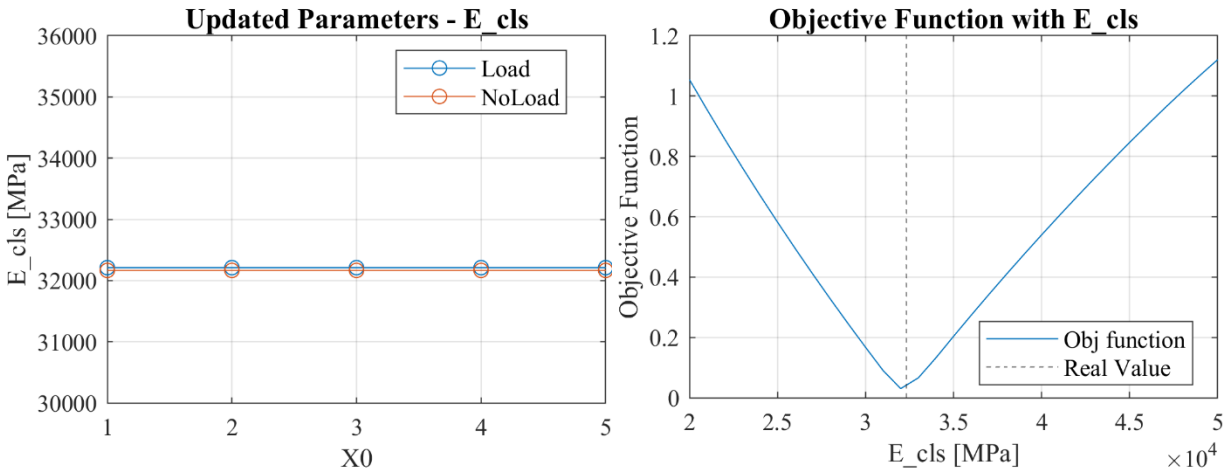

Figure 78: Result of the update for the five starting points and objective function.

In this case, it is not necessary to use the load term to find the best results. However, if the load term is considered, it can be seen that the function becomes steeper.

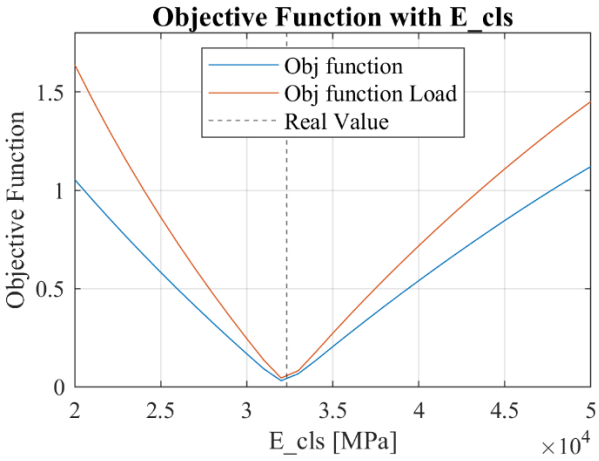

Figure 79: Difference between objective function with and without load term.

Update with Elastic Modulus and density

In a real structure, the density of the concrete may also be uncertain. In this case, it was also used as a parameter to update, which can result in a potentially ill-conditioned problem. This is because it is possible to obtain the same frequency and mode shapes using different combinations of stiffness and density (mass), as shown in the first example.

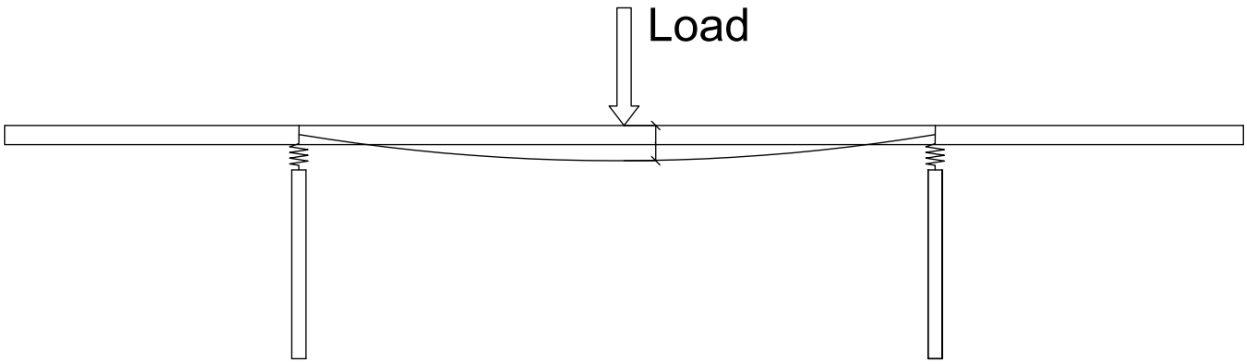

Figure 80: Application of the static load.

But this could be the reality, and the same procedure was used, starting the optimization from five starting points to see if the results are the same for all of them. Figure 81 shows that, in this case, the result can change depending on the initial guess. This occurs because, as mentioned earlier, the same set of natural frequencies and mode shapes can be obtained by multiple mass–stiffness combinations. However, when the load term is added to the objective function, this quantity depends only on the stiffness. As a result, the outcome remains consistent for every initial x_0.

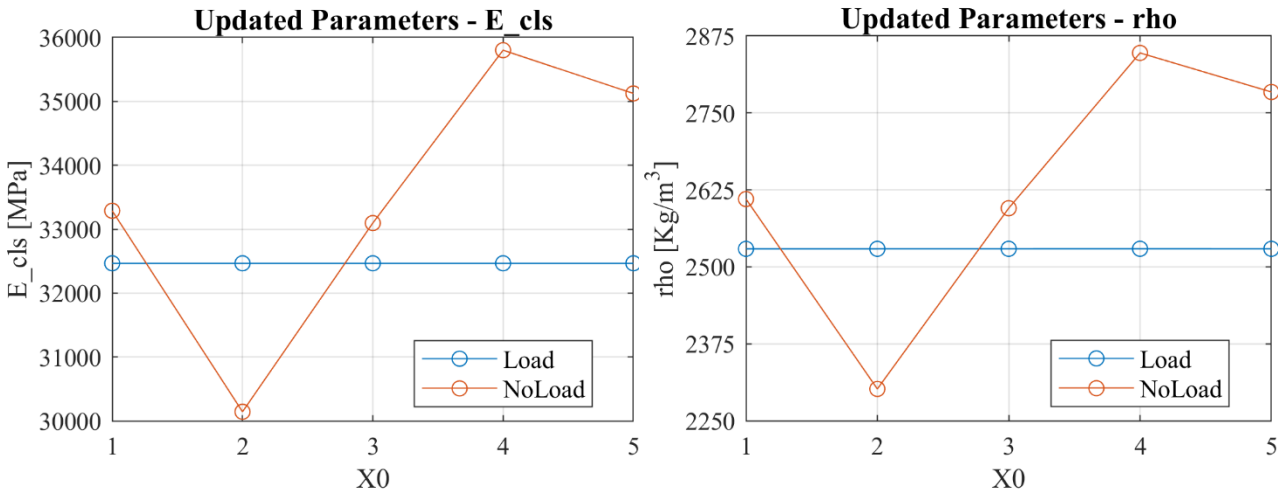

Figure 81: Result of the update for the five starting points.

Also, in this case, since the objective function depends on two variables, it can be evaluated over a grid of points to provide a visual representation. The resulting surface, shown in Figure 82, and obtained with the load term, exhibits a single minimum, whereas the original function displays multiple minima embedded within a "valley" of local minima.

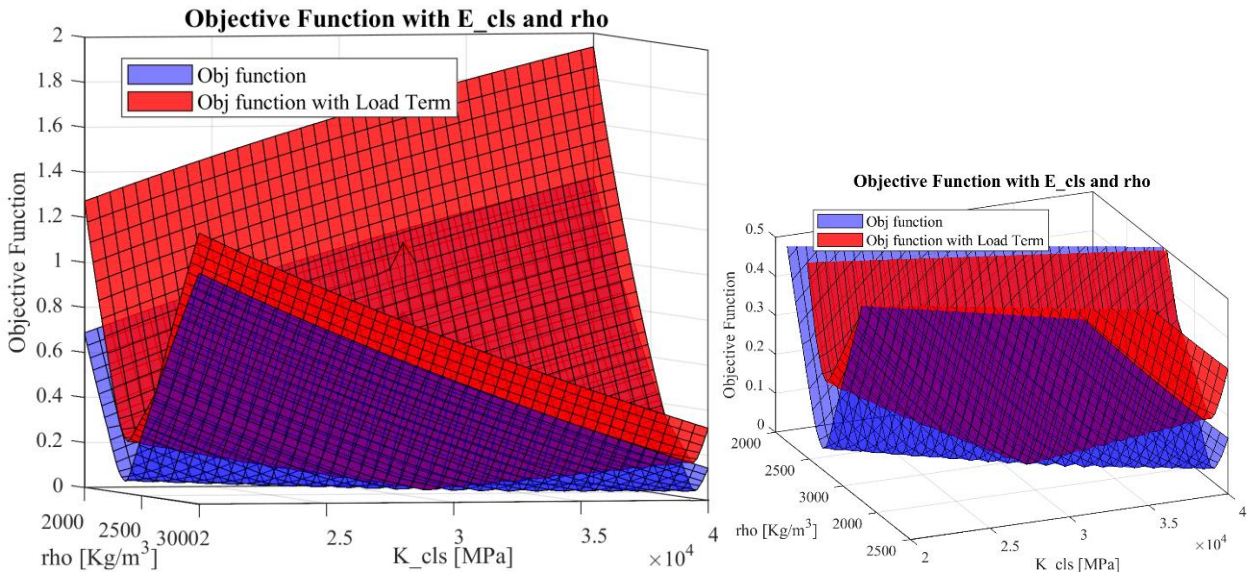

Figure 82: Objective function for two parameters case, with and without the load term.

Update with Elastic Modulus and Support Stiffness

In practice, an engineer may need to determine and calibrate the stiffness representing the soil at the abutments and the stiffness provided by the supports on the piers. To further explore the method, an additional step was taken in which the calibration parameters were the concrete elastic modulus and the stiffness of the pier bearings. In this scenario, an error term based solely on mid-span deflection may not be sufficient to address the problem, because the same mid-span displacement can result

from different combinations of concrete elastic modulus and support stiffness. Therefore, to improve the function as in the previous case, the load must be applied at points where the displacement depends only on the stiffness of the supports; these points could be located directly above the piers, as shown in Figure 83. If the load is applied on the piers, the displacement or deformation depends only on the support stiffness. Thus, another error term was introduced in the model, as follows:

$$\sum_{i=1}^{n} \omega_i^f \frac{|f_{ID,i} - f_{FEM,i}|}{f_{ID,i}} + \omega_i^{MAC} \sum_{i=1}^{n} (1 - MAC(\Phi_i^{ID}, \Phi_i^{FEM})) + \omega^d \frac{|sPila^{Num} - sPila^{Exp}|}{sPila^{Exp}}$$

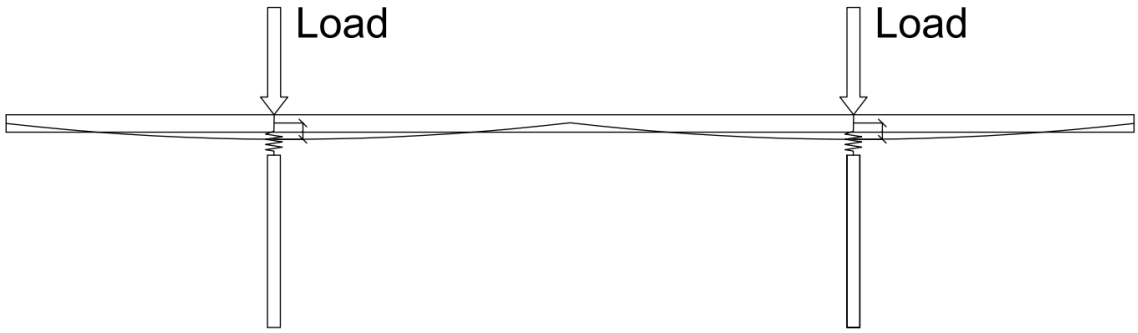

Figure 83: Application of the static load on piers.

By measuring the deformation of the supports in the MidasGen model and including this term in the objective function, it is possible to observe that, even in this case, starting from different x_0 values, the solution remains consistent. For the function with the load at mid-span, the result can vary based on the initial guess because the same mid-span deflection can be achieved with different combinations of the elastic modulus of concrete and the stiffness of the supports.

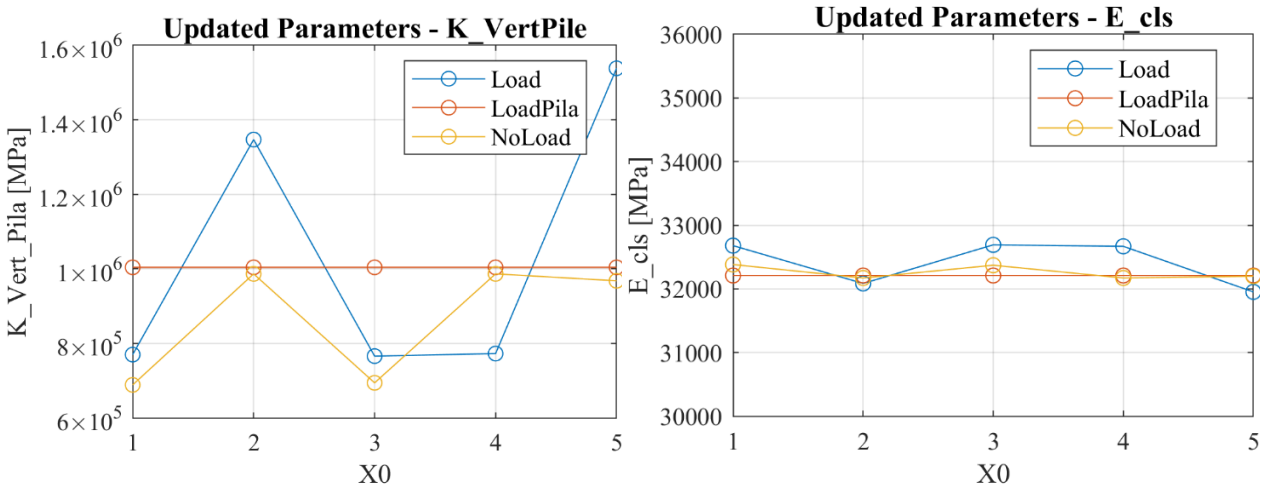

Figure 84: Result of the update for the five starting points.

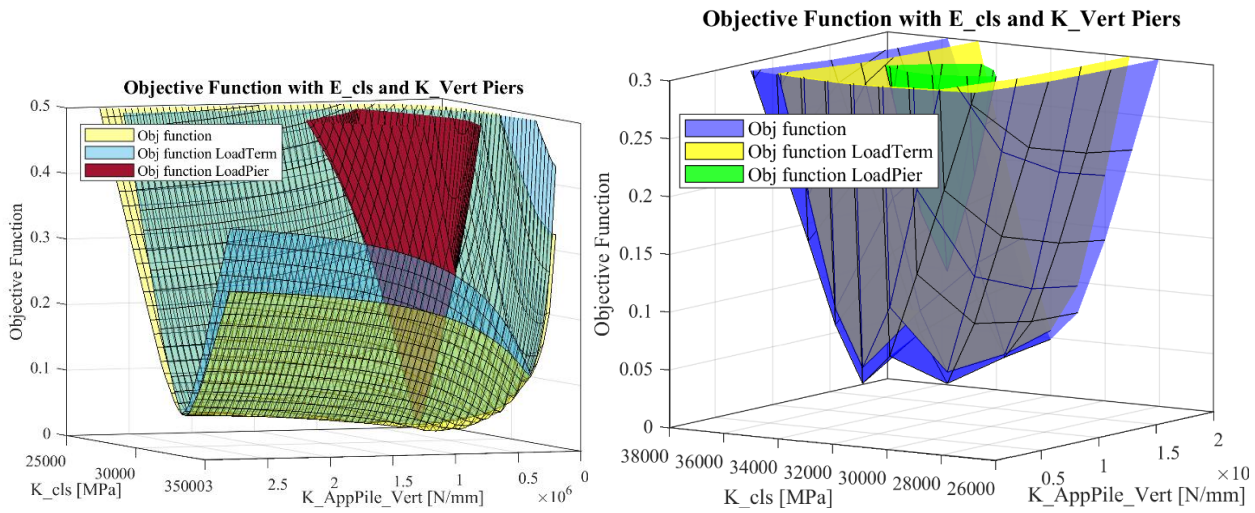

Figure 85: Objective function for two parameters case, with and without the load term.

If the three functions are evaluated on a meshgrid and plotted together in the same plot, it can be seen that for the function that considers the deformation of the supports and the load placed on them, the minimum becomes very clear.

Update with Elastic Modulus, density and support Stiffness

In a real case like this bridge, all three parameters could be of interest to calibrate. Therefore, in this part, all the parameters were taken into account for the model update procedure, using the function that considers both the error of the mid-span load and the error of the load on the piers. In Figure 86, it can be seen that only for the complete function are the results from the five starting points consistent.

$$\sum_{i=1}^{n} \omega_i^f \frac{|f_{ID,i} - f_{FEM,i}|}{f_{ID,i}} + \omega_i^{MAC} \sum_{i=1}^{n} (1 - MAC(\Phi_i^{ID}, \Phi_i^{FEM})) + \omega^d \frac{|s^{Num} - s^{Exp}|}{s^{Exp}} + \omega^d \frac{|sPila^{Num} - sPila^{Exp}|}{sPila^{Exp}}$$

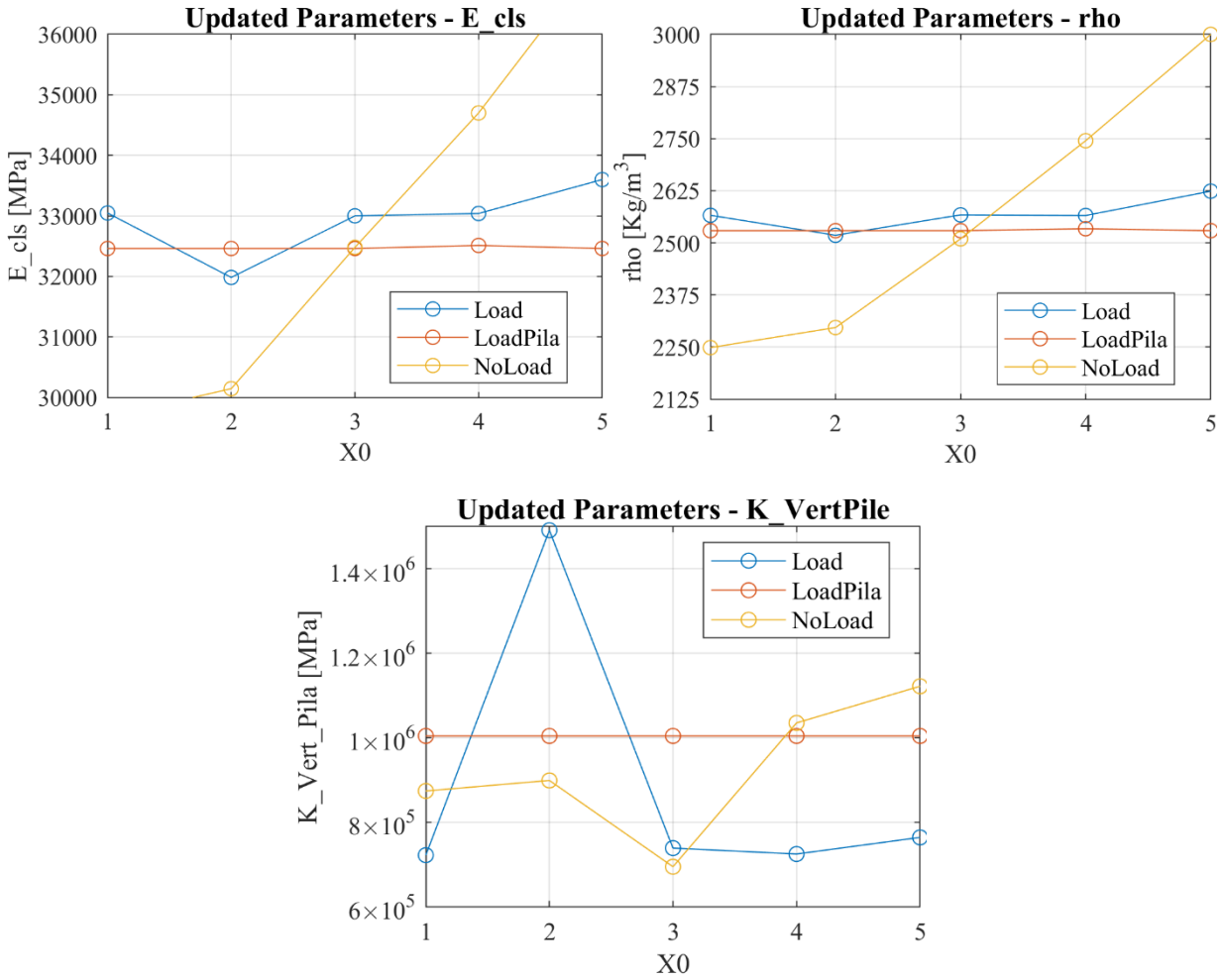

Figure 86: Result of the update for the five starting points.

For the objective plot in this case, it is not possible to display a 3D surface because the function is a three-variable function. Therefore, the idea is to demonstrate the presence of a unique minimum using a plot that can represent three dimensions. To achieve this, a series of contour plots was generated using Matlab's contourf function. Specifically, cross-sections of the function were considered by fixing one parameter at a time and varying the other two. This approach made it possible to highlight the differences between two scenarios, as shown in Figure 87: in the first case, the function exhibits multiple local minima, while in the second case, thanks to the inclusion of the static term, it shows a single minimum, as seen in the plots. In particular, it is clear that in the first case (Figure 87, top), regions of minima occur for several values of K_{vert}, whereas in the second case (Figure 87, bottom), the minimum is located in the plot where K_{vert} = 1e+6, which is exactly the stiffness value assigned to the springs in the finite element model.

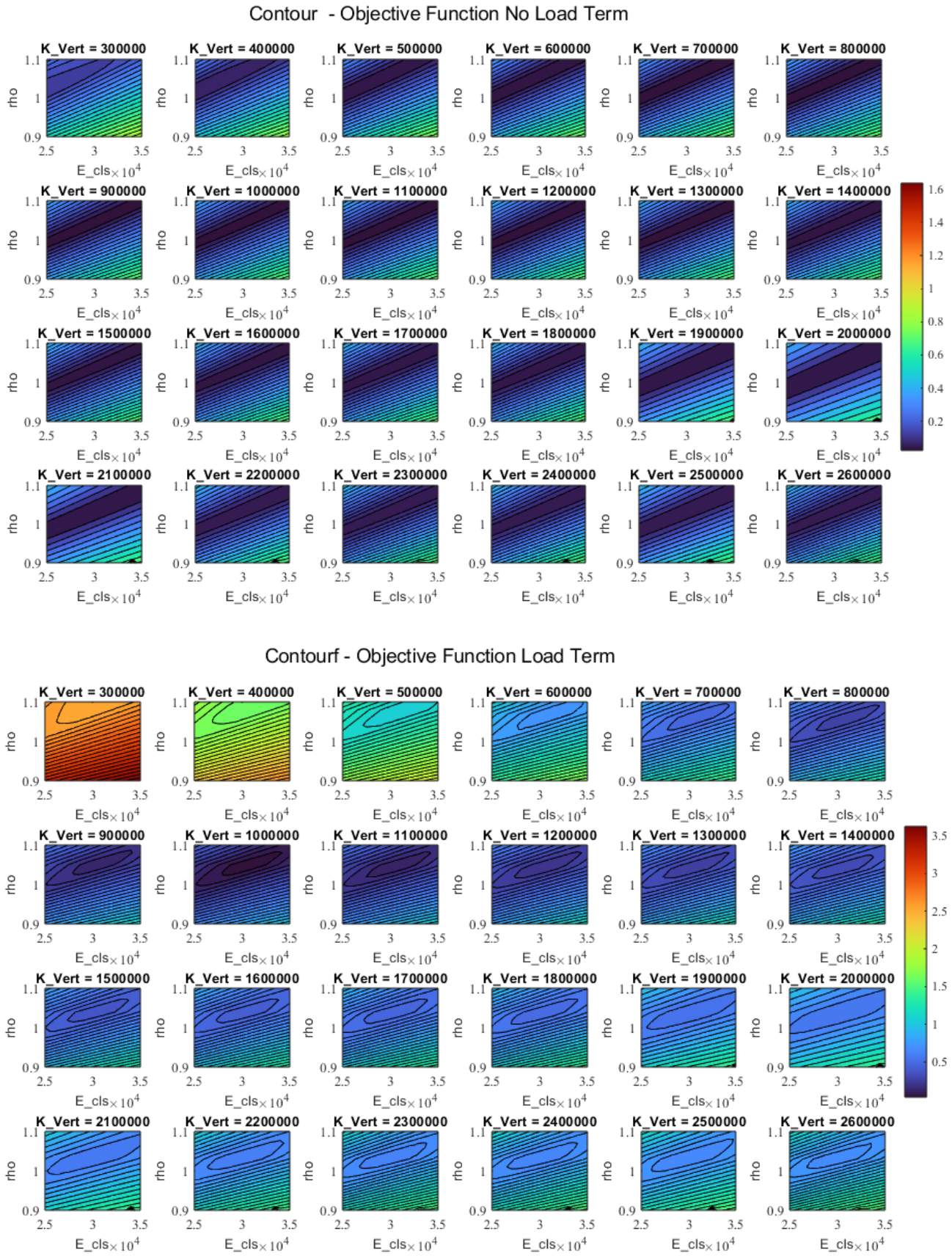

Figure 87: Objective function for three parameters case, with (up) and without the load term (down).

The simplified example discussed in this chapter was designed to introduce and clarify the proposed improvement to the model updating procedure. Using a basic structure made it possible to explain the different steps of the method and demonstrate how including a static term error in the objective function can improve the calibration of the numerical model. Even in this simple context, the results showed that combining static and dynamic information reduces uncertainty, increases the stability of the optimization, and leads to models that better reflect actual structural behaviour. At the same time, the limitations of this example are clear. The boundary conditions, material properties, and applied loads were all defined in a straightforward manner, far from the complexity and variability of real structures. This simplicity was intentional: it allowed the procedure to be tested in a controlled environment and the specific contribution of the static term to be isolated without interference from external factors. With this foundation established, the next step is to apply the approach to a real structure. The case study of an existing bridge introduces the typical challenges of practical applications, such as incomplete knowledge of construction details, environmental effects, and measurement noise. Testing the methodology under these conditions is essential to understand its effectiveness and to evaluate how integrating static and dynamic data can support a more reliable structural assessment.

Chapter 5

Application to a Real Case Study

In the previous chapter, a simplified structural example was presented to explain the proposed model updating procedure step by step and to illustrate the role of the static contribution in the objective function. That preliminary case served mainly as a demonstration tool, highlighting the potential and advantages of combining dynamic and static information in a controlled and straightforward setting. Building on that foundation, the research now moves to a real application: an existing bridge selected as a case study. Unlike the simplified example, this structure introduces the complexity and uncertainties typical of real infrastructures, such as material properties and boundary conditions that are not always fully known. Applying the model updating strategy in this context provides an opportunity to test its effectiveness under realistic conditions and to evaluate how including a static term can improve the reliability of the results. This transition from a didactic example to a real case marks an important step: it demonstrates not only the feasibility of the approach, but also its practical relevance for structural assessment and monitoring.

Canonica Bridge

The case study concerns an arch bridge located between the towns of Canonica d'Adda and Vaprio d'Adda in the province of Bergamo, Italy. The bridge, with a span of approximately 90 meters, was built around 1950 and is shown in Figure 88. As the bridge plays an important role in the region, the authorities decided to replace the hangers due to a high probability of corrosion. This maintenance intervention provided an opportunity to conduct a structural study of the bridge. Specifically, the aim was to investigate whether changes introduced by the hanger replacement could lead to variations in the dynamic properties of the structure. To this end, a series of vibration tests were performed, followed by an Operational Modal Analysis (OMA) to extract the modal parameters of the bridge both before and after the intervention. These experimental results provided the fundamental dataset for the model updating process. By comparing the measured modal parameters with those predicted by the numerical model, it was possible to calibrate the finite element model of the bridge and assess

the effectiveness of the proposed updating strategy, including the static contribution to the objective function.

Figure 88 Canonica Bridge.

History notes

After the Second World War, the old late 19th-century iron bridge could no longer support the increasing traffic loads. The provinces of Milan and Bergamo launched a competition for its replacement. Krall's design proposal fully met the stringent requirements of the tender, and the contract was awarded to the Ferrobeton group. The project consisted of a tied-arch bridge with an intermediate deck, resting on the existing masonry abutments, which were incorporated and structurally integrated into a new deep foundation system supported by piles. A notable feature of the design was the use of the old bridge as a temporary cantering structure during construction. Work began with the shoring and removal of the ballast from the old bridge, which was then lowered to an appropriate height for use as centring. A cantilevered pedestrian walkway was installed to allow people to cross the river while construction proceeded. The pile foundations were built first, followed by the arch, and finally the double-deck superstructure. The Nielsen/Krall tension rods were prestressed before the centring was dismantled. Load testing, conducted by Prof. Stabilini, concluded with praise for both the designer and the construction team. The bridge was inaugurated on May 18, 1957 (Figure 89). Structurally, the arch and the deck beam are completely independent. The two parabolic arches are connected at the top by cross beams forming a spatial truss. The deck rests on the abutments and is held in place by the tension rods.

Figure 89: Historical photo of the Canonica bridge.

'Senza accennare ai minori esempi (non li conto neanche) veniamo all'ultimo, il maggiore di tutti: il ponte tipo Nielsen costruito a Vaprio sull'Adda. A monte avevamo appena ultimato il ponte di Trezzo riuscito assai bene, economico per la trovata di far lavorare come centina, con un allettante risparmio per la Provincia, il vecchio celebre ponte in ferro, carico d'anni ed istologicamente mal sicuro. Questo ponte sostituiva una bella travata di 92,00 m carica d'anni e con lamiere ed aste distorte dai fuggenti Panzer, verso Nord, con tanta foga da dimenticare di farlo saltare all'ultimo. Comunque, di smontare quella travata con ci pensai nemmeno, perché la nostra fine, come quella di ogni cosa al monda, è bene, secondo un pensiero crociano, non avvenga in stupido ozio (cfr. l'ultimo Suo soliloquio). Con tre puntelli in acqua questo ponte servì egregiamente e funzionò come centina, non solo, ma anche come portante una passerella, coperta per sicurezza, in sostituzione di una che si sarebbe dovuta fare a valle. Ma là, l'Adda, confluendo con il Brembo diviene spesso impetuoso quando uno meno se lo aspetta (la colpa è del Brembo) e la passerella eccentrica venne approvata dalla Direzione dei Lavori e a vederlo far da passerella eccentrica sembrava un richiedere troppo a chi ormai era prossimo alla fine. A me, a vero dire, quella passerella non piaceva molto forse perché arieggiava necessariamente in modo dimesso certi ponti svizzeri in legno che sono un lusso. Sia. come si vuole, l'idea

si dimostrò geniale e Dio lo sa dove la passerella evitata sarebbe volata o quanto meno costata, se mi avessero ascoltato. Tutto andò quindi per il meglio. Costruttori furono quegli stessi di Trezzo d'Adda, oggi Direttori Generali della Ferrobeton. Al collaudo il prof. L. Stabilini si gratulò con tutti, ammirò il ponte, i disegni del'Ufficio Tecnico e richiese più copie per farli vedere a Scuola, perché occorse valersi del ponte in ferro che aveva le traverse oblique e presentava tante altre difficoltà. Pensai che l'orditura in c.a. dell'impalcato che ne saltò fuori meglio era nasconderla con una soletta d'intradosso. La soletta d'intradosso trasformò in scatola chiusa l'impalcato con la sua torsiorigidezza equilibrò, o quasi, ogni carico eccentrico rispetto all'asse ponte, prendendosi il momento per torsione e collocando ogni carico al mezzo perché ogni arco lavorasse egualmente, o quasi indipendentemente da ogni eccentricità.'

CITAZIONE LIBRO E KRALL Prof. ing. Giulio Krall

Travate reticolari tipo Nielsen - Varianti e divagazioni sul tema Industria delle Costruzioni n.4 mar.apr 1968)

Figure 90: Historical photo of the old steel bridge.

Bridge Structure

The bridge, designed in the mid-1950s by Giulio Krall, has a span of 91.20 meters and a rise at the crown of approximately 14.5 meters. It is constructed entirely of reinforced concrete and has a total width of 12.60 meters, with 8.0 meters dedicated to the roadway. The deck, slightly skewed in plan,

has a longitudinal slope of approximately 2.5%. Structurally, the bridge consists of two reinforced concrete arches with a T-shaped cross-section (Figure 92). These arches support the deck through a system of inclined hangers made of conventional smooth reinforcing bars. The deck is a reinforced concrete structure with a box girder cross-section, as shown in Figure 93. The anchors for the hangers are positioned within two lateral rectangular sections of the box girder. Originally, the hangers had a specific cross-section, also illustrated in Figure 93. However, in recent decades, a repair intervention introduced modifications to enhance durability. The current cross-section of the hangers includes an additional outer layer of fiber-reinforced concrete (with plastic fibers) and a 2 mm thick stainless steel cover plate to protect the reinforcement bars from corrosion (Figure 93). The 12.70-meter-wide girder accommodates two traffic lanes and two pedestrian walkways, one on each side. Cross beams are placed at regular intervals of four meters along the length of the deck to provide additional structural stability and load distribution. In figures the plan and elevation views of the bridge are shown.

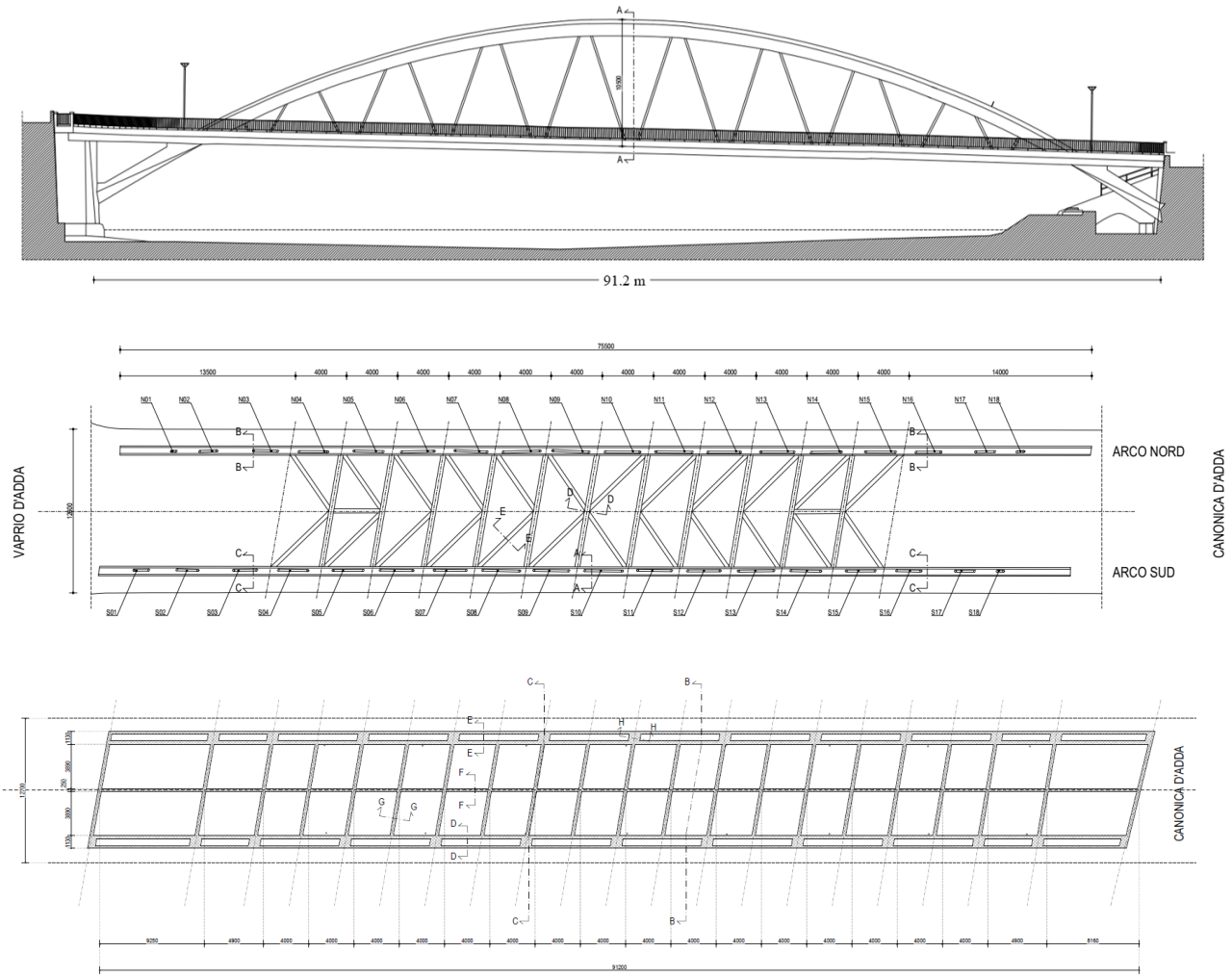

Figure 91: Canonica Bridge drafts.

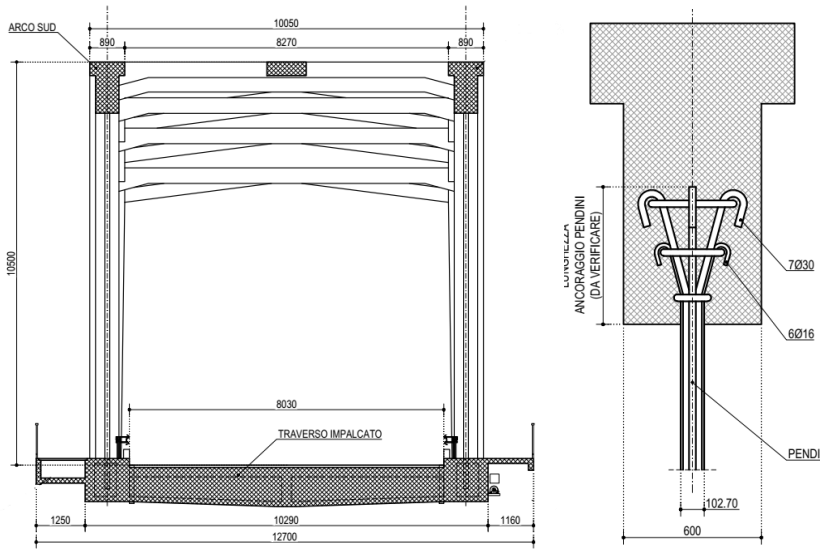

Figure 92: Deck and arch sections

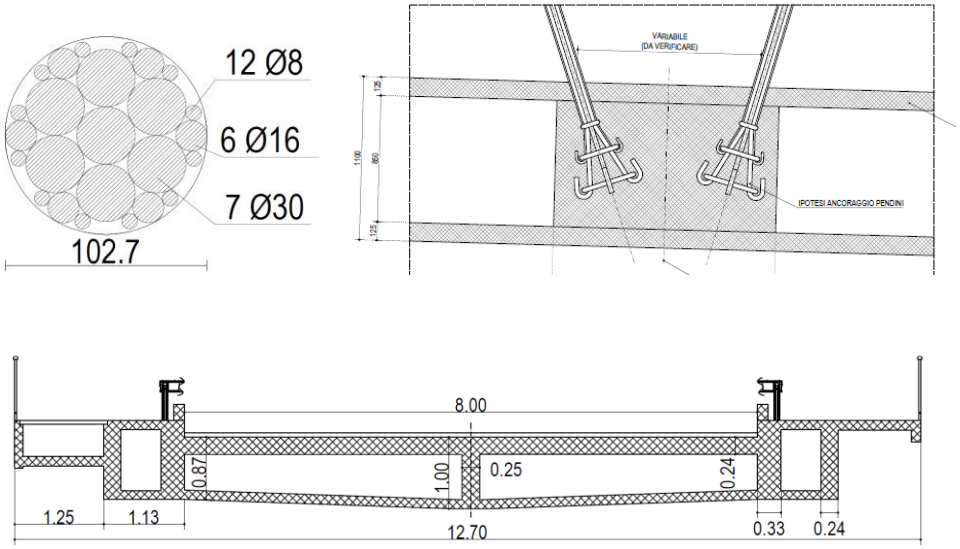

Figure 93: Tendons and their anchors and deck sections.

In addition to the bridge geometrical scan, some material and in situ tests of the bridge were found. Two main experimental campaigns were conducted on the Canonica d'Adda bridge, one in 2006 and the other in 2020, providing complementary insights into the structural condition of the infrastructure. The 2006 investigations focused mainly on geometrical surveys, direct inspections, material sampling, vibrational measurements, and static load tests. Concrete cores showed good compressive strength (ranging approximately from 39 to 78 MPa depending on location) and no critical problems, indicating satisfactory durability at that time.

Figure 94: Image from the first campaign.

The test was conducted by repeatedly positioning eight trucks (3- and 4-axle types) on the deck, following progressive loading and unloading sequences. The positions and loading phases were coded, and for each phase, both instrument readings and optical measurements were recorded. Measurements were taken using a data acquisition unit to record all sensor signals in real time. Vertical displacements of the deck were measured with an optical level.

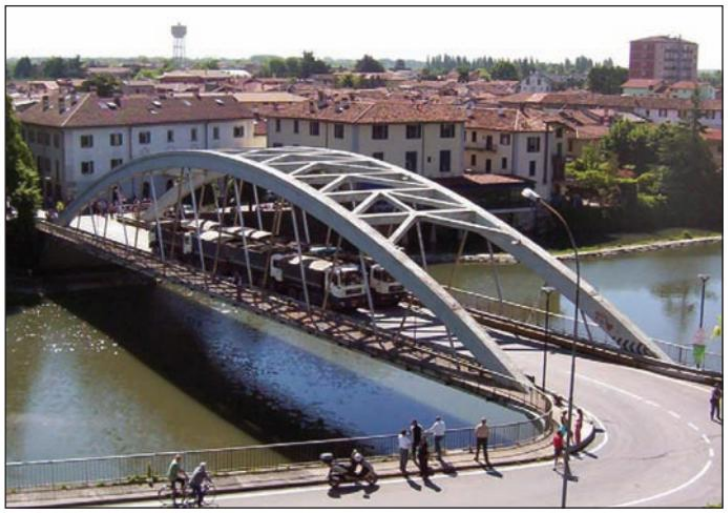

Truck	Total Mass [kg]
1	20100
2	35040
3	34980
4	20140
5	19880
6	30660
7	35220
8	19880

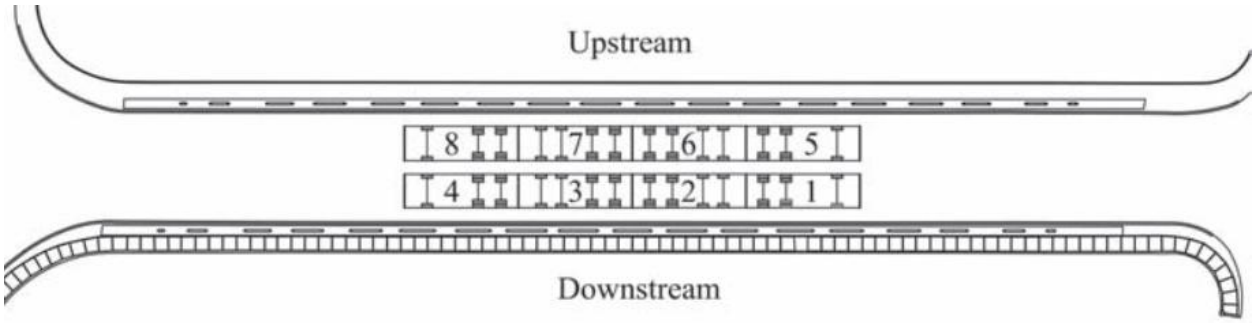

Figure 95: Static load test.

From the data, it can be seen that when all eight trucks were in operation, the total load applied to the deck was 215,900 kg (approximately 2,118 kN), based on the sum of all trucks.

The 2020 campaign was more extensive and specifically focused on the mechanical characterization of both concrete and reinforcement. The following tests were conducted:

- Rebar mapping with a pachometer to identify reinforcement position, diameter, and cover depth.
- Hardness tests on reinforcement bars correlated Rockwell B (HRB) hardness values to tensile strength. Results showed strength values between 310 and 410 MPa, depending on the element (arches, beams, slabs).
- Concrete characterization using both destructive and non-destructive methods:
    - Sclerometric tests showed compressive strengths in the range of 51–60 MPa, with slabs reaching the upper values.
    - Ultrasonic pulse velocity tests revealed values for P-waves between ~3800 and 5200 m/s, consistent with a dense and compact concrete.

- The SonReb combined method confirmed the above results, providing reliable estimates of compressive strength by integrating rebound hammer and ultrasonic measurements.

A summary of the 2020 results is reported in the following tables:

ID	Element	fs MPa	Rcub (SonReb) MPa	Rc (sclero, mean) MPa
L.1A / S.1A	Arch	410	48.1	60
L.2A / S.2A	Arch	340	98.0	60
L.3A / S.3A	Arch	350	97.2	60
L.4A / S.4A	Arch	340	62.2	52
L.5T / S.5T	Edge beam	410	90.2	60
L.6T / S.6T	Edge beam	320	56.3	51
L.7S / S.7S	Slab	310	98.2	60
S.8T	Edge beam	–	88.6	60
L.8S / S.9S	Slab	310	72.2	60
S.10T	Edge beam	–	54.9	51
S.11T	Edge beam	–	82.2	51
S.12T	Edge beam	–	82.4	52

Table 8: Summary of 2020 material characterization results.

These data show that, despite localized degradation phenomena already observed in 2006, the mechanical performance of both the concrete and reinforcement is quite good, and the available data will be useful for the next steps. Additionally, data from the static load test will be used in further analysis.

Figure 96: Image from the second campaign.

Repair Intervention

The maintenance intervention involved the complete replacement of the existing hangers with Haslinger HRM 750 steel bars (or equivalent) in M76 and M85 diameters, as specified in the structural calculation report and shown in Figure 97. The new bars are galvanized for durability and secured with metal anchors. The system allows for potential future retensioning of the hangers, ensuring long-term adaptability. After the hanger replacement, the bridge cannot yet be classified in the highest load category. Therefore, a restriction on the maximum allowable nominal load remains in effect. According to the Highway Code, the permissible live load is limited to 26 tons.

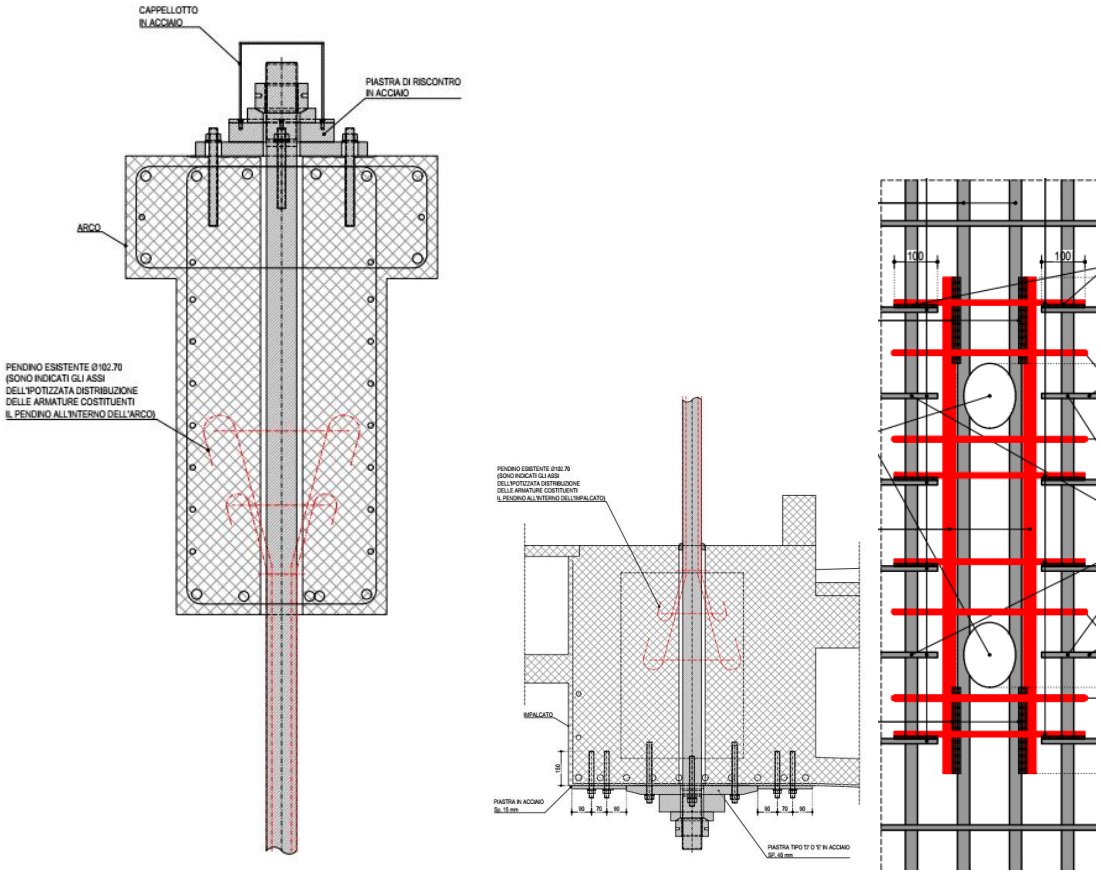

Figure 97: Repair interevent details.

Dynamic Identification of the Canonica d'Adda Bridge

This section provides a description of the application of modal analysis techniques to a reinforced concrete arch bridge. The dynamic identification technique using Operational Modal Analysis (OMA) has proven to be highly promising and reliable for evaluating the structural dynamics of bridges. By using appropriate sensors and advanced data analysis techniques, it is possible to obtain detailed information on the dynamic behaviour of the structure and to identify any anomalies or damage. Dynamic identification is therefore a key tool for assessing the structural health of reinforced concrete bridges and forms the basis for effective long-term monitoring. A key factor in obtaining reliable results is the careful design of the test setup, which includes the selection and placement of sensors, the routing and protection of cables, and the organization of data acquisition systems. Ensuring that the sensors are securely fixed, properly connected, and correctly synchronized is critical for capturing accurate measurements and avoiding noise or artifacts in the recorded signals.

Test Setup

For the modal analysis, the sensors were positioned to maximize the likelihood of capturing the main modal shapes of the structure. Fourteen piezoelectric sensors were available: seven accelerometers were mounted on each side of the deck. Additionally, six MEMS sensors were placed at the same locations as the piezoelectric accelerometers, with five on one side of the deck and one on the other, to better capture the primary torsional modes (Figure 100). The piezoelectric accelerometers used were Wilcoxon 731A-P31 models with a sensitivity of 10 V/g and a spectral noise of 0.01 µg/√Hz (10Hz). Each is equipped with a battery that also performs anti-aliasing filtering and is connected to a Quantum Gateway (manufactured by HBM), which synchronizes the sensors and transmits the data to a personal computer. The MEMS sensors are BeanScape 2.4 GHz AXE-3D XRange accelerometers (manufactured by BeanAir) with a sensitivity of 0.1 mg and a noise spectral density of 35 µg/√Hz, connected via a 2.4 GHz wireless network to a gateway (BeanGateway) that manages the sensor connections and synchronizes data acquisition. The piezoelectric accelerometers were mounted on small metallic blocks, which were securely attached to the bridge deck using anchors. The accelerometers were screwed onto the blocks to ensure stability during testing. The following figure shows a measurement point with the metal block, the piezoelectric accelerometer, and the MEMS accelerometer.

Figure 98: Accelerometers installed during the dynamic test campaign.

Cables from the sensors were routed along the sides of the bridge and connected across the deck using the underside of the structure to minimize interference and maintain organization. The data acquisition computer was positioned at the edge of the bridge, with all sensors, gateways, and the

power generator connected and ready for operation (Figure 99). After setup was completed, preliminary tests were conducted to verify correct functioning and signal quality.

Figure 99: Experimental setup for dynamic data acquisition.

Preliminary setup tests were conducted on the bridge before the hanger replacement, followed by two data acquisition sessions of 25 minutes each, with a sampling frequency of 500 Hz for the piezoelectric sensors and 100 Hz for the MEMS sensors. After the hanger replacement was completed, the bridge was revisited and the preliminary setup was repeated, including repositioning and calibrating the equipment. Two longer acquisition sessions of about 50 minutes each were then performed, maintaining the same sampling frequencies. During this stage, the MEMS sensors experienced unexpected battery failures, so only the results from the piezoelectric sensors are reported. These measurements provided a robust set of experimental data for the subsequent operational modal analysis, forming the basis for model updating and evaluating the effects of structural interventions such as the hanger replacement.

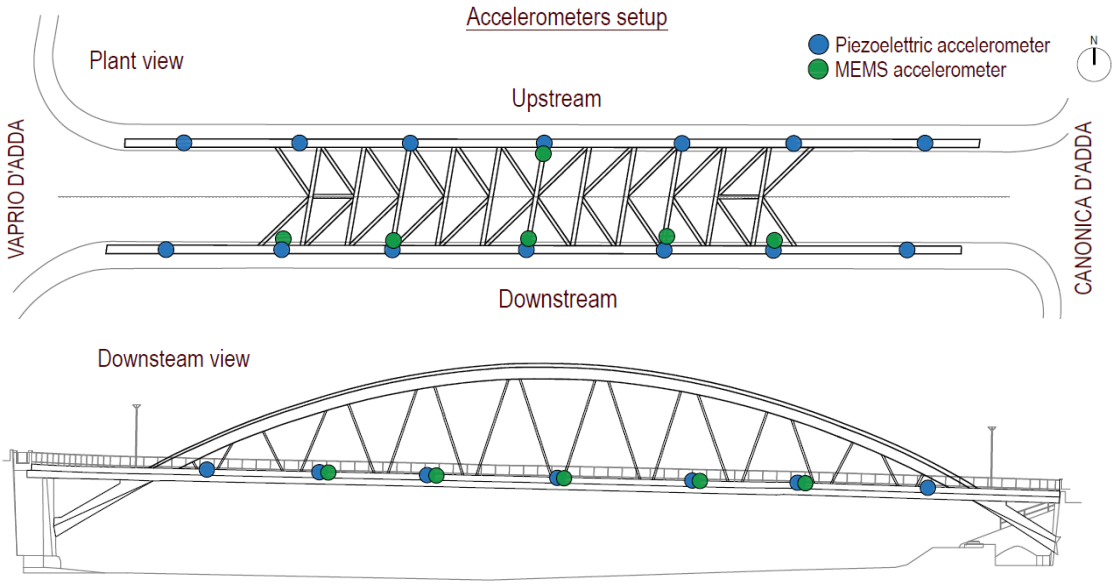

Figure 100: Position of the sensors.

Figure 101 and Figure 102 present examples of signals recorded during the acquisition on the bridge. The figures were generated using a Matlab application developed for this thesis, which enables signal analysis through preprocessing (filtering, detrending, and windowing) and examination of key quantities such as autocorrelation and power spectral density (PSD) with various window types. This offers an initial insight into the dynamics present in the signals.

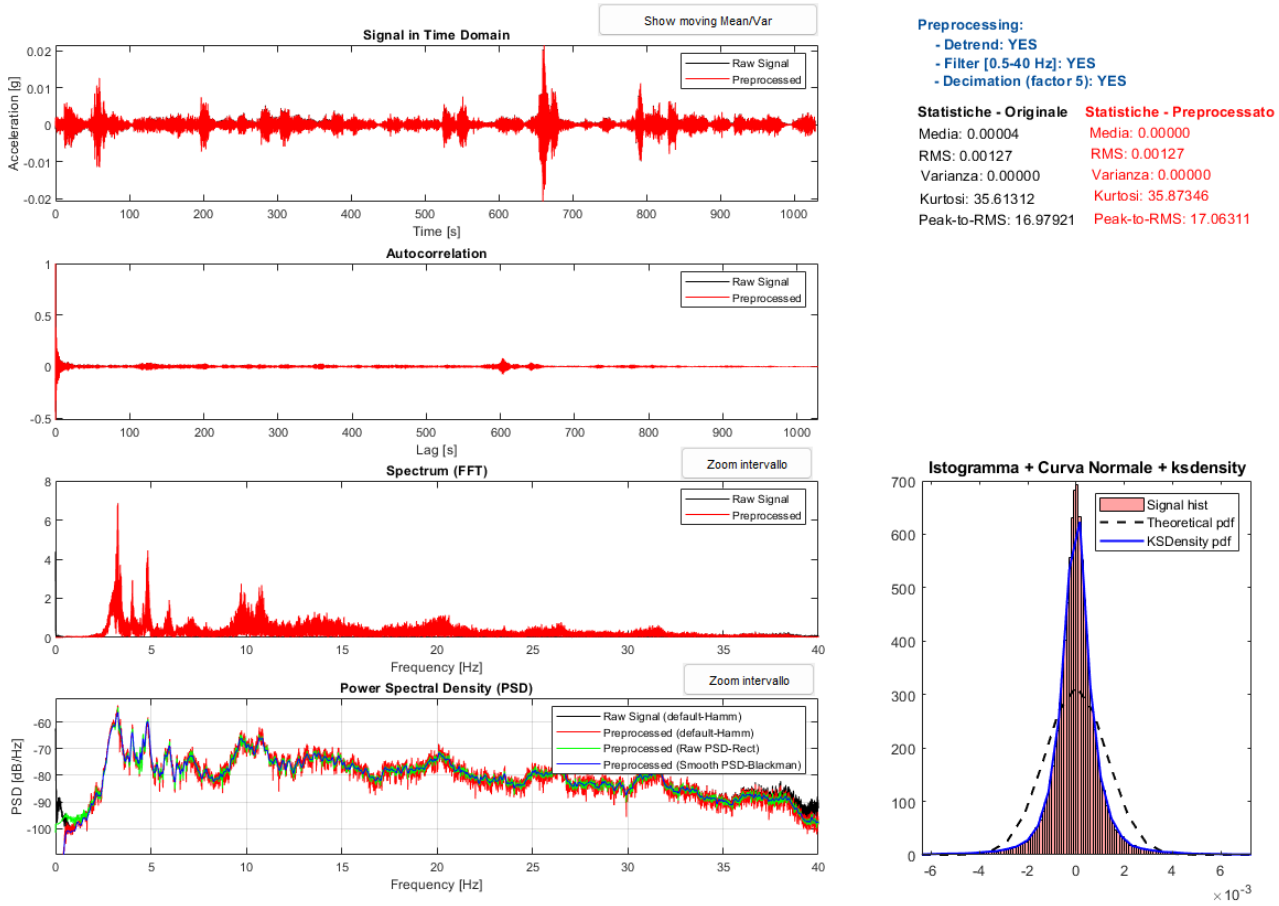

Figure 101: Single signal plotted in an analysis scrip.

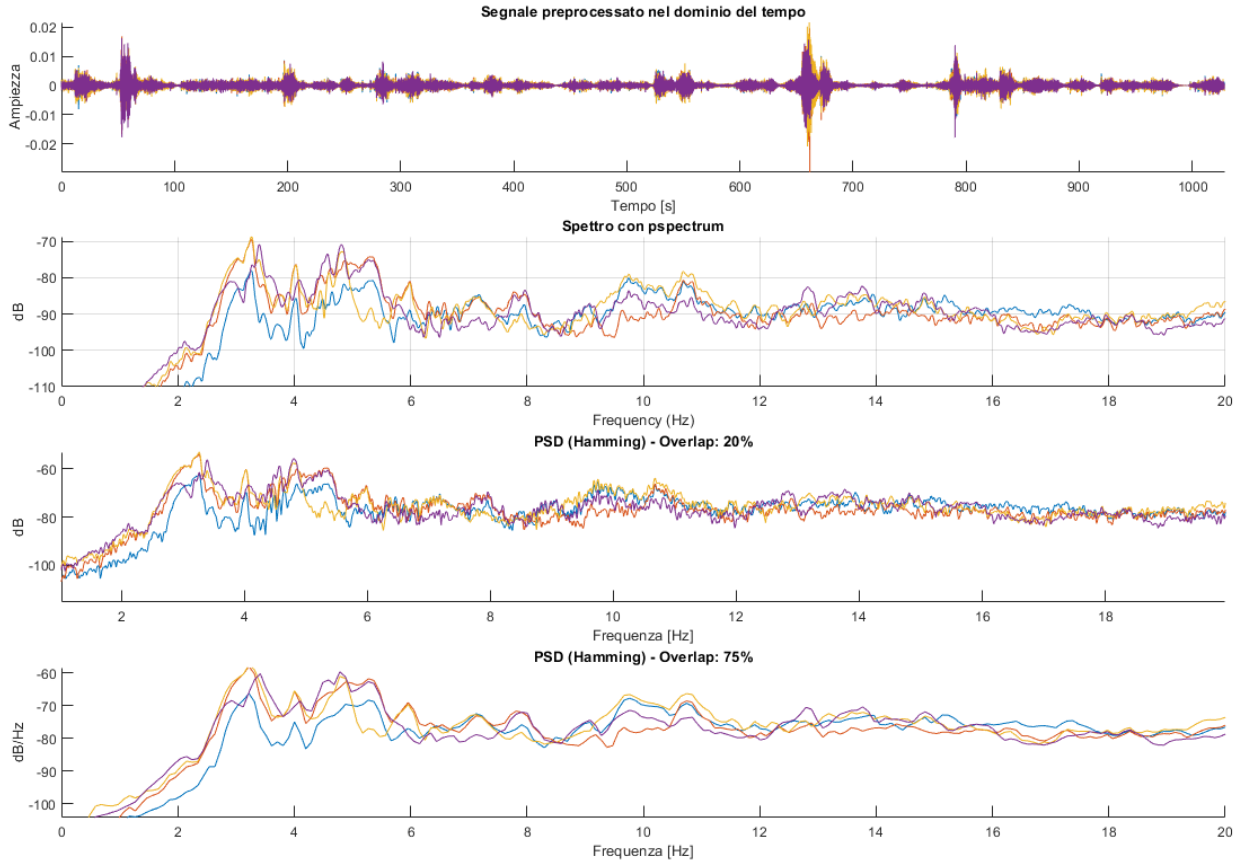

Figure 102: Signals plotted in an analysis scrip.

To accurately capture the dynamic behaviour of the bridge, an operational modal analysis was conducted. The study was performed both before and after the hanger replacement, allowing comparison of the structural response under the two conditions.

Modal Identification before

To obtain a more reliable estimate of the modal properties, two algorithms were selected: FDD (Frequency Domain Decomposition) and SSI-Cov (Stochastic Subspace Identification – Covariance Driven). The first is a frequency domain method that identifies natural frequencies and mode shapes by computing the power spectral matrix through auto and cross-correlation of the signals, followed by Singular Value Decomposition (SVD) of that matrix. SSI is a time-domain method that estimates modal parameters by fitting a stochastic state-space model to the measured output data sequence. Both methods are widely used in operational modal analysis and in assessing the modal characteristics of civil structures. The two methods were applied using the MACEC software from KU Leuven, a Matlab toolbox for the modal analysis of structures. This tool enables the extraction of natural

frequencies, damping ratios, mode shapes, and modal scaling factors from measured input-output or output-only vibration data. The interface is shown in Figure 103.

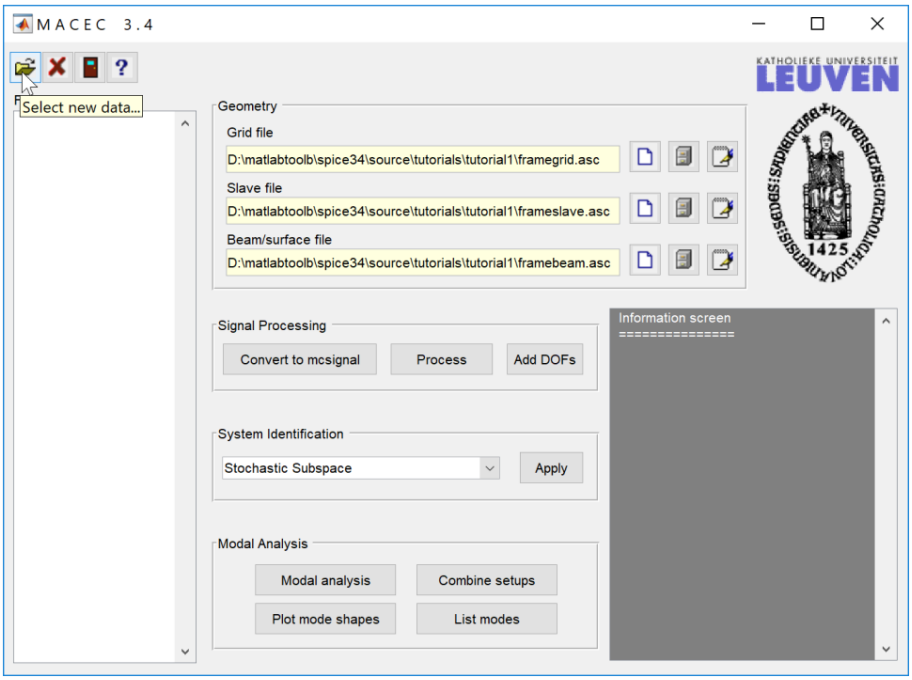

Figure 103: MACEC toolbox interface.

MACEC also includes a pre-processing toolbox in which the signals were resampled at 50 Hz, a 4th-order Butterworth bandpass filter (0.2–20 Hz) and detrending were applied, and a 20-minute window was selected for the first recording (before the replacement) and a 45-minute window for the second (after the replacement). After pre-processing, the two algorithms were applied.

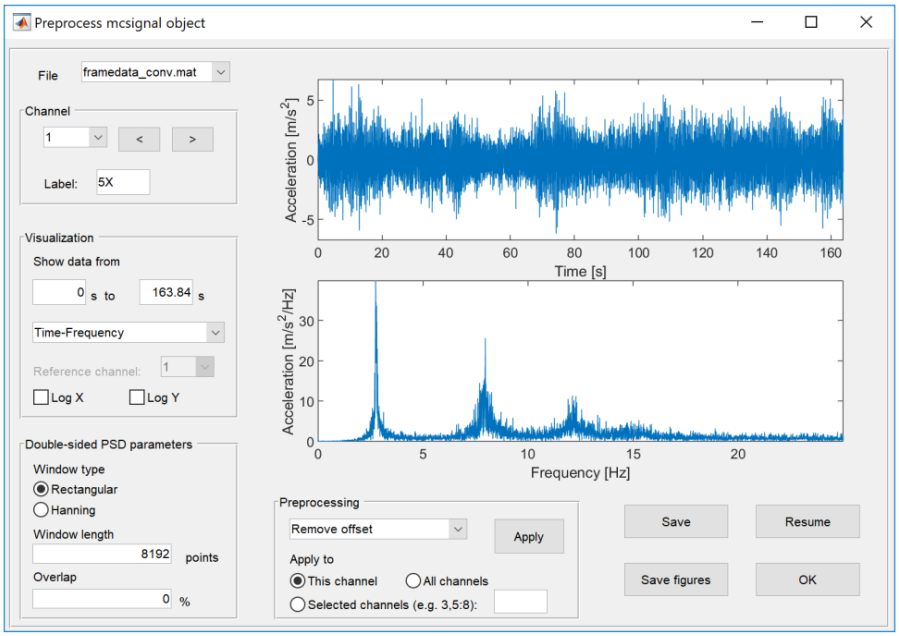

Figure 104: MACEC pre-processing interface.

Piezoelectric sensors

Once that the geometry is created (Figure 105), modal analysis was performed in these steps, following MACEC toolbox:

1. Data acquisition and preprocessing: the raw measurements are imported into MACEC and converted into an *mcsignal* object, which centralizes all signal information. At this stage, data can be filtered, resampled, or detrended, and the measurement channels must be linked to the geometry nodes of the model
2. System identification: based on the pre-processed signals, MACEC estimates a mathematical model of the system. Several identification methods are available, such as stochastic subspace identification, poly-reference frequency domain, and combined deterministic-stochastic approaches.
3. Modal analysis: it involves extracting modal parameters – natural frequencies, damping ratios, and mode shapes – from the identified model. Visualization tools such as singular value plots (FDD) and stabilization diagrams (SSI) help distinguish real physical modes from spurious ones

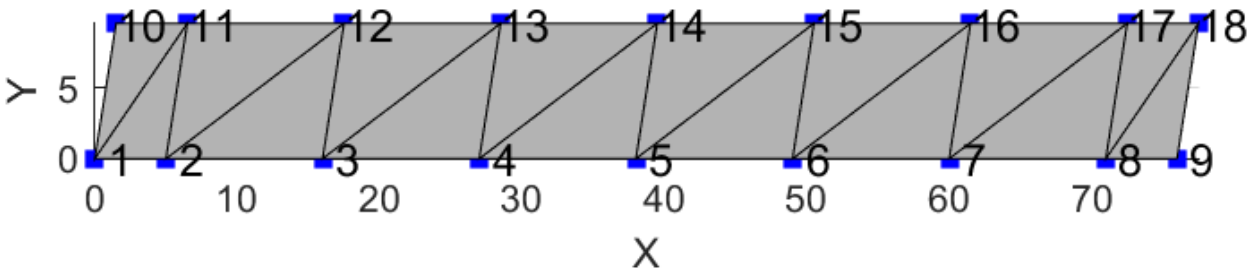

Figure 105: MACEC geometry.

The following images (Figure 106 and Figure 107) show the singular values obtained from the FDD (the PSD matrix was calculated using a rectangular window with 30% overlap) and the stabilization curve derived from the SSI (applied with model order 50). The figures display the selected peaks corresponding to real modes. Before identifying this solution, other peaks were analysed and discarded by evaluating modal indicators such as modal phase collinearity (MPC), mean phase deviation (MPD), and the imaginary part, which can also be checked with MACEC and may be useful for selecting real modes, as described in the previous chapter.

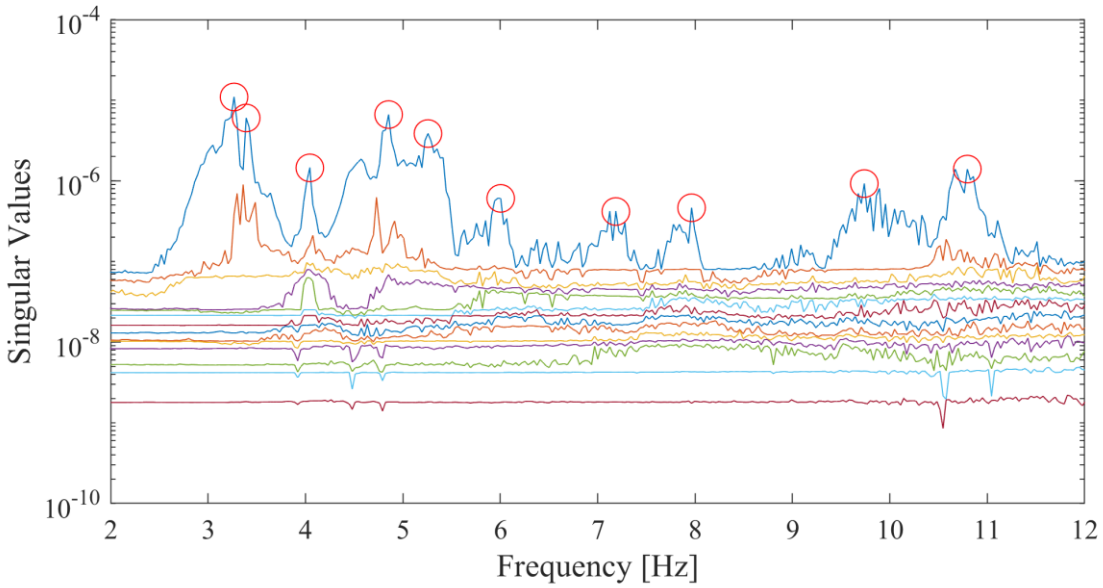

Figure 106: Singular Values of pre intervention data.

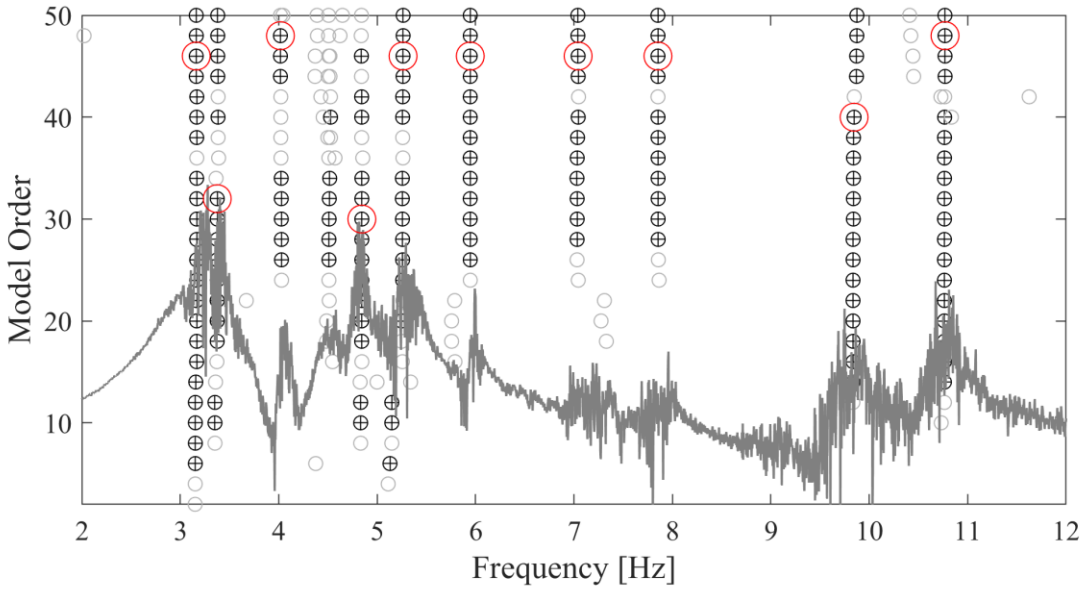

Figure 107: Stable Plot of pre intervention data.

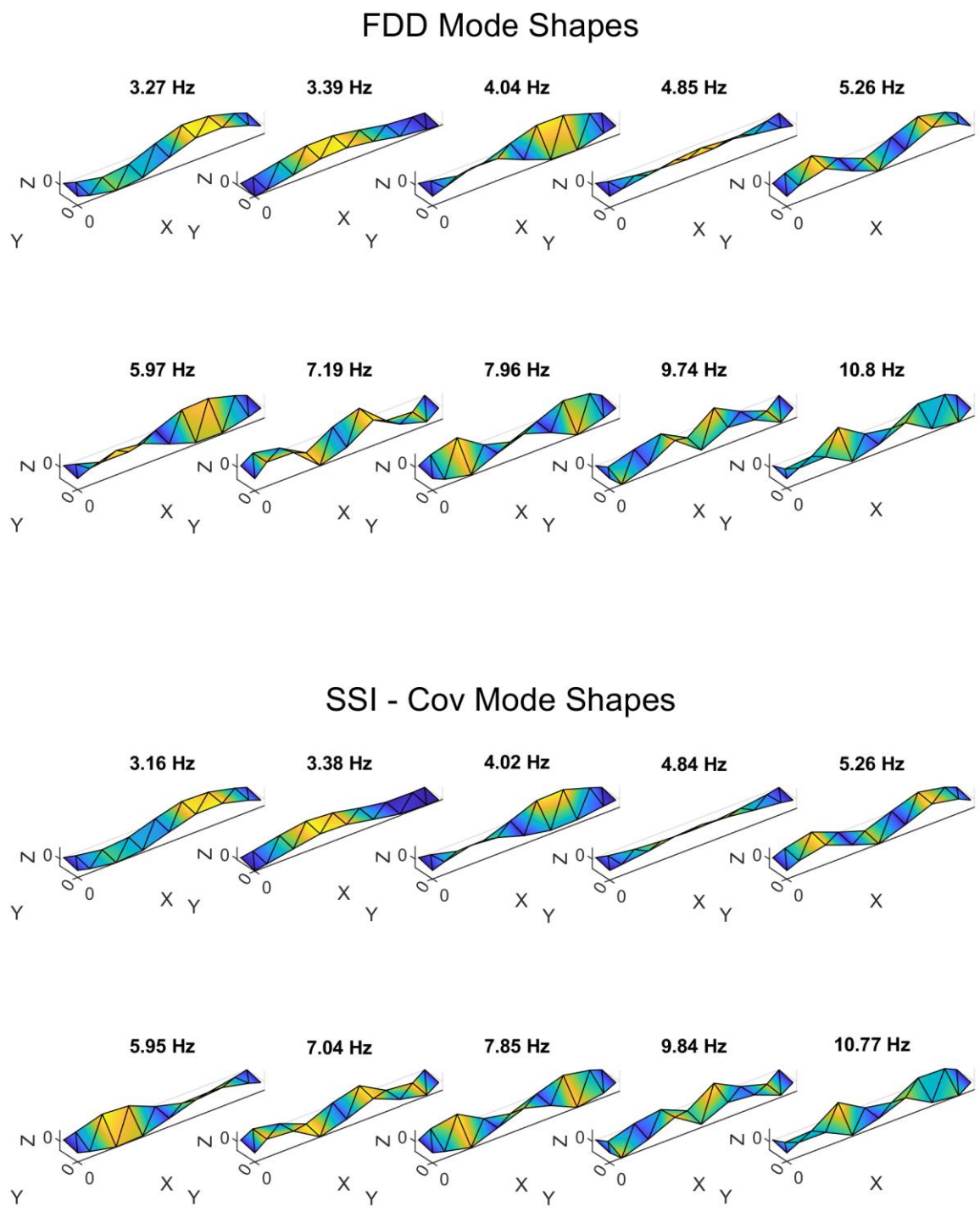

Figure 108: FDD and SSI-Cov identified mode shapes.

From Figure 108, it is clear that ten modes were identified for both algorithms. Except for the first mode, where SSI found a frequency at 3.16 Hz and FDD found it at 3.27 Hz, the remaining modes show a high correspondence in both mode shapes and frequencies. The difference in the first mode is attributable to the passage of a heavy truck during the recording; in fact, when this load is removed from the data and SSI is applied, the identified frequency is 3.26 Hz. The modes include both bending

and torsional modes. The results of the identification and the modal indicators used in the selection can be found in Table 9.

f FDD [Hz]	*f* SSI [Hz]	MAC FDD-SSI	MPC FDD	MPC SSI	MPD FDD [°]	MPD SSI [°]	Mode Type
3.27	3.16	1.00	0.96	1.00	5.09	0.75	Bending
3.39	3.38	0.95	0.94	0.74	7.78	18.29	Bending
4.04	4.02	0.92	0.90	0.98	9.21	3.84	Torsional
4.85	4.84	0.99	0.94	0.85	5.63	11.03	Torsional
5.26	5.26	1.00	0.98	1.00	3.57	1.93	Bending
5.97	5.95	0.97	0.94	0.98	6.87	3.23	Torsional
7.19	7.04	0.98	0.97	0.93	4.56	6.76	Bending
7.96	7.85	0.97	0.97	0.98	4.77	4.03	Torsional
9.74	9.84	0.99	0.95	0.97	6.57	5.20	Bending
10.80	10.77	1.00	0.97	0.99	4.19	1.88	Torsional

Table 9: Result of the identification before.

MEMS

After presenting the results from the piezoelectric sensors, as previously mentioned, measurements were also conducted using MEMS accelerometers. The goal was to evaluate the effectiveness of the identification procedure with data from low-cost sensors. Fewer in number than the piezoelectric sensors, the MEMS accelerometers were placed at the same locations to capture comparable modal information. The signals acquired from the MEMS sensors were processed in the same manner, and the results of the dynamic identification using both the FDD and SSI algorithms are presented below. This comparison enables an assessment of the reliability and limitations of using MEMS accelerometers for operational modal analysis, providing insight into their potential for broader monitoring applications where cost or deployment constraints are critical.

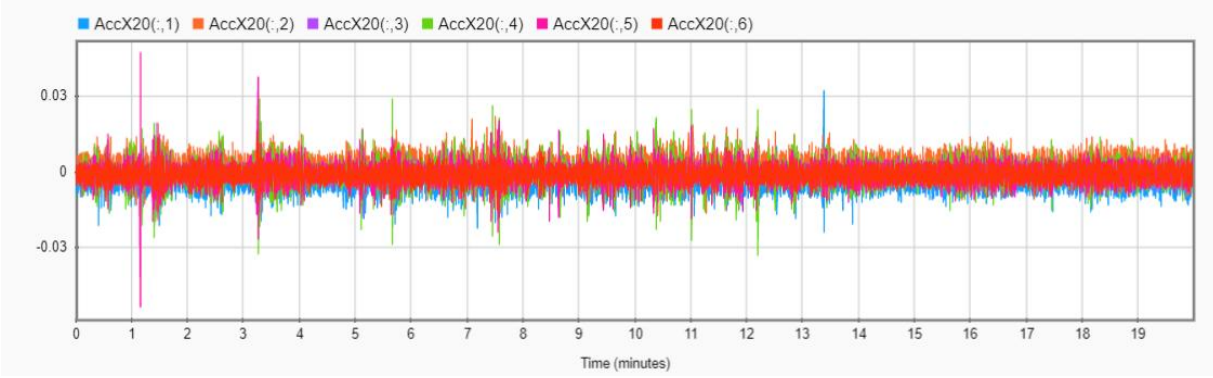

Figure 109: MEMS signals.

The same pre-processing was applied to the MEMS signals to evaluate the differences from the piezoelectric signals. For these signals, both the FDD and SSI algorithms were used for the dynamic identification of the MEMS data, and the corresponding results are shown in Figure 110 and Figure 111. The main difference observed was the need to lower the stabilization criteria in the stabilization diagram, as the indicators from the MEMS signals were less clear than those from the piezoelectric sensors. Despite this adjustment, the analysis still provided useful information on the modal properties of the bridge, suggesting both the potential and limitations of low-cost sensors for operational modal analysis.

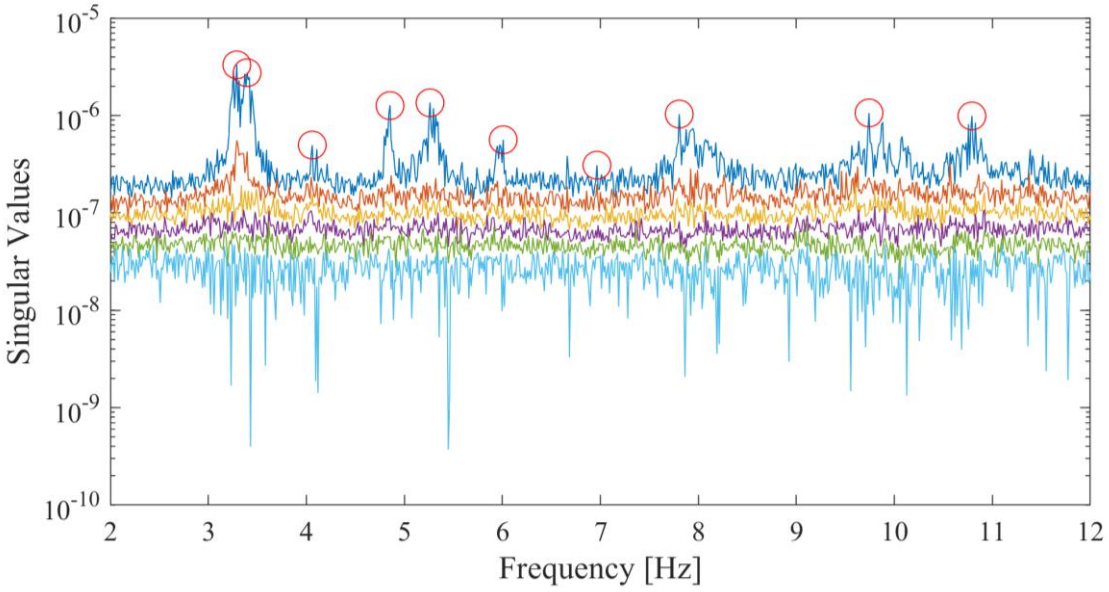

Figure 110: Singular Values of pre intervention data, MEMS accelerometers.

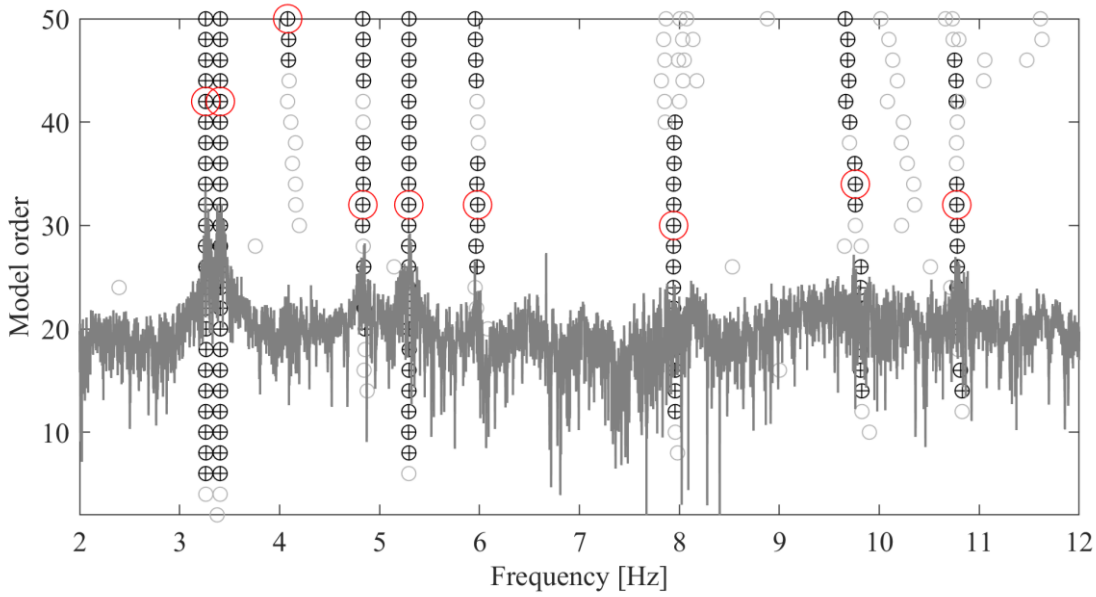

Figure 111: Stable Plot of pre intervention data, MEMS accelerometers.

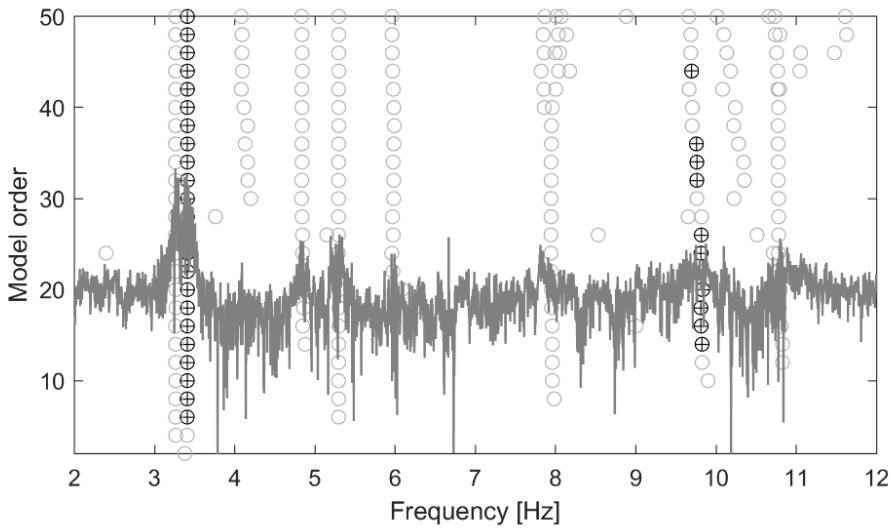

Figure 112: Stable Plot for MEMS sensors without decreasing stable criteria.

In Figure 113, the mode shapes identified through modal analysis using the MEBS sensor signals are shown. The identified mode shapes are similar for both algorithms, except that the 6.97 Hz frequency could not be identified using the SSI algorithm.

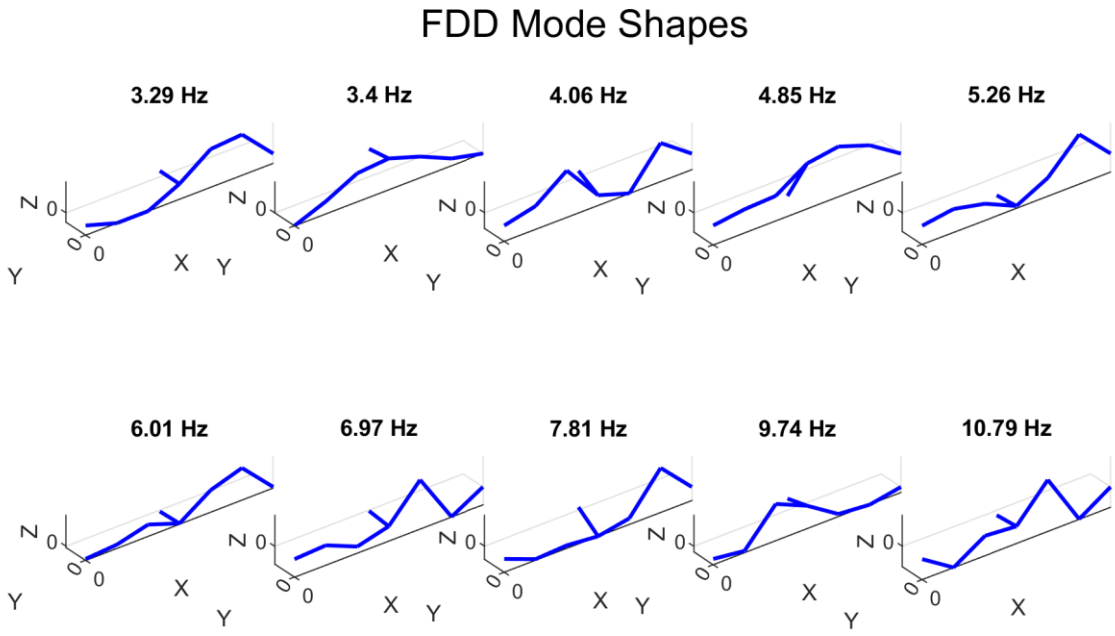

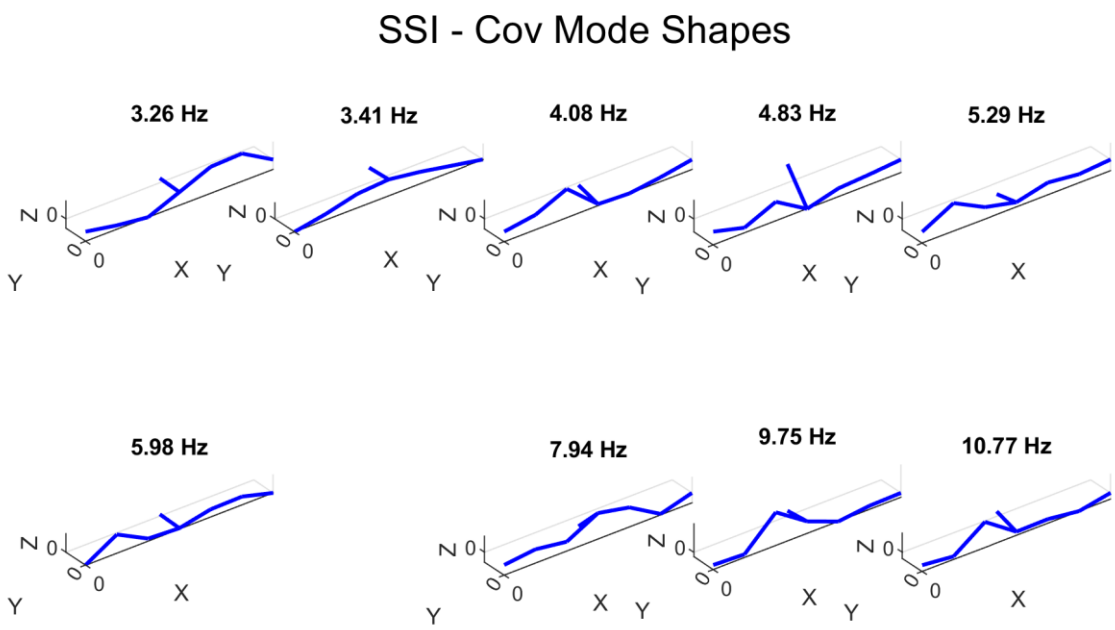

Figure 113: FDD and SSI-Cov identified mode shapes, MEMS accelerometers.

Table 10 presents the modal characteristics of the piezoelectric and MEMS data using both FDD and SSI methods, with the modal indicators MPC and MPD. The MAC values are calculated at the node where both types of accelerometers were installed. The frequencies identified by the two algorithms align well, with the first frequency being higher for FDD (3.27 Hz). This may be because a heavy truck was passing during the analyzed window, potentially causing a slight frequency shift. However, when examining a short data window, SSI performs well, identifying the frequency at 3.26 Hz. In this short window, the last two modes are also difficult to identify due to low excitation. The frequencies estimated with the MEMS sensors are very similar to those from the piezoelectric sensors. The main difference is in the modal indicators, which are less reliable with the MEMS sensors due to higher noise and possibly imperfect synchronization of the recordings.

FDD							SSI						
f [Hz]	f *MEMS* [Hz]	MPC	MPC MEMS	MPD	MPD MEMS	MAC FDD	f [Hz]	f MEMS [Hz]	MPC	MPC MEMS	MPD	MPD MEMS	MAC SSI
3.27	3.29	0.96	0.41	5.09	25.68	0.94	3.16	3.26	1.00	0.37	0.75	22.82	0.96
3.39	3.40	0.94	0.65	7.78	18.16	0.99	3.38	3.41	0.74	0.70	18.29	14.56	0.93
4.04	4.06	0.90	0.23	9.21	25.80	0.20	4.02	4.08	0.98	0.04	3.84	40.50	0.59
4.85	4.85	0.94	0.15	5.63	33.91	0.81	4.84	4.83	0.85	0.08	11.03	35.03	0.49
5.26	5.26	0.98	0.27	3.57	25.51	0.77	5.26	5.29	1.00	0.10	1.93	30.80	0.52
5.97	6.01	0.94	0.75	6.87	20.36	0.19	5.95	5.98	0.98	0.16	3.23	30.43	0.02
7.19	6.97	0.97	0.71	4.56	21.14	0.53	7.04	-	0.93	-	6.76	-	-
7.96	7.81	0.97	0.20	4.77	32.31	0.23	7.85	7.94	0.98	0.07	4.03	36.45	0.50
9.74	9.74	0.95	0.33	6.57	27.65	0.07	9.84	9.75	0.97	0.14	5.20	33.90	0.19
10.80	10.79	0.97	0.33	4.19	25.01	0.23	10.77	10.77	0.99	0.00	1.88	44.02	0.26

Table 10: Result of the identification before.

Two types of accelerometers were investigated on the Canonica d'Adda bridge: higher-performance piezoelectric sensors and lower-cost MEMS sensors. The results show that the natural frequencies obtained from both sensor types were generally very similar, and the first mode shapes showed good agreement. However, data from the piezoelectric sensors proved more reliable and accurate. These observations confirm that, while MEMS sensors can provide useful information and offer potential for cost-effective monitoring, piezoelectric sensors remain the preferred choice for precise structural assessment. With the characterization before the hanger replacement complete, the next step in this study is to analyse the bridge after the intervention, applying the same identification procedures to evaluate any changes in the modal properties resulting from the replacement.

Modal Identification after

Once the replacement worksite was completed, it was possible to return to the bridge to conduct a new acquisition campaign and check for any differences in the modal parameters. As previously mentioned, the test setup remained the same as in the pre-replacement tests; however, longer recordings were possible. The same preprocessing procedure was applied (resampled at 50 Hz, a 4th-order Butterworth bandpass filter [0.2–20 Hz], and detrending), and the results from both algorithms are presented below. In particular, Figure 114 shows the singular values obtained from the post-intervention data, where improved resolution can be observed due to the longer recording, and Figure 115 presents the stabilization plot for the post-intervention data.

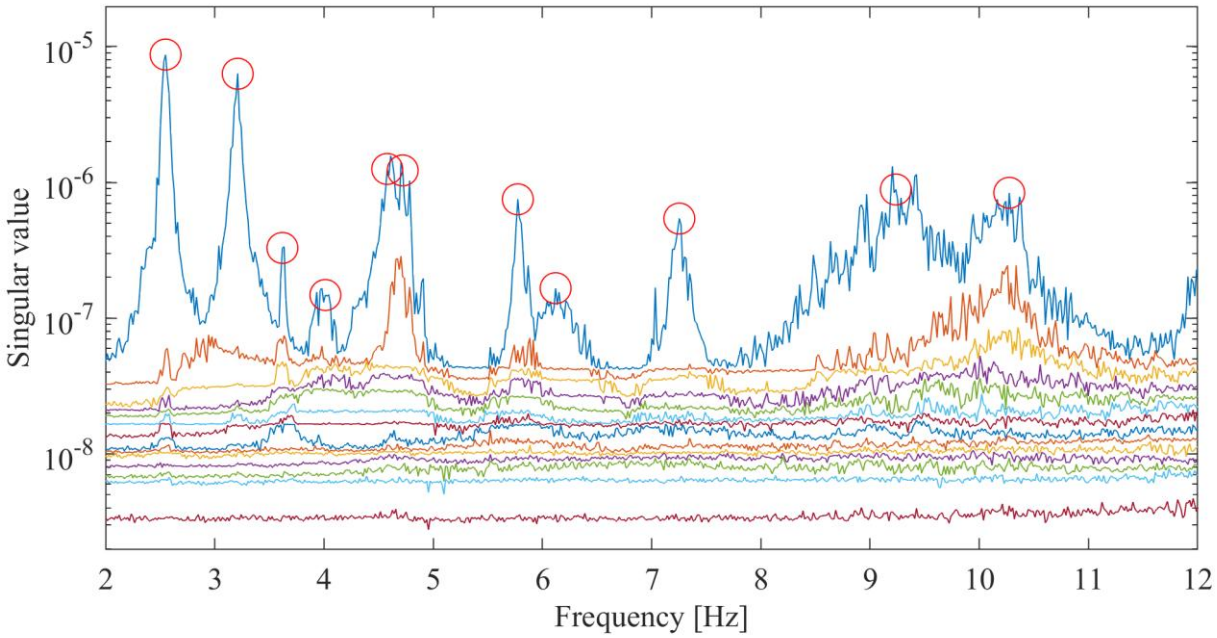

Figure 114: Singular Values of post intervention data.

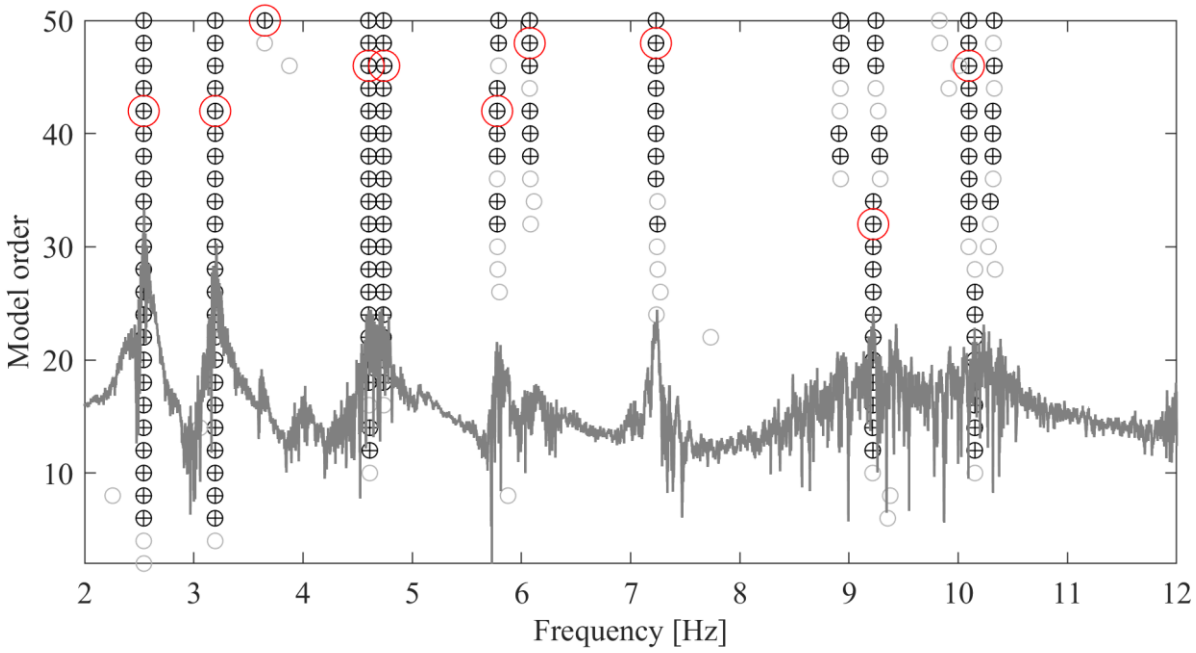

Figure 115: Stable Plot of post intervention data.

It was observed that the SSI algorithm, with a model order of 50, could not capture the frequency around 4 Hz. However, increasing the model order to 100 made the corresponding mode shape identifiable. **Errore. L'autoriferimento non è valido per un segnalibro.**, illustrates this, highlighting the stable plot with model order 100.

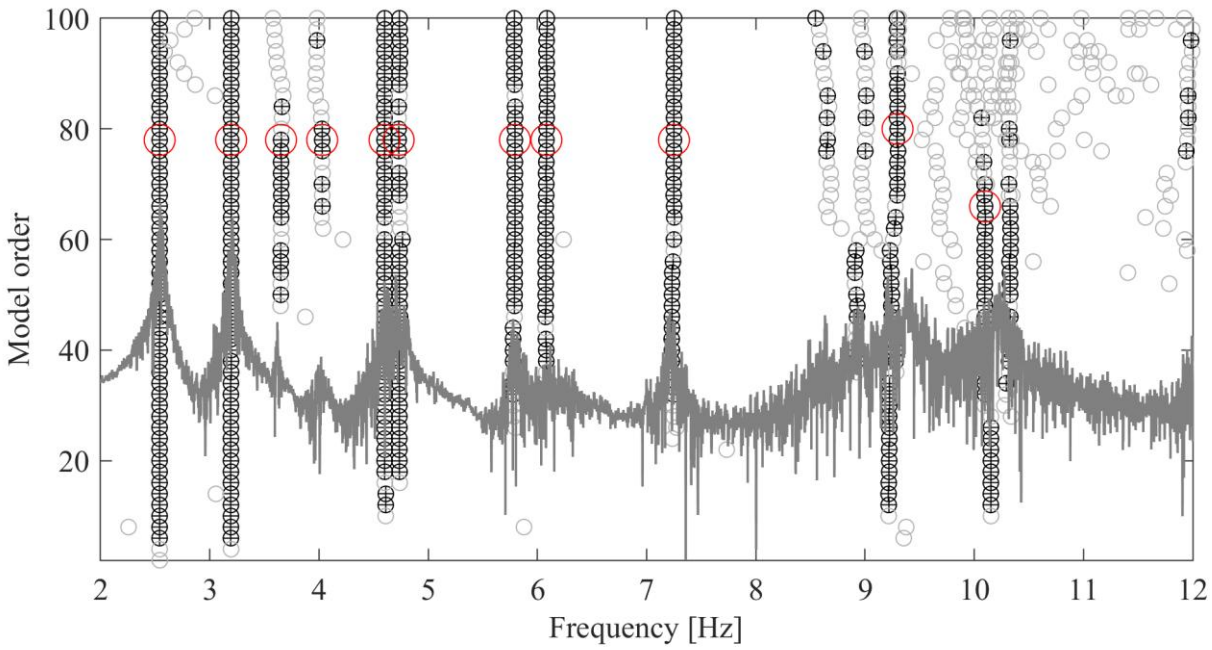

Figure 116: Stable Plot of post intervention data, increased order to 100.

Further analysis indicated that this mode corresponds to the transverse mode of the bridge. Its detection is now possible due to the shift of the double bending mode from 4.04 Hz (pre-intervention) to 3.62 Hz (post-intervention). In the pre-intervention identification, this mode was not visible, likely because it overlapped with the second bending mode. To support this interpretation, a transverse accelerometer was installed during the pre-intervention tests, and the corresponding signal showed a peak around 4 Hz, reinforcing the hypothesis about the presence of the transverse mode. The identified mode shapes are presented in Figure 117, along with a summary table listing the natural frequencies and other relevant modal parameters for the bridge after the hanger replacement.

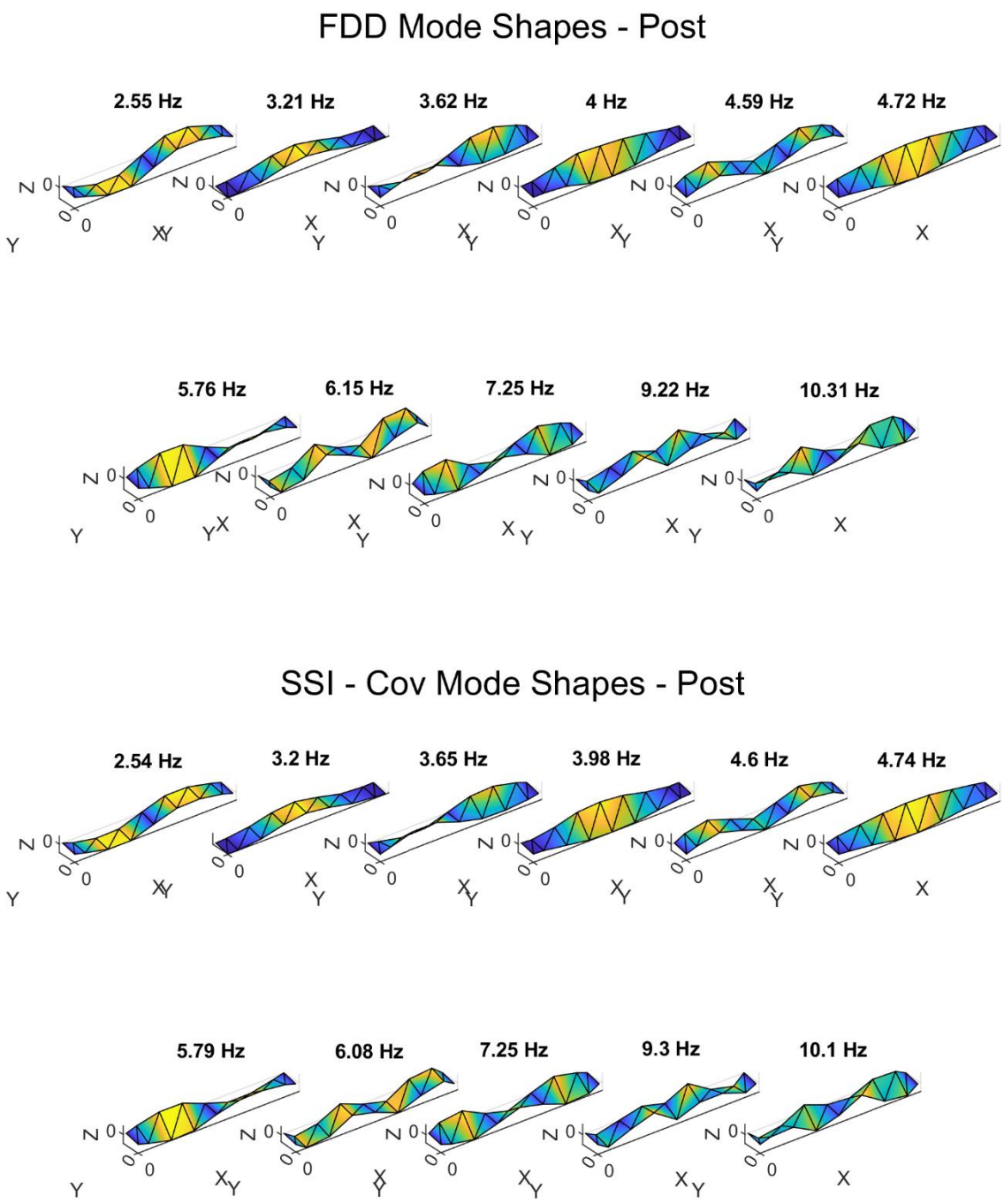

Figure 117: FDD and SSI-Cov identified mode shapes post intervention.

f FDD [Hz]	f SSI [Hz]	MAC FDD-SSI	MPC FDD	MPC SSI	MPD FDD [°]	MPD SSI [°]	Mode Type
2.55	2.54	1.00	1.00	1.00	1.37	0.47	Bending
3.21	3.20	1.00	1.00	1.00	0.94	0.44	Bending
3.62	3.65	0.99	0.94	0.99	6.14	2.97	Torsional
4.00	3.98	0.95	0.97	0.95	5.78	6.16	Transversal
4.59	4.60	0.99	0.99	0.99	2.29	1.96	Bending
4.72	4.74	1.00	1.00	1.00	1.10	0.97	Torsional
5.76	5.79	1.00	1.00	1.00	1.89	0.88	Torsional
6.15	6.08	0.99	0.99	1.00	2.38	1.60	Bending
7.25	7.25	1.00	0.99	1.00	2.86	1.23	Torsional
9.22	9.30	0.98	0.97	0.95	4.64	6.20	Bending
10.31	10.10	0.90	0.97	0.96	3.82	5.14	Bending

Table 11: Result of the identification after.

Difference

With the post-intervention results now available, the next step is to analyse and compare the modal parameters obtained before and after the hanger replacement, highlighting any changes in the bridge's dynamic behaviour resulting from the intervention. These results can be used to analyze the differences in the bridge's dynamic parameters, which will also be discussed in the following sections on finite element modelling, allowing an assessment of how the structural intervention could modify and influence the structural behaviour of bridges.

Figure 118 Figure 119 present the singular values obtained from the FDD analysis, allowing a direct comparison of the bridge's dynamic behaviour before and after the replacement of the hangers. The improved frequency resolution observed in the post-intervention results is due to the longer acquisition time during the second campaign. Comparing the two plots reveals shifts in the natural frequencies, indicating changes in the structural response of the bridge due to the intervention.

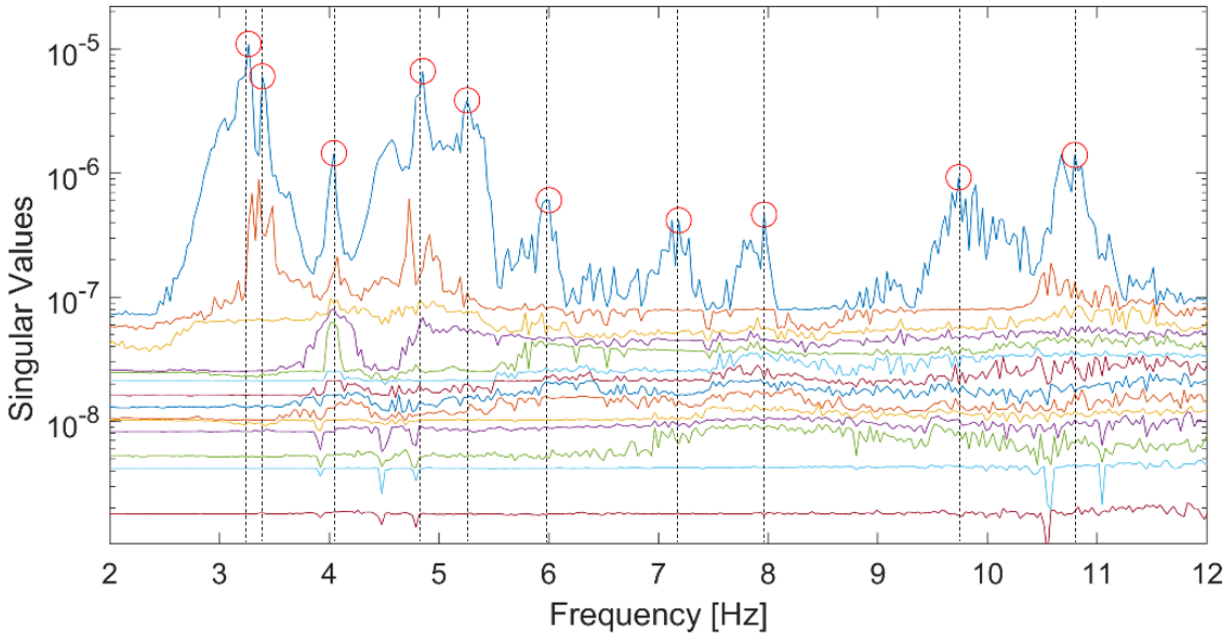

Figure 118: Singular Values before the replacement of the hangers.

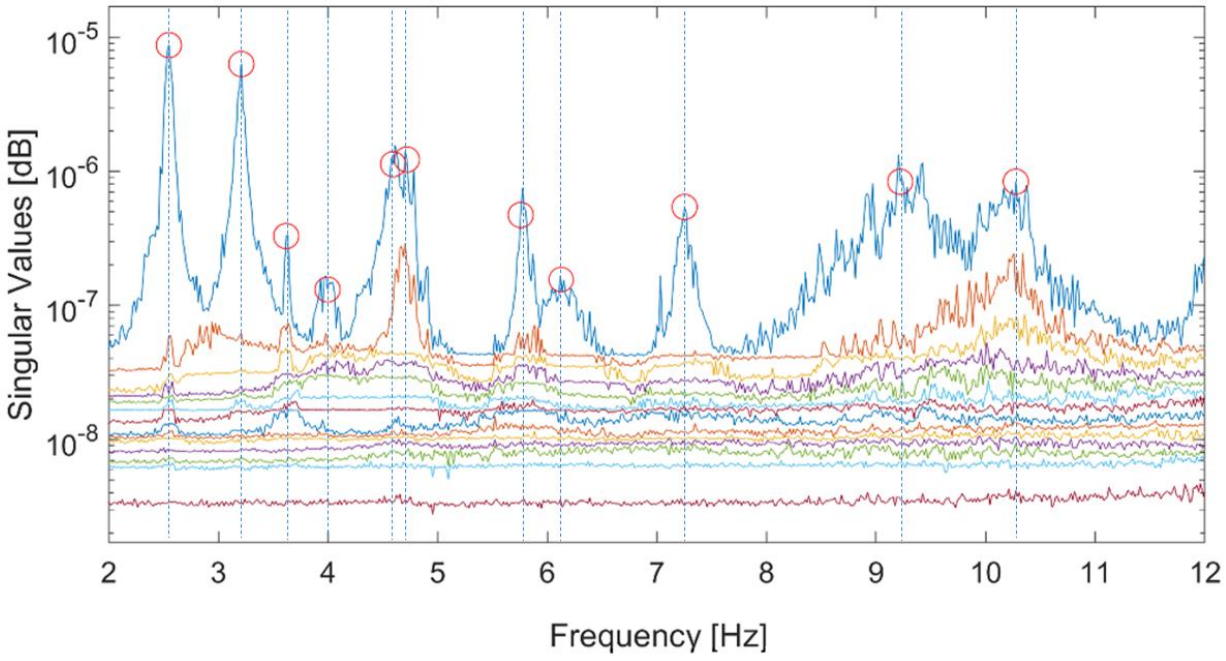

Figure 119: Singular Values after the replacement of the hangers.

The first thing to notice is a split between the first two picks, which is better illustrated in Figure 120, as the first frequency is clearly lower than the second. If we examine the mode shape plots in Figure 121 and Figure 122, we also observe a reversal between shapes 4 and 5. This occurs because the torsional mode at 5.26 Hz undergoes a greater frequency reduction than the bending mode at 4.85 Hz, resulting in the observed exchange. The corresponding peak values are highlighted in Figure 120. It can be seen that the overall frequencies have decreased, with differences of up to 22% for the first

mode, as shown in Table 12. Using the mode shapes and a finite element model (which will be explained later), we also note that in the second recording, another frequency at 4.00 Hz was identified, corresponding to the vertical component of a transverse mode shape of the bridge.

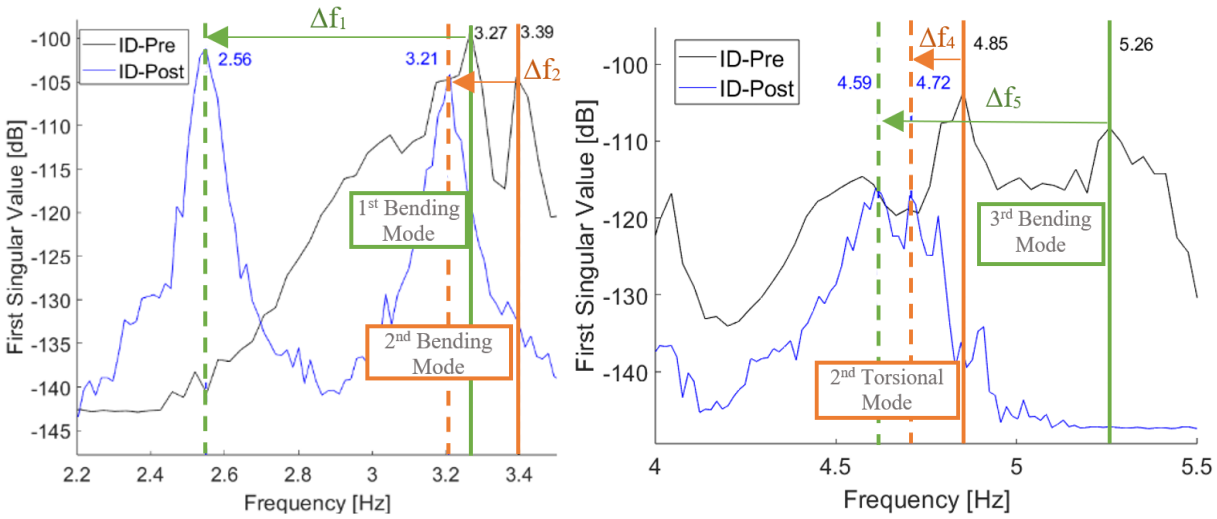

Figure 120: Particular of the frequency change.

The mode shapes remain essentially unchanged, although the MAC values for the first one, which is also most affected by the frequency change, never fall below 0.90. This change could be due to a non-uniform variation in stiffness following the replacement of the hangers. The table summarizes the frequencies determined before and after the intervention. To calculate the differences and the MAC values, the frequencies were reordered after pairing the modal shapes.

ID_Frequency Before [Hz]	3.27	3.39	4.04	-	4.85	5.26	5.97	7.19	7.96	9.74	10.80
ID_Frequency After [Hz]	2.55	3.21	3.62	4.00	4.72	4.59	5.76	6.15	7.25	9.22	10.31
Δf [%]	22	5.3	11	-	2.7	13	3.6	14	8.9	5.3	4.53
MAC	0.89	0.96	0.91		0.96	0.93	0.98	0.95	0.93	0.91	0.98

Table 12: Differences in identification before and after.

The images below show the mode shapes obtained from the modal analysis. To facilitate comparison, the 4 Hz mode shape, which corresponds to the vertical component of a transverse mode, is not shown.

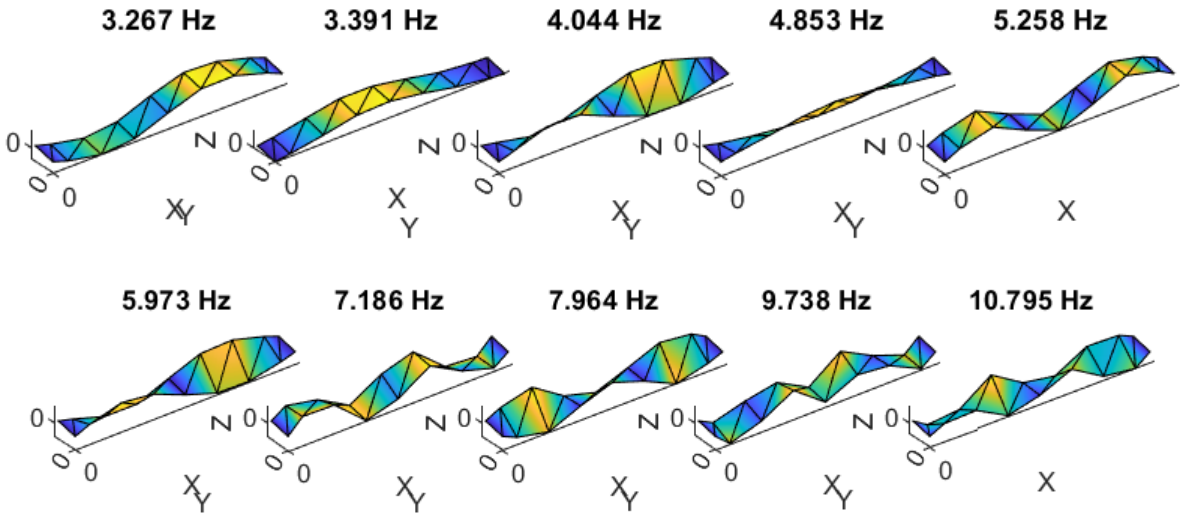

Figure 121: FDD identified mode shapes post intervention.

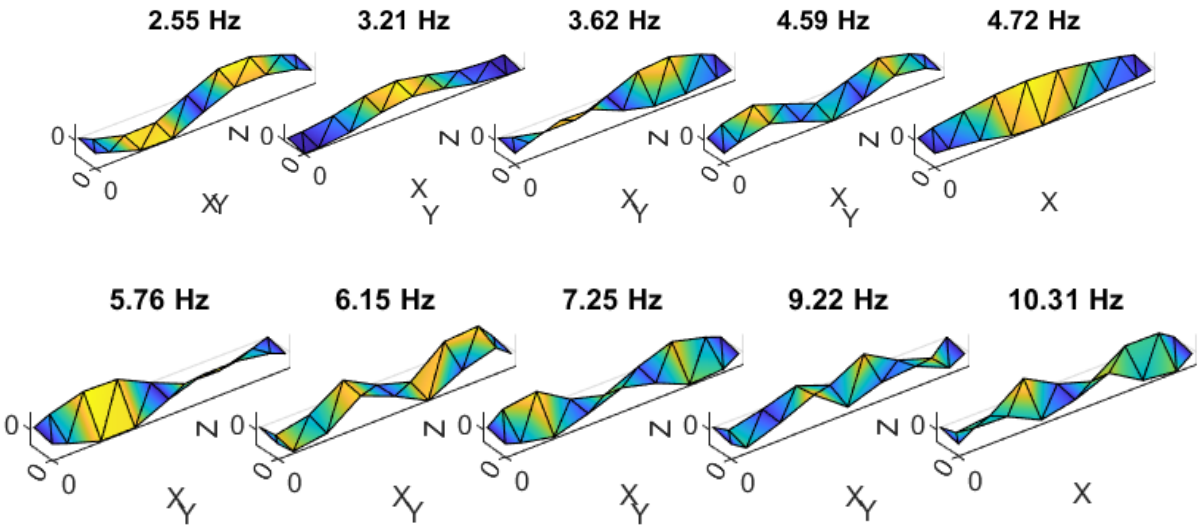

Figure 122: SSI-Cov identified mode shapes post intervention.

After the survey, which was conducted before the rehabilitation intervention, a finite element (FE) model was created to better understand the dynamic behaviour of the bridge and to use it for further studies, such as safety assessments. The FE model was developed in MidasGen [134] and STKO [133] (running OpenSees software [132]) to enable comparative analysis. Plate elements were used for the deck, and beam elements were used for the arch and hangers. The arches were considered fixed at the base, and the deck was modelled as simply supported. The MidasGen model was used for an initial manual update based on engineering judgment, while the OpenSees model underwent an automated finite element model update (FEMU) using a Matlab-OpenSees procedure, allowing a more representative simulation of the bridge's dynamic behaviour, which will be discussed later in this work. After the second set of recordings, this updated model was used to analyse the effects of

the hanger replacement. After replacing the cross-section of the original hangers with the new ones, it was observed that the differences between the FE model and the post-intervention identification remained significant. This first change is referred to as Step 1 to illustrate the results. Further analysis revealed that, in addition to the modified cross-section, the length and boundary conditions of the hangers had also been altered. The intervention involved replacing the old hangers, anchored with three-dimensional hooks, with new hangers attached with large bolts to the top of the arch and to the underside of the side beam of the deck (Figure 123). Including this modification in the model, shown as Step 2, resulted in a reduction of the natural frequencies and a better match with the identified modes, particularly improving the agreement for the first mode shape.

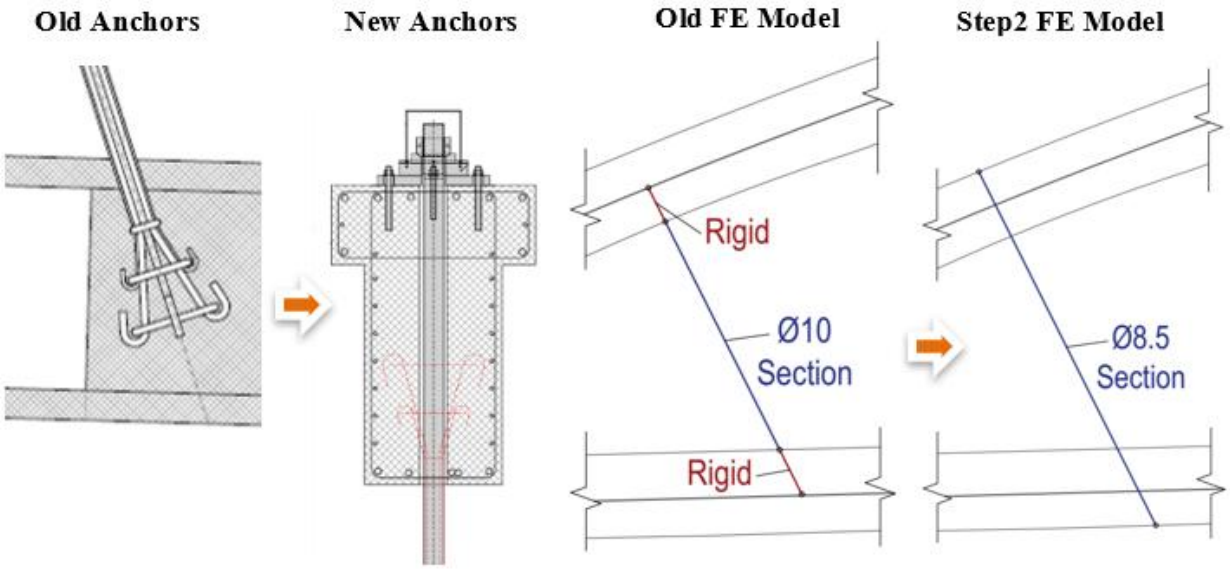

Figure 123: Particular of FE model changes.

Table 13 summarises the frequencies obtained before and after the replacement of the hangers, as well as the frequencies from the modal analyses of the finite element models with the changes in step 1, that is, with only the cross-section changed, and in step 2, where the length of the hanger was changed in addition to the cross-section.

Identified Frequency Before [Hz]	Identified Frequency After [Hz]	Frequency After Model Update [Hz]	Frequency FEM 1 step	Frequency FEM 2 step	Δf [%]	Δf [%] 1 step	Δf [%] 2 step
3.27	2.55	3.27	2.81	2.66	28.16	10.26	4.49
3.39	3.21	3.47	3.33	3.30	7.98	3.79	2.94
4.04	3.62	4.04	3.76	3.62	11.73	3.91	0.16
5.26	4.59	5.23	4.83	4.64	13.94	5.20	0.99
4.85	4.72	4.85	4.76	4.80	2.81	0.95	1.66
5.97	5.76	6.05	5.85	5.79	5.08	1.67	0.57
7.19	6.15	7.07	6.59	6.34	14.90	7.15	3.09
7.96	7.25	8.04	7.63	7.34	10.90	5.23	1.23

Table 13: Result of the FE model modification in Step 1 and Step 2.

In this chapter, the differences between the operational modal analysis of the reinforced concrete arch bridge before and after the rehabilitation intervention, during which the steel hangers were replaced, were analysed. The investigation focused on understanding the significant reduction in natural frequencies, which reached up to a 20% decrease in the first mode. Using a finite element model, the initial analysis concentrated on the effects of the change in the cross-section of the hangers. However, comparison with the experimental results revealed that this modification alone was not sufficient to explain the observed reduction in frequencies. A deeper investigation showed that the increase in hanger length, resulting from the new anchoring points, contributed to a reduction in the overall stiffness of the hangers, which in turn affected the dynamic properties of the bridge. Additionally, some modal interactions were observed, including an exchange between certain modes, as well as the identification of an additional mode in the post-intervention recordings, corresponding to the vertical component of a transverse mode shape. These observations highlight how both geometric modifications and changes in boundary conditions can have a considerable impact on the dynamic behaviour of a structure. Overall, the results underline the importance of an integrated approach that combines experimental modal analysis with finite element modelling. Such a strategy allows for a more accurate interpretation of structural responses, provides insight into the effects of interventions, and supports the development of more reliable models for future assessment and monitoring of existing bridges. The findings of this study demonstrate that careful consideration of both geometry and boundary conditions is essential for understanding and predicting the dynamic behaviour of complex civil infrastructures. In the next sections, the model update procedure will be presented, starting with manual tuning, followed by automatic model updating, and including the application of the static load term in the objective function.

Manual Tuning

To achieve a more accurate representation of the bridge structure, manual tuning of the finite element model was also performed. This approach considered only the frequencies detected by the accelerometers and involved manually adjusting key model parameters. Essentially, this simulates the work an engineer might do when evaluating a rehabilitation intervention, providing an initial reduction of uncertainties in the numerical model. Additionally, manual tuning can serve as a preliminary step before a fully automated model updating procedure, helping to bring the model parameters closer to realistic values, particularly when using information from experimental tests. The finite element model was developed in MidasGen, using plate (shell) elements for the deck and beam elements for the arches and hangers (Figure 124). This modelling choice was made to capture the dynamic properties of the bridge as accurately as possible, providing a comprehensive representation of its vibration modes and interactions between components. Using shell elements for the deck enables a more detailed description of bending, torsional, and local effects, which are essential when focusing on dynamic behaviour and modal identification. Alternatively, simpler models could be used for other types of analyses. For example, a grillage model of beam elements could be adopted to evaluate structural safety, assess internal forces, or study the effects on individual components more efficiently. Such simplified models are computationally lighter and easier to adjust, but they may not capture all the nuances of the bridge's dynamic response. During the tuning process, only the modal frequencies were used to guide adjustments. The parameters modified included the modulus of elasticity of the arches, tendons, deck, and abutments. Additional attempts were made to adjust the deck density and boundary conditions, exploring their influence on the dynamic response.

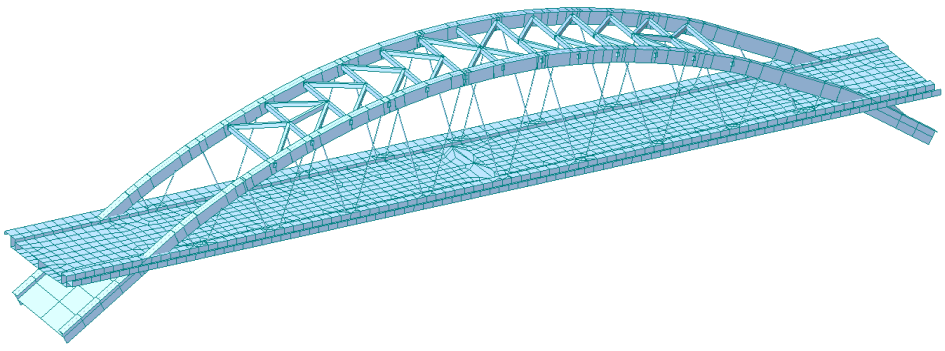

Figure 124: Midas Gen finite element model.

Table 14 summarizes the results of the manual tuning, showing the natural frequencies obtained from the finite element model before and after the adjustments, along with the corresponding deviations from the experimental values. The table demonstrates that manual tuning improved the agreement

between the model and the measured data, reduced the frequency errors, and provided a more representative simulation of the bridge dynamics.

f_ID [Hz]	f_FEM [Hz]	err. before [%]	MAC before	f_FEM_Update [Hz]	err. after [%]	MAC after
3.27	2.69	17.55	0.86	3.15	3.64	0.98
3.39	2.75	18.81	0.74	3.28	3.28	0.99
4.04	3.53	12.73	0.86	4.00	1.18	0.91
4.85	3.58	26.17	0.99	4.53	6.70	0.98
5.26	3.65	30.60	0.97	5.18	1.51	0.96

Table 14: Result of the manual tuning.

Figure 125 shows the mode shapes after manual tuning. The mode shapes provide qualitative validation of the tuning, allowing direct comparison with the experimental modal shapes identified through OMA and illustrating how adjustments to material properties and boundary conditions influenced the dynamic response.

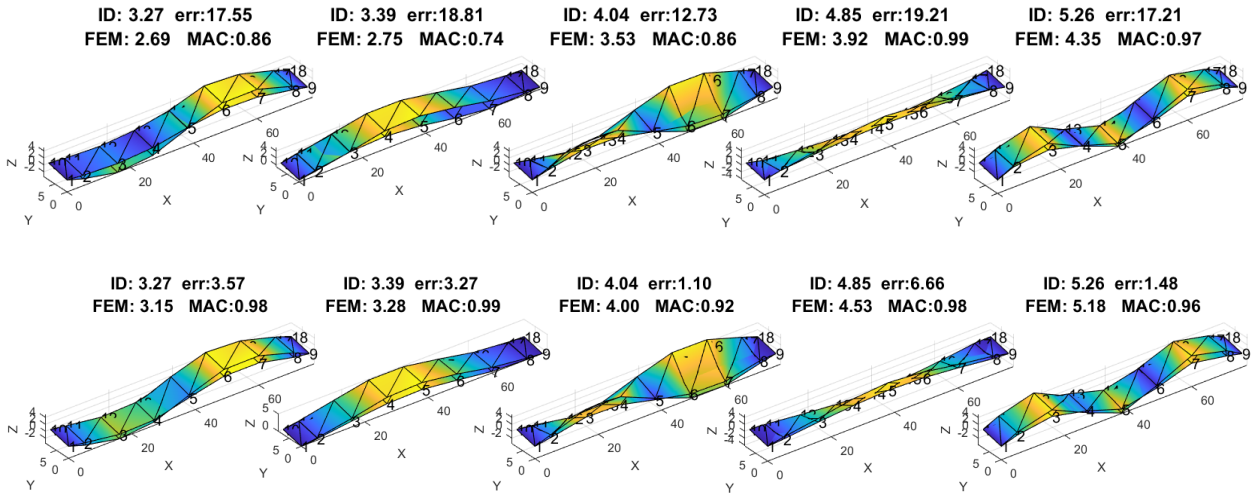

Figure 125: Mode shapes after the manual tuning.

Figure 126 shows the MAC (Modal Assurance Criterion) matrix and the frequency errors before and after manual tuning. The MAC values indicate the correlation between the modelled and experimentally identified mode shapes, confirming that manual tuning significantly improved the model's predictive capability. The reduction in frequency errors further demonstrates that targeted manual adjustments, guided by experimental data, can effectively enhance the accuracy of a finite element model.

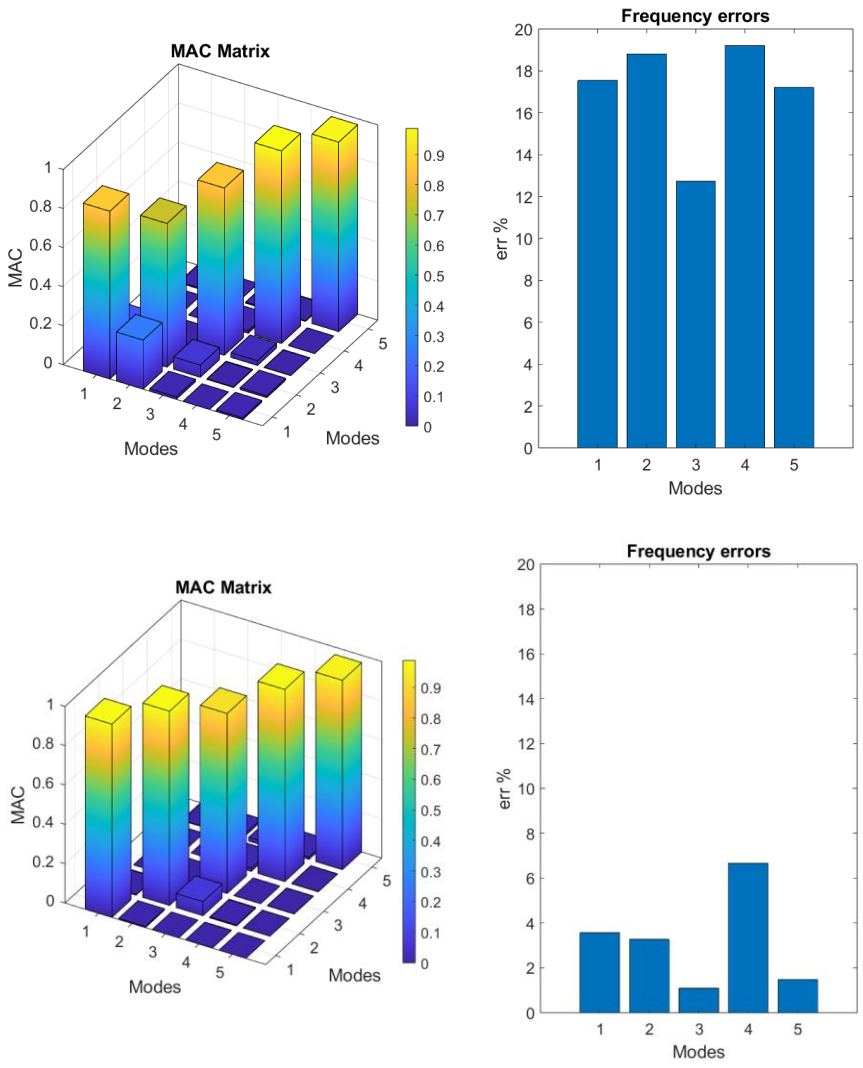

Figure 126: MAC matrix and frequency errors before and after the manual tuning.

The results of the manual tuning show that targeted adjustments of key model parameters, guided by experimental observations, can significantly reduce uncertainties in the finite element model and improve its agreement with measured data. While this approach offers valuable preliminary refinement, it is inherently limited by the subjectivity of parameter selection and reliance on the engineer's judgment. To address these limitations and achieve a more systematic and objective calibration, the study proceeds to an automated finite element model update (FEMU). In this procedure, the experimental modal data are used to define a comprehensive objective function, which includes not only the dynamic properties captured during operational modal analysis but also, in this study, a static term derived from measured displacements. The study aims to determine whether including static information helps constrain the optimization, reduce ambiguities in the solution, and ensure that the updated model more accurately reflects both the dynamic and static behaviour of the bridge.

By combining insights from manual tuning with the robustness of an automated updating procedure, it is possible to generate a refined finite element model that is both reliable and representative, providing a solid foundation for further analyses, safety assessments, and decision-making regarding the bridge's structural health and maintenance strategy.

Automatic Model Update

To further improve the representation of the bridge's dynamic behaviour, an automatic model updating procedure was implemented. A finite element model was reconstructed in STKO using the same element types, geometry, and properties as the previous MidasGen model. This ensured a consistent basis for comparison and facilitated the transfer of manual tuning insights into an automated framework. STKO (Scientific ToolKit for OpenSees) was selected for its robust pre- and post-processing capabilities. It provides an intuitive graphical interface for defining geometry, assigning material and element properties, meshing, boundary conditions, and load cases. The model built in STKO, shown in Figure 127, was then exported as an OpenSees .tcl file. The model uses plate (shell) elements for the deck and beam elements for the arches and hangers, mirroring the MidasGen representation. This setup ensures consistency in comparing results and interpretations between the two software packages.

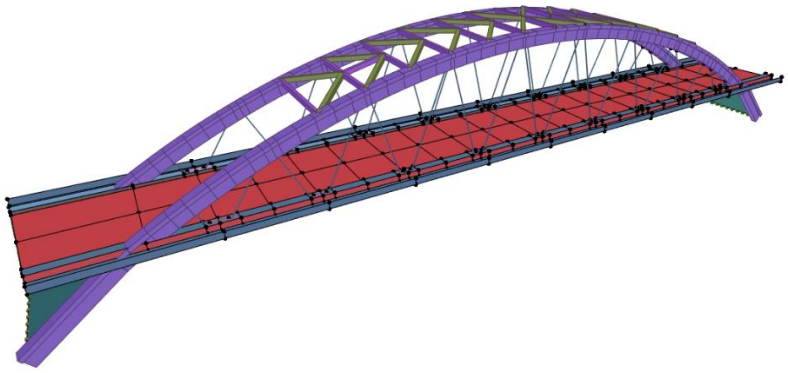

Figure 127: OpenSees (STKO) FE model.

The .tcl files were integrated with a Matlab routine to enable an automatic finite element model update (FEMU) procedure. This combined environment allowed the definition of an iterative procedure in which the model parameters were systematically modified to minimize the discrepancy between the experimental results from the operational modal analysis and the numerical predictions.

Calibration method

The workflow of the procedure, shown in Figure 128, demonstrates how model parameters are optimized by minimizing the discrepancy between identified modal properties from the OMA and the numerical predictions. The workflow illustrates the interaction between Matlab, which manages the optimization loop, OpenSees, which performs the structural analyses, and the experimental data, which serve as the reference for comparison. Before entering the optimization process in Matlab, the parameters are normalized.

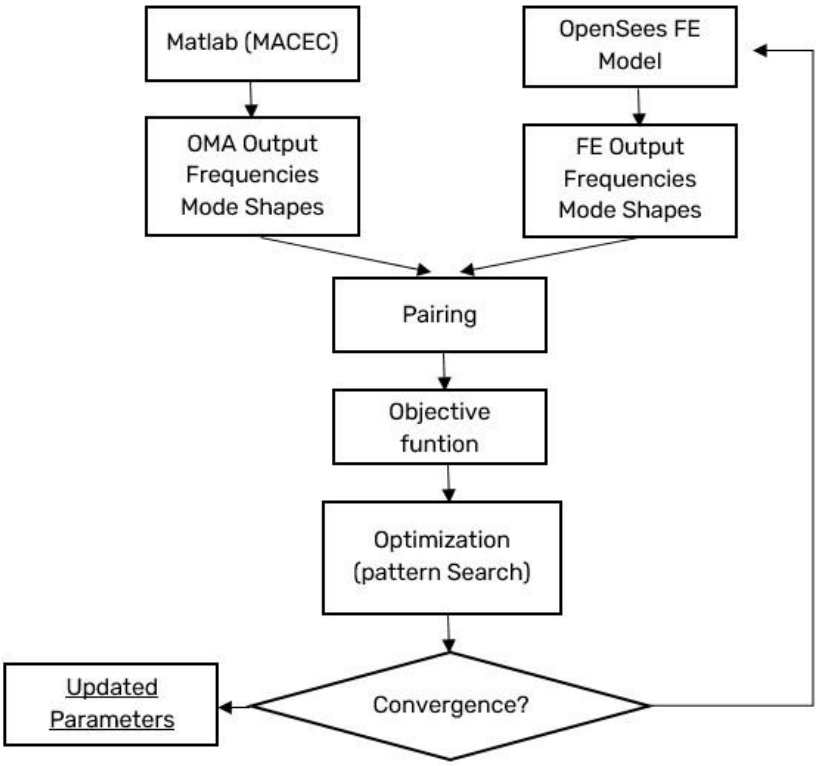

Figure 128: Finite element model update procedure.

The objective function selected for the optimization is the following:

$$\sum_{i=1}^{n} \frac{|f_{ID,i} - f_{FEM,i}|}{f_{ID,i}} + \sum_{i=1}^{n} (1 - MAC(\Phi_i^{ID}, \Phi_i^{FEM}))$$

Here, $f_{ID,i}$ and $f_{FEM,i}$, represent the identified and numerical frequencies, respectively, while $MAC(\Phi_i^{ID}, \Phi_i^{FEM})$ is the Modal Assurance Criterion comparing experimental and numerical mode shapes. The first six frequencies and corresponding mode shapes are used, as they provide a comprehensive snapshot of the bridge's global dynamic characteristics.

After testing several options, the adopted formulation – a linear combination of frequency relative errors and MAC discrepancies – was selected for this application. Its linear structure allows more direct control over the balance between the two contributions, avoiding excessive penalization of outliers while ensuring that both frequency alignment and modal consistency are preserved. Moreover, it simplifies weight adjustment if future analyses focus more heavily on one aspect (e.g., prioritizing frequencies in safety checks or mode shapes in damage localization).

Selection of Updating Parameters

The image below shows the parameters selected for model updating. Each parameter was chosen to capture the main sources of uncertainty in the finite element representation of the bridge and to provide sufficient flexibility during the calibration phase.

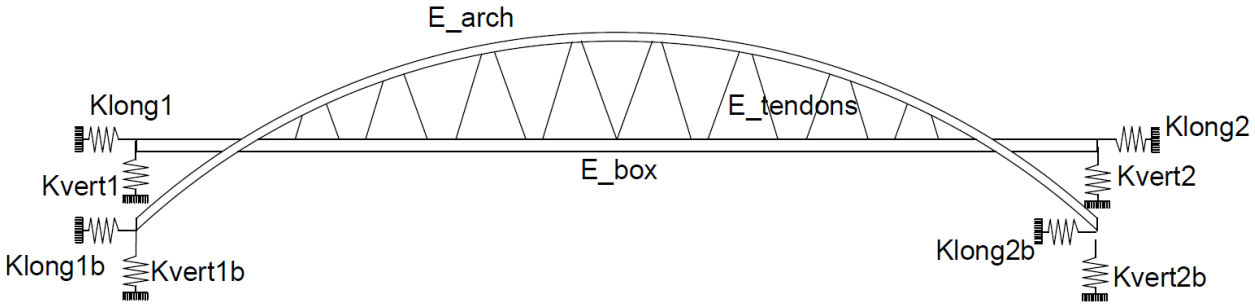

Figure 129: Parameters.

In particular, E_Arch represents the elastic modulus of the arches; E_Tendons refers to the elastic modulus of the hangers; E_Box denotes the elastic modulus of the box-girder section of the deck; and Rho_box corresponds to its density, thus affecting the mass distribution and consequently the dynamic response of the system. The parameter E_Spalla indicates the elastic modulus of the abutments, which could significantly influence the boundary stiffness of the structure. To better account for soil–structure interaction, several ground stiffness components were introduced: K_Vert (vertical stiffness) and K_Long (longitudinal stiffness). In addition, a K_Trasversal component was defined to allow further analyses that explicitly consider the transversal flexibility of the foundations, and K_rot represents rotational stiffness. It should also be noted that the connection stiffness between the hangers and the arch was not considered as an updating parameter. This choice was made because

it is reasonable to assume a rigid connection, given that the tendons are fully embedded in the concrete at both the top and bottom.

This set of parameters, shown in Figure 129, was selected to balance the need for a sufficiently accurate representation of the bridge's dynamic behaviour. At the initial stage, all potentially relevant parameters were included in the updating process. This was a deliberate choice: starting with a broad set of variables allows exploration of the full range of possible influences on the dynamic response and subsequent reduction to the most significant parameters. While an excessive number of updating variables can lead to an ill-posed optimization problem, progressively reducing them allows monitoring of the stability and reliability of the solution.

This approach introduces sections dedicated to sensitivity analysis, where the relative influence of each parameter is examined. This analysis makes it possible to distinguish variables that significantly affect the solution from those with negligible impact, ultimately allowing for the construction of a more robust and parsimonious updating strategy.

Local Sensitivity Analysis

To address model variability, a local sensitivity analysis was performed to assess the influence of individual input parameters on the model response. This approach involves varying one parameter at a time within a defined range while keeping all other parameters fixed at their nominal values. The objective is to quantify the sensitivity of the output to small or moderate changes in each parameter, isolating the direct effect of that parameter on system behaviour. The methodology consists of the following steps. For each parameter Xk:

- All other parameters are held constant at their nominal or baseline values.
- The parameter Xk is systematically varied between its minimum and maximum prescribed bounds.
- The corresponding variation in the output feature y is monitored and analysed.

This process is repeated for each parameter in the model, enabling both qualitative and quantitative comparisons of their individual impacts. Figure 130 shows the results of the local sensitivity analysis performed using the procedure described above. The X-axis represents the parameters, while the Y-axis shows the values of the points representing the frequency values at the parameter levels. It can be observed that the parameters with the greatest influence on the solution are the elastic modulus of the arch, the elastic modulus of the hangers, the density of the box girder, and its elastic modulus. In

some cases, certain boundary conditions representing soil stiffness, such as the longitudinal stiffness K and the vertical stiffness K, also make a significant contribution.

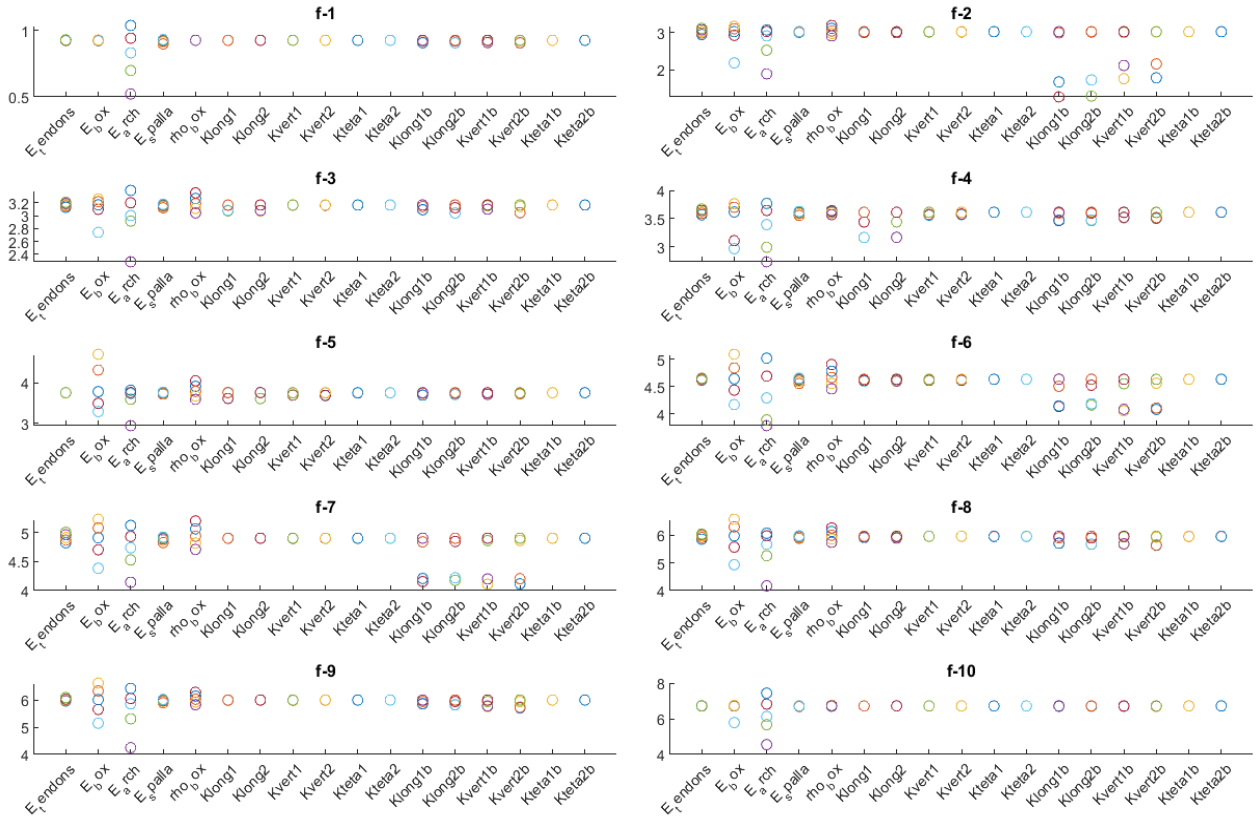

Figure 130: Result of local sensibility analysis.

The main advantage of this approach is its simple implementation, making it suitable for quick evaluations even in complex models. By varying one parameter at a time, it offers an intuitive understanding of how each parameter individually affects the system response. This method is especially useful for preliminary screening or when computational resources are limited, as it requires fewer simulations than more complex global sensitivity analyses. However, the technique is inherently limited to capturing only local effects near the nominal configuration of the model. It does not account for possible interactions between parameters or provide information on the combined or nonlinear influence that multiple parameters may exert simultaneously. As a result, this method may underestimate the impact of parameters involved in nonlinear, coupled, or highly interactive phenomena. In this work, local sensitivity analysis was used as a preliminary step to identify parameters with potentially significant influence, which were then further investigated through global variance decomposition and R2 estimation based on Design of Experiments.

ANOVA- Global Sensitivity Analysis Procedure

To evaluate the influence of model parameters on the response variability of the Finite Element (FEM) model, a Global Sensitivity Analysis was performed.

Design of Experiments

Design of Experiments (DoE) is a structured methodology for systematically planning, executing, and analysing simulations or physical experiments to efficiently explore the influence of multiple input factors on system responses. In the context of numerical models, DoE enables identification of the most significant parameters, quantifies their effects, and supports model calibration, uncertainty quantification, and sensitivity analysis. Depending on problem complexity and computational resources, different experimental designs can be used, including:

- Full-factorial designs, where all possible combinations of input levels are tested, ensuring maximal coverage but at high computational cost.
- Fractional-factorial or orthogonal arrays, which reduce the number of runs while preserving statistical independence between factors.
- Central Composite Designs (CCD) or Latin Hypercube Sampling (LHS), suitable for exploring nonlinearities or higher-dimensional parameter spaces.

In this work, DoE was applied to efficiently explore the input space of the finite element model, enabling the decomposition of output variance and the computation of sensitivity indices such as the generalized coefficient of determination R^2.

Example of Full-factorial Design

To better understand how the procedure works, an example of full factorial design is provided. A Full-factorial design explores all combinations of parameter levels, providing a complete picture of main effects and interactions. Suppose a finite element model is influenced by:

- X1: fiber orientation angle [Low = -5°, High = +5°].
- X2: Young's modulus [Low = 130 GPa, High = 140 GPa].

A Full-factorial 2 levels design includes all 2^2=4 possible combinations:

Run	X1 (Fiber Angle)	X2 (Elasticity Modulus)
1	-5°	130 GPa
2	-5°	140 GPa
3	+5°	130 GPa
4	+5°	140 GPa

Table 15: Example of full factorial design, 2 levels.

Or in a case of a three levels full factorial:

Parameters:

- X1 = [−5°, 0°, +5°]
- X2 = [130 GPa, 135 GPa, 140 GPa]

Total combinations: 3^2 = 9

Run	X1 (Angle)	X2 (Modulus)
1	−5°	130 GPa
2	−5°	135 GPa
3	−5°	140 GPa
4	0°	130 GPa
5	0°	135 GPa
6	0°	140 GPa
7	+5°	130 GPa
8	+5°	135 GPa
9	+5°	140 GPa

Table 16: Example of full factorial design, 3 levels.

The output (e.g., natural frequency) is computed for each combination, and the data are used to estimate the influence of each parameter and their interactions using variance decomposition and sensitivity indices. The full-factorial design offers several advantages, as it enables complete estimation of all main effects and interaction terms, making it possible to clearly identify the most influential parameters and interpret the results straightforwardly. However, this approach also has some limitations. In particular, the number of required simulations increases exponentially with the number of factors (2^n), making the method computationally expensive when dealing with large models or many parameters.

Analysis of Variance (ANOVA)

ANOVA decomposes the total variance of the model output into contributions from each parameter and their interactions. To quantify the influence of discrete input parameters on the variability of numerical model outputs, a variance decomposition approach based on the Analysis of Variance (ANOVA) framework was used. This method identifies the most significant factors controlling output dispersion and allows computation of a generalized coefficient of determination, denoted as R^2. The total variance of a selected output feature y can be decomposed as:

$$\sigma^2(y) = \sigma^2(E[\,y \mid X_k\,]) + E\big(\sigma^2(\,y \mid X_k\,)\big)$$

Where:

- $\sigma^2(y)$ is the total variance of the output.
- $\sigma^2(E[\,y \mid X_k\,])$ represents the variance explained by the input parameter X_k.
- $E\big(\sigma^2(\,y \mid X_k\,)\big)$ is the residual variance, i.e., the portion of variability that remains unexplained after accounting for X_k.

Based on this decomposition, the generalized coefficient of determination R^2 is defined as:

$$R_k^2 = \frac{\sigma^2(E[\,y \mid X_k\,])}{\sigma^2(y)} = 1 - \frac{E\big(\sigma^2(\,y \mid X_k\,)\big)}{\sigma^2(y)}$$

This coefficient expresses the fraction of the total output variance that can be attributed to the selected parameter X_k.Values of R^2 close to 1 indicate that the parameter has a strong influence on the output, whereas values close to 0 suggest negligible influence.

Figure 131 illustrates the fundamental concept of ANOVA. The total variability observed in the data can be divided into two main components: variability within groups and variability between groups, relative to the overall mean. The term "within" refers to the spread of data within each group, measuring how much individual observations differ from their group mean. These differences often result from random fluctuations, measurement uncertainties, or inherent variability in the system studied. The term "between" captures how much the group means differ from the overall mean, reflecting the effect of the factor under investigation. If the group means are far apart, the between-group variability will be large, indicating that the factor (such as a material property, construction method, or experimental condition) plays a significant role in explaining the observed differences.

ANOVA compares these two sources of variability. If the between-group variability is substantially greater than the within-group variability, the analysis provides evidence that the factor being tested has a statistically significant effect, rather than the observed differences being due to random noise alone.

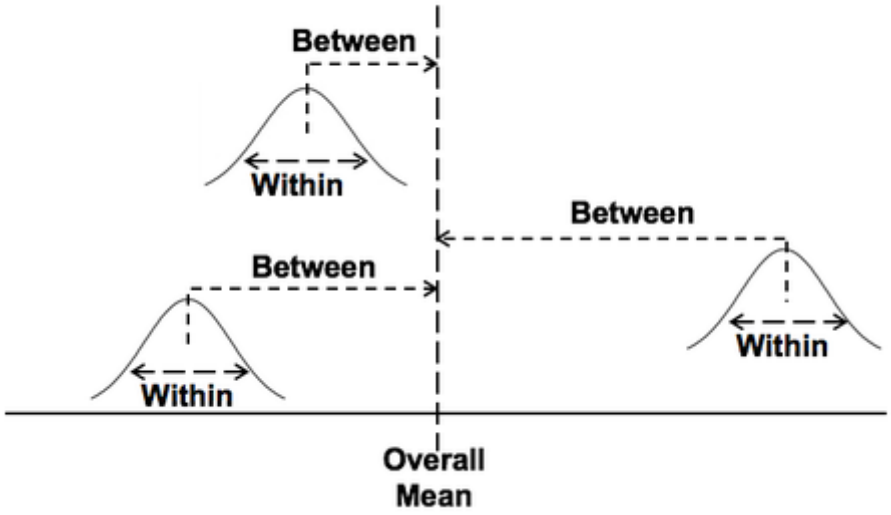

Figure 131: Representation of ANOVA meaning.

In practice, the quantities involved are estimated based on the results of a Design of Experiments (DoE) campaign, grouping the simulation outputs according to the levels of the parameter X_k, and applying the following expressions:

- The total variance is computed as:

$$\sigma^2(y) = \frac{1}{N-1}\sum_{i=1}^{N}(y_i - \bar{y})^2$$

- The residual variance, corresponding to intra-group variability, is computed as:

$$E\left(\sigma^2(y \mid X_k)\right) = \frac{1}{N-1}\sum_{j=1}^{N_{levels}}\sum_{i=1}^{n_j}\left(y_i^{(j)} - \overline{y^{(j)}}\right)^2$$

Where:

- N is the total number of simulations.
- $N_{levels}$is the number of distinct levels of the parameter X_k.
- n_j is the number of simulations associated with level *j*.
- $\overline{y^{(j)}}$ is the mean output for group *j*.
- $y_i^{(j)}$s the overall mean output.

Once these quantities are computed, the R^2 statistic provides a quantitative measure of the impact of X_k on the variability of the model response. This methodology has been implemented to analyse the sensitivity of the selected output features (e.g., natural frequencies, modal displacements) to different input parameters in the finite element model, with the goal of identifying the most influential variables for subsequent uncertainty quantification or model calibration activities. The procedure was implemented in MATLAB by adapting the built-in function *anova1* into a script.

The results of the ANOVA-based approach for the selected updating parameters on the dynamic response of the bridge model are presented. The parameters considered, along with their upper and lower bounds, are shown in Table 17. These include the elastic moduli of the main structural components (arches, tendons, and box), the density of the box, and the stiffness values of the longitudinal springs at the abutments.

Parameters	**Levels**	
	-1	1
E_Tendons	195000	230000
E_Box	20000	50000
E_Arch	20000	50000
E_Spalla	20000	50000
rho_box	2000	2700
Klong1	1.00E+06	1.00E+10
Klong2	1.00E+06	1.00E+10
Kvert1	1.00E+06	1.00E+10
Kvert2	1.00E+06	1.00E+10
Kteta1	1.00E+08	1.00E+14
Kteta2	1.00E+08	1.00E+14
Klong1b	1.00E+06	1.00E+10
Klong2b	1.00E+06	1.00E+10
Kvert1b	1.00E+06	1.00E+10
Kvert2b	1.00E+06	1.00E+10
Kteta1b	1.00E+08	1.00E+14
Kteta2b	1.00E+08	1.00E+14

Table 17: Parameters limits for ANOVA.

Figure 132 shows the determination coefficient (R^2) for each parameter and for each of the first ten natural frequencies. The parameters E_Arch and E_Box have the greatest influence, with contributions above 0.7–0.9 for certain modes, especially the first mode, which is the only arch mode and is governed purely by E_Arch. This result indicates that the stiffness of the arch plays a dominant role in governing the global dynamic behaviour of the bridge. The density of the box (rho_box) and

the longitudinal stiffnesses (Klong1b, Klong2b) have a more moderate but still significant effect. In contrast, E_Tendons shows minimal impact across all modes.

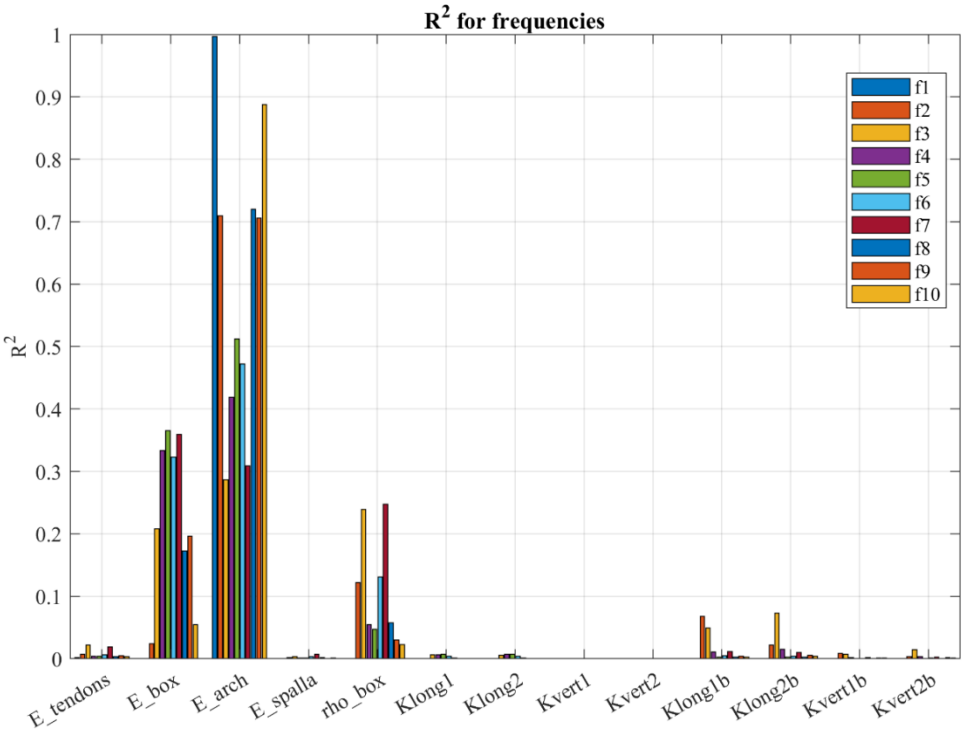

Figure 132: R^2 for the first 10 frequency

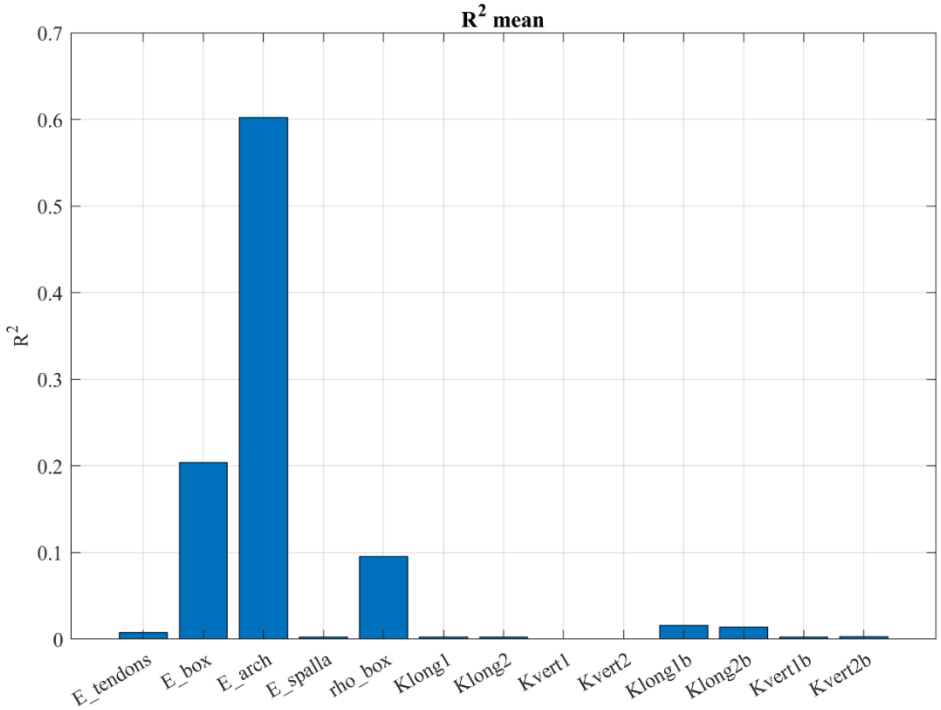

Figure 133: R^2 mean for the first 10 frequency

By averaging across all modes, the relative importance of the parameters becomes clearer. Here, E_Arch emerges as the most influential factor, with a mean R^2 of about 0.6. The contribution of E_Box is also significant (about 0.2), while rho_box plays a secondary but noticeable role. The other parameters remain negligible, except for the base longitudinal stiffness.

Restricting the analysis to the central modes (f2–f6) highlights some additional details. In this range, E_Arch remains a key parameter, but rho_box and E_Box gain importance. This suggests that, by excluding the first mode, which is related only to the arch, the girder becomes more important in the response.

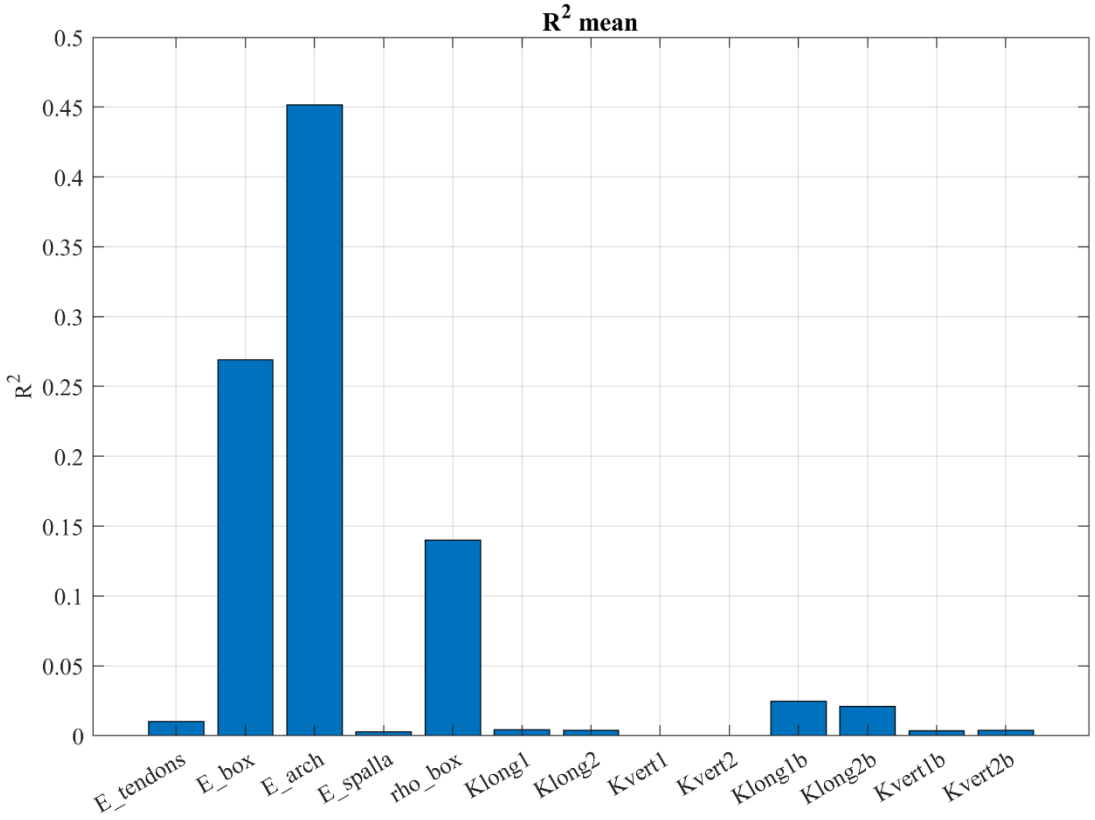

Figure 134: R^2 mean for frequency from 2 to 6

When the analysis is extended to include the mode shapes using the MAC (Modal Assurance Criterion), the relative contributions shift slightly. The K_Long parameters gain more weight in the sensitivity analysis. This aligns with the physical role of the longitudinal stiffness of the abutments, which influences the global deformation pattern of the structure and, consequently, the mode shapes. Although their effect on natural frequencies alone is limited, they become more significant when considering both frequency and shape together.

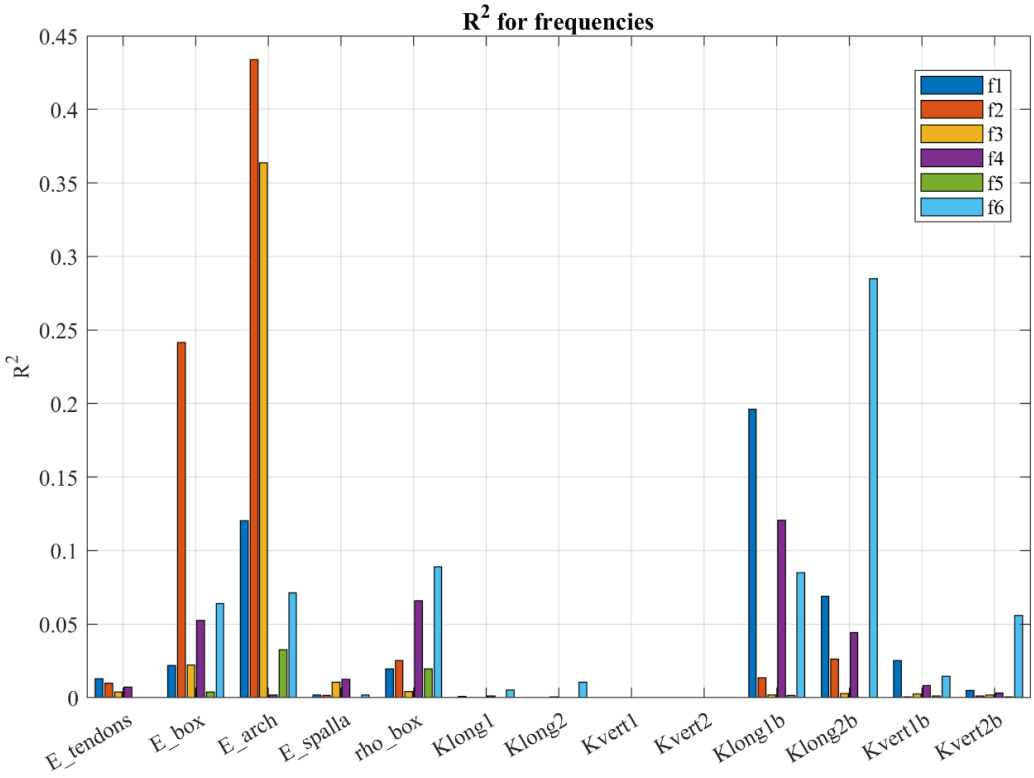

Figure 135: R^2 for frequency considering MAC

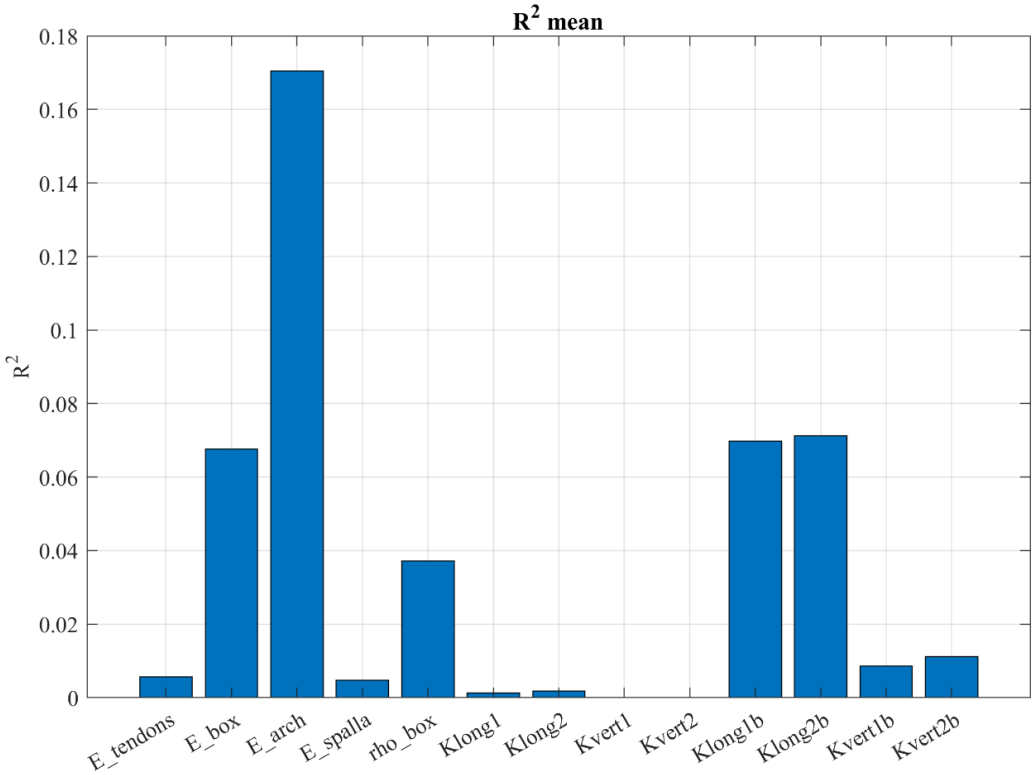

Figure 136: R^2 mean considering MAC

The ANOVA results confirm that E_Arch is the most critical parameter to calibrate, followed by E_Box and, to a lesser extent, rho_box. The stiffness of the longitudinal supports (Klong1b, Klong2b) becomes more relevant when the MAC is introduced, which justifies their inclusion in the updating procedure. Conversely, the modulus of elasticity of the tendons has little effect on the global dynamic response, reflecting the relatively secondary role of these elements in the overall modal behaviour of the bridge. This analysis guided the selection of parameters to retain for the optimization, balancing accuracy and the well-posedness of the problem.

Update results

The optimization was performed using the parameters previously identified through the ANOVA sensitivity analysis, which allowed the update to focus on the most influential variables. The updating procedure used the Matlab Pattern Search algorithm. After several preliminary tests to determine the most suitable settings, five different starting points were used, and the best result is reported here. Figure 137 shows the result of the algorithm, specifically the window containing the four control figures used during the optimization process.

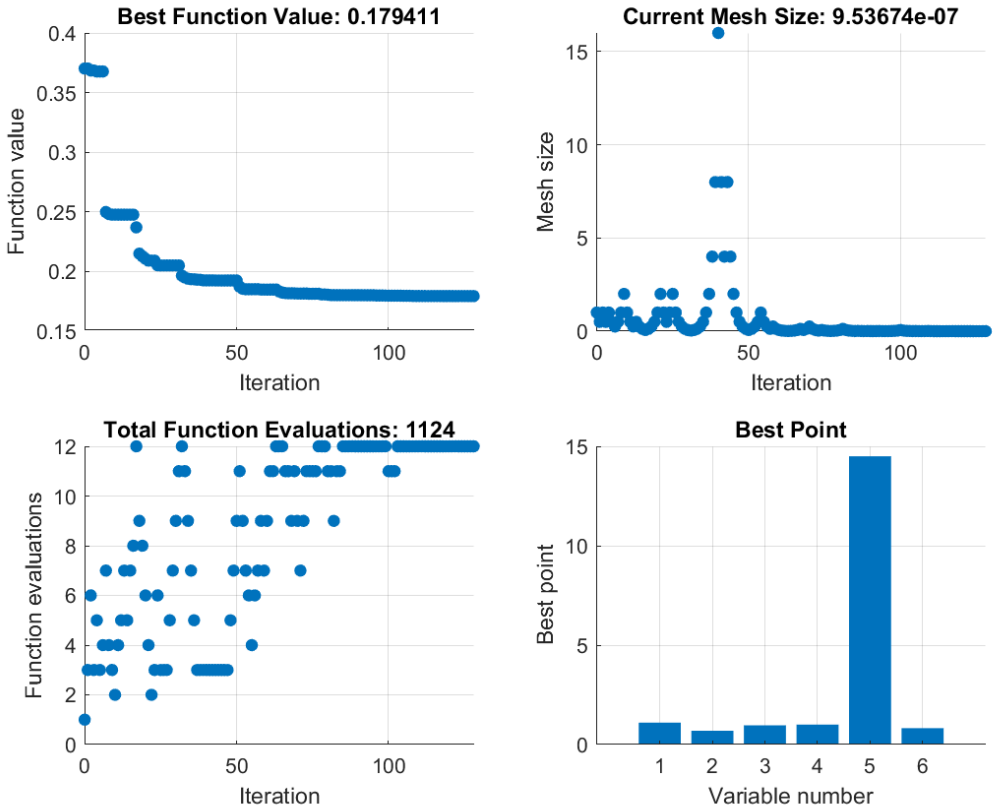

Figure 137: Control charts during optimization process, final step.

The updated values are reported in Table 18, along with the corresponding initial assumptions. The following sections present additional results, including an evaluation of the effect of progressively reducing the number of updating parameters to assess the stability and reliability of the optimization process, as well as the same analysis performed with different algorithms to ensure reliable results.

Parameters	Initial Value	Updated Value
E_Tendons [MPa]	205000	225420
E_Box [MPa]	40000	27881
E_Arch [MPa]	45000	43330
rho_box [kg/m^3]	2500	2500
Klong1b [N/mm]	1E+08	9.3E+08
Klong2b [N/mm]	1E+08	3.9E+08

Table 18: Result of update procedure.

Figure 138 shows the individual mode shapes, visualizing the eight lowest frequency modes of the structure both before and after the update. The ID and FEM values represent the experimental and updated model frequencies, respectively, while 'err' indicates the percentage error. The MAC values confirm a high degree of consistency between the updated model and the experimental results. The chart on the left in Figure 139, the MAC Matrix, shows the cross-correlation between the first ten modes of the updated model. The high values along the main diagonal indicate that each mode of the model is well-correlated with itself and not with other modes. The chart on the right presents the frequency errors, showing that after the update, the frequency errors for all modes are less than 2.5%, which is a good result in engineering practice.

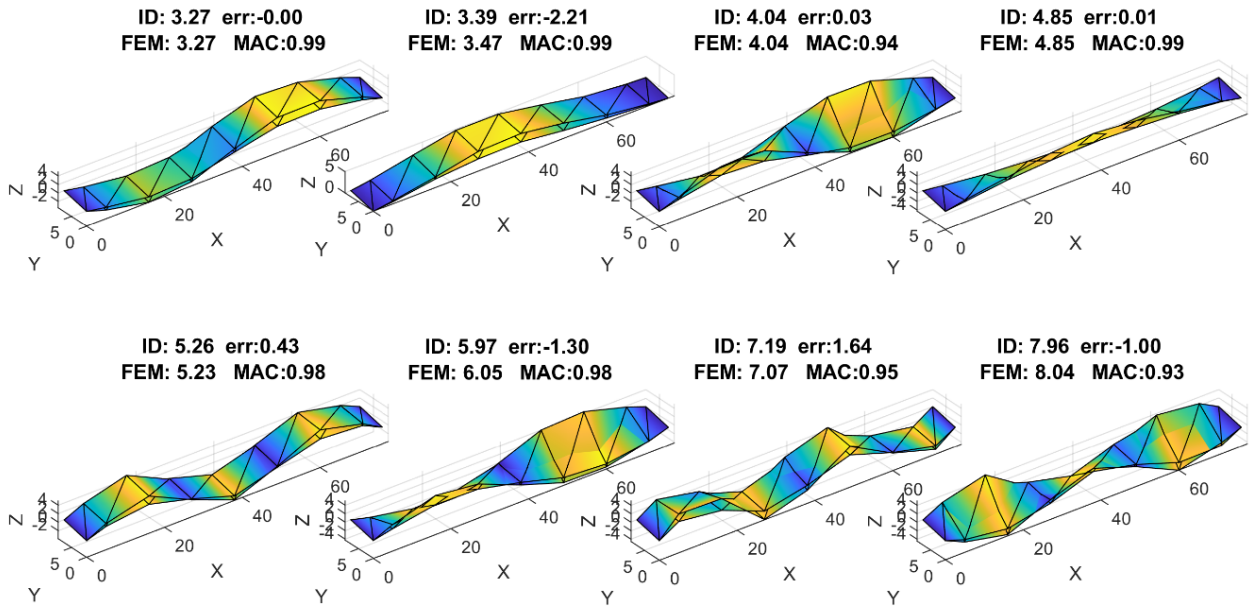

Figure 138: Mode shapes pre and post update procedure.

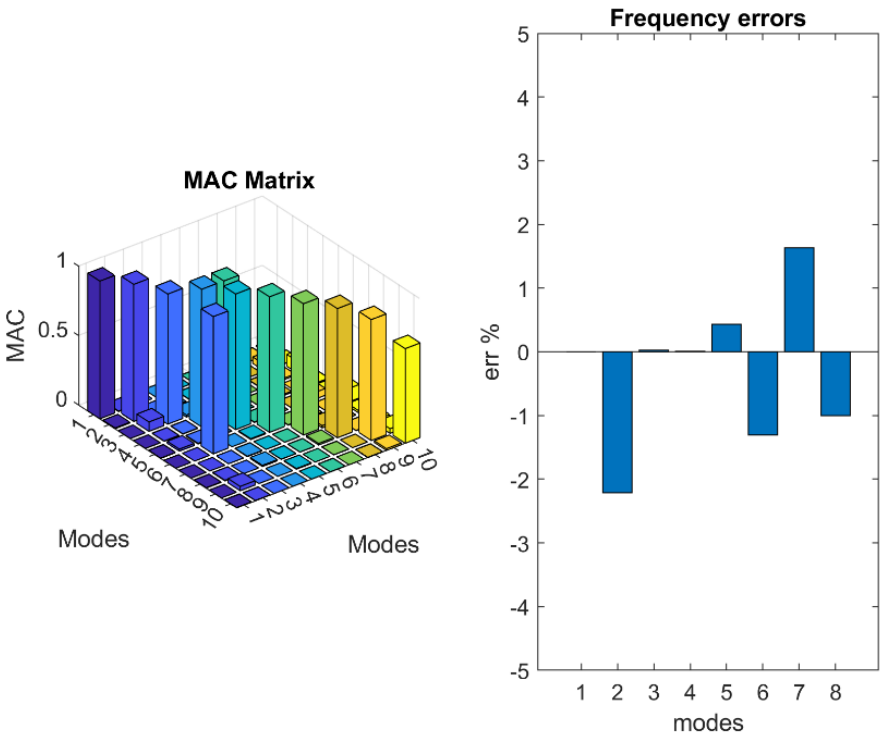

Figure 139: MAC Matrix end frequencies errors.

The results from the model update are considered good, partly due to the small errors and the fact that the updated parameter values are physically meaningful. This demonstrates the effectiveness of the optimization process. The bar charts in Figure 140 (top) compare the model's accuracy before and after the update. The plot shows that frequency errors have been significantly reduced for all modes. While some modes, such as modes 6 and 8, still have slight errors, the overall improvement is clear. The bottom plot, which displays the Modal Assurance Criterion (MAC) values, shows how well the updated model's mode shapes match the experimental data. For every mode, the MAC value is close to or greater than 0.9, which is excellent and confirms a strong correlation between the model and the real-world measurements.

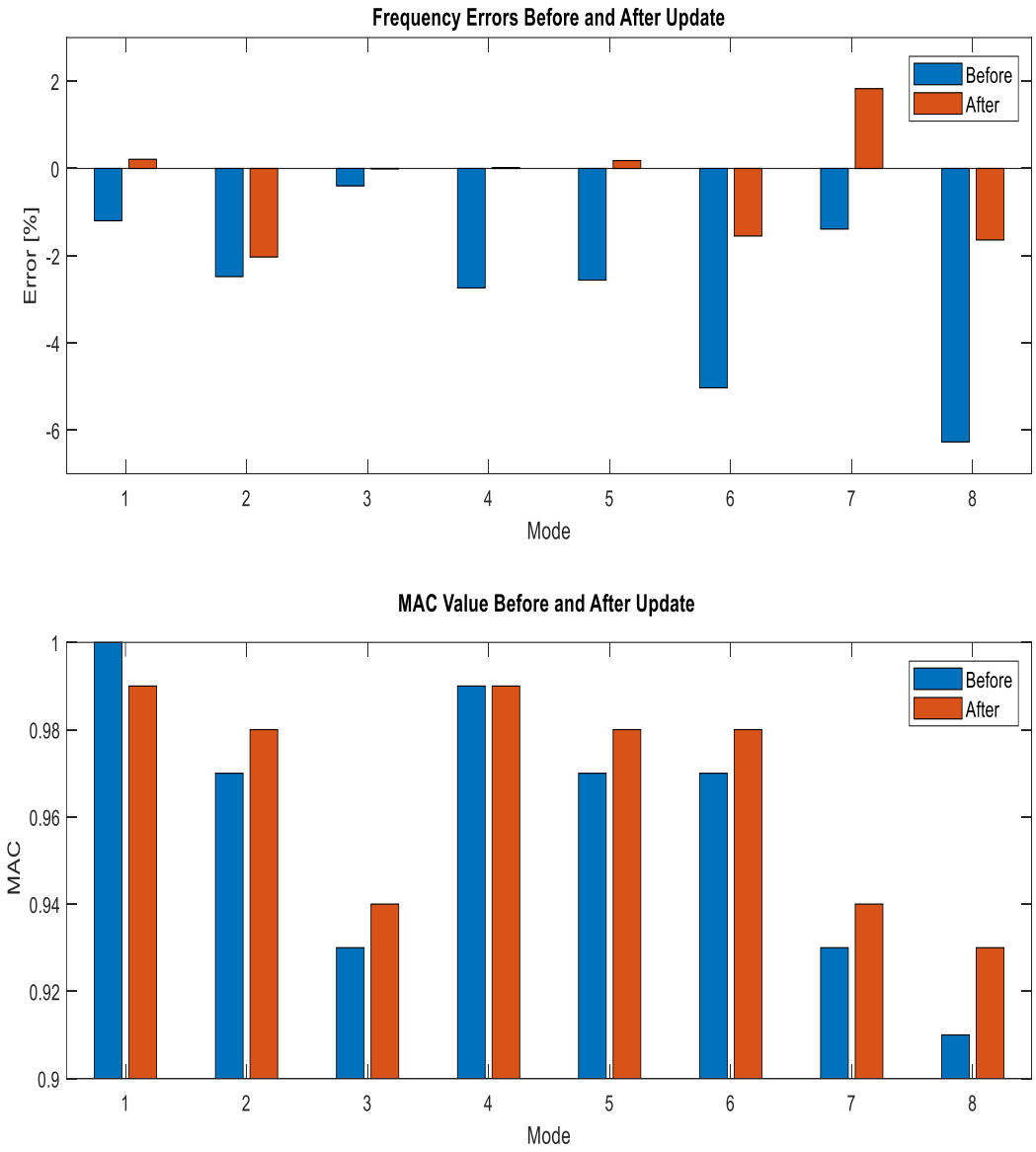

Figure 140: Frequency errors (above) and MAC pre and post the update procedure (below).

The results highlight good agreement between the updated model and the experimental data. The updated parameters remain within physically reasonable ranges. In particular, the elastic modulus of the tendons, although slightly higher than the initial estimate, is consistent with the structural configuration, since the contribution of the concrete infill layer and the external steel sheath was not explicitly modelled. Similarly, the values obtained for the longitudinal stiffnesses of the abutments reflect a realistic interaction between the bridge and the boundary soil. A high value for the modulus of elasticity of the arch is also confirmed by the previously presented in situ test.

Difference between updated and original model

After presenting the results for frequency differences, a further comparison is conducted to evaluate additional structural parameters before and after the model update. This analysis quantifies how certain parameters are affected by the updating process and assesses potential errors that may result from using a model with parameters not fully representative of the actual structure. To this end, specific actions and displacements were examined for thorough verification, as reported in Table 19.

	Load			**PP**		
	Model Pre-Update	**Model Post-Update**	**Diff**	**Model Pre-Update**	**Model post-update**	**Diff**
N max arch [kN]	-1680	-1700	-1.2%	-7550	-7690	-1.9%
M+ max arch [kNm]	207	242	-16.9%	1160	1140	1.7%
M- max Arch [kNm	332	378	-13.9%	-665	-709	-6.6%
Max sigma box [MPa]	197	198	-0.5%	493	364	26.2%
Max N tendons [kN]	312	321	-2.9%	795	759	4.5%
Nmin tendons [kN]	-162	-166	-2.5%	-367	-263	28.3%
Max Disp [mm]	9.54	8.83	7.4%	31.10	25.90	16.7%

Table 19: Differences in structural quantities between updated and non-updated model.

The comparison between the pre- and post-update models highlights several important aspects of the structural response under two different load conditions: the self-weight load and a distributed load applied at midspan. Overall, the differences in axial forces for the arch are relatively small, generally within a few percent. The bending moment under the PP load shows a higher variation, with a maximum difference of 16.9% for the positive bending under this load condition. Significant changes are observed in certain parameters of the box girder and the tendons. In particular, the maximum stress in the box girder under the PP load decreases by 26.2%, reflecting a redistribution of internal forces after updating. Similarly, the minimum axial force in the tendons under the PP load changes by 28.3%, suggesting that the updated parameters capture the stiffness along the bridge differently. The maximum displacements are also affected: the midspan deflection under the PP load is reduced by 16.7%, while the deflection under the first load case decreases by 7.4%. These results confirm that the updated model provides a more accurate representation of the bridge's behaviour, capturing the influence of updated stiffness parameters and better reflecting the actual structural performance. Beyond the static load cases considered, the comparison can also be extended to response spectrum analyses. Since the results of such analyses are directly influenced by the natural frequencies, mode shapes, and modal participation factors, any changes in these parameters between the pre- and post-

update models could lead to significant differences in the calculated actions. Therefore, using the pre-update model for a response spectrum analysis could potentially produce inaccurate results, highlighting the importance of updating the model to ensure a reliable representation of the bridge's dynamic behaviour.

Optimization with Genetic Algorithm and Simulated Annealing

To further assess the reliability and robustness of the updating procedure, different optimization algorithms were tested and compared, and the procedure was extended to ten different starting points. The purpose of this analysis is to evaluate the consistency of the obtained solutions and to verify whether the identified parameter set corresponds to a global optimum rather than being influenced by algorithm-specific convergence paths. By comparing the performance of multiple algorithms, additional confidence in the quality of the update can be achieved. The comparative analysis was carried out using two algorithms: Simulated Annealing (SA) and Genetic Algorithm (GA). Both algorithms were tested under different parameter configurations to reproduce three distinct search strategies. In the first case, the settings were chosen to favour a more global exploration of the parameter space, allowing the algorithms to investigate wide regions and avoid premature convergence. A second configuration was designed as a balanced search, combining exploration and exploitation to achieve a compromise between robustness and efficiency. Finally, a more conservative setup was adopted to simulate a local search, aimed primarily at refining already promising solutions and improving convergence near good candidate points. This preliminary investigation was not intended to provide an exhaustive parametric study, but rather to establish rational criteria for setting the main control parameters of the algorithms (such as initial temperature, annealing and reannealing functions, population size, crossover rate, mutation function, maximum number of iterations, and function tolerance) and to calibrate the algorithms according to the specific features of the optimization problem under investigation. After this comparative phase, two final configurations were selected as the most suitable for the validation analysis:

- **Simulated Annealing (SA)**
  - Initial temperature: 0.2
  - Temperature function: @temperatureboltz
  - Annealing function: @annealingboltz
  - Reannealing interval: 100
  - Maximum iterations: 1500
  - Maximum function evaluations: 4000
  - Function tolerance: 1e-4

- **Genetic Algorithm (GA)**
  - Population size: 50
  - Crossover fraction: 0.8
  - Mutation function: @mutationgaussian with parameters [0.1, 0.4]
  - Elite count: 5
  - Maximum generations: 100
  - Maximum stall generations: 30
  - Function tolerance: 1e-4
  - Maximum execution time: 3 hours

For the Genetic Algorithm, a time-based stopping criterion was introduced due to the long computational times observed during the trials. For the Simulated Annealing algorithm, a stopping criterion based on the number of iterations was set according to the results obtained during the preliminary runs. It was observed that after a certain number of iterations, the algorithm had already reached the minimum but continued to run excessively, remaining stuck at the same solution without actually achieving convergence on the objective function. All configurations were executed with normalized parameters and bounds. In Figure 141 and the table, it can be observed that all algorithms obtain similar solutions; for SA, the solution is more stable than for PS and GA. The best solution in terms of updated parameters is practically the same for all algorithms, and the residuals are very similar. What changes is the computational time: for PS, it is 1.5 hours, while for GA and SA, the time is more than 3 hours. For GA, this can be considered significant, while for SA, the solution remains stable even after the selected number of iterations, and the time is approximately 3 hours. Note that the solution for pattern search is slightly different compared to what was provided in the previous section because the extended procedure with 10 xo led to a slightly better solution, which will be presented for clarity in the next section.

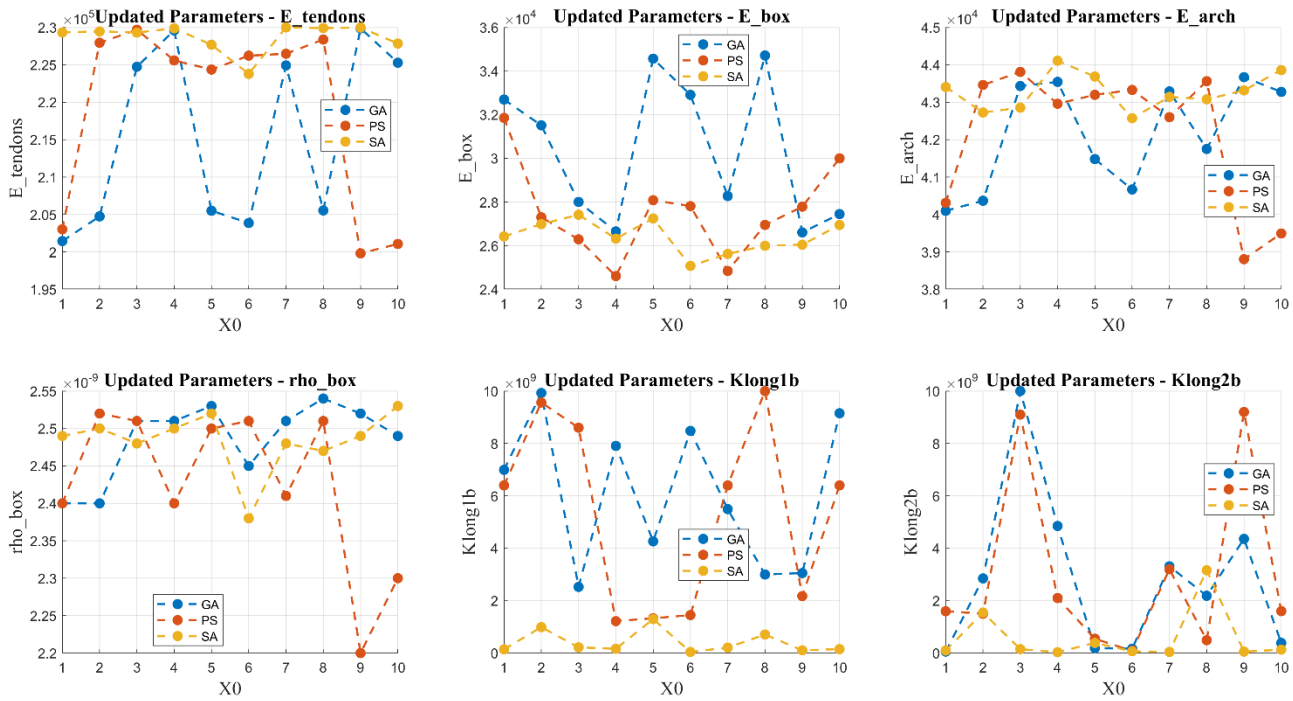

Figure 141: Result of the update procedure with three different algorithms, Pattern Search (PS), Genetic Algorithm (GA) and Simulated Annealing (SA).

	Pattern Search	Simulated Annealing	Genetic Algorithm
Residual	0.1794	0.1825	0.1804
Computational Time	1.5 hours	3 hours	> 3 hours
Updated Par			
E_Tendons [MPa]	226221	229328	225280
E_Box [MPa]	27815	26426	27450
E_Arch [MPa]	43329	43407	43277
rho_box [kg/m^3]	2510	2490	2490
Klong1b [N/mm]	1.45E+09	1.43E+08	9.15E+09
Klong2b [N/mm]	8.20E+07	9.72E+07	3.86E+08

Table 20: Result of update using different algorithms, six parameters.

The same procedure using the three algorithms – Pattern Search, Genetic Algorithm, and Simulated Annealing – was also applied to the case with the three most significant parameters. The solution and results are essentially the same, as shown in the corresponding Figure 142 and table. In this case, all three algorithms converge to comparable solutions. The main difference is in computational time: while the Genetic Algorithm and Simulated Annealing require significantly longer execution times, Pattern Search reaches the same solution in 0.6 hours.

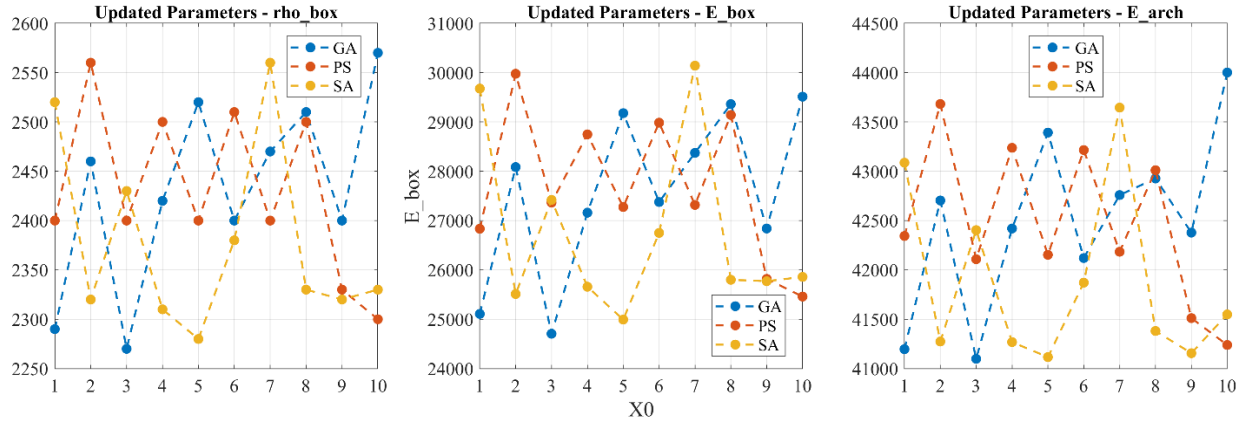

Figure 142: Frequency errors (above) and MAC pre and post the update procedure

	Patter Search	Simulated Annealing	Genetic Algorithm
Residual	0.1989	0.1978	0.1975
Computational Time	0.6 hours	3.3 hours	3.6 hours
Updated Par			
rho_box [kg/m3]	2300	2280	2290
E_Box [MPa]	25459	24993	25107
E_Arch [MPa]	41239	41116	41197

Table 21: Result of update using different algorithms, three parameters.

Differences with different numbers of updated parameters

To investigate how the number of updating parameters affects result quality, several optimization runs were conducted with progressively fewer parameters. Starting with the full model of 17 parameters, the number of variables was gradually reduced to 13, 8, 6, and finally 3, to assess how this reduction influenced both solution accuracy and computational cost. The rationale is that too many parameters may cause overfitting and ill-posed problems, while a smaller, well-chosen set can provide stable, physically meaningful solutions with much lower computational times. The update procedure was also initialized from five different starting points, selected based on engineering judgment. These included average values of the elastic moduli, parameters from in-situ tests, and other reasonable assumptions, to determine whether the algorithm would consistently converge to the same solution. The following figures show the best case among the different starting points.
The update was made using all parameters to find the best solution. When all 17 parameters were considered, the update matched the identified modal data, although this required high computational cost.

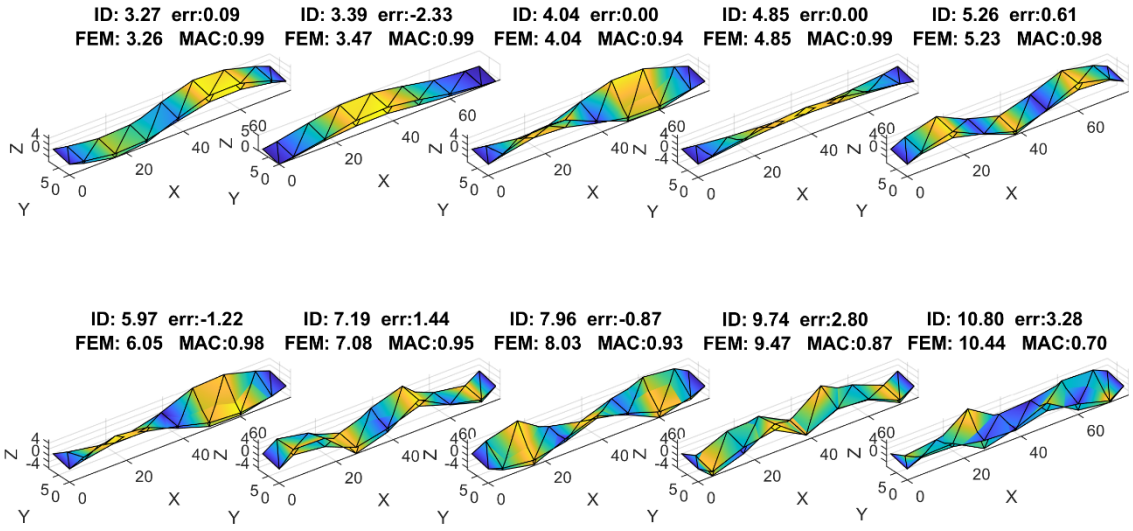

Figure 143: Result of update procedure considering 17 parameters.

The number of parameters was then reduced to 13, as also supported by sensitivity analysis. The assumption of fixed arches and a simply supported deck was verified, and additional tests with the FE model confirmed that using high rotational stiffness produced equivalent results in terms of moment distribution.

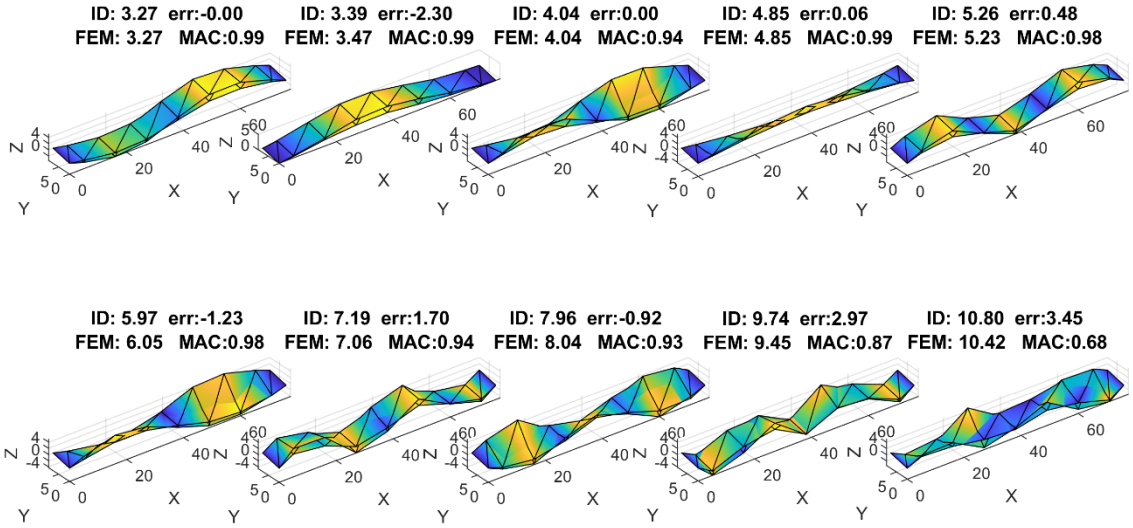

Figure 144: Result of update procedure considering 13 parameters.

After that passage, the update was performed with eight parameters, taking into account the results of the ANOVA and also including the parameters K_vert1 and K_vert2 to assess the influence of the deck's supporting stiffness.

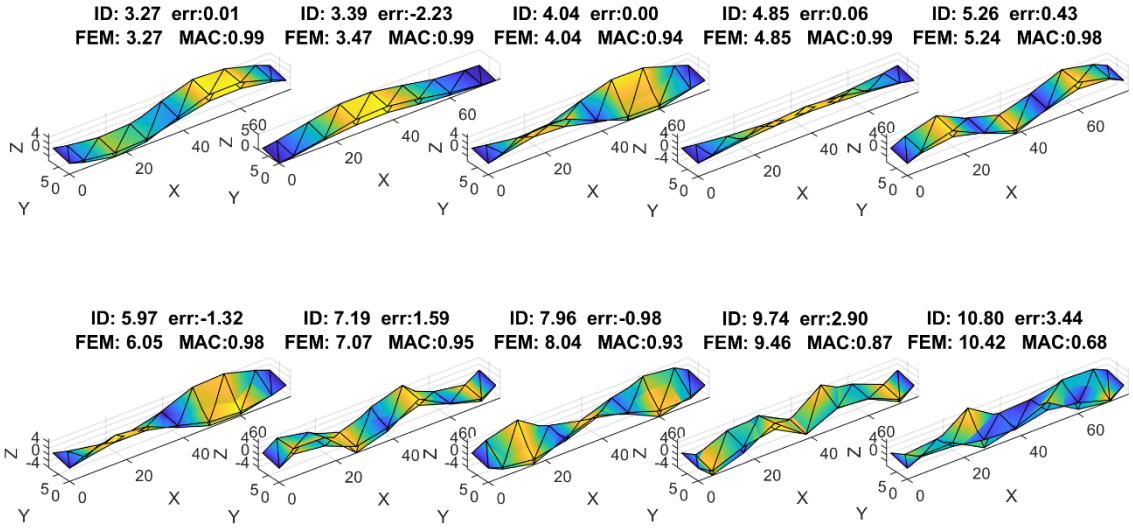

Figure 145: Result of update procedure considering 8 parameters.

Then removing the parameters with less influence 6 parameters model update was done.

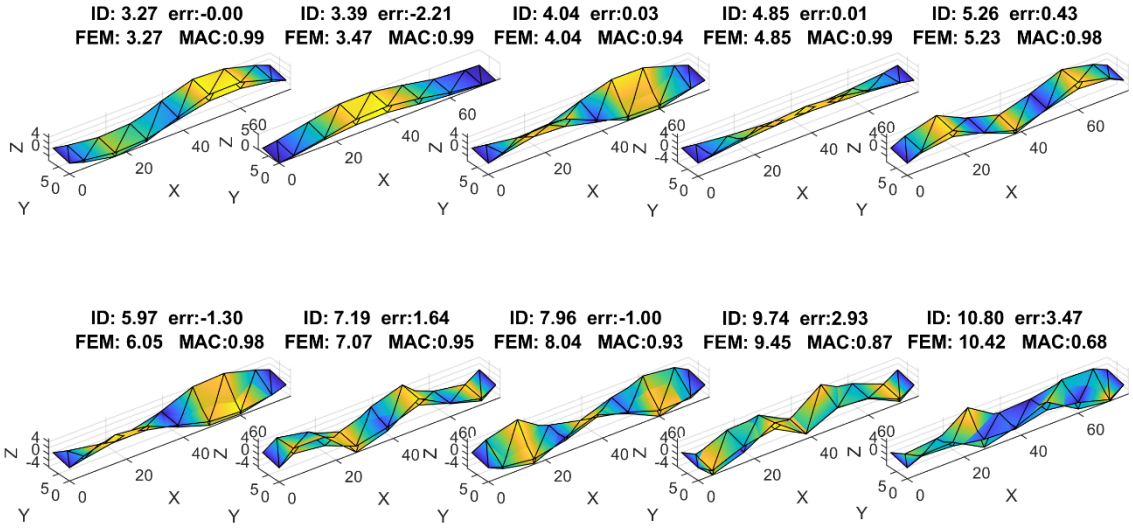

Figure 146: Result of update procedure considering 6 parameters.

Finally, only three parameters were considered. Two different trials were conducted by fixing the density of the box girder at 2500 kg/m³ and 2400 kg/m³, respectively, to eliminate possible multiple solutions arising from mass-stiffness compensation effects.

This is the case with ρ fixed at 2500 kg/m³:

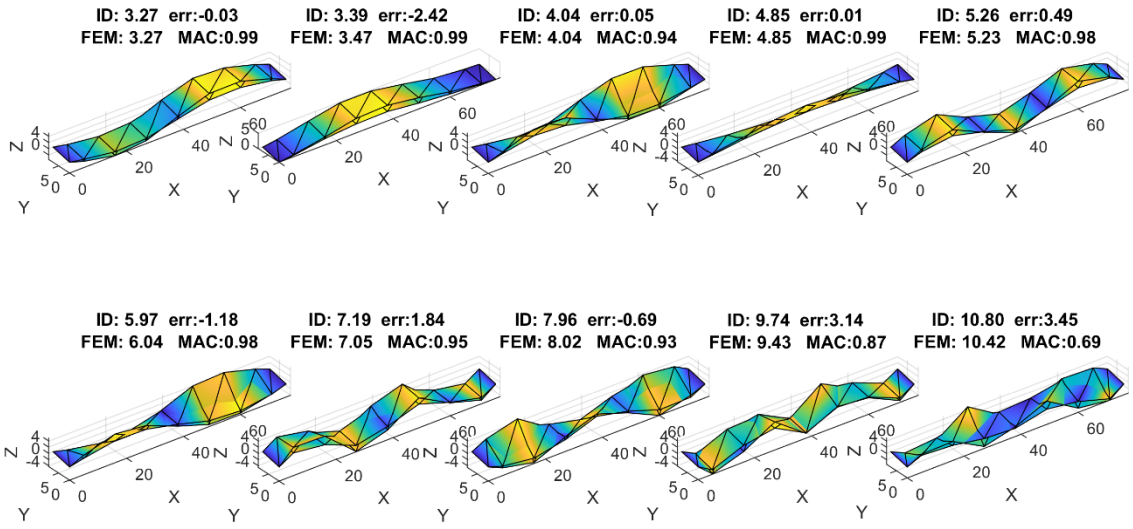

Figure 147: Result of update procedure considering 3 parameters, fixing density at 2500kg/m3.

And this for ρ fixed at 2400 kg/m^3.

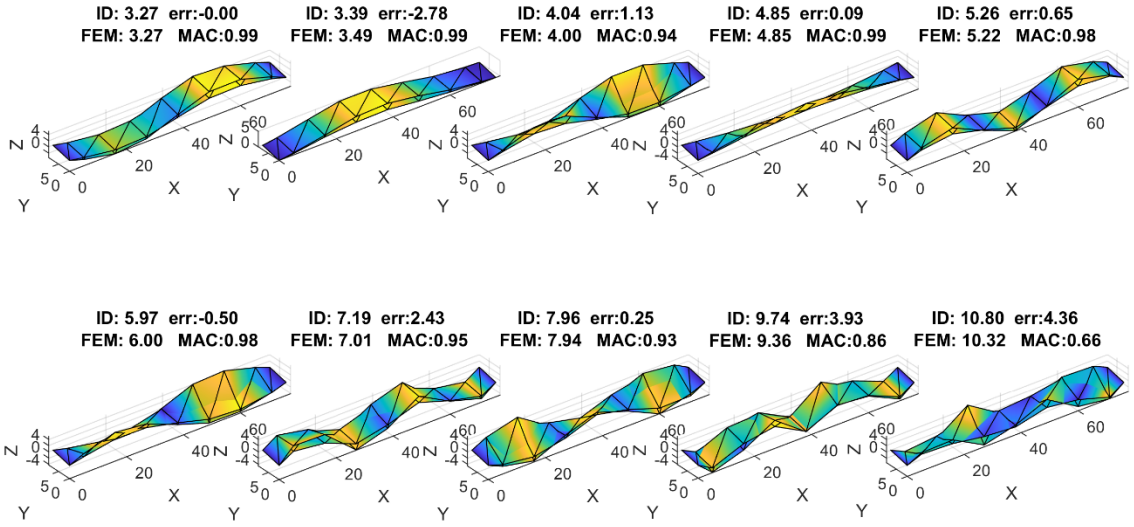

Figure 148: Result of update procedure considering 3 parameters, fixing density at 2400kg/m3.

Another trial with three parameters was performed by keeping the tendon modulus fixed at 210000 MPa, allowing only rho_box, E_Arch, and E_Box to vary.

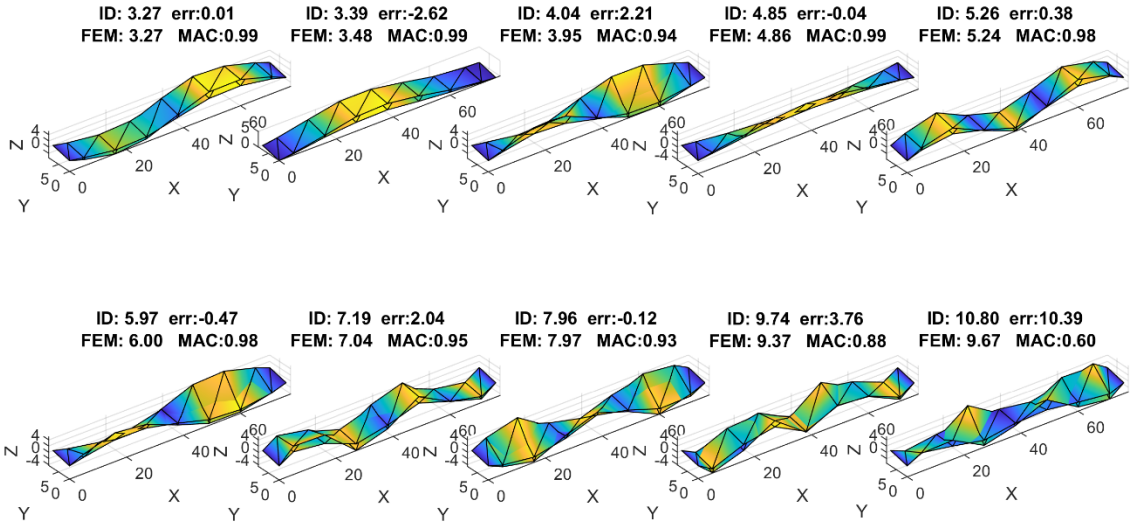

Figure 149: Result of update procedure considering 3 parameters, fixing E_Tendons at 210000 MPa.

As a final trial, an update with only two parameters (rho_box and E_Box) was attempted, with both E_Tendons and E_Arch fixed and in order to later compare the result with the load term. The module of tendons was fixed at 210000 MPa and E_Arch at 42000 MPa.

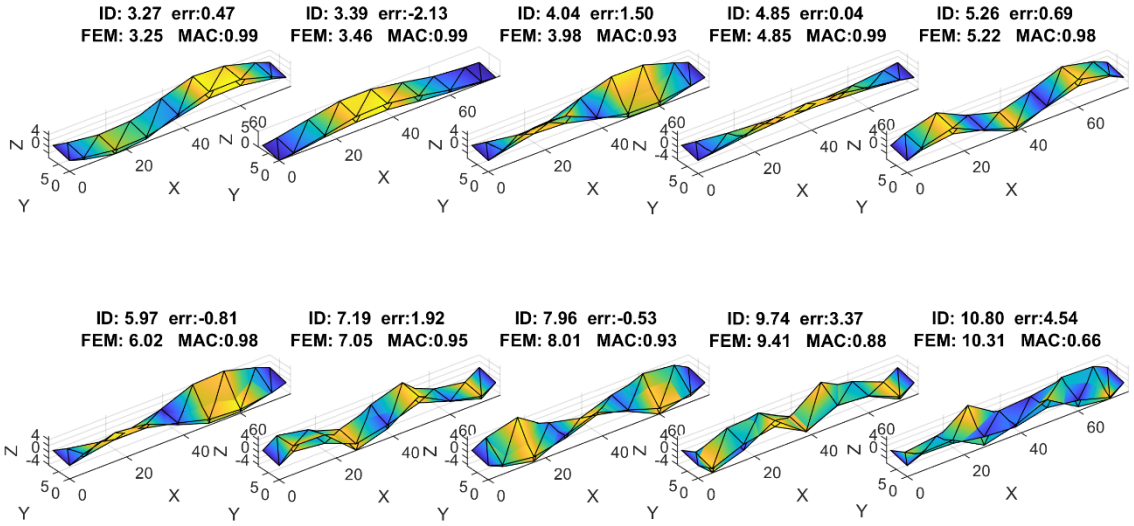

Figure 150: Result of update procedure considering 2 parameters.

The procedure was carried out using different optimization algorithms and five distinct starting points. These initial guesses were not determined solely by mathematical sampling strategies but were selected based on engineering judgment and critical reasoning, reflecting realistic and physically meaningful values for the structural parameters. This approach was also intended to simulate a professional practice scenario, where initial assumptions are typically guided by experience, prior knowledge of the structure, and plausibility checks, rather than by abstract or random sampling of the parameter space. The comparison shows that reducing the number of updating parameters does not significantly compromise the quality of the results. The residual values remain almost unchanged (Table 22), and the optimized parameters are consistent across all cases, as shown in Figure 151. What changes substantially is the computational effort: from about 8 hours with 17 parameters to less than 1 hour with only 3 parameters, while maintaining a very similar level of accuracy. This highlights the advantage of parameter reduction, both in terms of efficiency and in making the optimization procedure more practical for engineering applications.

n° Parameters	17	13	8	6	3
Residual	0.1827	0.1809	0.1793	0.1796	0.1821
n° Iteration (mean on 5 x0)	3494	3407	1218	766	255
Computational Time [hours]	8.1	7.9	2.8	1.8	0.6

Table 22: Difference between different numbers of update parameters.

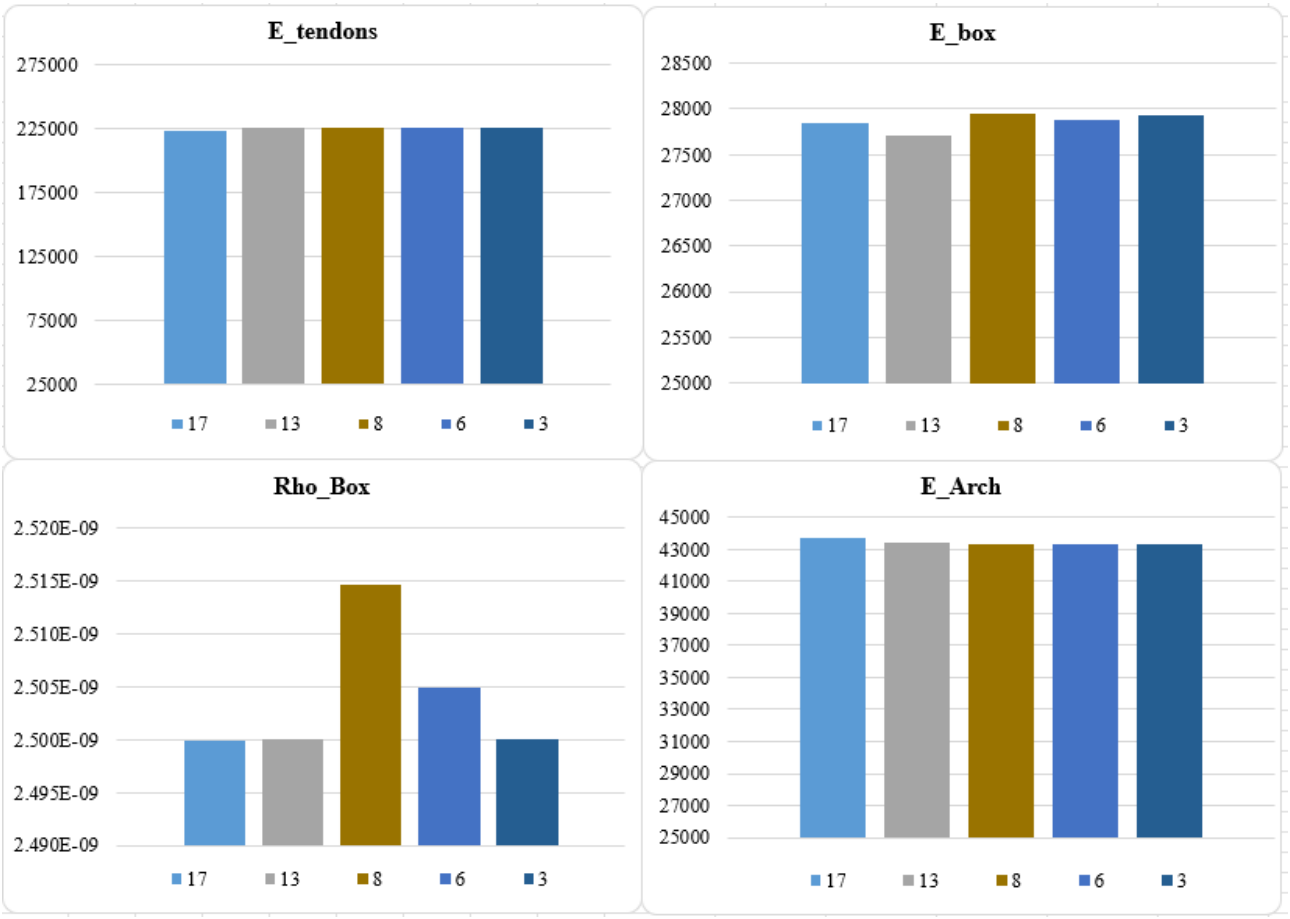

Figure 151: Updated Parameters for the cases of different numbers of parameters.

In Figure 151, the case with three parameters is shown, with rho_box fixed at 2500, which yields the lowest residual. The stiffness of the arch remains stable around 43,000 MPa, the box around 28,000 MPa, and the tendons show a value of 225,000 MPa. Figure 152 displays, in the top left, the best iteration for the case with 17 parameters, while the top right presents the case with 3 parameters. Below, the corresponding diagrams compare the total number of function evaluations for the 17- and 3-parameter cases. It is clear that the number of evaluations is significantly lower in the latter case, and the algorithm converges in far fewer iterations.

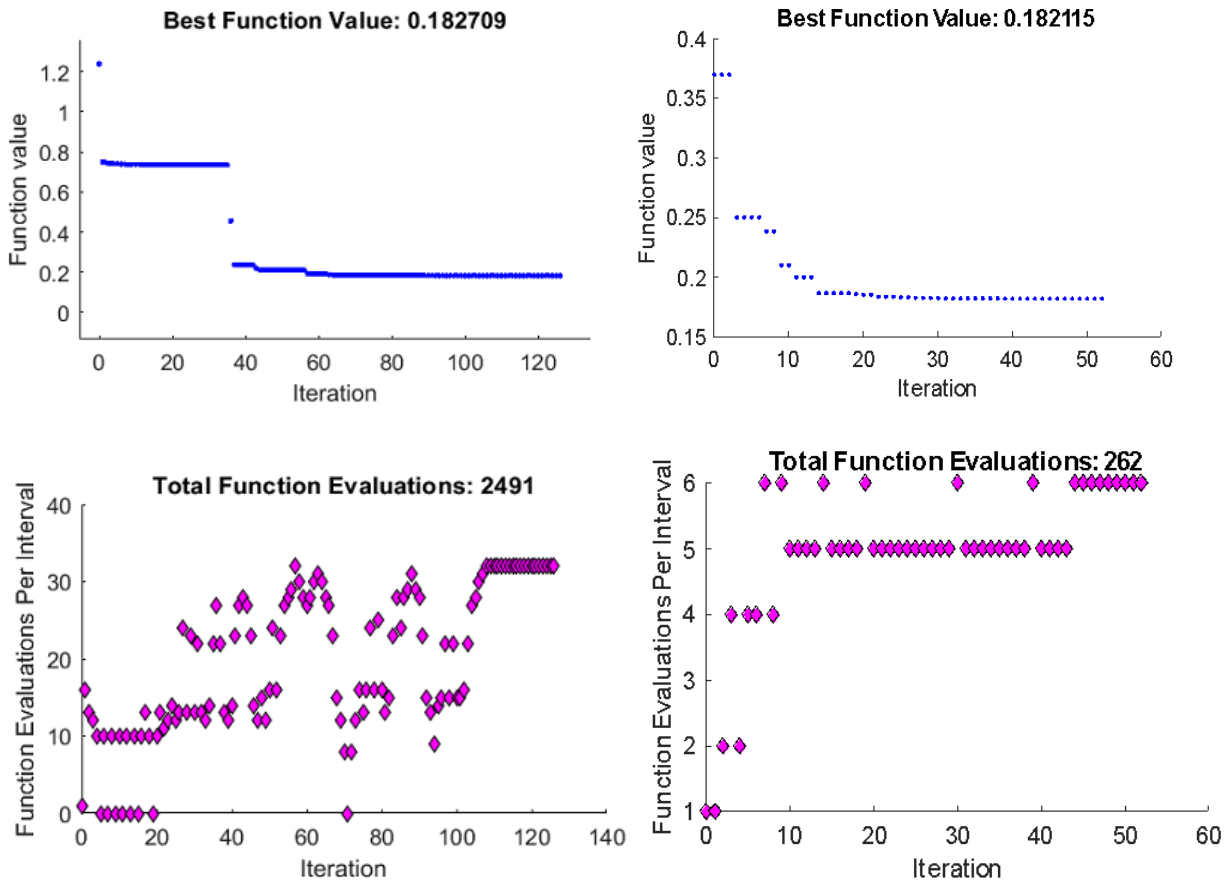

Figure 152: Example of update result for 17 and 3 parameters.

Update with Load term

After the simplified example discussed in the previous chapter, the methodology for applying an error term based on static displacement (also referred to in this work as the “load term”) to the objective function of the model update was applied to the real case study of the Canonica bridge. This step marks the transition from a theoretical demonstration to a practical application of the function with the load term, including all the additional complexities and uncertainties associated with a real structure. Unlike the bridge model, where boundary conditions, material properties, and loads were fully controlled, the goal here was to evaluate the performance of the proposed updating procedure under conditions more representative of reality.

The Canonica bridge is particularly suitable for this purpose because static load tests were available both before and after the replacement interventions. This made it possible to apply the procedure and validate the approach of introducing the load term into the objective function, which could improve the quality and robustness of the finite element model updating process.

The updating procedure was carried out using the same steps described in the previous sections for the case without the load term. The same sets of parameters were considered, and the optimization was repeated with ten different initial guesses. This approach was chosen to demonstrate, in a quasi-statistical sense, the stability of the solutions: despite variability in the starting points, the procedure consistently converged to very similar results. This confirms that introducing the load term does not alter the logic of the process but rather strengthens the robustness of the final solution, as was done for the bridge model.

The load data are derived from the static test conducted in 2002, as described in the previous chapter. By analysing the report data and comparing them with those used by other authors for the same bridge but for different purposes [118], the mid-span displacement is considered. The figure below shows the static load test data. In this case, the full load configuration is considered, resulting in a displacement of 8.7 mm. This displacement was used for the comparison in the objective function.

$$\sum_{i=1}^{n} \omega_i^f \frac{\left|f_{ID,i} - f_{FEM,i}\right|}{f_{ID,i}} + \omega_i^{MAC} \sum_{i=1}^{n} (1 - MAC(\Phi_i^{ID}, \Phi_i^{FEM})) + \omega^d \frac{|s^{Num} - s^{Exp}|}{s^{Exp}}$$

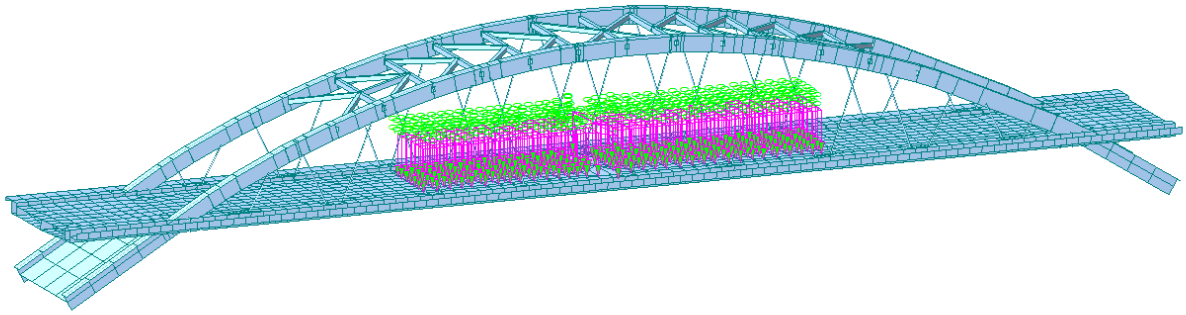

Figure 153: Load on finite element model.

In the finite element model, to reduce uncertainty, the displacement was calculated by evaluating five points along the midspan and taking the average value. This approach helps smooth out possible local effects of the mesh in the FE model.

Update with six parameters

The first stage of the analysis considered six parameters. Figure 154 shows the best results obtained without the load term, while Figure 155 presents the updated solution when the load term was included in the objective function. In both cases, the procedure used ten different initial guesses. When the extended procedure with ten initial guesses was applied, the optimization without the load term produced a solution that was even better than the one reported in the previous section, where only five initial guesses were used, but the results were very similar. In both cases, the errors in frequency and mode shapes are very low. It is possible to observe a “best-fitting” behaviour of the overall model, especially at the highest frequency, which was initially less accurate but improved when the load term was included. This indicates that the inclusion of static information helped to obtain a model that is more closely aligned with reality.

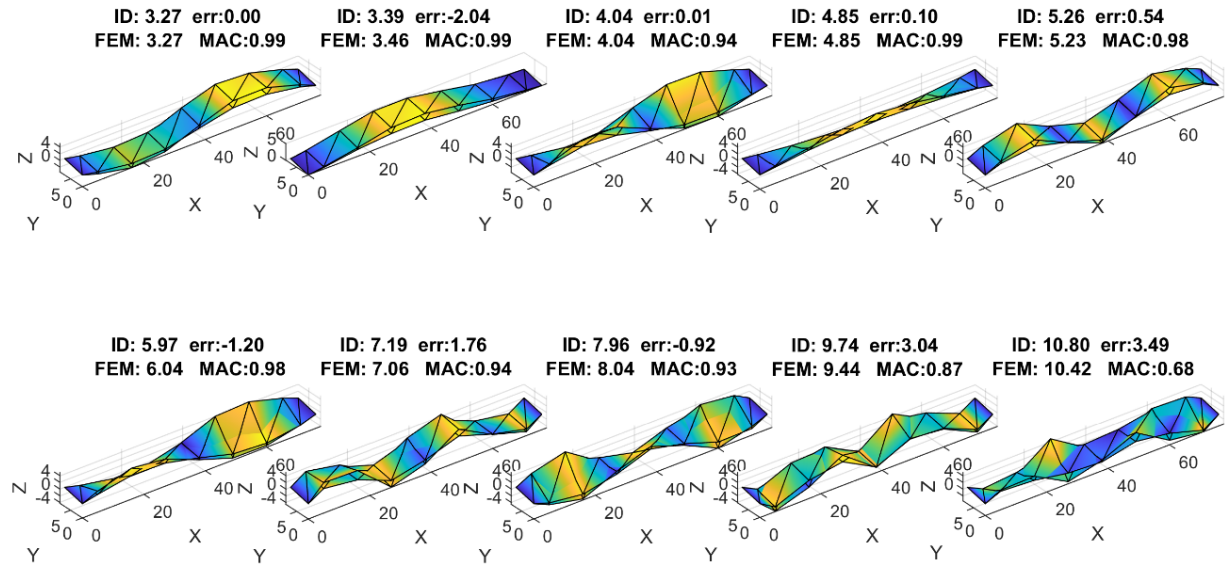

Figure 154: Best result of ten starting points using six parameters without load term.

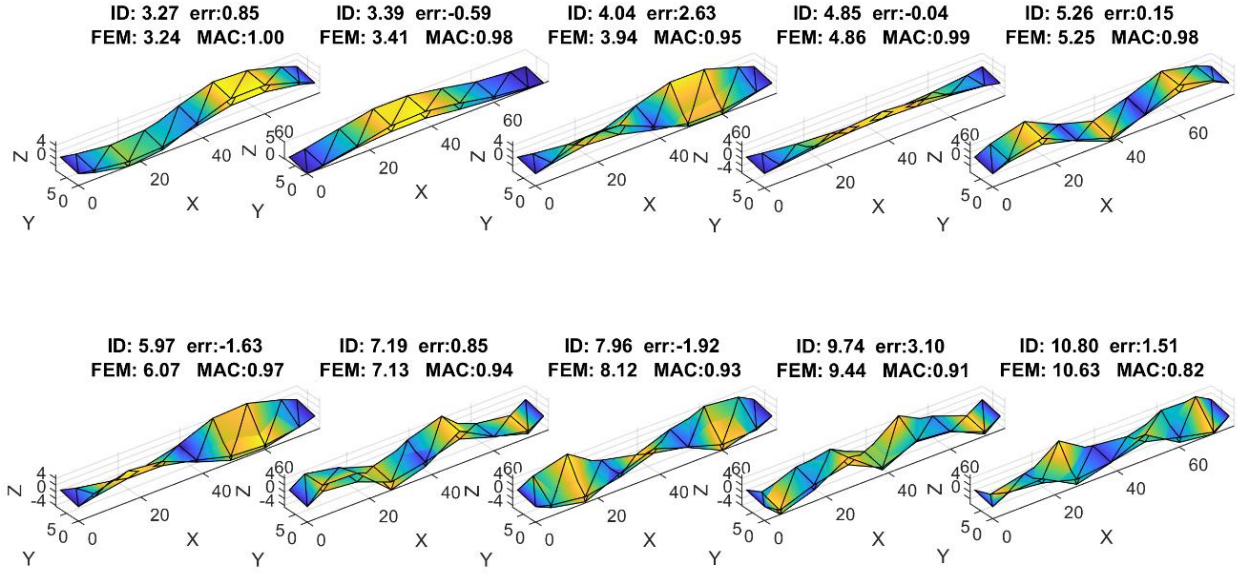

Figure 155: Best result of ten starting point using six parameters with load term.

In general, the identified parameter values tend to be lower, as shown in Figure 156. Apart from a possible improvement in the case of E_Arch, the stability of the solution does not increase. This is most likely due to the high number of parameters involved: several different parameter combinations can yield essentially the same set of frequencies, mode shapes, and displacements, making it difficult for the load term to provide an additional stabilizing effect.

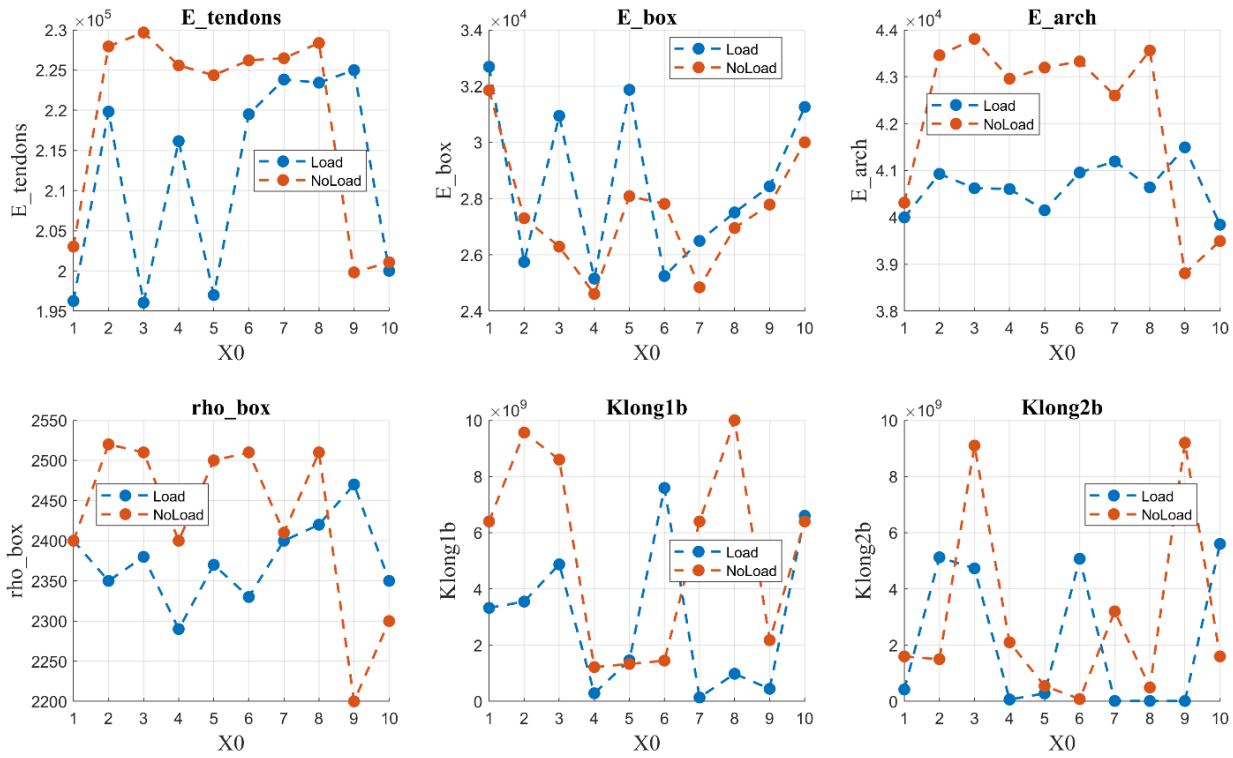

Figure 156: Variation of the solution of the six parameters.

The following table summarizes the parameters after the update, both with and without the displacement term. The solutions differ: in one case, the elastic modulus of the hangers and the density are reduced, while the elastic modulus of the box girder and the spring stiffnesses are higher. In the second solution, the displacement reaches 8.69 mm, which is very close to the target value of 8.7 mm, effectively eliminating the error. This indicates that this particular set of parameters provides a better representation of the overall static and dynamic behaviour of the bridge, as the residuals for both frequencies and mode shapes remain very small.

	No Load	**Load**
E_Tendons [MPa]	226221	200005
E_Box [MPa]	27815	31260
E_Arch [MPa]	43329	39844
rho_box [kg/m3]	2510	2350
Klong1b [N/mm]	1.5E+09	6.6E+09
Klong2b [N/mm]	8.2E+07	5.6E+09
Residual	0.1794	0.1924
Displacement	8.09	8.69
err	7.01%	0.11%

Table 23: Difference between updated parameters with and without the load term.

Update with three parameters

To further investigate the influence of parameter selection, the update procedure was repeated using three parameters, including density, to validate the hypothesis regarding the reduced effect of mass-related uncertainties. For the case without load, extending the process to ten initial guesses resulted in the same solution observed previously. The following figures show the mode shapes before and after the update, both with and without the static term.

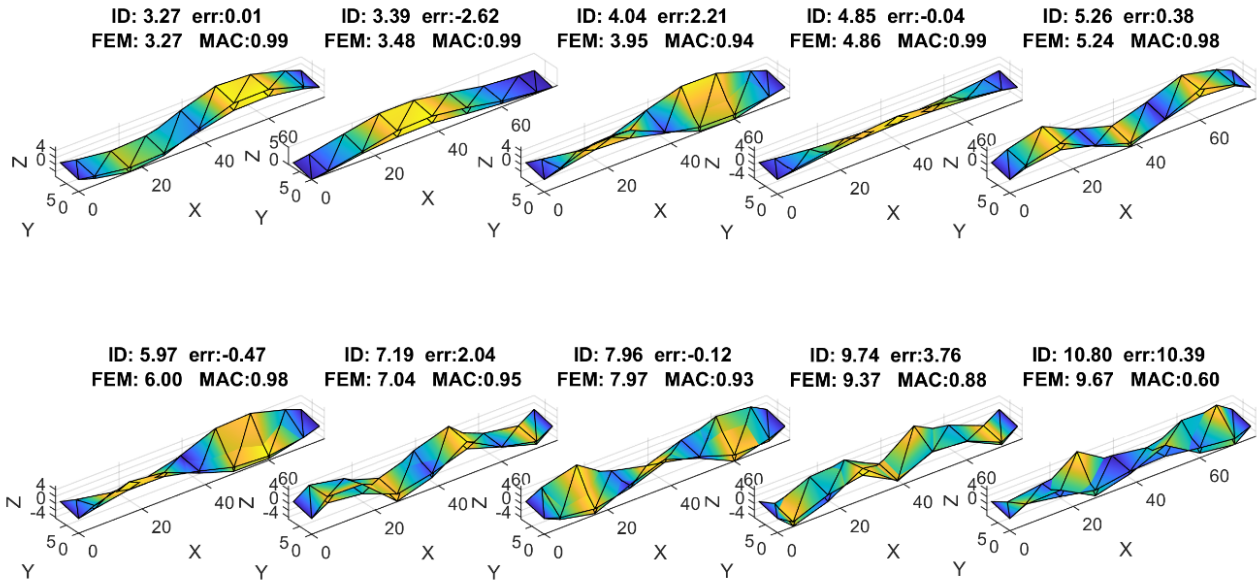

Figure 157: Best result of ten starting point using three parameters without load term.

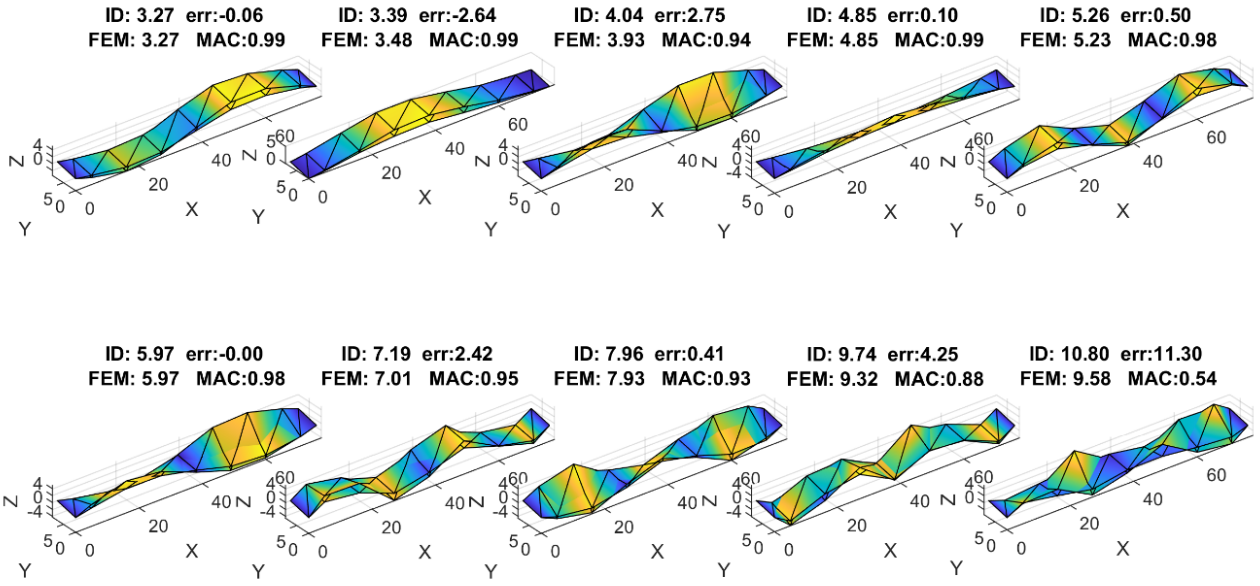

Figure 158: Best result of ten starting point using three parameters with load term.

It is possible to notice in Figure 159 that when the load term is added, the results highlighted the stabilizing role of static information: regardless of the starting point, the same final solution was consistently reached.

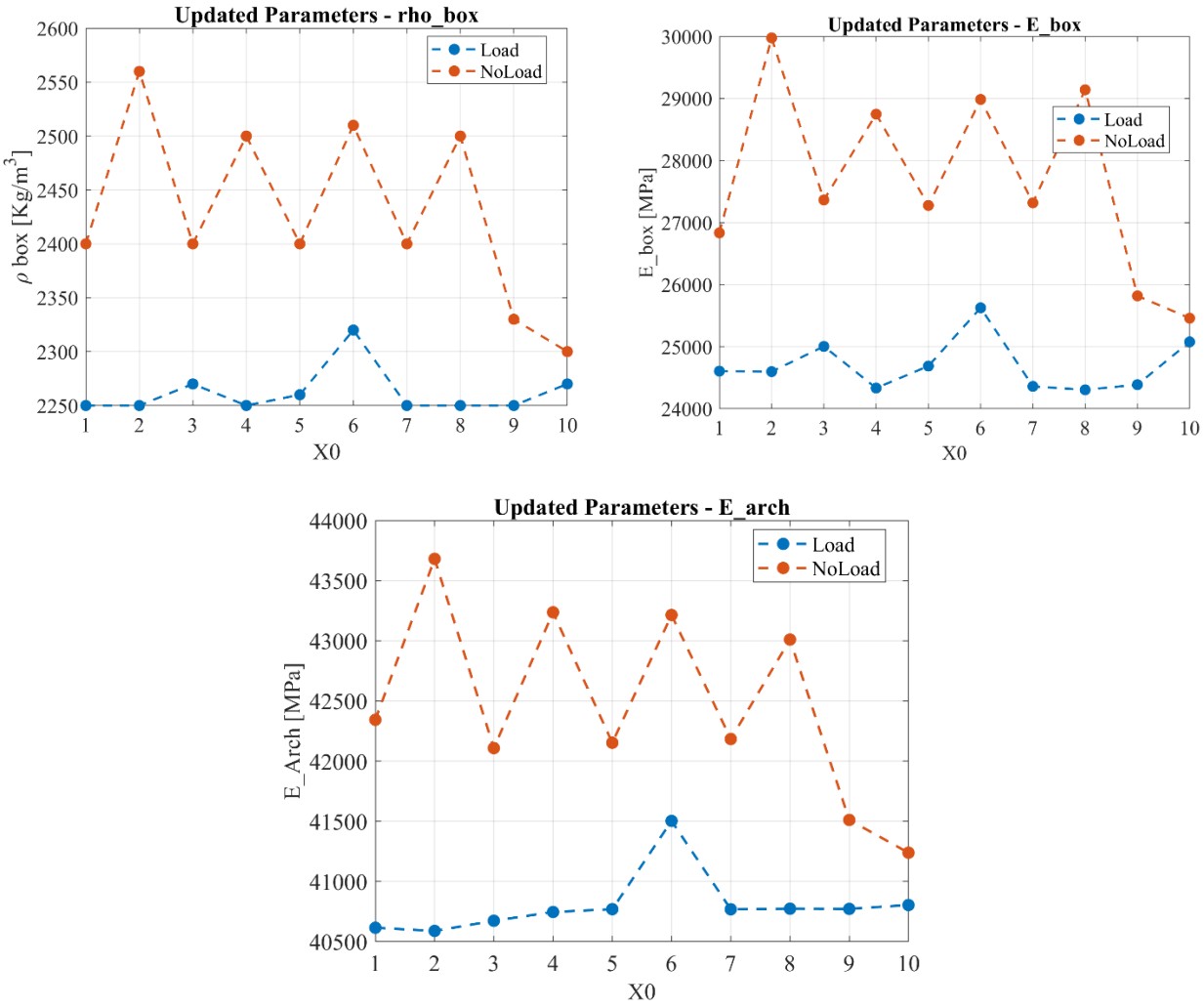

Figure 159: Variation of the solution of the three parameters.

Table 24 shows the post-update parameters with the displacement term included. In this case, as in the six-parameter scenario, the residuals for frequencies and mode shapes remain very small, and the residual for displacement is also very low, improving from 2% to 0.8%. The most significant result, however, is that the solution is stabilized. Using Simulated Annealing, the result is consistent, as shown in Figure 160, and the best solution is presented in Table 24.

	No Load	Load	Load SA
rho_box [kg/m3]	2300	2225	2200
E_Box [MPa]	25459	24333	2322
E_Arch [MPa]	41239	40746	40530
Residual	0.1989	0.2071	0.2066
Disp	8.53	8.63	8.65
err	1.95%	0.80%	0.57%

Table 24: Difference between updated parameters with and without the load term.

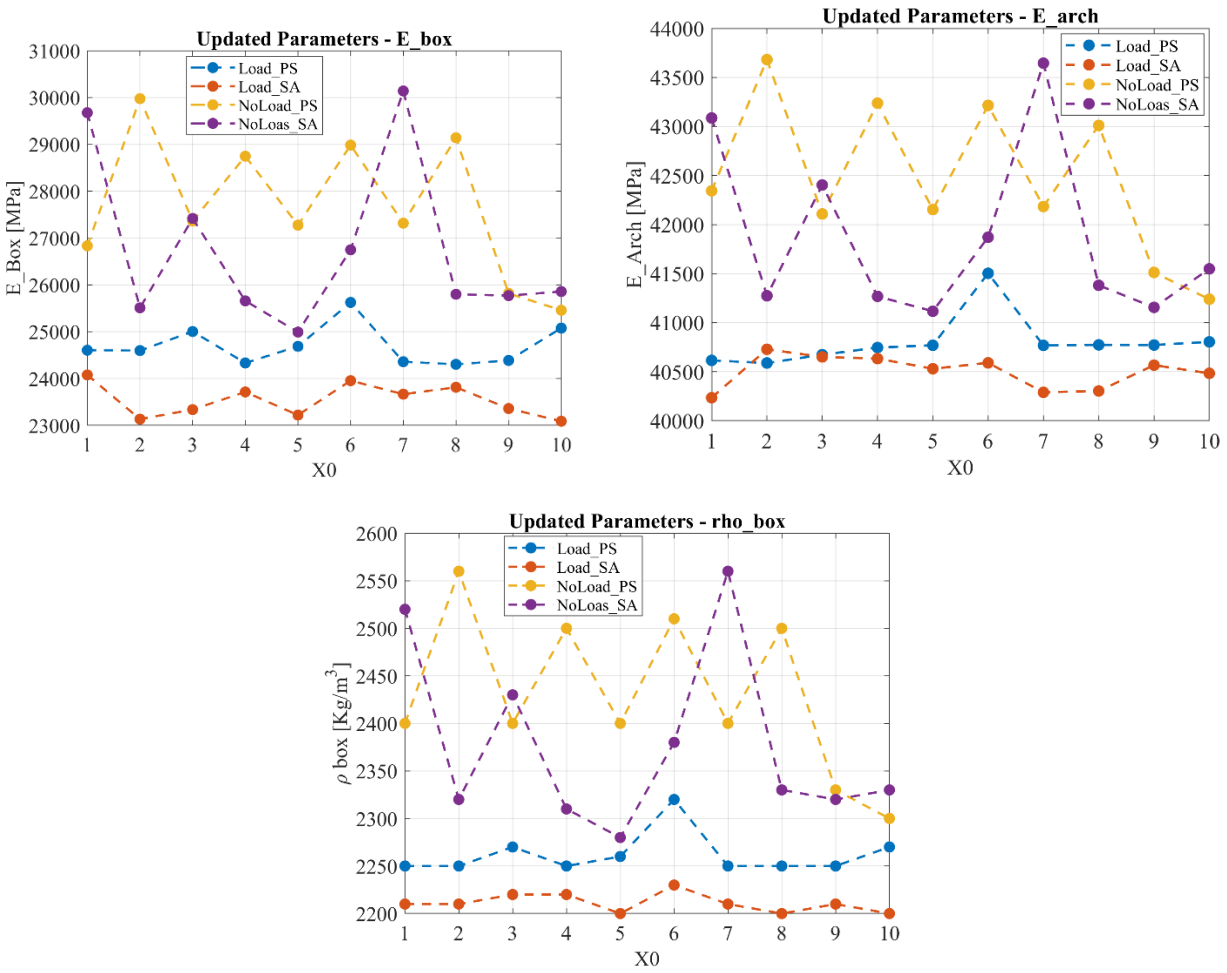

Figure 160: Variation of the solution of the three parameters, compared with Simulated Annealing algorithm.

An additional test was carried out by fixing the values of *K_long* and *E_tendons* to those corresponding to the best six-parameter solution. This led to a result that was practically identical for *E_arch*, *E_box*, and *ρ_box*, confirming the reliability of the update procedure.

Finally, the objective function was plotted using slice contour plots, following the same methodology as in the simple bridge example. The plots clearly showed that the version with the load term has a single minimum, while the case without it retains multiple minima distributed along valleys of nearly equivalent solutions.

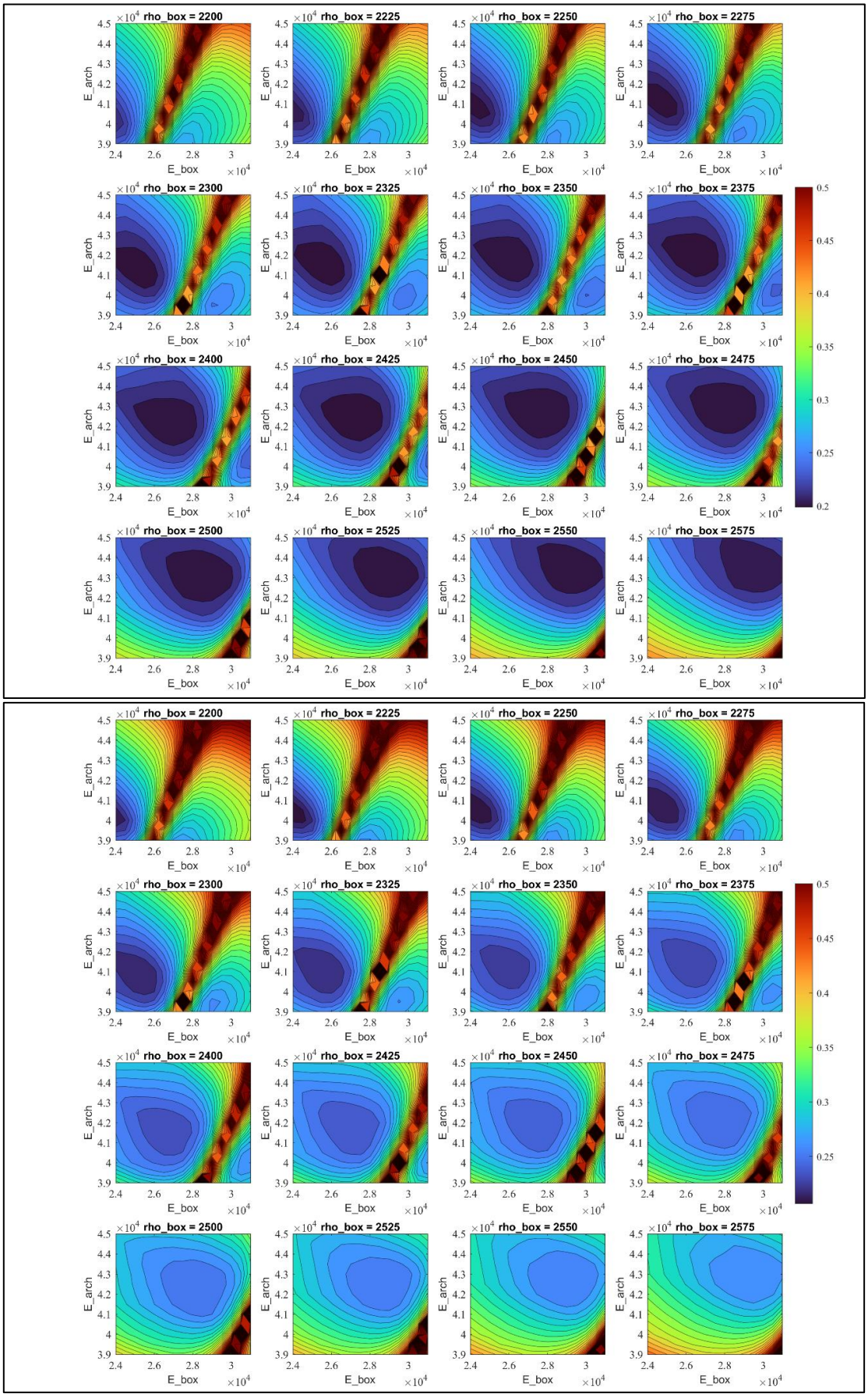

Figure 161: Objective functions with (down) and without (up) load term in slice contour plot.

Update with two parameters

The procedure was also repeated with only two parameters, both with and without the displacement-based error term. Figure 162 and Figure 163 show the best solutions obtained from ten starting points, the residuals on frequencies and mode shapes remain very low in both cases, confirming the overall accuracy of the procedure. However, the stability of the solution does not show a clear improvement: as illustrated in Figure 167.

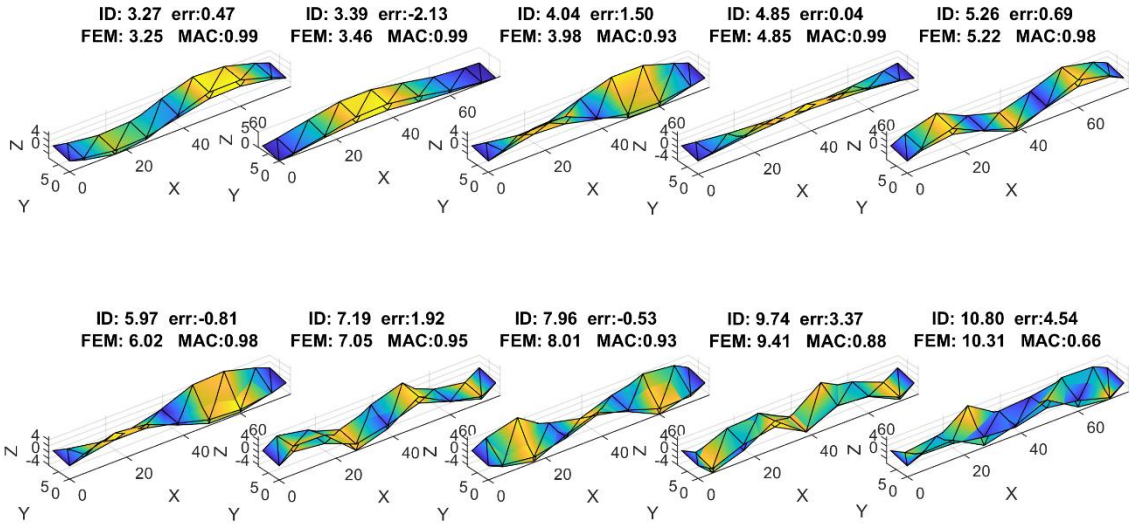

Figure 162: Best result of ten starting point using two parameters.

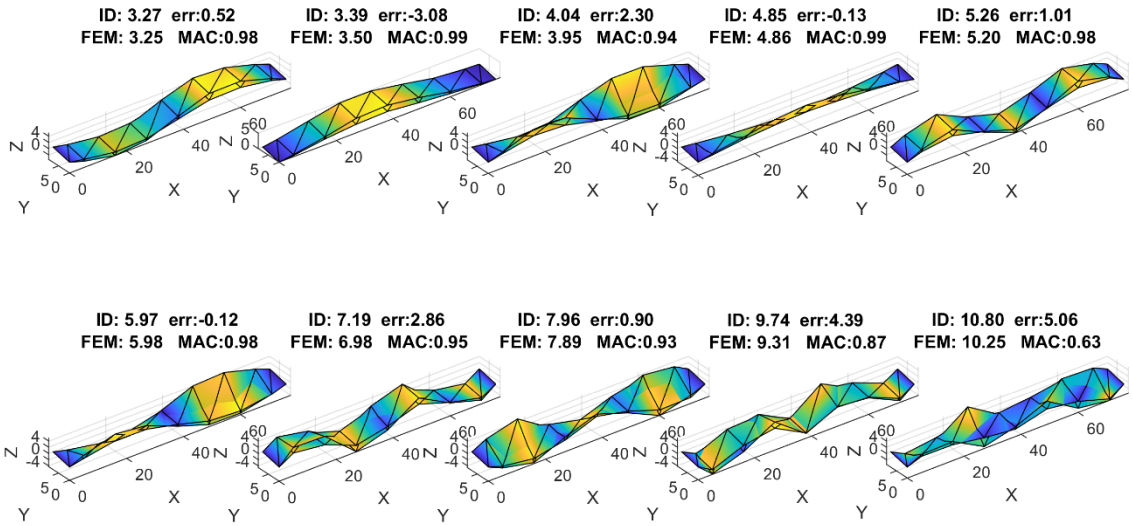

Figure 163: Best result of ten starting point using two parameters with load term.

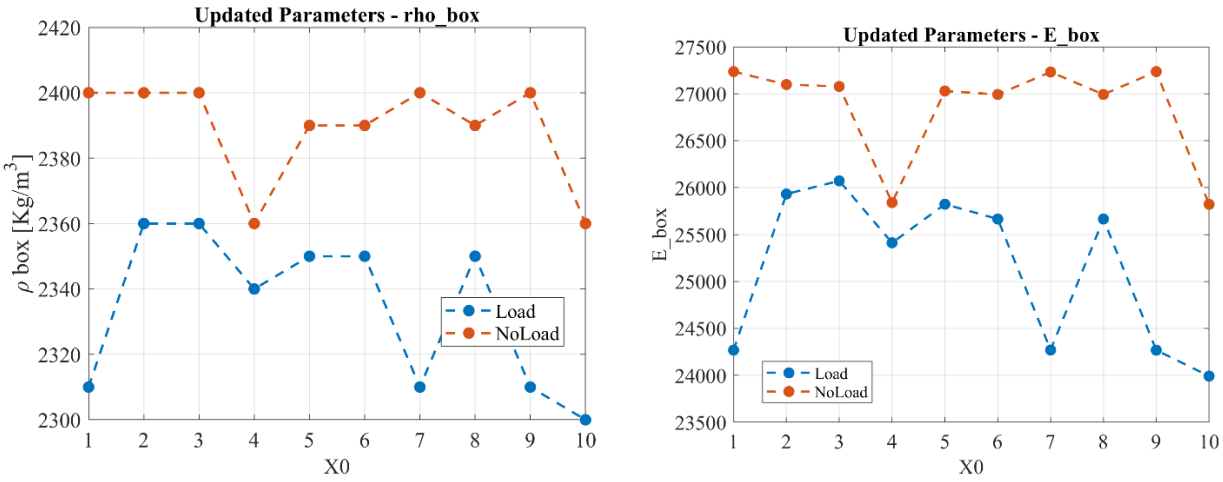

Figure 164: Variation of the solution of the two parameters.

By evaluating the function over a grid corresponding to the rho_box and E_Box space, the objective function can be plotted in two dimensions, both with and without the static term. The result is shown in Figure 165 , making it possible to observe differences between the two cases.

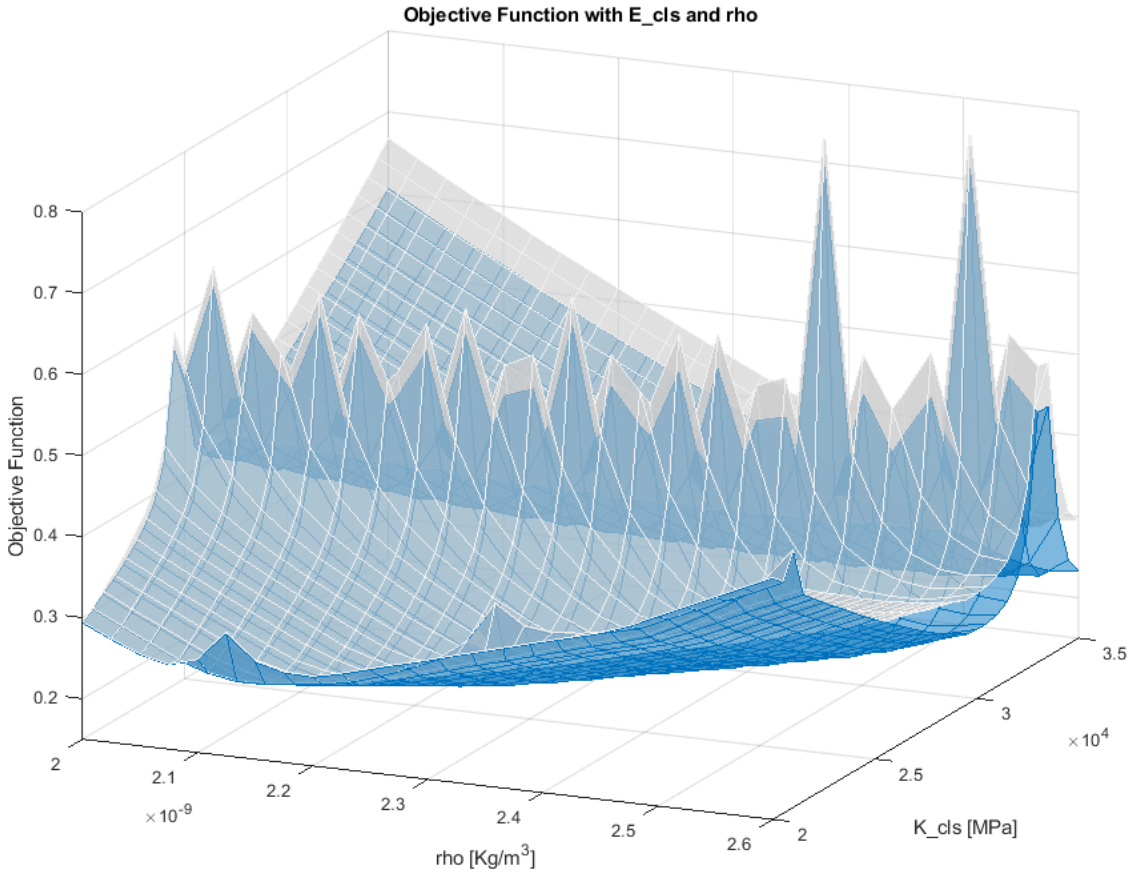

Figure 165: Objective function evaluated for two parameters with and without load term.

The two objective functions have almost identical shapes, with only a slightly steeper slope and a more concave profile in the case without the load term. When the static load is introduced into the objective function, as shown by the contour representation in Figure 166, the minimum shifts to another region of the parameter space. This point corresponds to a solution that describes the structure as more flexible, an adjustment required to accommodate the discrepancy introduced by the displacement error term. In other words, including the load term does not necessarily increase the robustness of the solution but instead modifies the equilibrium point, redistributing the balance between stiffness and mass to better fit the imposed static response.

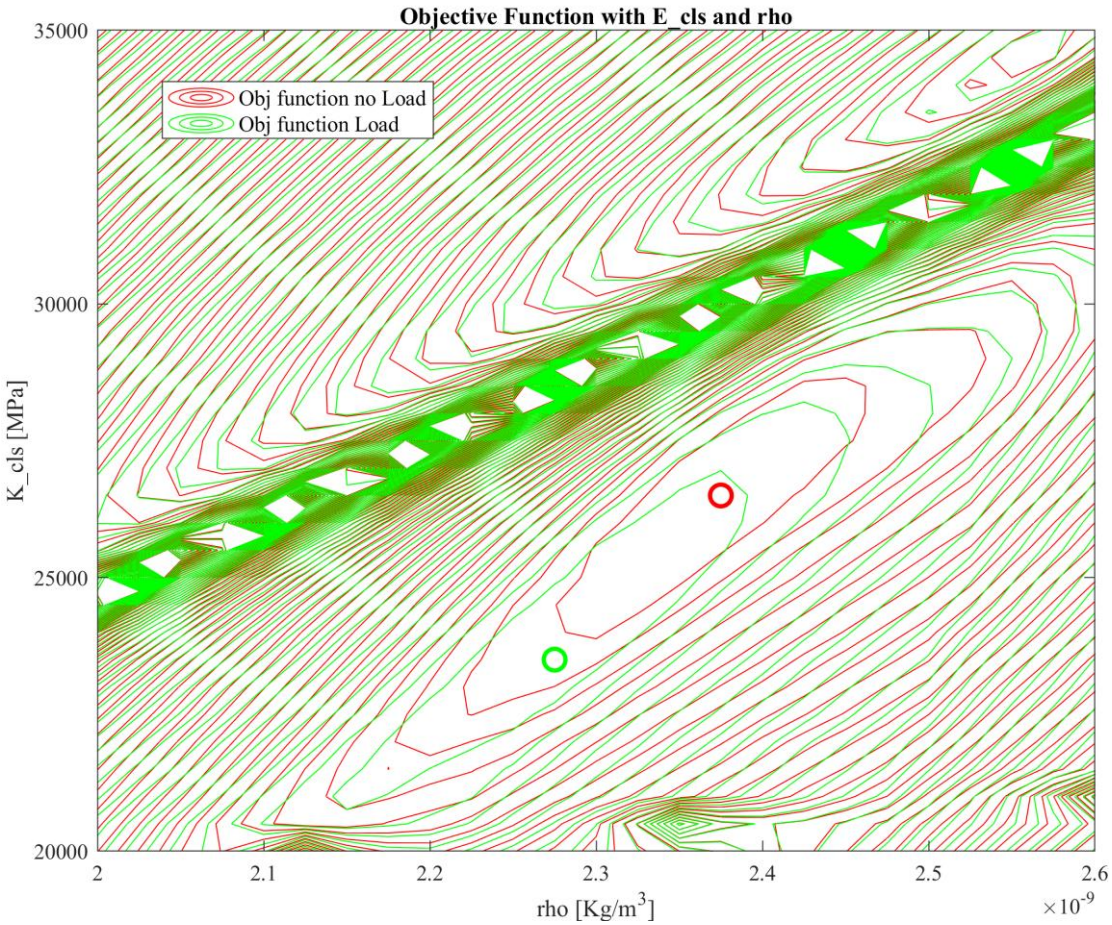

Figure 166: Objective function (contour plot) evaluated for two parameters with and without load term and respective minima.

Even when assigning double weight to the displacement term, the solution shifts further to better accommodate the displacement difference, at the expense of the differences in frequencies and mode shapes. The analysis with the double weight on the displacement term is show in Figure 164.

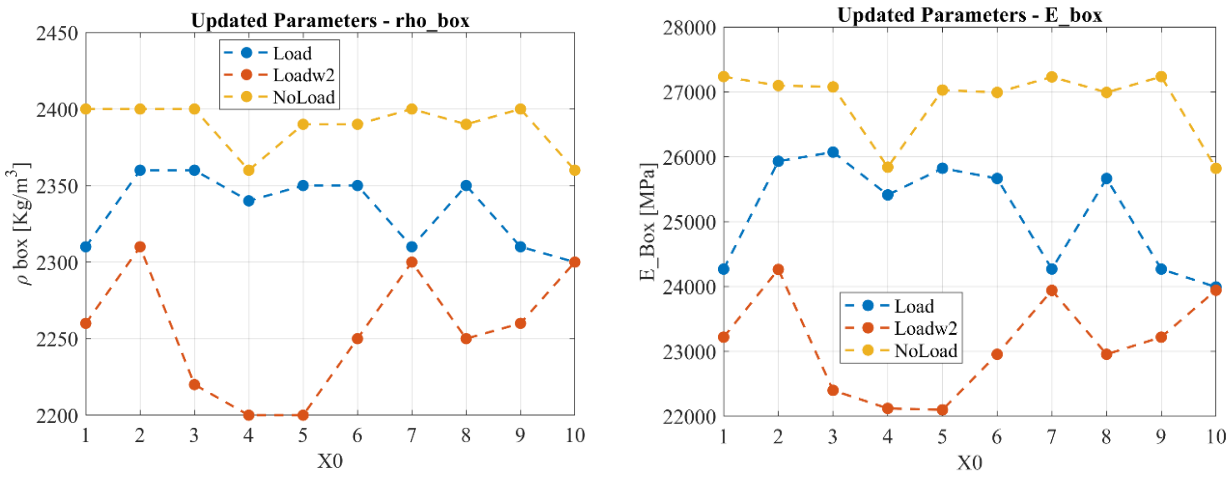

Figure 167: Variation of the solution of the two parameters, considering a double weight on displacement term.

Update post intervention

After analyzing the pre-intervention condition, attention shifted to the post-intervention scenario. As described earlier, the finite element model initially created in MidasGen and STKO was modified to account for the intervention. In particular, the cross-section and length of the hangers were replaced. The original hangers, which were anchored with three-dimensional hooks, were substituted with new elements bolted to the arch at the top and to the underside of the side beams of the deck. These changes, previously described as Step 1 and Step 2, improved agreement with the identified modal properties, especially for the first mode. The updating process was then repeated using the same methodology as in the pre-intervention phase. Initially, an update was performed using only one parameter. All parameters identified in the pre-intervention update were kept fixed, while only the elastic modulus of the hangers was allowed to vary, under the assumption that everything else remained unchanged except for this modulus. The result of this analysis is presented in Figure 171. It can be observed that, for almost all 10 different initial guesses in the procedure, the elastic modulus converges to 180,000 MPa.

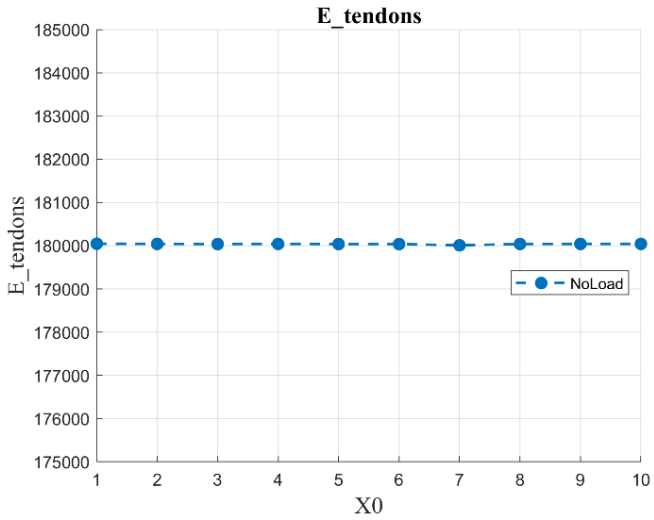

Figure 168: Result of update with E_Tendons.

The update with the six most influential parameters was then performed. As a first step, an attempt was made using the optimized values obtained in the pre-intervention update as the initial point (x_0). This allowed verification of whether the update would again converge to the same parameter values, as one might reasonably expect. The results of the update, using the optimized values from the pre-intervention phase as starting points, are reported in Table 25 below. As expected, the parameters

remain essentially consistent with those previously identified. The only notable differences are a decrease in the elastic modulus of the hangers and a slight increase in the density of the box.

Parameters	Initial Value	Updated Value
E_tendons [MPa]	226221	190415
E_Box [MPa]	27815	30115
E_Arch [MPa]	43329	42305
rho_box [kg/m^3]	2510	2610
Klong1b [N/mm]	1.45E+09	3.82 E+09
Klong2b [N/mm]	8.20E+07	9.48 E+07

Table 25: Result of the update procedure, post intervention.

Figure 169 shows the comparison of the mode shapes for the updated model, reporting the identified frequencies, relative errors, and MAC values. The results confirm that the update provides a close match, with MAC values generally very high and frequency errors less than 2%, indicating strong correspondence between experimental and numerical modes. Figure 170 complements this by presenting the MAC matrix (left) and the frequency errors (right). The diagonal dominance in the MAC matrix highlights the clear separation of the modes, while the frequency error plot confirms that discrepancies after the update remain very limited, further supporting the reliability of the procedure.

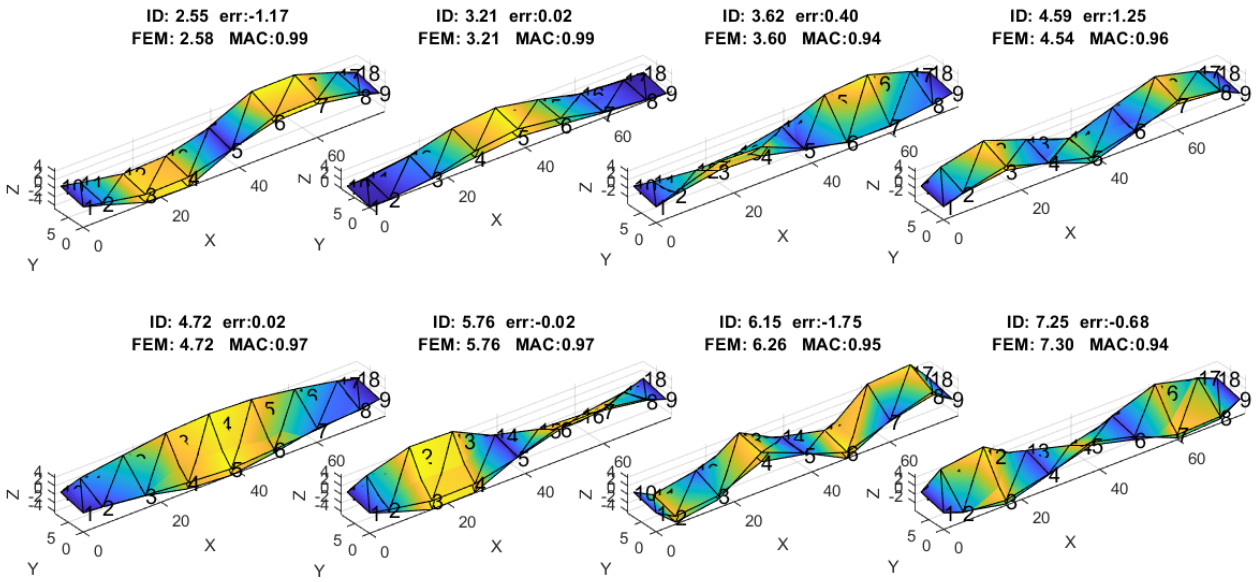

Figure 169: Mode shapes pre and post update procedure, post intervention case using six parameters.

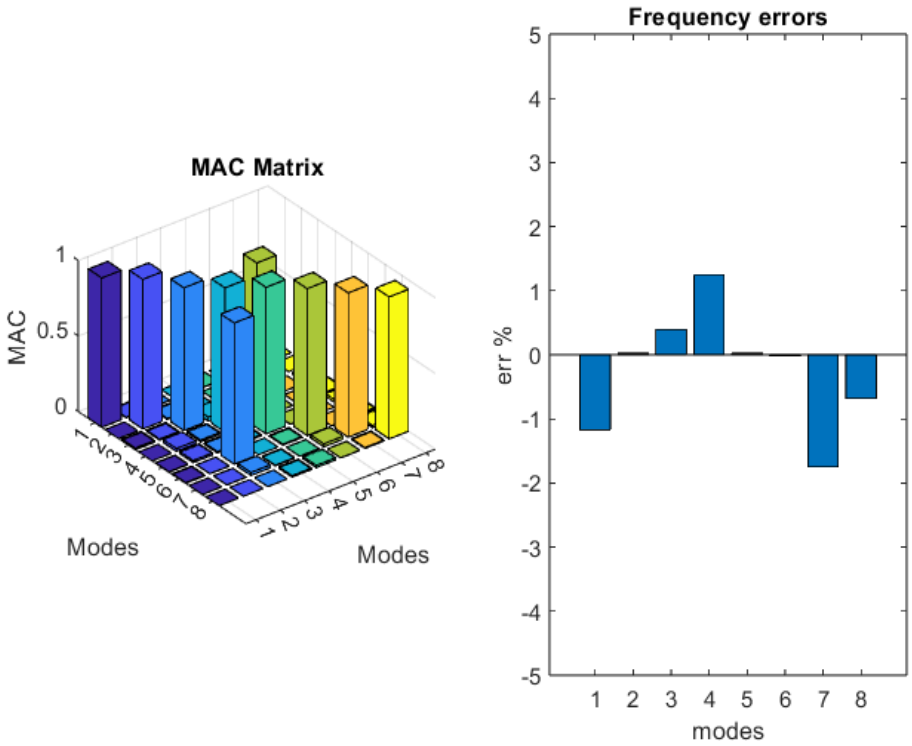

Figure 170: MAC Matrix end frequencies errors, post intervention case using six parameters.

Subsequently, the update was repeated using the extended set of ten starting points. This step aimed to provide a more robust assessment of the solution and to verify the stability of the identified parameters. Table 26 below shows the results of the update using the starting point with the pre-intervention results and the best obtained from the ten starting points. The parameters obtained are slightly different from those identified in the previous case with a single starting point, and the total residual is lower in the best case of the ten starting points – not by much, but it is lower.

Parameters	**Updated Value X0 like pre-intervention**	**Updated Value Best of 10 x0**
E_tendons [MPa]	190415	197226
E_Box [MPa]	30115	25312
E_Arch [MPa]	42305	45178
rho_box [kg/m^3]	2610	2640
Klong1b [N/mm]	3.82 E+09	1.18 E+09
Klong2b [N/mm]	9.48 E+07	1.17 E+07
Res	**0.2103**	**0.2049**

Table 26: Result of the update procedure.

In particular, while the frequency errors appear marginally higher, on the other hand, the MAC values show an upgrade in certain modes compared to the single-starting-point case, indicating that the modal shapes are better captured reducing the total residual as in Table 27.

Mode	f, ID	f, FEM, x0	f, FEM, best 10 x0	err, x0	err, best 10 x0	MAC, x0	MAC, best 10 x0
1	2.55	2.58	2.55	-1.17	-0.01	0.99	0.99
2	3.21	3.21	3.25	0.02	-1.10	0.99	0.99
3	3.62	3.60	3.58	0.40	1.06	0.94	0.98
4	4.59	4.54	4.44	1.25	3.26	0.96	0.96
5	4.72	4.72	4.73	0.02	-0.15	0.97	0.97
6	5.76	5.76	5.73	-0.02	0.43	0.97	0.97
7	6.15	6.26	6.04	-1.75	1.89	0.95	0.95
8	7.25	7.30	7.05	-0.68	2.74	0.94	0.95

Table 27: Result of the update procedure.

Figure 171 presents the updated mode shapes. The MAC matrix and the frequency errors are reported in Figure 172 for the best case that have the less residual.

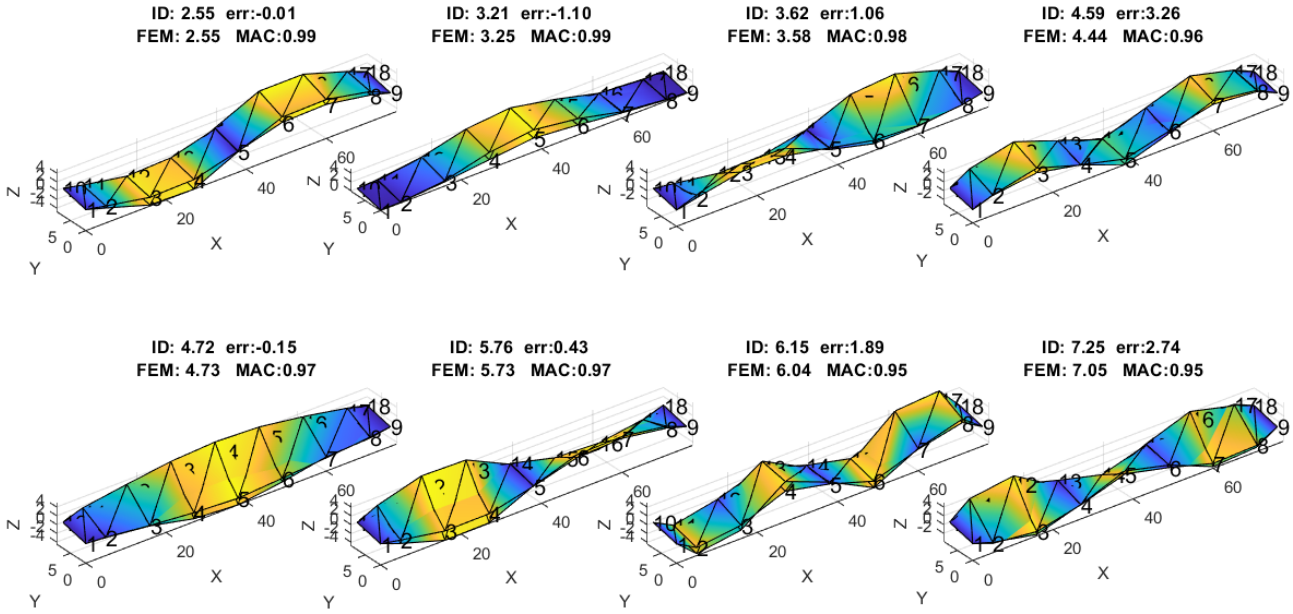

Figure 171: Mode shapes pre and post update procedure, post intervention case using six parameters, best of 10 starting points.

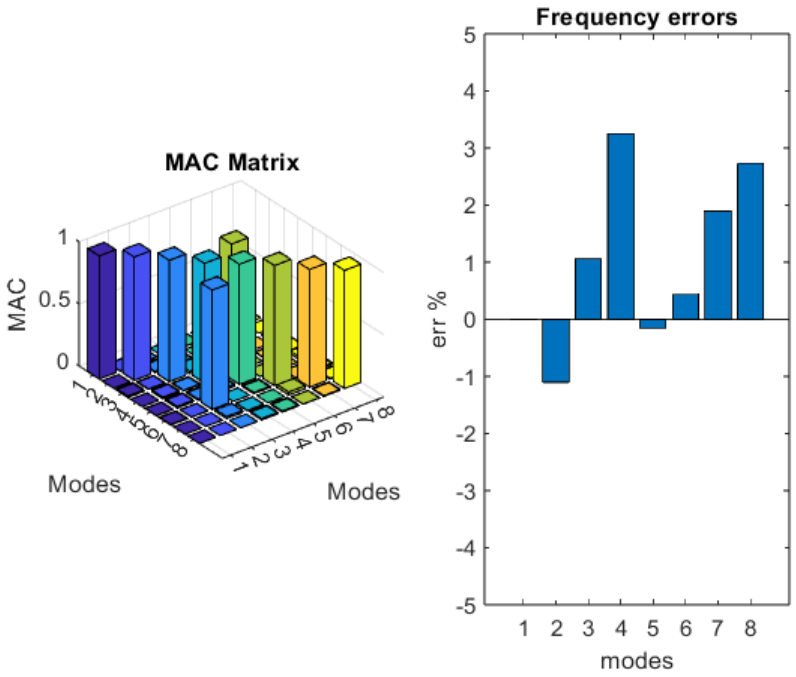

Figure 172: MAC Matrix end frequencies errors, post intervention case using six parameters, best of 10 starting points.

The following Figure 173 shows the result of the algorithm, specifically the window containing the four control figures used during the execution of the optimization process.

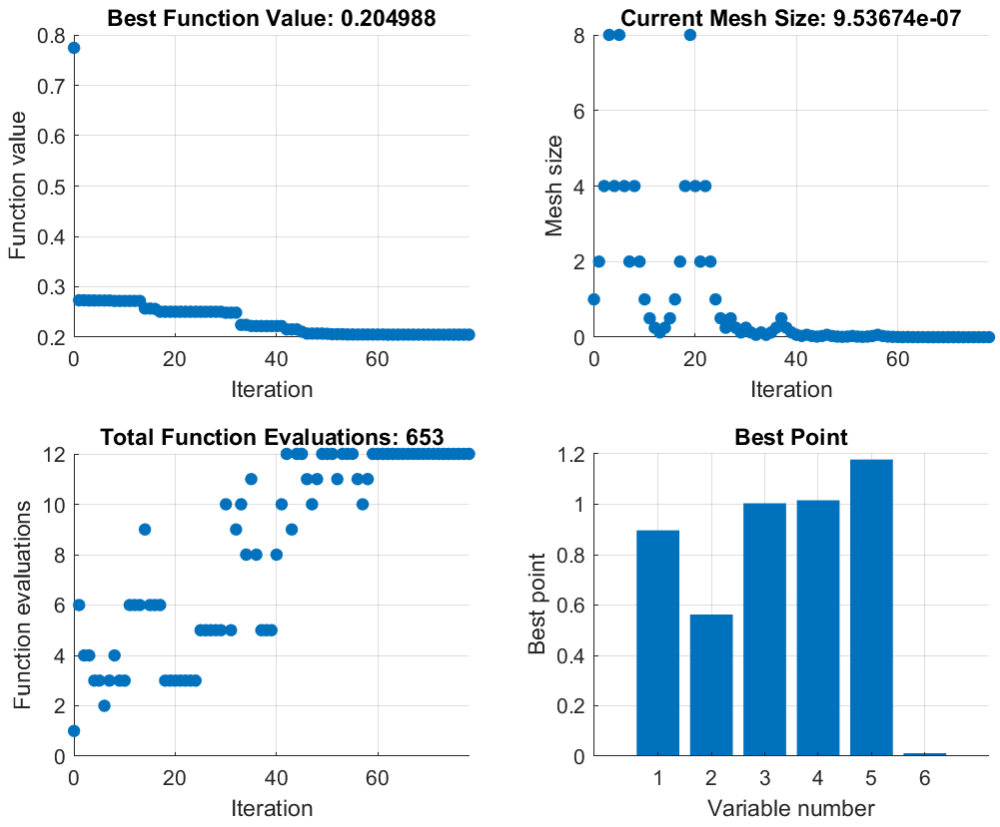

Figure 173: Control charts during optimization process, final step.

The results of the model update confirm the effectiveness of the procedure, not only because of the limited residual errors but also because the identified parameter values remain physically consistent. The bar charts in the following figure provide a direct comparison of the model's accuracy before and after the update. The upper diagram highlights the reduction in frequency errors, which are significantly lower across almost all modes after calibration. Although some residual discrepancies persist for specific modes, the overall improvement is clear. The lower diagram shows the Modal Assurance Criterion (MAC) values, illustrating the degree of correlation between the experimental and numerical mode shapes. In this case, the MAC values are consistently above 0.9, confirming that the updated model reproduces the experimental modal shapes with good fidelity.

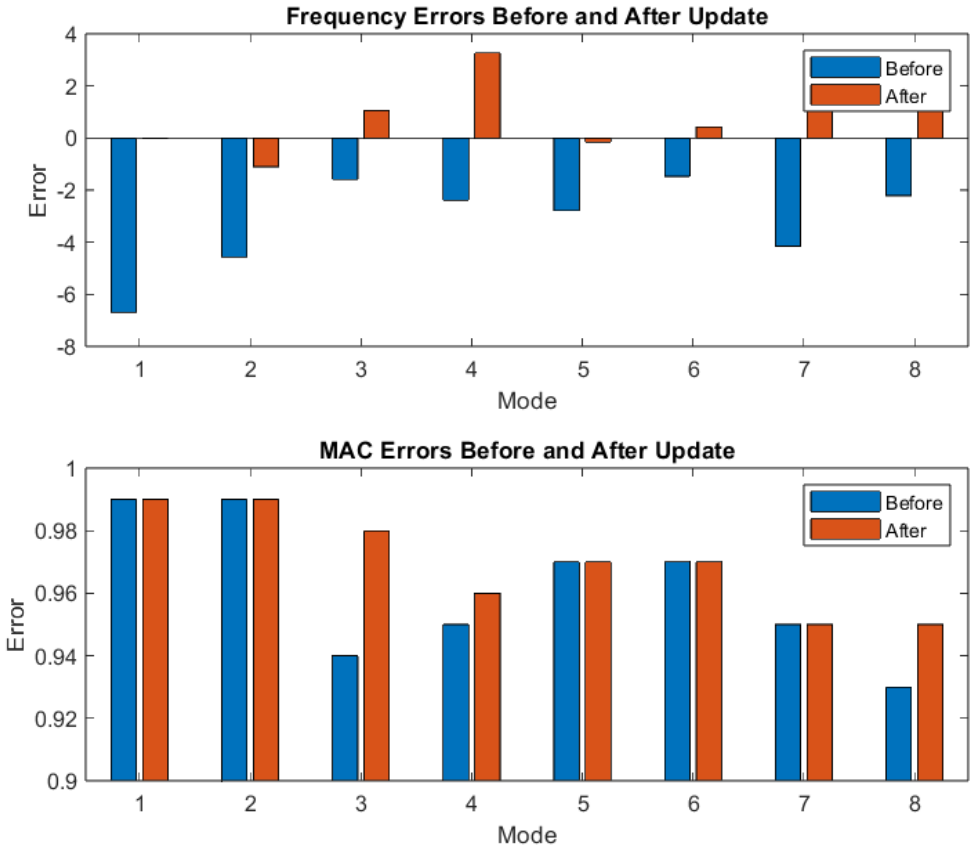

Figure 174: Frequency errors (above) and MAC pre and post the update procedure (below).

In addition to the six-parameter update, a further analysis was conducted by reducing the set of variables to three parameters, allowing only rho_box, E_Arch, and E_Box to vary. This approach maintains consistency with the pre-update procedure and enables a direct comparison with the load term in the next section.

Figure 175 below presents the results of the update procedure conducted with ten different starting points and six parameters. For each starting point, the identified values of the six parameters are

shown, allowing direct comparison of their variability. It is clear that, regardless of the initial guess, the elastic modulus of the hangers consistently converges to relatively low values.

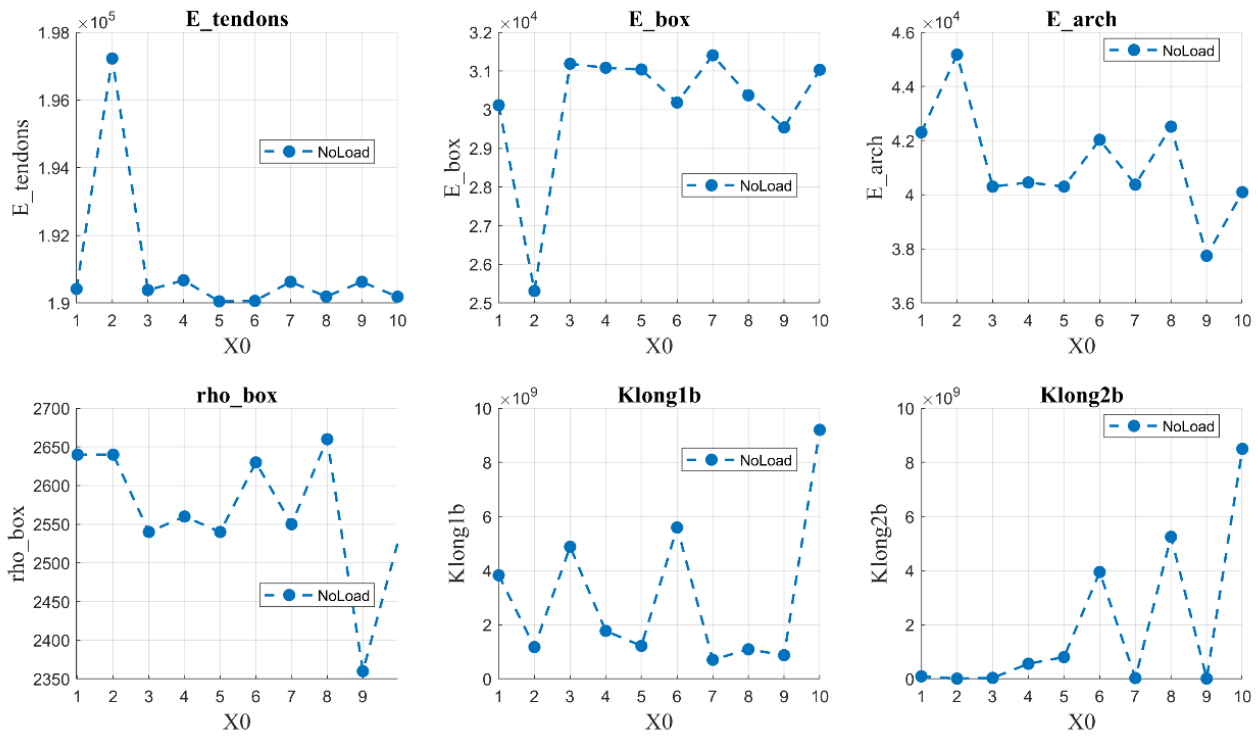

Figure 175: Variation of the solution of the six parameters.

Notice this, and to investigate this behaviour more closely, the update was repeated while fixing the elastic modulus of the hangers at three different reference values: 210,000 MPa 190,000 MPa and 180,000 MPa.

The results of the three-parameter update are shown in Figure 176, where the identified values for the ten different starting points are reported. The plot shows that when the elastic modulus of the hangers is set to 210,000 MPa, the identified solution tends to have high values for the arch and box girder modulus, as well as a high density (to balance the same frequency). These values are somewhat beyond typical engineering limits. In contrast, when the modulus is set to 180,000 or 190,000 MPa, the results are more reasonable and closely aligned with those obtained in the pre-update analysis.

This behaviour may be related to the fact that, although the finite element model was modified by changing the section and lengthening the hangers, it does not yet account for the additional elongation caused by the bolts inserted above and below in a specific section. Furthermore, since the hangers are now longer and do not all have the same length, this non-uniform increase in length leads to a difference in stiffness distribution, which likely influences the identified parameters.

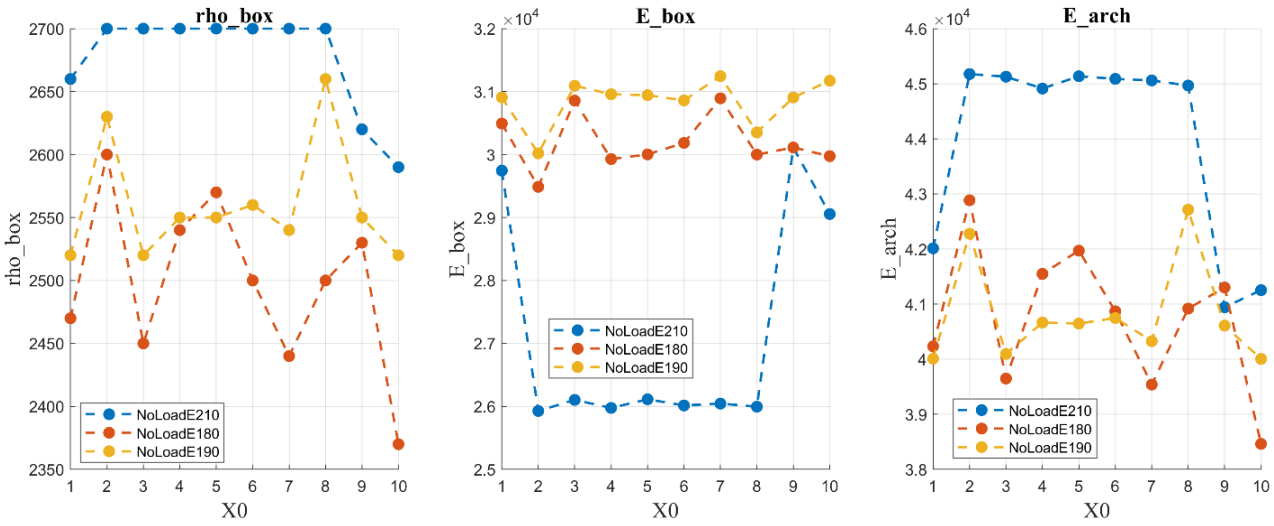

Figure 176: Variation of the solution of the three parameters.

Based on the previous analysis, the result of the update with the elastic modulus of the hangers was set to 190,000 MPa is presented because it provides the lowest value of the objective function, even though it is very similar but slightly lower than the 180,000 MPa case. The results of the update using this value are presented below. First, Figure 177 shows the modal shapes along with the corresponding errors. This is followed Figure 178 presenting the MAC matrix and the differences in the frequencies.

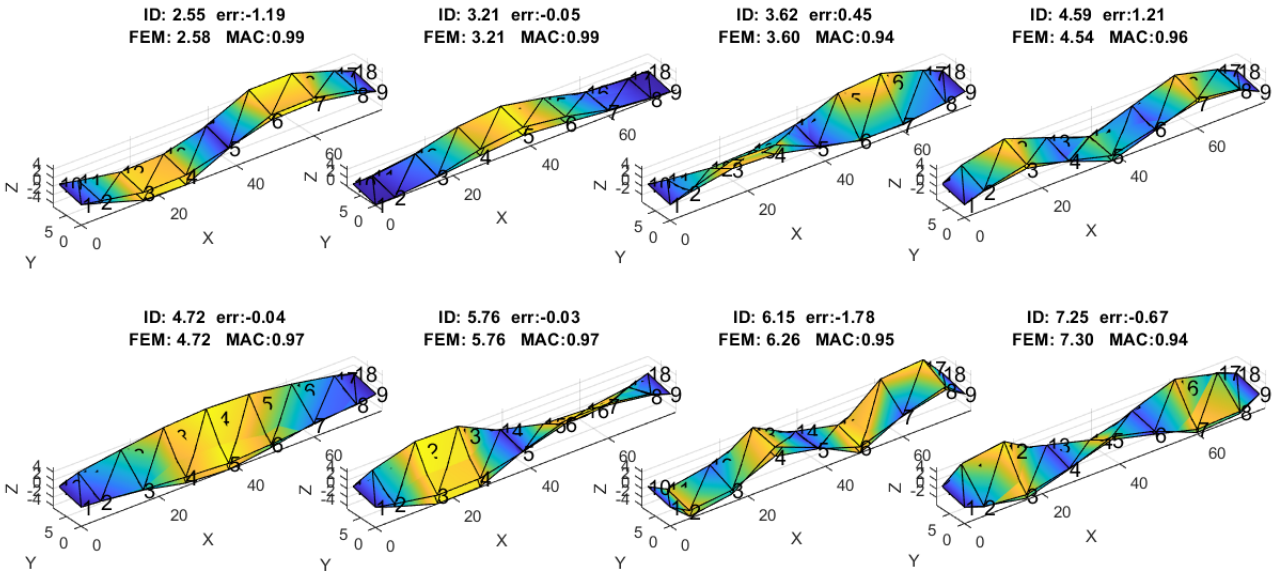

Figure 177: Mode shapes pre and post update procedure.

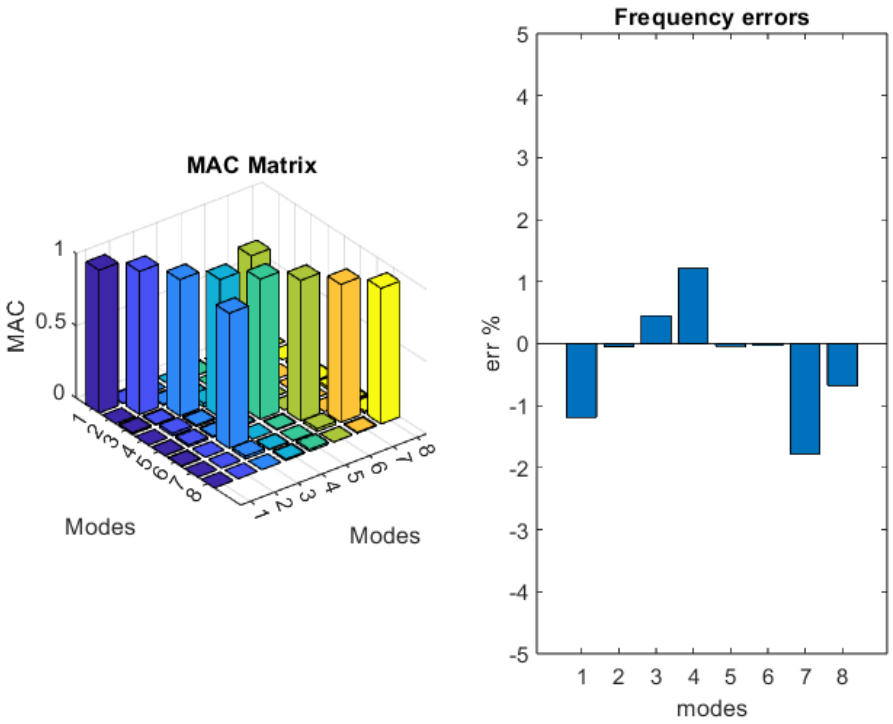

Figure 178: MAC Matrix end frequencies errors.

Since the intervention has likely altered the geometry of the hangers, it would be advisable to verify this aspect through a bridge check, for example by means of photogrammetry or other geometric survey methods, given the potential change in stiffness.

Update with Load term

The update procedure was then extended, following the approach used in the previous section for the last update, by including in the objective function a term representing the displacement difference observed during a static load test. This extension allows the model calibration to account not only for modal properties but also for the actual structural response under applied loads, providing a more comprehensive and realistic identification of the parameters. The results of the static load test are briefly summarized below, as data from the post-rehabilitation load test are available. These measurements provide a reference for the displacements observed at key points of the structure under the applied load, allowing comparison with the predictions of the current finite element model. Subsequently, the outcomes of the update procedure incorporating this additional term in the objective function are presented. This enables a detailed assessment of how including the static load data influences the identified parameters and the overall model behaviour, showing whether and how the updated model aligns more closely with both the dynamic and static responses of the structure.
After the intervention, a static load test was conducted to verify the bridge following the replacement of the hangers. The purpose of the test was to assess the structural response of the bridge under controlled loading conditions. The load was applied using three trucks, each weighing approximately 40 tons, arranged in different configurations to simulate various load distributions on the deck. Measurements of vertical displacements (deflections) were taken using a digital optical level at eight reference points – four on the downstream side and four on the upstream side. Each load configuration was applied and then completely removed, allowing monitoring of both the maximum displacements and the elastic recovery of the structure.

Truck No.	Load [kg]
1	40,180
2	40,200
3	40,320

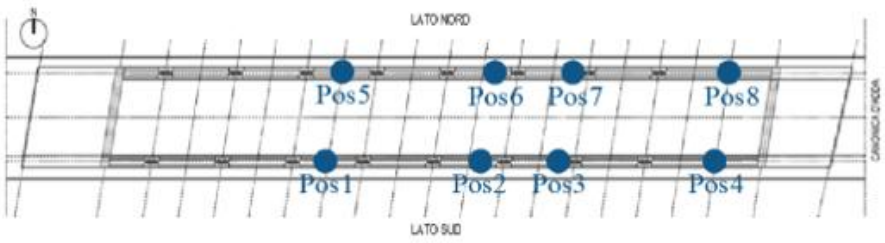

Figure 179: Truck weight and measurements positions of the static load test.

Load Scheme	Total Load [kg]	Maximum Deflection [mm]	Location (Point)
Scheme 1	80,380	4.10	Pos3
Scheme 2	120,700	4.80	Pos7
Scheme 3	80,380	7.20	Pos2
Scheme 4	120,700	8.60	Pos2

Figure 180: Load scheme used in the static load test and photo of trucks during the test.

For the application of the load procedure, Load Scheme No. 3 was selected, as shown in Figure 181. According to the test data, this configuration produced a maximum displacement of 7.20 mm, as reported in the corresponding table. Consequently, the finite element model was updated by introducing the corresponding load configuration. The update was performed by adding the static load term to the objective function and comparing the results with those obtained from the static load test. To minimize possible issues related to local mesh effects in the FEM models, the comparison was carried out using the average displacement of two points at position 2.

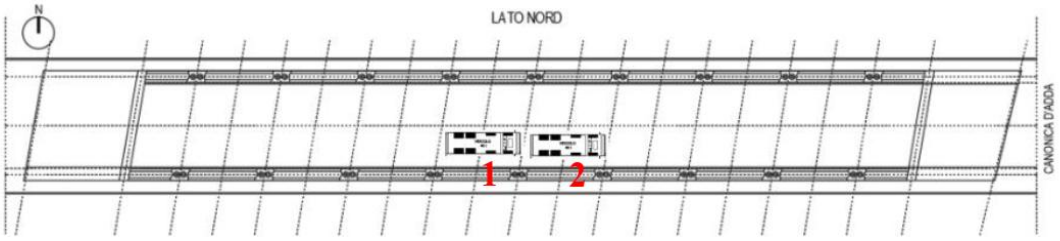

Figure 181: Load Scheme n°3.

As shown in Figure 182, in the six-parameter case and in the pre-intervention update, introducing the static load difference does not improve the stability of the solution. This behaviour may generally be attributed to the fact that the static load alone does not eliminate possible parameter combinations, such as those between the stiffness of the boundary restraints and the elastic modulus of the box girder, or other similar interactions.

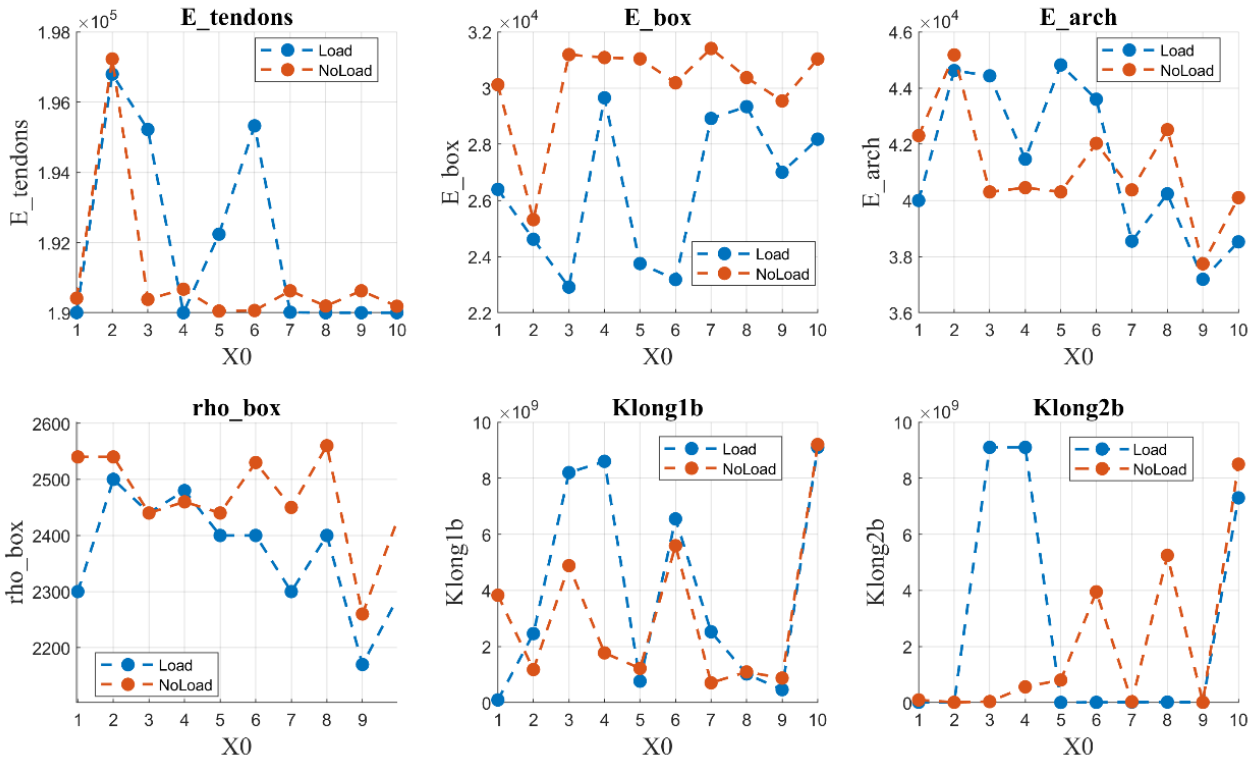

Figure 182: Variation of the solution of the six parameters.

In this case as well, the best solution provides an excellent match between frequencies and mode shapes, as shown in Figure 183. Nevertheless, the best solution is very similar to the case without the static load. No significant improvement is observed in terms of displacement or in the reduction of the displacement difference.

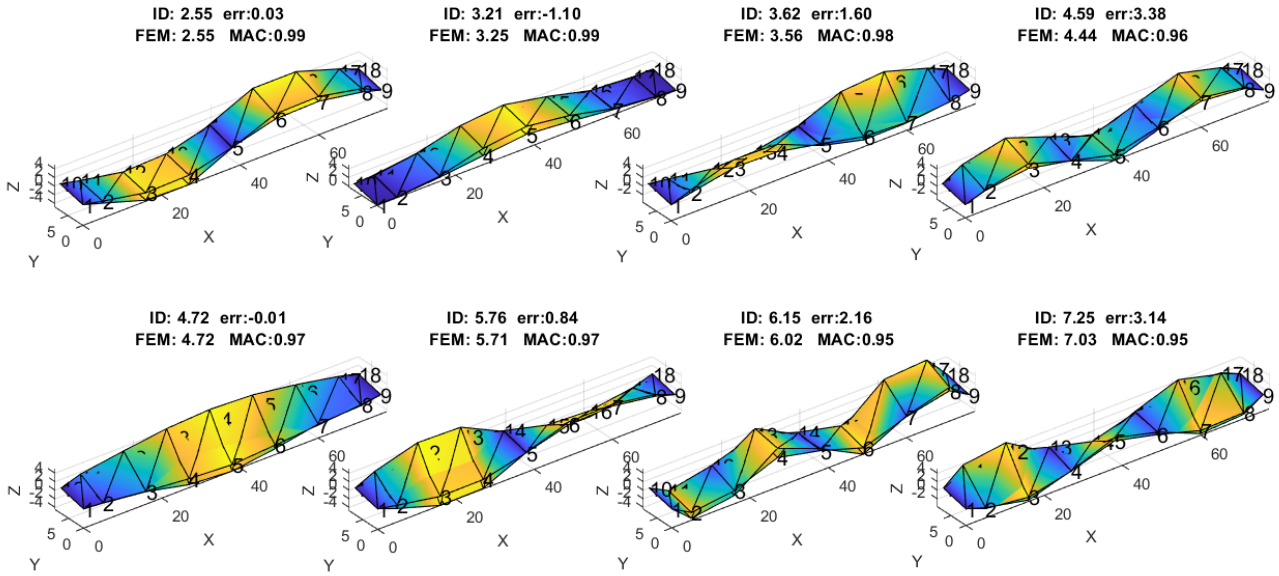

Figure 183: Mode shapes pre and post update procedure.

	No Load	Load
E_tendons [MPa]	197227	196794
E_Box [MPa]	25313	24615
E_Arch [MPa]	45179	44621
rho_box [kg/m^3]	2.64E+03	2600
Klong1b [N/mm]	1.18E+09	2.46E+09
Klong2b [N/mm]	1.17E+07	1.12E+07
Residual	0.2049	0.5105
Disp	5.4	5.6
err	25.00%	22.22%

Table 28: Result of the update procedure with six parameters.

After completing the six-parameter case, the analysis was extended to the three-parameter configuration. Based on the previous analysis, which identified an elastic modulus of 180,000 MPa using the parameters from the pre-intervention update, this value was selected for the analyses.

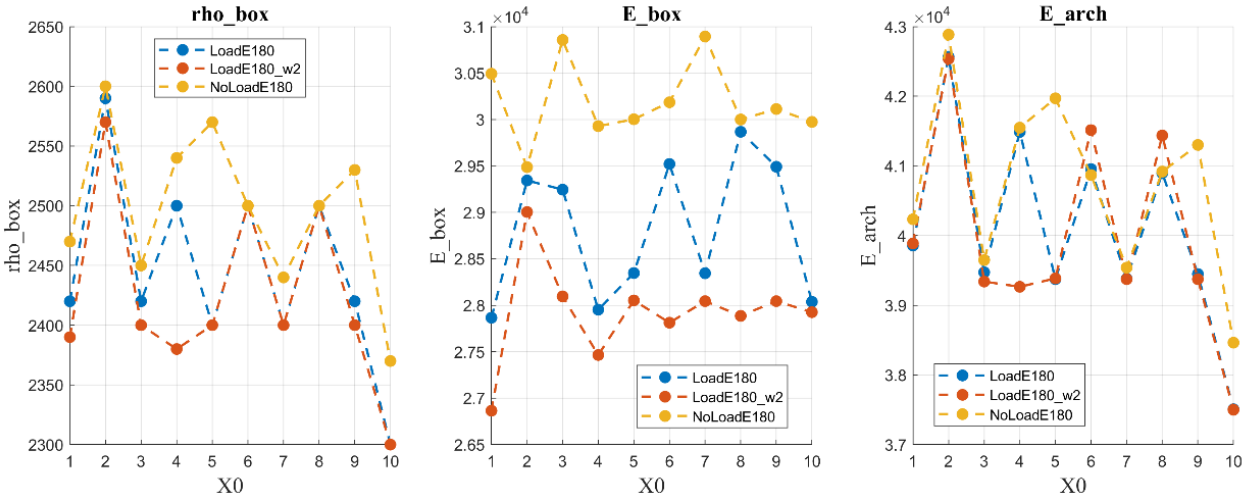

Figure 184: Variation of the solution of the three parameters.

As shown in Figure 184, both with and without the static load term, and even when increasing the weight of the load term (w2), no improvement in the stability of the solution is observed, except possibly for the elastic modulus of the box girder when the weight is doubled. This indicates that, in this case, including the static load term does not improve the stability of the solution by reducing it to a single minimum. This may be because the finite element model is not yet able to accurately represent the static behavior of the structure. Possible reasons include the hangers not being modeled with the same length as in reality, or modifications to the structure's geometry during rehabilitation, resulting in a stiffness distribution that is not accurately represented.

Even regarding differences in frequencies and mode shapes, the results are very good, as shown in the following figures. This holds true for both a load with a weight of 1 and a load with a weight of 2. The displacement obtained from the load test improves slightly when the weight is set to 2, but it is still not sufficient to fully match the measured results, as summarized in Table 29. The improvement in displacement differences comes at the expense of increased differences in frequencies and mode shapes.

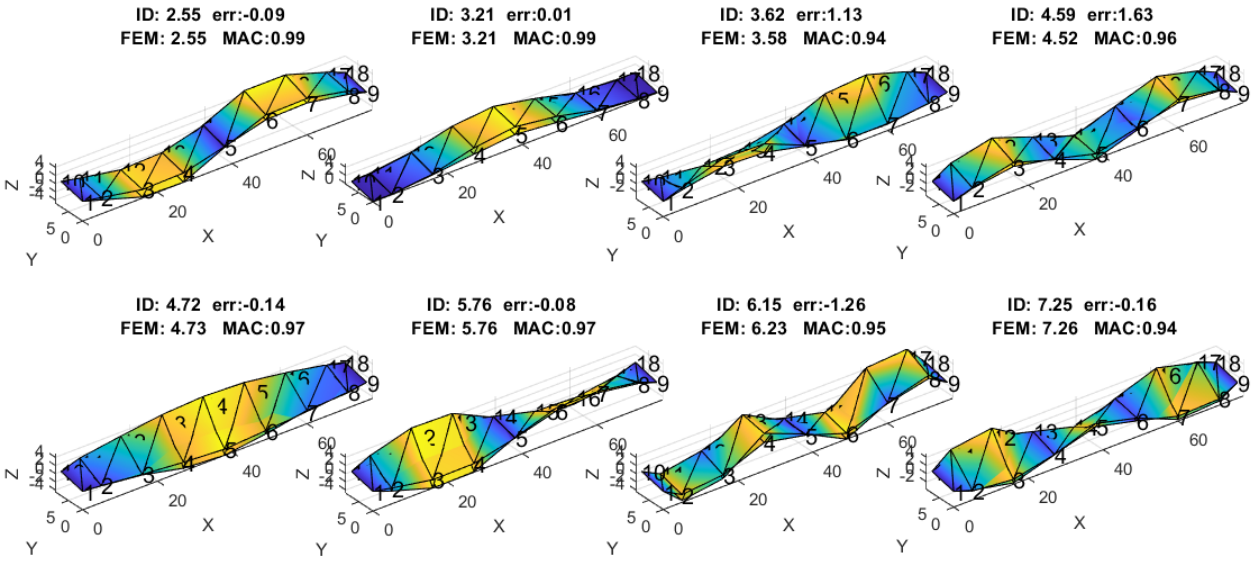

Figure 185: Load w1.

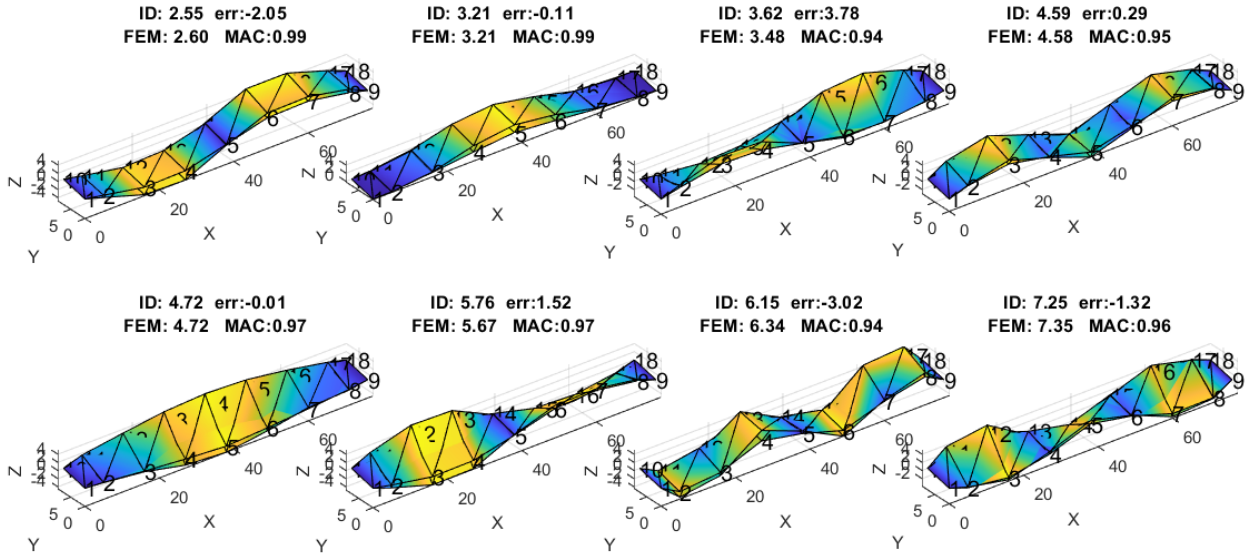

Figure 186: Load w2.

	No Load	Load	Load w2
rho_box [kg/m3]	2660	2590	2300
E_Box [MPa]	30352	29344	27925
E_Arch [MPa]	42714	42567	37500
Residual	0.2118	0.502	0.7642
Disp	5.24	5.54	5.83
err	27.22%	23.06%	19.03%

Table 29: Result of the update procedure with different weight on load error.

Further analyses could be conducted, for example, by investigating the effect of reducing the weighting of frequencies and mode shapes to achieve a better match for the load-displacement response. Additional analysis can be performed by considering all measured points during the static load cases and all load combinations. However, it is believed that the first step should be to verify whether the geometry of the hangers on site has changed during the intervention. Such geometric modifications could be the factor with the most significant impact on the results. Therefore, in this case, it is considered that these more detailed analyses could be addressed in future studies, building upon the findings of this thesis. This approach would allow for a more focused investigation, ensuring that any discrepancies are not primarily due to unaccounted changes in the actual structure, and would provide a stronger foundation for subsequent model refinements.

In addition to modifying the model, multi-objective updating procedures can be used to select the optimal solution. For example, if a seismic analysis is performed, one can choose the set of parameters that minimizes discrepancies in the dynamic behaviour. Conversely, if a static analysis is intended, the set of parameters that results in the smallest differences in the static response may be preferred.

Conclusions

The doctoral research presented in this thesis addresses the challenge of assessing and monitoring existing civil infrastructure through an integrated approach that connects large-scale observation with detailed structural modelling. The study demonstrates that combining satellite-based monitoring with finite element model updating provides both a scientific contribution to the field and a practical framework for infrastructure management. This work aims to bridge the gap between large-scale observation and detailed structural modelling to meet the growing demand for effective tools to ensure the safety of the built environment and to improve model updating, thereby reducing uncertainties between real structures and numerical models.

The first outcome of the research is the implementation of a complete and replicable framework for processing SAR data. The methodology enables the extraction of displacement time series, their interpolation into deformation surfaces, and their translation into practical indicators of potential structural vulnerability. This process has been tested in real territorial contexts, demonstrating that remote sensing can provide systematic and reliable information on the condition of large networks of buildings and infrastructure. The creation of standardized evaluation sheets further strengthens the approach's applicability, making it easier to integrate satellite evidence into everyday professional practice.

In addition to the remote sensing component, the research also applied the "Class of Attention" methodology proposed by the Italian Ministry of Infrastructure and Transport. This procedure was tested on real case studies to classify and prioritize structures according to regulatory and risk-based criteria. The application confirmed the usefulness of the method as a complementary tool for infrastructure assessment, providing a benchmark independent of satellite data but consistent with institutional practices and technical regulations.

The Canonica Bridge case study provided an opportunity to test the methodology proposed in Chapter 4 on a real structure. The bridge was examined using static load tests, operational modal analysis, and long-term sensor measurements collected before and after strengthening interventions. These data enabled the implementation and validation of a model updating procedure specifically developed in this research. The most innovative contribution of the thesis is the introduction of a static displacement term in the objective function of the finite element model updating. While traditional approaches rely mainly on dynamic information such as natural frequencies and mode

shapes, the inclusion of static data has improved the stability of the optimization process. The updated models demonstrated greater robustness and reliability, aligning more closely with the actual behaviour of the structure and reducing the risk of ambiguous solutions.

From a scientific perspective, the thesis proposes extending the conventional model updating framework by incorporating static information alongside dynamic parameters. Although further validation is needed, this integration may help address the limitations of relying solely on modal properties and could represent progress toward more stable and comprehensive updating strategies.

From a practical standpoint, the research presents a workflow that links different levels of structural assessment: satellite-based screening at the territorial scale, prioritization of assets according to existing regulatory criteria, and more detailed analysis using refined numerical models.

Although still at the research stage, the work has also highlighted limitations that suggest directions for further investigation. First, the precision of DInSAR measurements is not sufficient to rely directly on them for accurate evaluations of single structures and must be complemented with traditional in-situ sensors such as GNSS or inclinometers to obtain reliable displacement information. The proposed model updating strategy, which incorporates static response terms, deserves a more systematic evaluation. In particular, the role of the weighting between static and dynamic contributions in the objective function, its sensitivity to measurement uncertainties, and its practical applicability across different structural typologies require deeper analysis. Addressing these aspects will be essential to consolidate the robustness of the approach and to move closer to its adoption in engineering practice.

In conclusion, this thesis has examined the combined use of satellite-based monitoring techniques and finite element model updating within a broader framework for infrastructure assessment. The research demonstrates how various levels of analysis, from large-scale screening to detailed numerical modelling, can be integrated into a single workflow. Although the approach is still experimental, the findings indicate that such integration could improve current practices in evaluating and managing civil structures, provided its limitations are further investigated and its applicability tested across a broader range of case studies.

Acknowledgements

The author thanks SITRASB S.p.A. (Società Italiana Traforo del Gran San Bernardo) for granting access to data from the T2 section of the Gran San Bernardo highway, which were essential for this study. Special thanks are also extended to the Province of Bergamo and to Ing. D. Chiodi for their availability and for providing surveys on the Canonica Bridge. The research presented here used material analyzed in projects that are part of the Agreement between the High Council of Public Works (CSLLPP) and the ReLUIS Consortium. The contents of this work represent the author's views and do not necessarily reflect the opinions of the individuals and institutions acknowledged.

Appendices

Appendix 1

Stick Model

As part of the Model Update, the use of that method has also been investigated for Damage Detection. A preliminary example of a simplified building was constructed in order to perform initial analyses on how the Model Update could be used to estimate stiffness reductions due to damage. In this appendix, preliminary work is presented using a simplified building scheme, where the Model Update was carried out on selected parameters to assess whether this simplified model is able to capture stiffness reductions. In this section the study is described that was carried out to create a simplified finite element model named 'Stick Model' able to describe with good approximation the dynamic behaviour of a real structure. By updating some target parameters through optimization algorithms, it is possible to make the modal parameters of the Stick Model converge to the modal parameters of the considered structure (obtained for example through dynamic identification), doing a matching between real structure and simplified model. In this way it is possible, for example, to perform continuous monitoring with possible identification of structural damages without the need of a more complete, complex and expensive model.

In literature there are similar studies on simplified models used for different purposes and realized with different methods, also by using mathematical models. An example is reported in [119] where a continuous Timoshenko beam element was considered to describe the behaviour of a multi-story building, taking the stiffness of the model from the equations governing the elastic problem applied to the building [120]. Other authors [121] [122] used the Hamilton energy variation principle to describe and solve the elastic problem of a continuous beam element, expressing the stiffness as parameters to be optimized by minimizing the difference between estimated modal parameters and target modal parameters. Also the soil-structure interaction is considered in [123], using flexible constraints with stiffness estimated by numerical optimization. Other methodologies use non-linear analyses to calibrate the simplified model, by assigning as constitutive law of intermediate constraints the capacity curves obtained from the analyses. This approach has been also used for large scale analysis and for estimation of economic losses related to exceptional events such as earthquakes [124], [125], [126], [127]. Such models are very interesting because they allow to represent a complex

structure with simplified approaches, and so to perform studies and considerations with reduced computational effort and analysis time.

In the present study, the simplified model was thought as a Stick Model, that is a series of beam-type elements fixed at the base and with intermediate constraints at the floor levels, able to represent the stiffness of a frame structure. This model can be later investigated and adapted also to represent structures like bridges. The idea is then to realize a model that is able, through mathematical optimization, to modify some parameters like the stiffness of the beams and of the intermediate constraints, and to represent a more complex building of which only frequencies and mode shapes are known, obtained through dynamic identification.

Model Description

In a first phase, the question was how to realize this model and how to insert the constraints able to represent in the best way a frame structure, in particular the stiffness due to the presence of columns and beams. After several trials it was decided to build the model as in the scheme shown in Figure 187.

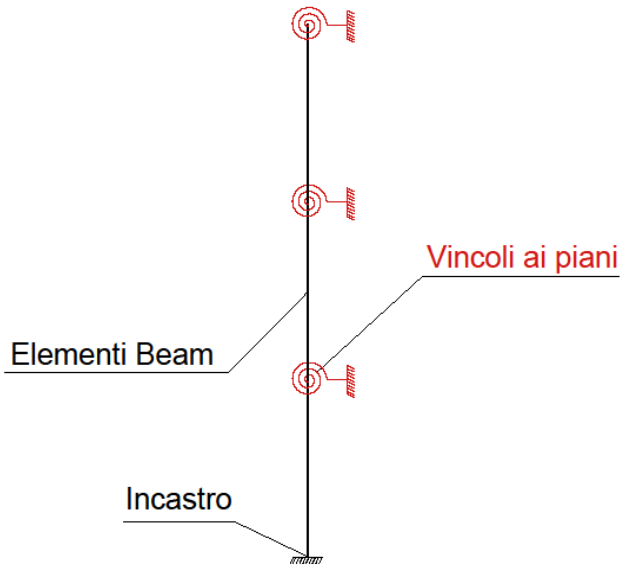

Figure 187: Stick Model scheme.

The model, created with the software Opensees, is then composed of beams (beam elements) fixed at the base, with constraints at the intermediate floors, realized with rotational springs with elastic law, that represent the rotational stiffness of the structure. This stiffness, obtained through the coefficients of the stiffness method, was calibrated considering only the rotational contribution of the beams, since

the contribution of the columns is already considered because a physical beam element is present in the model. A first starting point for assigning the stiffness to the Stick Model can be to assign to the elastic modulus of the beams the elastic modulus of the columns of the considered building multiplied by the number of columns (modelling the beam with the real dimensions), and to the rotational stiffness of the intermediate constraints assign the stiffness due to the beams, calculated following the scheme proposed in Figure 188.

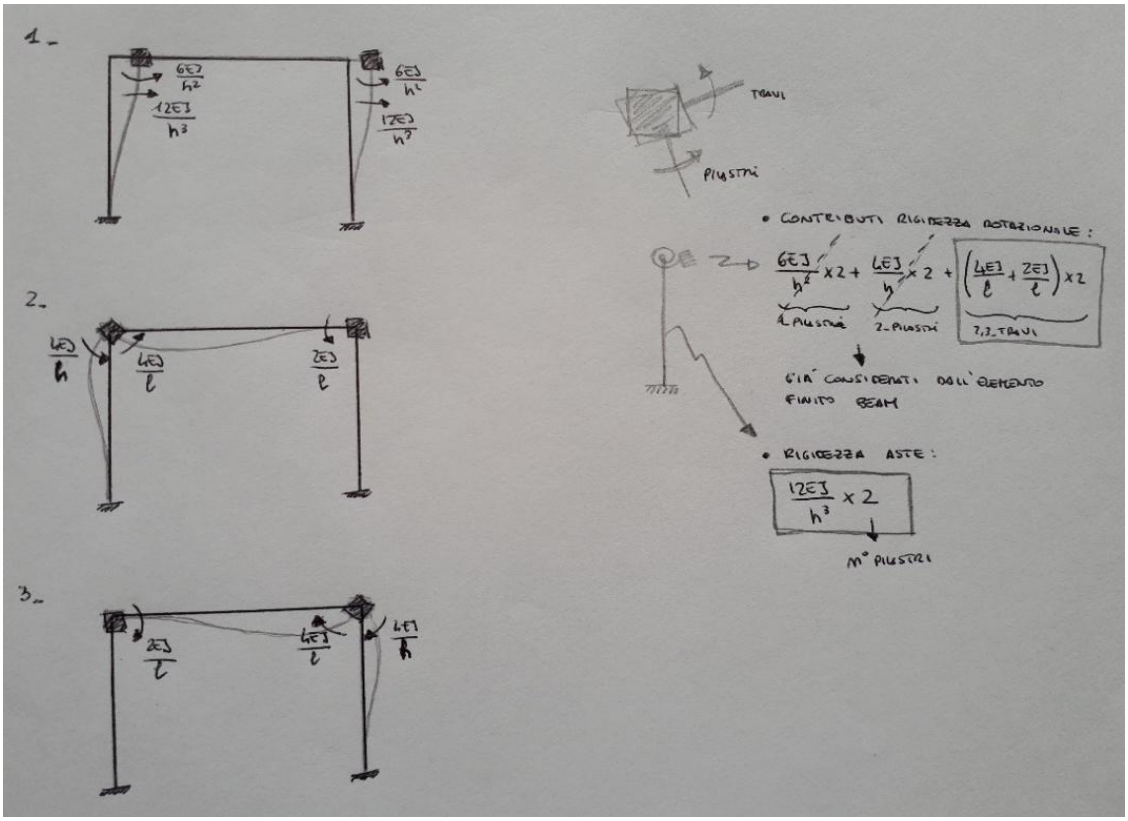

Figure 188: Stick Model stiffness scheme.

The masses were assigned at the intermediate nodes equal to the masses of the real structure. To validate the hypothesis, modal analyses (simulated in MidasGen) were carried out considering several frames with one, two, three floors and three floors with two spans, comparing the results obtained from the complete model and from the relative Stick Models, obtaining satisfactory results. In fact, the frequencies and mode shapes obtained from eigenvalue analysis of the frame were practically identical to the frequencies and mode shapes of the Stick Models. This starting point (initial stiffness values) could also be estimated by numerical optimization, but given the size of the optimization problem (two parameters for each floor) and the computational effort, a simple method was sought, easily applicable to a real structure, to have a good starting point. The study was then moved to a more complex frame, described in the following figure.

Element	Dimension	Rebars
Column	30cmx30cm	4 ϕ14 / 4 ϕ14
Spine beam	70cmx25cm	4 ϕ14+4 ϕ18 / 4 ϕ14+3 ϕ18
Edge beam	40cmx25cm	4 ϕ14 / 4 ϕ14

Figure 189: RC Structure.

The structure was realized in Midas environment and, in a first phase, only one frame was considered, the central one; later the possibility will be evaluated to insert an additional parameter (rotational stiffness) at the floors, which allows to represent the torsional stiffness of the building and therefore to consider the three-dimensional problem. The frame, besides being modelled in Midas, was also reproduced in OpenSees environment, in order to better handle series analyses and because it is more suitable for implementing the algorithm described afterwards. By estimating the stiffness parameters of the Stick Model as described previously and performing eigenvalue analyses on both the complete model and the simplified model, practically identical results are obtained, both in terms of frequencies and mode shapes, as shown in Figure 190.

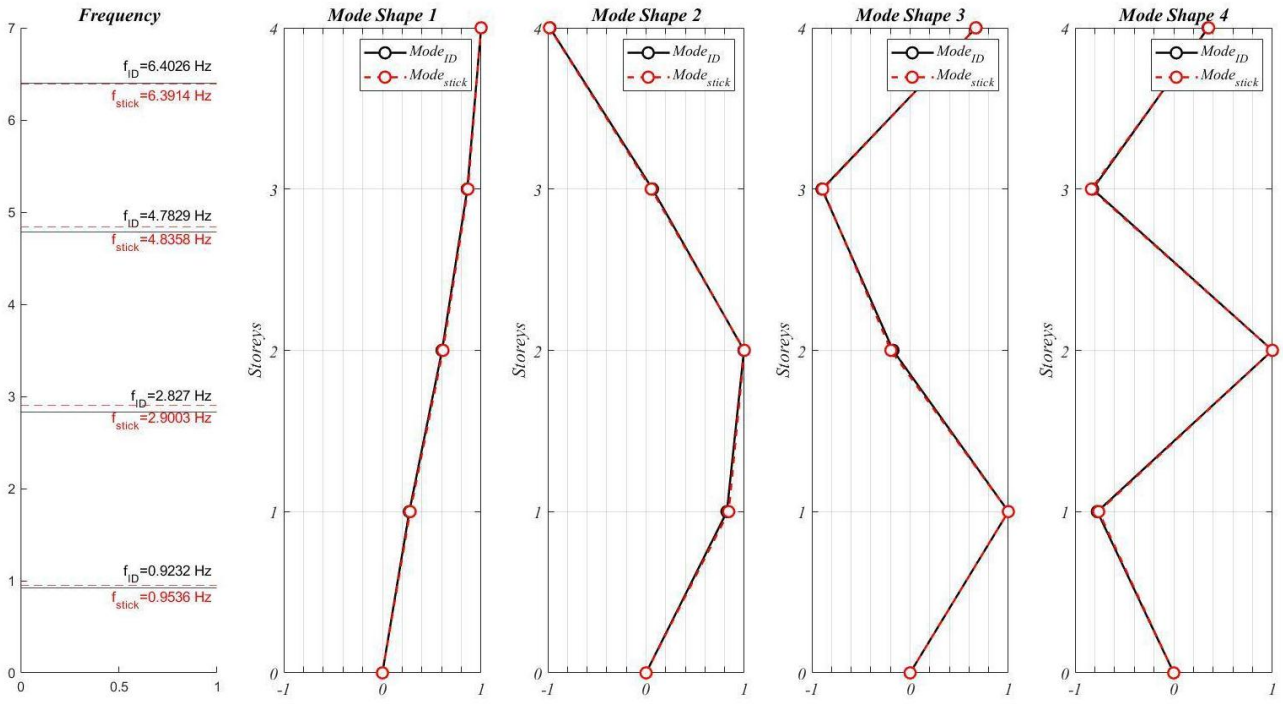

Figure 190: Frequencies and mode shapes of the real model and of the Stick Model with estimated target parameters.

In the document, the parameters derived from the complete structure model are indicated as fID, since in view of practical applications these parameters will be obtained from dynamic identification.

Optimization

After addressing the topic of modelling, the work moved to the part concerning optimization. The idea is to build an objective function that will then be minimized by mathematical optimization, in such a way as to minimize the difference between frequencies and mode shapes of the Stick Model and of the real structure, obtaining the parameters (stiffness of beams and of intermediate constraints) that allow to represent the behaviour of the real structure. Therefore, thinking of minimizing the difference between input data (obtained from the structure) and data obtained by numerical analysis of the Stick Model, the objective function was written in the following form:

$$f(K) = \|Data_{ID} - Data_{stick}(K)\|^2$$

"That is, by denoting with K the vector containing the target parameters, one seeks to minimize the quantity

$$res(K) = \sum_{i=1}^{n} (r_{f,i})^2 + \sum_{i=1}^{n} (r_{\phi,i})^2$$

A function of the stiffness parameters *K* and where r_f e r_ϕ are respectively the residuals on the frequencies and the modal shapes, and have been chosen as

$$r_f = \frac{f_{ID,i} - f_{stick,i}}{f_{ID,i}} \qquad r_\phi = 1 - MAC_i$$

Obtaining

$$res(K) = \sum_{i=1}^{n} \left(\frac{f_{ID,i} - f_{stick,i}}{f_{ID,i}} \right)^2 + \sum_{i=1}^{n} (1 - MAC_i)^2$$

The choice of the residuals was then analysed by trying to change the quantities involved, but with less satisfactory results.

The function was then implemented in Matlab environment; more generally, a set of functions was created to connect Matlab and OpenSees, to have a single algorithm able to perform the optimization based on the result of the finite element analysis. The procedure is better described in the following diagram and like to what is done in the previous chapters.
The final algorithm works in the following way: the target parameters, i.e. the modal parameters of the real structure, are given as input to the function containing the objective function and are set as targets. A first analysis is performed by another function that calls and executes the analysis of the simplified model in OpenSees, using the estimated stiffness parameters (this phase could be skipped by directly launching the optimization and letting the algorithm estimate the initial parameters, but in this way the computational effort is reduced, also considering the size of the problem). A first estimation of the parameters is therefore performed through optimization, which will converge to values very close to the manually estimated ones. The optimization is carried out with the PatternSearch algorithm available in Matlab, which in turn recalls the model in OpenSees and performs the eigenvalue analysis of the model with the updated parameters at each iteration. Once the difference between estimated parameters and target parameters is below a tolerance, the algorithm gives back the stiffness values of the Stick Model that represent the real frame.

Application

This algorithm is now described applied to the model. The first step is to perform the eigenvalue analysis of the complete model and obtain frequencies and mode shapes. In practice, the modal parameters will be obtained from dynamic identification, using accelerometers placed on the building and applying a proper procedure to extract frequencies and mode shapes.

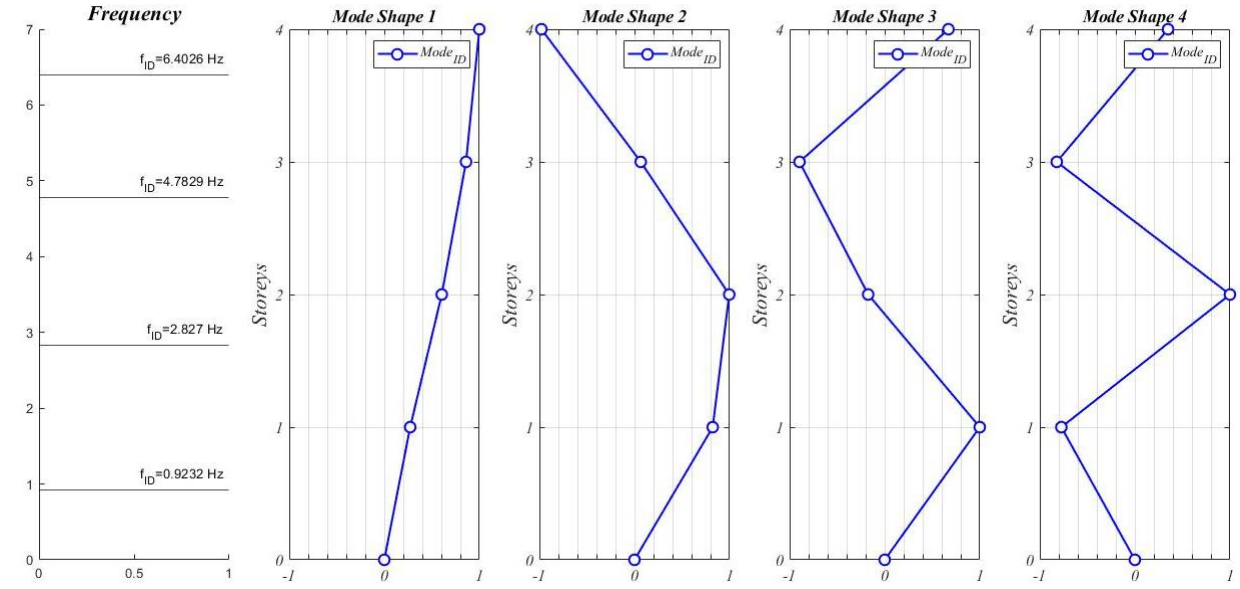

Figure 191: Frequencies and mode shapes of the real model.

First Stick Model analysis with estimated parameters.

After identifying the target frequencies and mode shapes, a first analysis of the Stick Model is performed using as parameters the manually estimated ones described before.

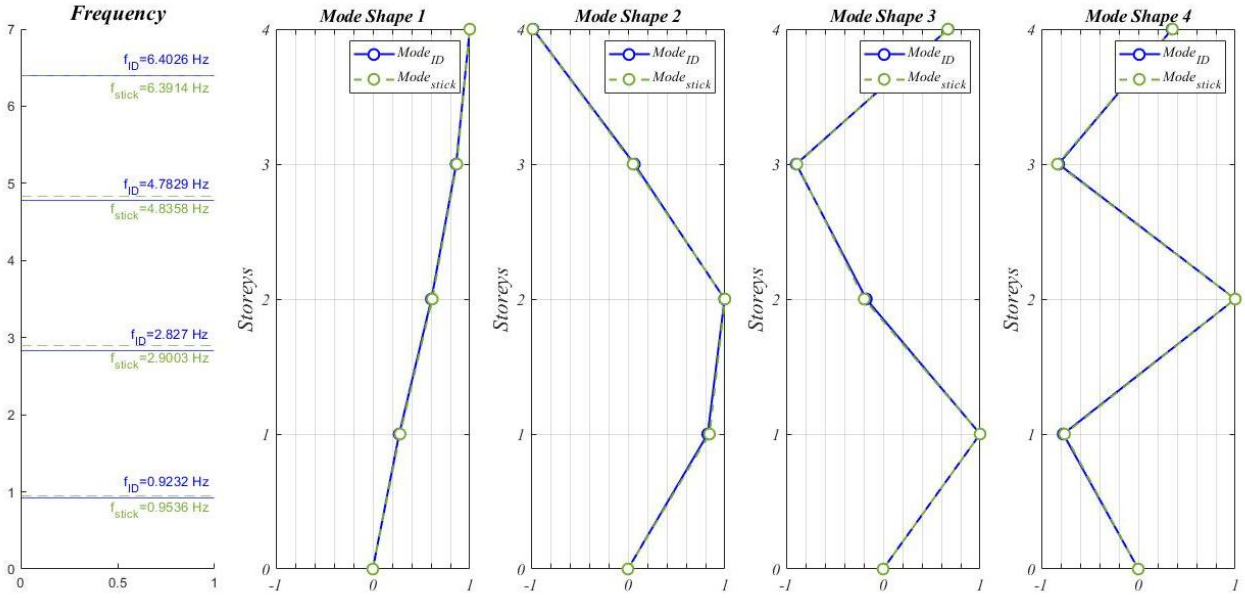

Figure 192: Frequencies and mode shapes of the real model and of the Stick Model with estimated target parameters.

Numerical optimization.

Although the estimated parameters give very similar results in terms of modal analysis of the Stick Model, the mathematical optimization is performed, in order to minimize the objective function described earlier and obtain the correct values.

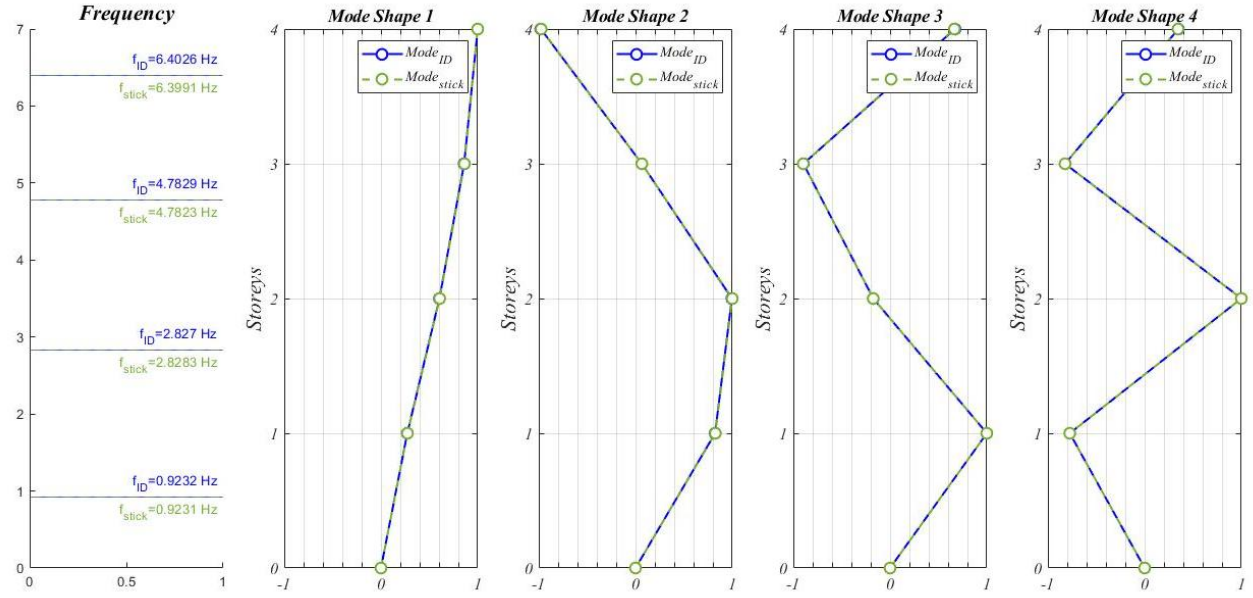

Figure 193: Frequencies and mode shapes of the real model and of the Stick Model with target parameters obtained from optimization.

At this point, the stiffness parameters of the beams and the rotational stiffness of the Stick Model are available, allowing to represent the initial model and making it usable for further developments. For example, some of the damage indexes could be applied and the results evaluated through simplified modelling. The real goal of the study is not only to represent the initial model, but also to detect and localize possible damage in the structure using the model update procedure [128] [99], [129], [130]. To do this, considering the vector of the target parameters K, a damage could be evaluated by associating it with the reduction of the initial stiffness of the target parameters.

$$damage = \frac{K_{iniziale} - K_{finale}}{K_{iniziale}} \cdot 100$$

To do this, the initial model was modified: in a first case, the stiffness of beams and columns was reduced by 50% (by directly acting on the elastic modulus, decreased from 30,000 MPa to 15,000 MPa); in a second case, the stiffness was reduced by 66% (⅔) for the beams and only for the columns at the first floor; and in a third example, the stiffness of beams at the first and second floor was

reduced to 1/3. In this way, by using the previously developed algorithm and applying the formula, it is possible to evaluate whether this Stick Model is able not only to dynamically represent a complete model but also to localize the damage, distinguishing whether the damage occurs on the columns or on the beams.

Global stiffness reduction

By reducing the stiffness of beams and columns by 50% and performing a new modal analysis, the following frequencies and mode shapes are obtained (indicated as ID, meaning a new set of identified modal parameters, in view of practical application). As expected, since the stiffness is reduced, the frequencies are also reduced.

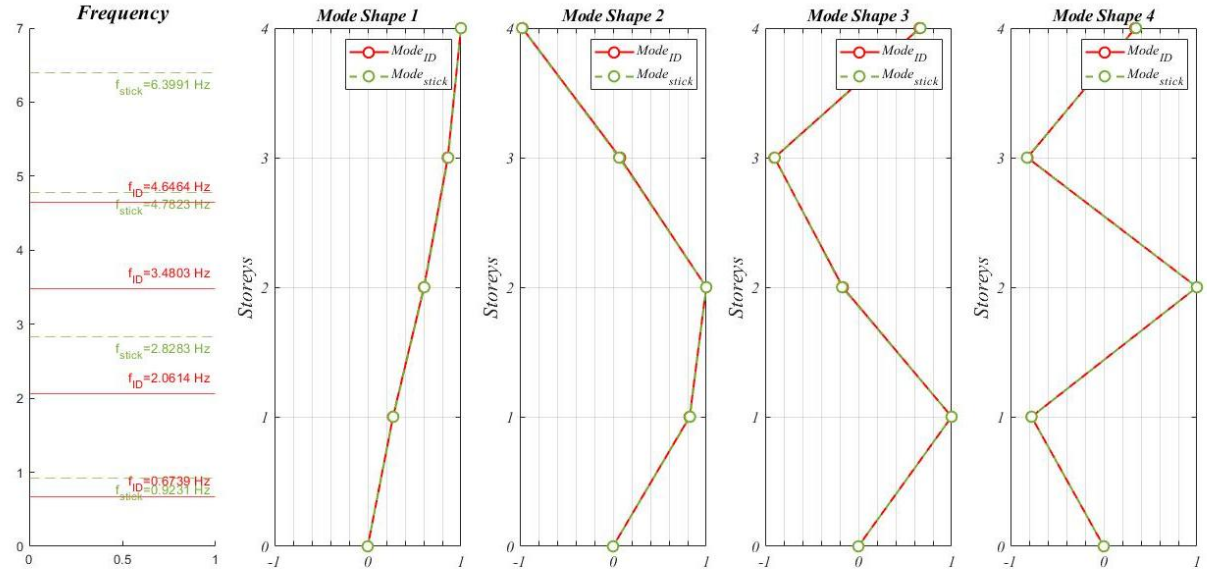

Figure 194: Frequencies and mode shapes of the real model with global stiffness reduction and of the Stick Model with initial target parameters.

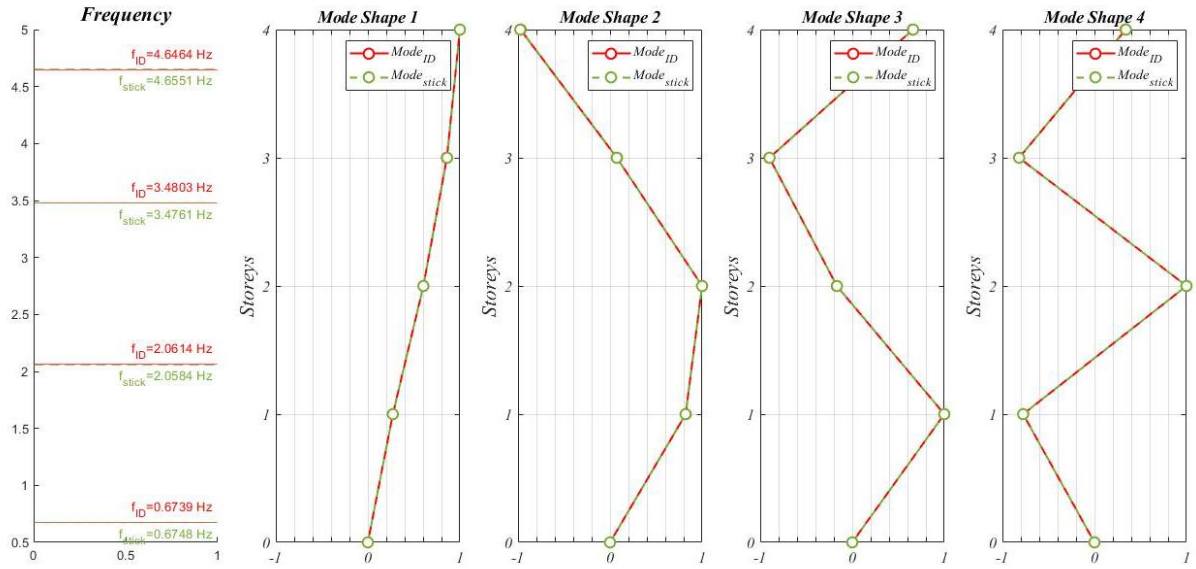

Figure 195: Frequencies and mode shapes of the real model with global stiffness reduction and of the Stick Model with target parameters obtained from optimization.

By performing the optimization, the stiffness parameters of the beams and of the intermediate constraints are updated, obtaining a matching between the real model and the Stick Model. It can be seen that frequencies and mode shapes are practically identical like see in Figure 195. The optimization carried out with the PatternSearch algorithm also provides the following parameters, which are compared with the initial target parameters to assess the possibility of identifying the damage.

E	125900	128076	127180	125900
Kr	273641430528	272542522880	269581344256	285083491840

Table 1: Limits for possible damage in buildings in relation to parameter teta.

On the x-axis is indicated the percentage reduction of the parameter with respect to the initial value.

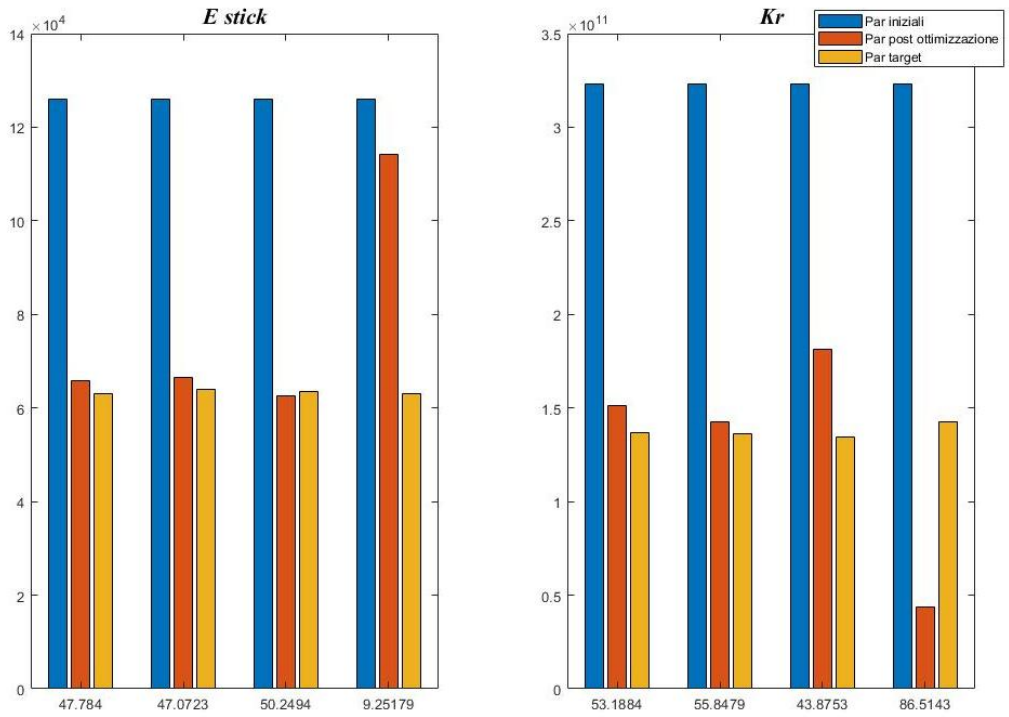

Figure 196: Difference between initial target parameters and identified parameters after stiffness reduction.

It can be seen that, apart from the top floor where the rotational stiffness is reduced more than the beam stiffness, the stiffness values are reduced in a homogeneous way and close to what was expected. In this case, looking at the Stick Model results, one could hypothesize a global reduction of stiffness associated with a general damage of the structure affecting both beams and columns. The issue of the incorrect reduction at the top floor could be due to the fact that this combination of rotational stiffness and beam stiffness generates a minimum in the objective function surface, which is not discriminated by the algorithm used; this aspect will need to be further investigated.

In the next examples, the aim is to understand whether it is possible to recognize damage at a specific floor and to distinguish whether it occurs in the beams or in the columns.

Stiffness reduction at one floor

By reducing the stiffness of beams and columns by 66% (reduction of 2/3 of the elastic modulus, from 30,000 MPa to 10,000 MPa) at the third floor, the new identified parameters are obtained:

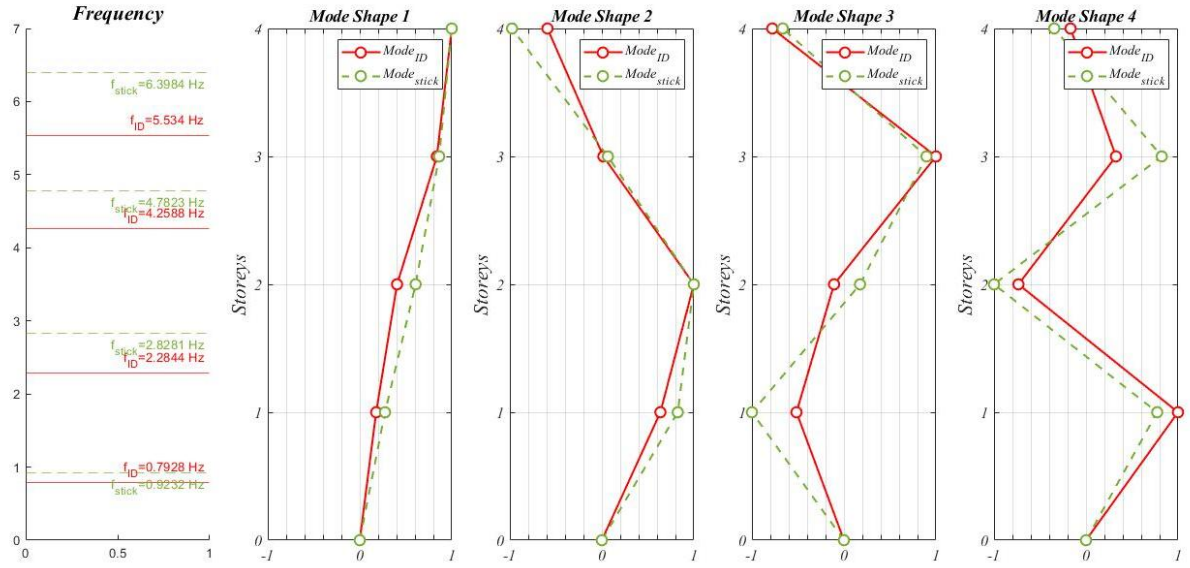

Figure 197: Frequencies and mode shapes of the real model with stiffness reduction at the third floor and of the Stick Model with initial target parameters.

Then, launching the optimization with PatternSearch and evaluating the differences between initial and post-optimization parameters:

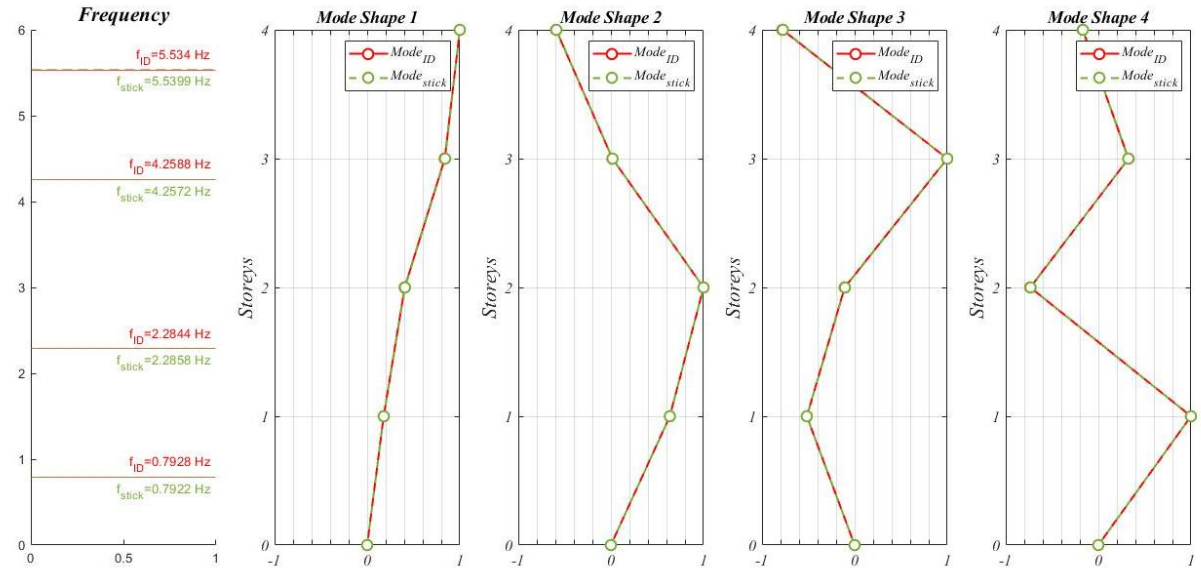

Figure 198: Frequencies and mode shapes of the real model with stiffness reduction at the third floor and of the Stick Model with target parameters obtained from optimization.

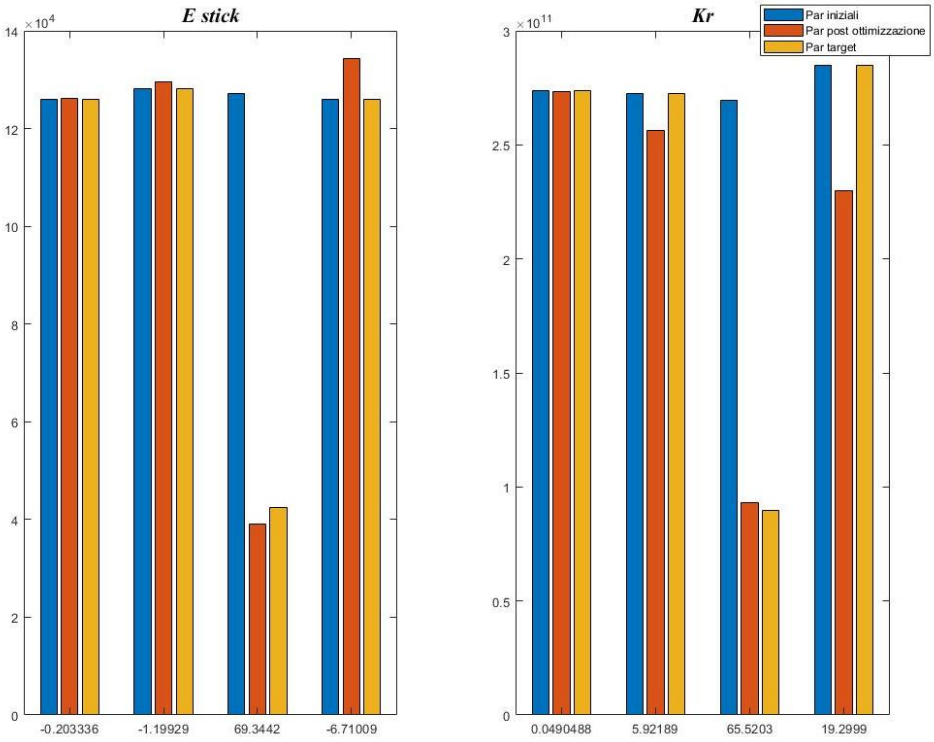

Figure 199: Difference between initial target parameters and identified parameters after stiffness reduction at the third floor.

It is possible to see in Figure 199 that, despite some inaccuracies, the reduction of stiffness at the third floor is visible, affecting both the parameter related to beam stiffness and the one related to rotational constraints. This suggests damage in both beams and columns, which is exactly what was assumed. In this case, it can be noted that some parameters, although by just a few percentage points, have increased, which would indicate an increase of stiffness that is not physically possible. The explanation could be similar to the global stiffness reduction case; for this reason, in the next section the effect of target parameters on frequencies and mode shapes is investigated.

Stiffness reduction of beams at the first and second floor

In this case, the aim is to see if it is possible to discriminate between damage in beams and damage in columns. By reducing the stiffness of beams at the first and second floors, the following new identified parameters are obtained:

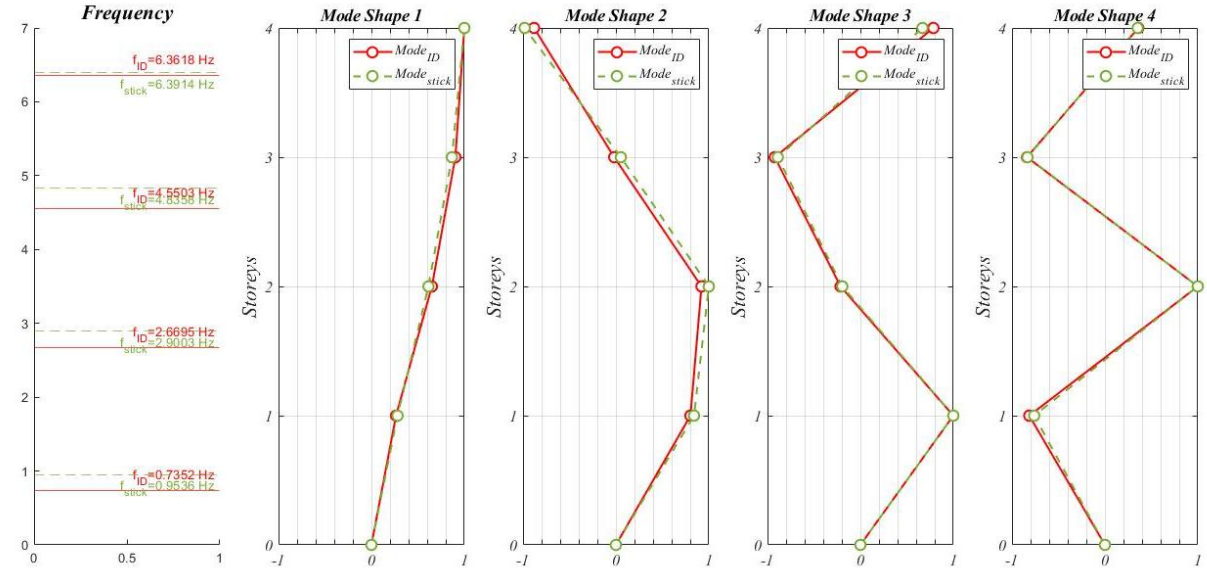

Figure 200: Frequencies and mode shapes of the real model with stiffness reduction of beams at the first and second floors and of the Stick Model with initial target parameters.

Then, launching the optimization:

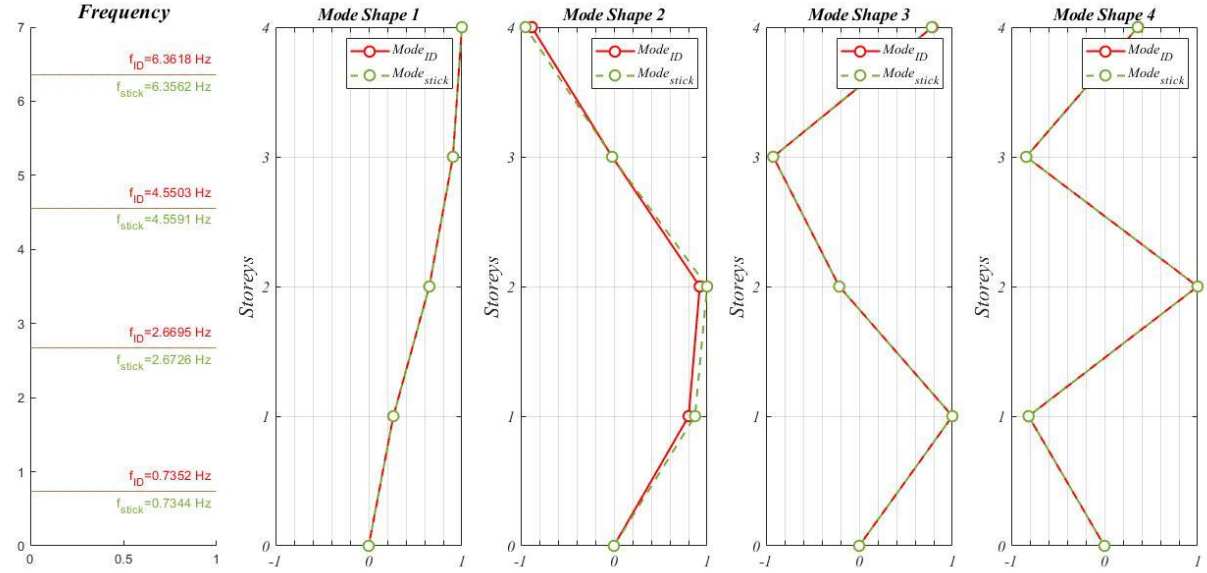

Figure 201: Frequencies and mode shapes of the real model with stiffness reduction of beams at the first and second floors and of the Stick Model with target parameters obtained from optimization.

And obtaining the graph related to the differences between initial and final parameters:

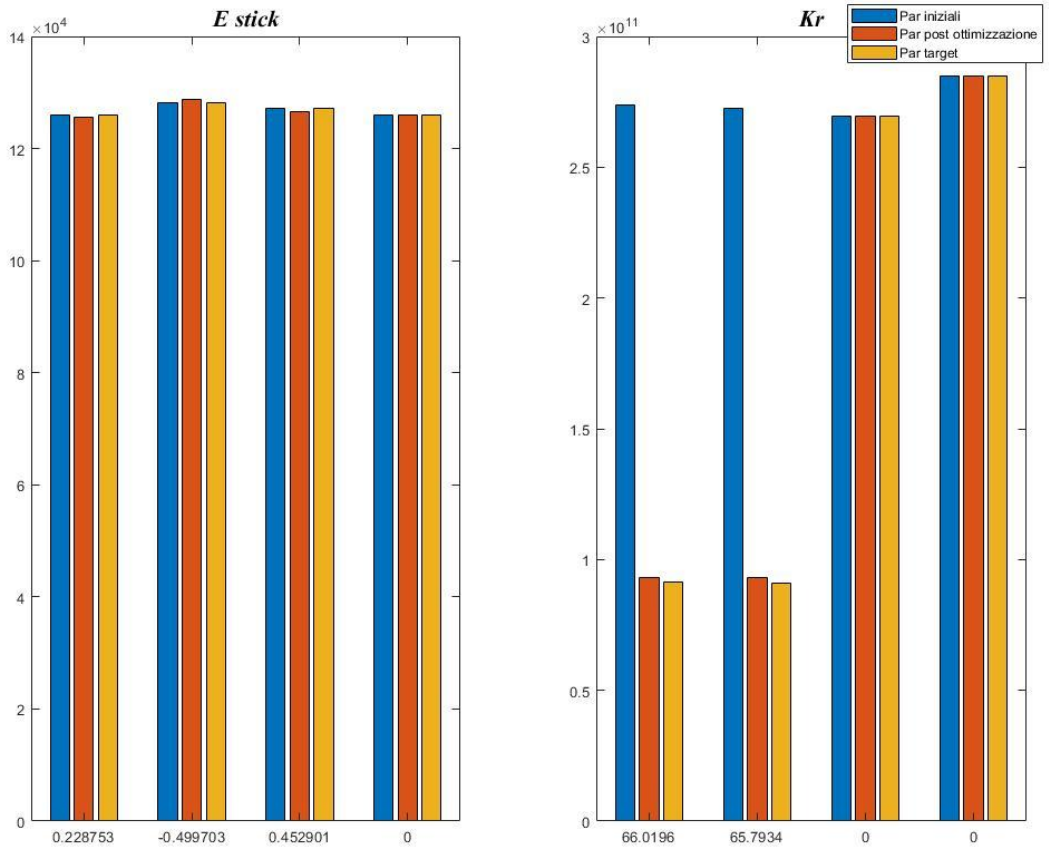

Figure 202: Difference between initial target parameters and identified parameters after stiffness reduction of beams at the first two floors.

It can be seen that the reduction of parameters occurs only for the rotational constraints, which suggests damage only at the level of the beams, exactly as expected. Considering the three presented examples, it is possible to see that the simplified model provides satisfactory results, being able to discriminate damage between beams and columns with good accuracy.

Sensitivity analysis of target parameters

In addition to what has been shown above, a sensitivity analysis was performed to evaluate the effect of the chosen target parameters on frequencies and mode shapes. To do this, the previously developed code was modified and, by varying one parameter at a time from 10% to 200% of the initial value, the following figures were obtained. In Figure 203, the percentage variation of the considered parameter is shown on the x-axis and the corresponding frequency value on the y-axis; in each graph four lines are present, corresponding to the four frequencies of the model.

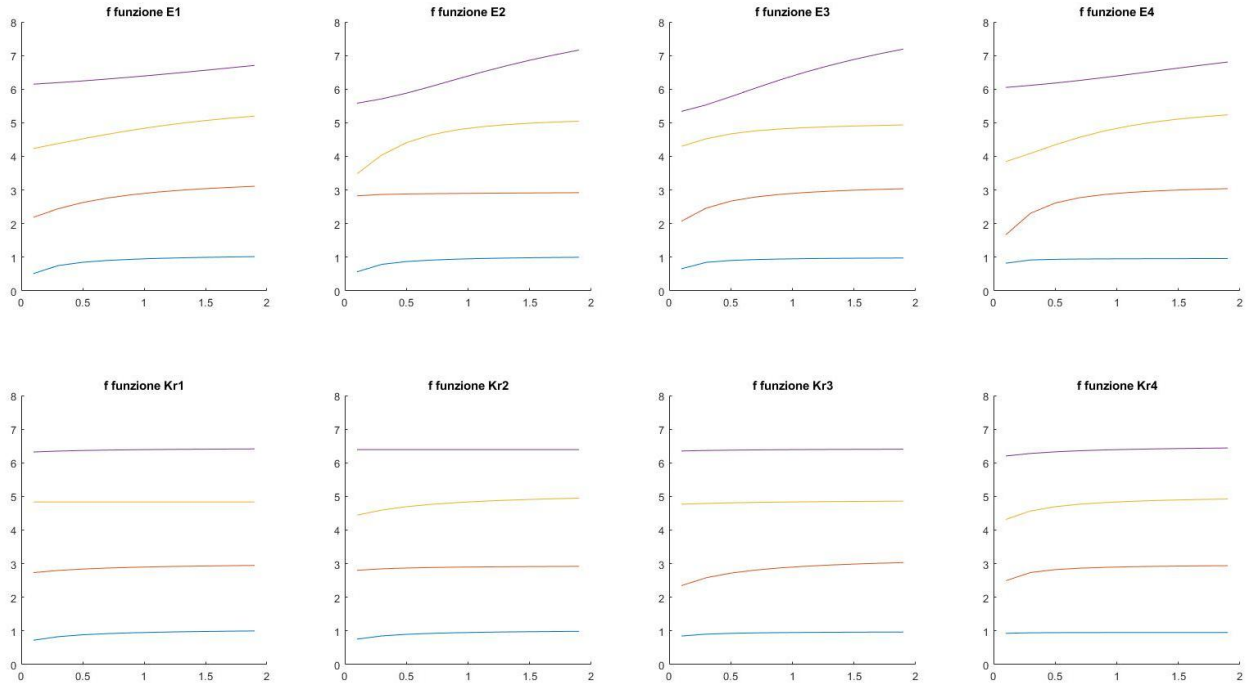

Figure 203: Frequencies as a function of the different target parameters.

Looking at the frequency values, it is possible to notice that they are more dependent on the stiffness of the columns compared to the rotational stiffness parameters, with a more significant variation for the third and fourth frequency. The rotational parameters practically do not affect the fourth frequency, while they have more impact on the third frequency, which, considering the associated mode shape, is reasonable.

For the mode shapes, each deformed shape corresponding to the amplified/reduced value of the parameter is shown. Figure 204 and Figure 205 are divided into four blocks related to the four mode shapes.

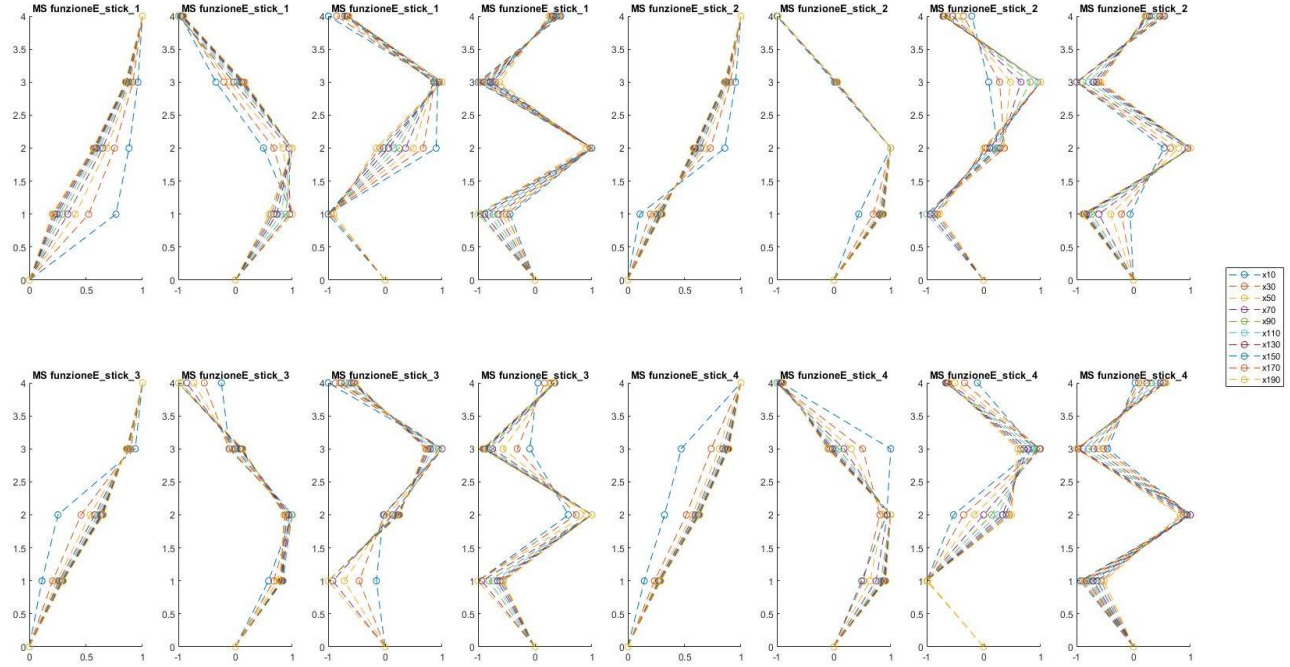

Figure 204: Mode shapes as a function of the different target parameters (E columns).

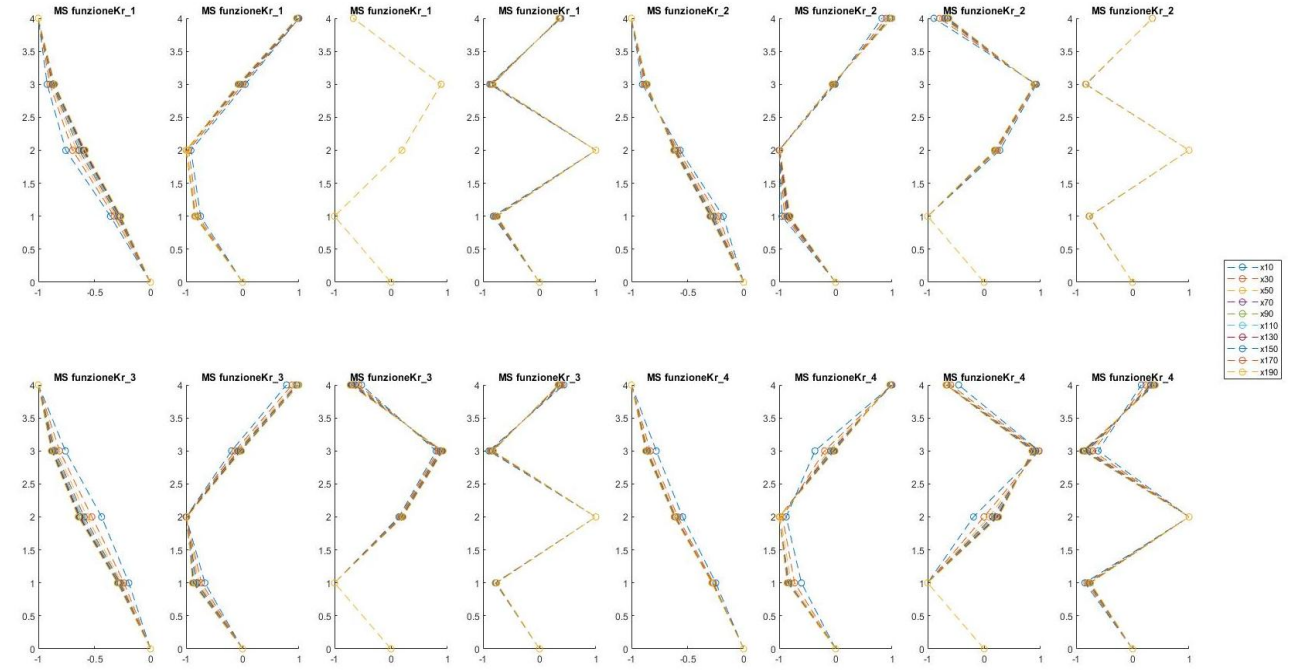

Figure 205: Mode shapes as a function of the different target parameters (K rotational).

It is possible to see also in this case that the stiffness of the columns has a stronger influence on the shape of the modal deformations compared to the rotational constraints, which in some cases have no effect (e.g., third mode for Kr1 and fourth mode for Kr2). It is visible that in some cases the stiffness changes the curvature of the deformation even only in some parts, for example in the first mode

related to the parameter Estick_4, where for very low values there is a sort of cantilever at the fourth floor that tends to deform more than the rest of the structure. In addition to these parameters, it is intended in the future to investigate also the variation of modal curvature, considering also the possible inclusion of infill walls as an additional structural parameter.

Removal of the assumption on frequencies and mode shapes

As mentioned previously, one of the fundamental assumptions of the procedure was the knowledge of the frequencies and mode shapes, hypothesizing that they were obtained through dynamic identification. In reality, this may not always be correct, as it might not be easy to identify all frequencies and mode shapes for example in rigid buildings. To investigate the influence of this assumption, the objective function was modified by introducing weights on the vector of frequencies and mode shapes, so that by inserting a zero, that specific frequency/mode shape is excluded from the residual calculation in the objective function. A test was then conducted considering only the first two frequencies and the first mode shape, and the procedure was reapplied in the cases of stiffness reduction to see whether the optimization still identifies the correct minimum of the objective function.

Global stiffness reduction

For the case with global stiffness reduction, the following results were obtained:

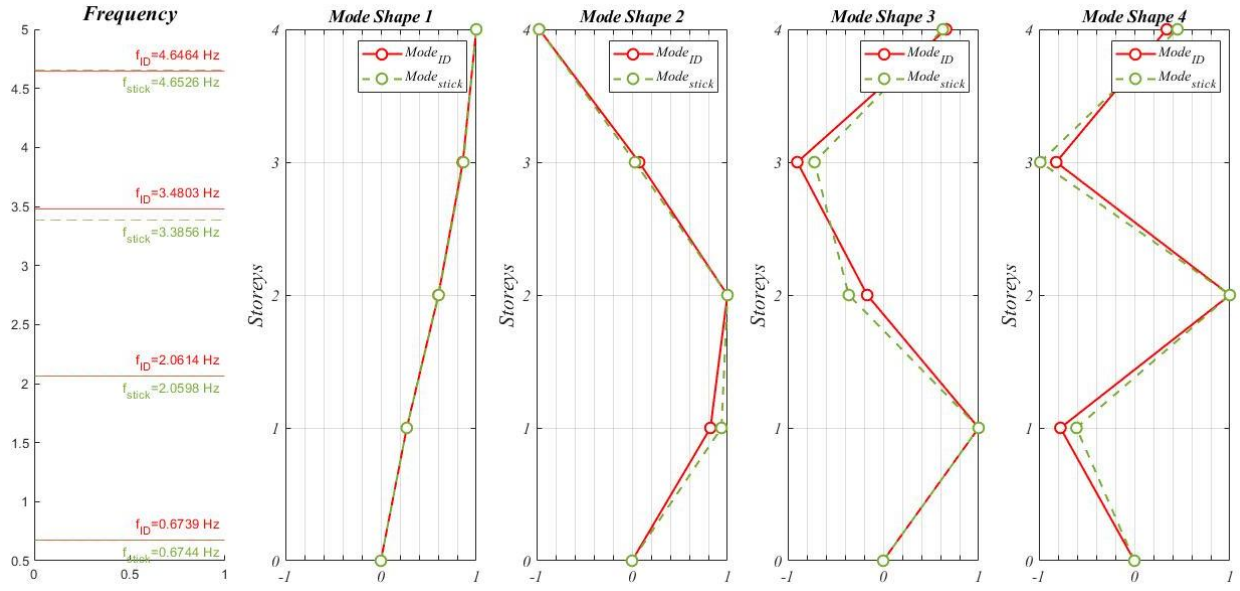

Figure 206: Frequencies and mode shapes of the real model with global stiffness reduction and Stick Model with target parameters obtained from optimization, considering two frequencies and one mode shape.

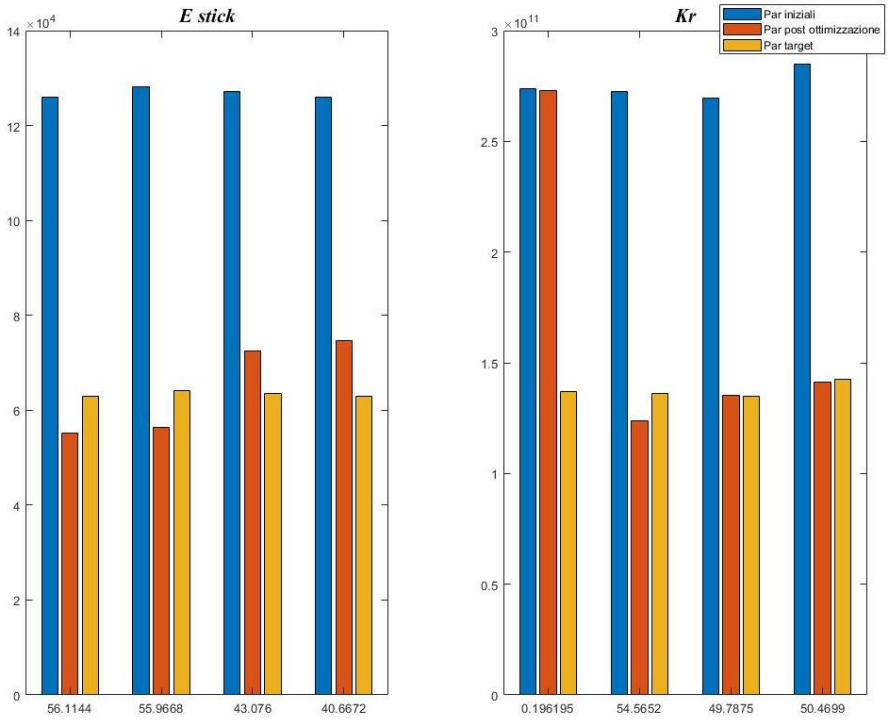

Figure 207: Difference between initial target parameters and identified parameters after global stiffness reduction, considering two frequencies and one mode shape.

Unlike the case where all modal parameters are considered in the calculation, in this case there is less uniformity in the reduction of stiffness parameters, with an error in the reduction of beam stiffness at the first floor. Despite this, the results are still acceptable, and further investigation could improve the estimates.

Stiffness reduction of beams at the first and second floors

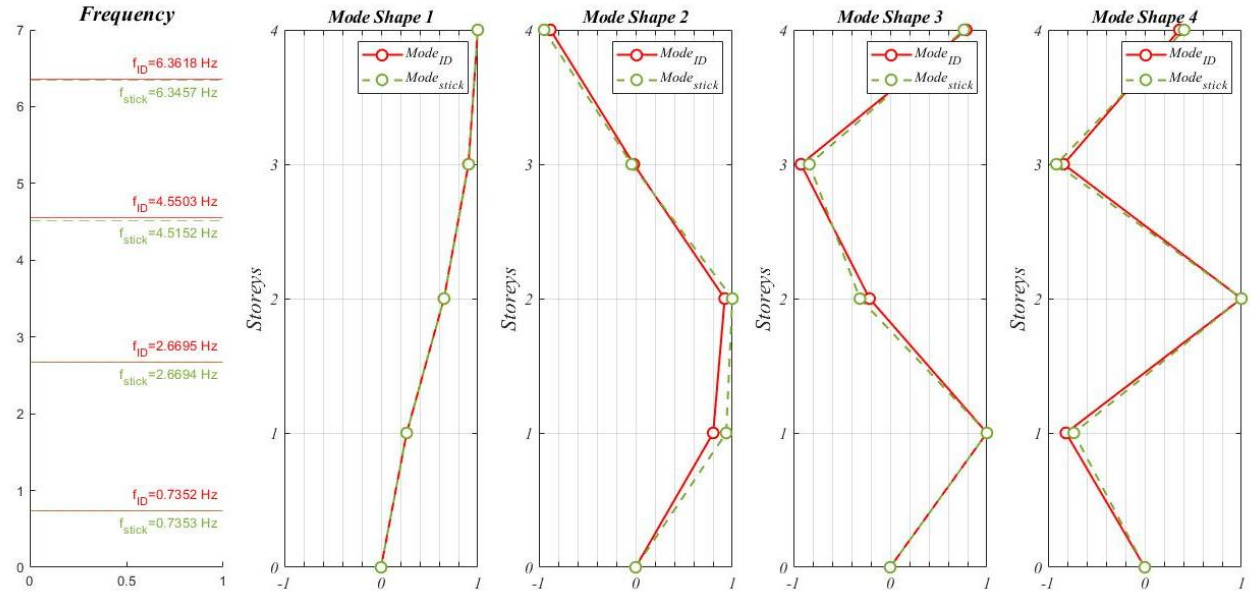

Figure 208: Frequencies and mode shapes of the real model with stiffness reduction of beams at the first and second floors and Stick Model with target parameters obtained from optimization, considering two frequencies and one mode shape.

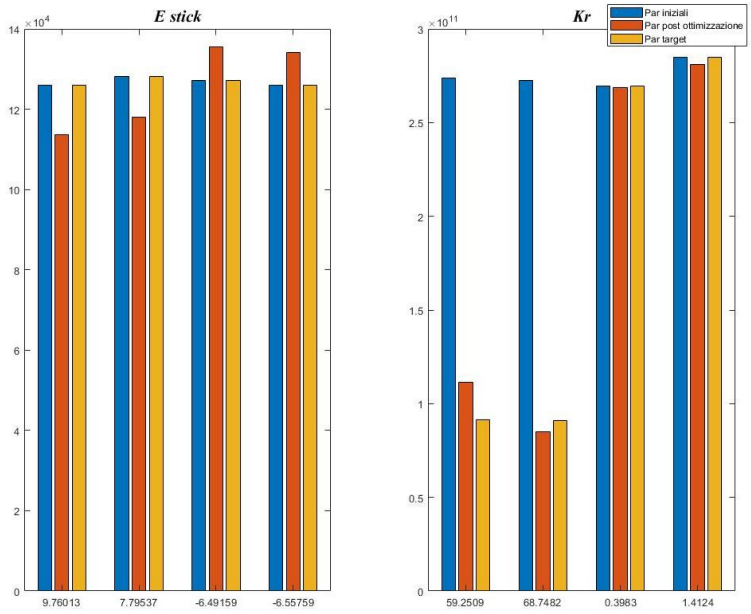

Figure 209: Difference between initial target parameters and identified parameters after stiffness reduction of beams at the first two floors, considering two frequencies and one mode shape.

Even with lower precision in damage estimation, considering only the first two frequencies and the first mode shape, the algorithm is able to quantify damage sufficiently accurately, showing a reduction in beam stiffness at the first two floors. An increase in column stiffness at the third and fourth floors, and a decrease at the first and second floors, can also be observed, similarly to what was shown in Figure 17 in the 50% reduction example.

Stiffness reduction at a single floor

For the test of stiffness reduction at the third floor, both beams and columns, the results are correct as visible in Figure 211, also showing an increase in stiffness of the other parameters.

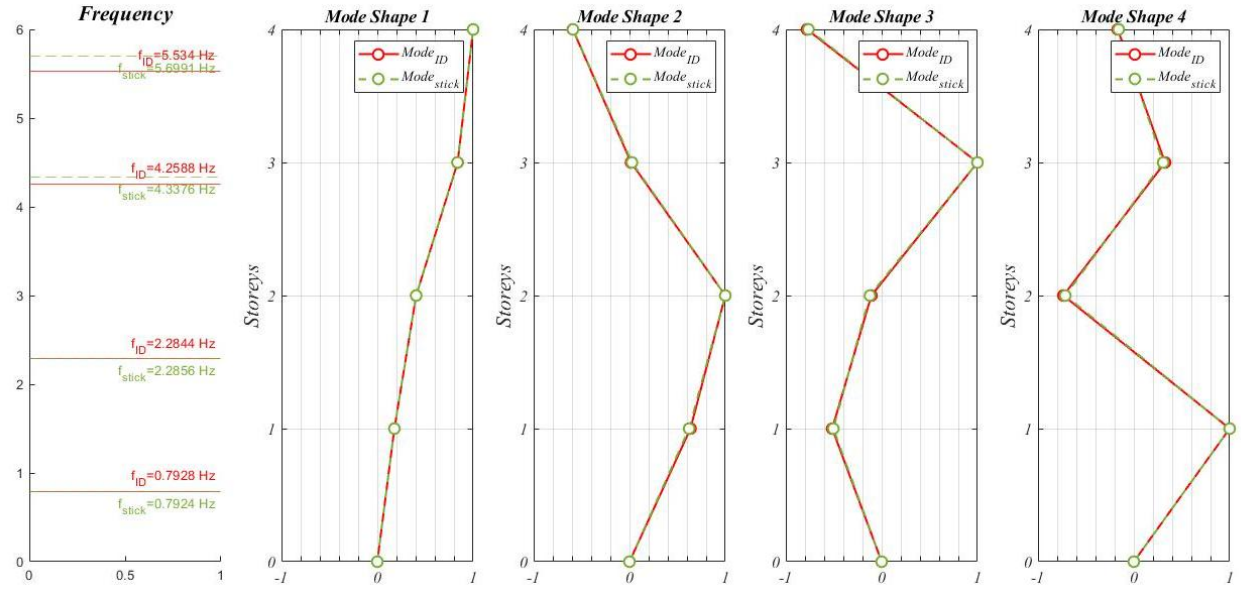

Figure 210: Frequencies and mode shapes of the real model with stiffness reduction of beams and columns at the third floor and Stick Model with target parameters obtained from optimization, considering two frequencies and one mode shape.

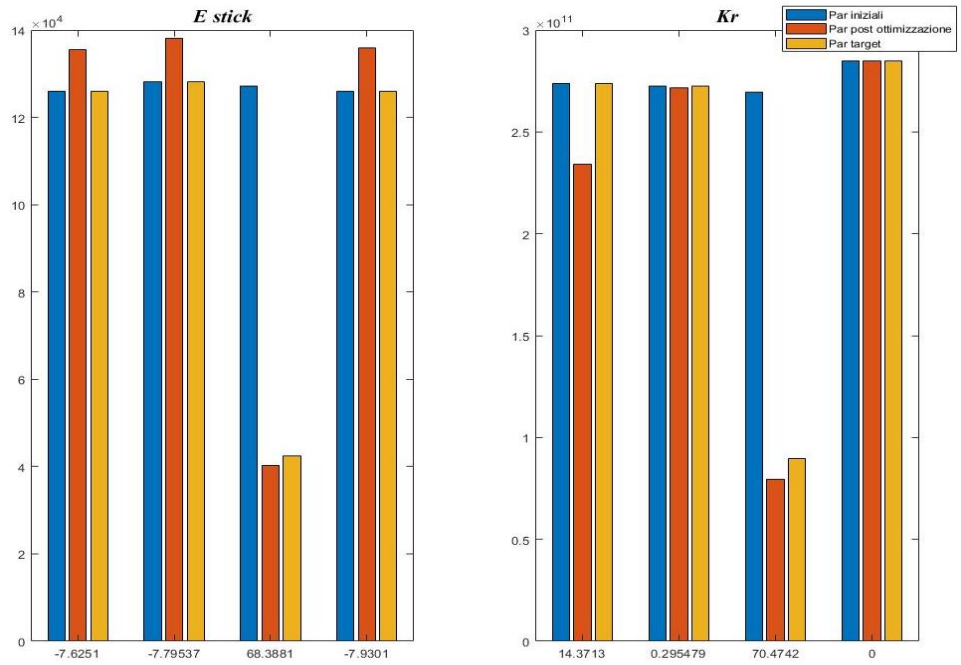

Figure 211: Difference between initial target parameters and identified parameters after stiffness reduction of beams and columns at the third floor, considering two frequencies and one mode shape.

Even in this last case, the results are consistent with previous findings, showing the reduction of stiffness at the considered floor, while unjustified stiffness increases are visible and a 15% reduction of the rotational stiffness at the first floor is also present. This suggests that this aspect should be further investigated, considering modifications to the optimization algorithm (e.g., lowering the tolerance) and/or studying the objective function in more detail. The increase in stiffness arises from the fact that an upper bound constraint equal to the initial stiffness values was not set in the optimization (constrained optimization), to avoid incorrectly setting the problem; otherwise, the algorithm would start the search from a point on the constraint.

Conclusions

As shown in the conducted study, the simplified model (Stick Model) realized as described in Section 3.1 proves to be a useful tool to represent a more complex frame structure, allowing discrimination of damage between structural elements with good approximation. Even in situations where the target parameters (frequencies and mode shapes) are not fully determined—for example, due to issues related to dynamic identification, which will be discussed in Section 4 of this document—the numerical optimization provides satisfactory results.

This model should be further investigated in detail, and new parameters should be added to represent the presence of infill walls and to study the three-dimensional response, including the torsional stiffness of the building. Adding new parameters could render the problem under-determined; for this reason, the objective function might be modified by including new terms related, for example, to modal curvature or modal rotation, for which initial studies have already begun.

References

[1] *A review of structural health monitoring literature : 1996-2001*. 2004.

[2] K. Worden, C. R. Farrar, G. Manson, and G. Park, 'The fundamental axioms of structural health monitoring', *Proc. R. Soc. Math. Phys. Eng. Sci.*, vol. 463, no. 2082, pp. 1639–1664, June 2007, doi: 10.1098/rspa.2007.1834.

[3] E. P. Carden and P. Fanning, 'Vibration Based Condition Monitoring: A Review', *Struct. Health Monit.*, vol. 3, no. 4, pp. 355–377, Dec. 2004, doi: 10.1177/1475921704047500.

[4] E. Caetano and R. Calc, 'Dynamic measurements on bridges: design, rehabilitation and monitoring'.

[5] B. Calandrino, M. D. Paola, A. Pirrotta, and B. Villa, 'Monitoraggio strutturale attraverso prove statiche e dinamiche. Un esempio rilevante: il monitoraggio del "passetto Vaticano"'.

[6] M. G. D'Urso, F. Cavaliere, and M. Crespi, 'Sensori accelerometrici per il monitoraggio in continuo di versanti in frana', 2010.

[7] Li, Hong-Nan, Li, Dong-Sheng, Ren, Liang, Yi, Ting-Hua, Jia, Zi-Guang, and LI, Kun-Peng, 'Structural health monitoring of innovative civil engineering structures in Mainland China', *Struct. Monit. Maint.*, vol. 3, no. 1, pp. 1–32, Mar. 2016, doi: 10.12989/SMM.2016.3.1.001.

[8] A. Cunha, E. Caetano, F. Magalhães, and C. Moutinho, 'Dynamic identification and continuous dynamic monitoring of bridges: different applications along bridges life cycle', *Struct. Infrastruct. Eng.*, vol. 14, pp. 1–23, Dec. 2017, doi: 10.1080/15732479.2017.1406959.

[9] F. Magalhães, Á. Cunha, and E. Caetano, 'Dynamic monitoring of a long span arch bridge', *Eng. Struct.*, vol. 30, no. 11, pp. 3034–3044, Nov. 2008, doi: 10.1016/j.engstruct.2008.04.020.

[10] C. Karakostas *et al.*, 'Seismic assessment of bridges through structural health monitoring: a state-of-the-art review', *Bull. Earthq. Eng.*, vol. 22, no. 3, pp. 1309–1357, Feb. 2024, doi: 10.1007/s10518-023-01819-3.

[11] C. Rainieri, M. A. Notarangelo, and G. Fabbrocino, 'Experiences of Dynamic Identification and Monitoring of Bridges in Serviceability Conditions and after Hazardous Events', *Infrastructures*, vol. 5, no. 10, p. 86, Oct. 2020, doi: 10.3390/infrastructures5100086.

[12] S. Beskhyroun and Q. Ma, 'Low-Cost Accelerometers for Experimental Modal Analysis'.

[13] R. Guidorzi, R. Diversi, L. Vincenzi, and V. Simioli, 'Evaluation of a MEMS–based sensing unit for structural health monitoring: results on a medieval tower'.

[14] J. P. Amezquita-Sanchez, M. Valtierra-Rodriguez, and H. Adeli, 'Wireless smart sensors for monitoring the health condition of civil infrastructure', *Sci. Iran.*, vol. 25, no. 6, pp. 2913–2925, Dec. 2018, doi: 10.24200/sci.2018.21136.

[15] R. Guidorzi, R. Diversi, L. Vincenzi, C. Mazzotti, and V. Simioli, 'Structural monitoring of a tower by means of MEMS-based sensing and enhanced autoregressive models', *Eur. J. Control*, vol. 20, no. 1, pp. 4–13, Jan. 2014, doi: 10.1016/j.ejcon.2013.06.004.

[16] B. Corsa, M. Barba-Sevilla, K. Tiampo, and C. Meertens, 'Integration of DInSAR Time Series and GNSS Data for Continuous Volcanic Deformation Monitoring and Eruption Early Warning Applications', *Remote Sens.*, vol. 14, no. 3, p. 784, Feb. 2022, doi: 10.3390/rs14030784.

[17] R. Bamler and P. Hartl, 'Synthetic aperture radar interferometry'.

[18] D. Massonnet and K. L. Feigl, ‘Radar interferometry and its application to changes in the Earth’s surface’, *Rev. Geophys.*, vol. 36, no. 4, pp. 441–500, Nov. 1998, doi: 10.1029/97RG03139.
[19] N. Oestreicher, A. Manconi, C. Roques, A. Gualandi, and S. Loew, ‘Spatial and temporal variability of surface deformation in a paraglacial alpine environment measured from satellite radars’, *Remote Sens. Environ.*, vol. 326, p. 114765, Aug. 2025, doi: 10.1016/j.rse.2025.114765.
[20] C. Giannico, A. Ferretti, and S. Alberti, ‘Satellite Radar interferometry: a new monitoring tool for cultural heritage sites’, 2013.
[21] D. Tapete and F. Cigna, ‘Appraisal of Opportunities and Perspectives for the Systematic Condition Assessment of Heritage Sites with Copernicus Sentinel-2 High-Resolution Multispectral Imagery’, *Remote Sens.*, vol. 10, no. 4, p. 561, Apr. 2018, doi: 10.3390/rs10040561.
[22] Y. Zheng *et al.*, ‘Long-Term SAR Data Analysis for Subsidence Monitoring and Correlation Study at Beijing Capital Airport’, *Remote Sens.*, vol. 16, no. 3, p. 445, Jan. 2024, doi: 10.3390/rs16030445.
[23] A. Ferretti, C. Prati, and F. Rocca, ‘Permanent Scatterers in SAR Interferometry’.
[24] A. A. Rather and S. K. Bukhari, ‘Ground Deformation Pattern in Parts of Kashmir Himalaya Using Persistent Scatterer Interferometry: A case study of Srinagar City’, *J. Indian Soc. Remote Sens.*, vol. 53, no. 3, pp. 827–846, Mar. 2025, doi: 10.1007/s12524-024-02030-w.
[25] A. Pepe and F. Calò, ‘A Review of Interferometric Synthetic Aperture RADAR (InSAR) Multi-Track Approaches for the Retrieval of Earth’s Surface Displacements’, *Appl. Sci.*, vol. 7, no. 12, p. 1264, Dec. 2017, doi: 10.3390/app7121264.
[26] S. Scifoni *et al.*, ‘On the joint exploitation of long-term DInSAR time series and geological information for the investigation of ground settlements in the town of Roma (Italy)’, *Remote Sens. Environ.*, vol. 182, pp. 113–127, Sept. 2016, doi: 10.1016/j.rse.2016.04.017.
[27] E. Sansosti *et al.*, ‘How second generation SAR systems are impacting the analysis of ground deformation’, *Int. J. Appl. Earth Obs. Geoinformation*, vol. 28, pp. 1–11, May 2014, doi: 10.1016/j.jag.2013.10.007.
[28] G. Luzi, M. Crosetto, and E. Fernández, ‘Radar Interferometry for Monitoring the Vibration Characteristics of Buildings and Civil Structures: Recent Case Studies in Spain’, *Sensors*, vol. 17, no. 4, p. 669, Mar. 2017, doi: 10.3390/s17040669.
[29] P. Berardino, G. Fornaro, R. Lanari, and E. Sansosti, ‘A new algorithm for surface deformation monitoring based on small baseline differential SAR interferograms’, *IEEE Trans. Geosci. Remote Sens.*, vol. 40, no. 11, pp. 2375–2383, Nov. 2002, doi: 10.1109/TGRS.2002.803792.
[30] F. Casu, M. Manzo, and R. Lanari, ‘A quantitative assessment of the SBAS algorithm performance for surface deformation retrieval from DInSAR data’, *Remote Sens. Environ.*, vol. 102, no. 3–4, pp. 195–210, June 2006, doi: 10.1016/j.rse.2006.01.023.
[31] R. Lanari, O. Mora, M. Manunta, J. J. Mallorqui, P. Berardino, and E. Sansosti, ‘A small-baseline approach for investigating deformations on full-resolution differential SAR interferograms’, *IEEE Trans. Geosci. Remote Sens.*, vol. 42, no. 7, pp. 1377–1386, July 2004, doi: 10.1109/TGRS.2004.828196.
[32] M. Bonano, M. Manunta, M. Marsella, and R. Lanari, ‘Long-term ERS/ENVISAT deformation time-series generation at full spatial resolution via the extended SBAS technique’, *Int. J. Remote Sens.*, vol. 33, no. 15, pp. 4756–4783, Aug. 2012, doi: 10.1080/01431161.2011.638340.
[33] M. Manunta, M. Marsella, G. Zeni, M. Sciotti, S. Atzori, and R. Lanari, ‘Two-scale surface deformation analysis using the SBAS-DInSAR technique: a case study of the city of Rome, Italy’, *Int. J. Remote Sens.*, vol. 29, no. 6, pp. 1665–1684, Mar. 2008, doi: 10.1080/01431160701395278.

[34] S. Arangio, F. Calò, M. Di Mauro, M. Bonano, M. Marsella, and M. Manunta, 'An application of the SBAS-DInSAR technique for the assessment of structural damage in the city of Rome', *Struct. Infrastruct. Eng.*, vol. 10, no. 11, pp. 1469–1483, Nov. 2014, doi: 10.1080/15732479.2013.833949.
[35] F. Calò *et al.*, 'Enhanced landslide investigations through advanced DInSAR techniques: The Ivancich case study, Assisi, Italy', *Remote Sens. Environ.*, vol. 142, pp. 69–82, Feb. 2014, doi: 10.1016/j.rse.2013.11.003.
[36] G. Giardina, P. Milillo, M. J. DeJong, D. Perissin, and G. Milillo, 'Evaluation of InSAR monitoring data for post-tunnelling settlement damage assessment', *Struct. Control Health Monit.*, vol. 26, no. 2, Feb. 2019, doi: 10.1002/stc.2285.
[37] F. C. Ponzo *et al.*, 'Transport Infrastructure SHM Using Integrated SAR Data and On-Site Vibrational Acquisitions: "Ponte Della Musica–Armando Trovajoli" Case Study', *Appl. Sci.*, vol. 11, no. 14, p. 6504, July 2021, doi: 10.3390/app11146504.
[38] L. Mitas and H. Mitasova, 'Spatial interpolation', *Geogr. Inf. Syst. Princ. Tech. Manag. Appl.*, vol. 1, no. 2, pp. 481–492, 1999.
[39] J. Burland and C. Wroth, 'Settlement of Buildings and Associated Damage', *Build. Res. Establ.*, vol. 65, Jan. 1975.
[40] L. G. Per, 'Ministero delle Infrastrutture e della Mobilità Sostenibili'.
[41] L. G. Per, 'Istruzioni Operative per l'applicazione delle'.
[42] S. W. Doebling, C. R. Farrar, and M. B. Prime, 'A Summary Review of Vibration-Based Damage Identification Methods', *Shock Vib. Dig.*, vol. 30, no. 2, pp. 91–105, Mar. 1998, doi: 10.1177/058310249803000201.
[43] L. Zhang, R. Brincker, and P. Andersen, 'An Overview of Operational Modal Analysis: Major Development and Issues'.
[44] Á. Cunha, E. Caetano, F. Magalhães, and C. Moutinho, 'FROM INPUT-OUTPUT TO OUTPUT-ONLY MODAL IDENTIFICATION OF CIVIL ENGINEERING STRUCTURES', *Sel. Pap.*, 2006.
[45] Á. Cunha and E. Caetano, 'Experimental Modal Analysis of Civil Engineering Structures', *SOUND Vib.*, 2006.
[46] B. Peeters and C. E. Ventura, 'COMPARATIVE STUDY OF MODAL ANALYSIS TECHNIQUES FOR BRIDGE DYNAMIC CHARACTERISTICS', *Mech. Syst. Signal Process.*, vol. 17, no. 5, pp. 965–988, Sept. 2003, doi: 10.1006/mssp.2002.1568.
[47] Á. Cunha, E. Caetano, and F. Magalhães, 'Output-only dynamic testing of bridges and special structures', *Struct. Concr.*, vol. 8, no. 2, pp. 67–85, June 2007, doi: 10.1680/stco.2007.8.2.67.
[48] J. M. W. Brownjohn, F. Magalhaes, E. Caetano, and A. Cunha, 'Ambient vibration re-testing and operational modal analysis of the Humber Bridge', *Eng. Struct.*, vol. 32, no. 8, pp. 2003–2018, Aug. 2010, doi: 10.1016/j.engstruct.2010.02.034.
[49] E. Caetano, A. Cunha, V. Gattulli, and M. Lepidi, 'Cable–deck dynamic interactions at the International Guadiana Bridge: On-site measurements and finite element modelling', *Struct. Control Health Monit.*, vol. 15, no. 3, pp. 237–264, Apr. 2008, doi: 10.1002/stc.241.
[50] F. Magalhães, E. Caetano, Á. Cunha, O. Flamand, and G. Grillaud, 'Ambient and free vibration tests of the Millau Viaduct: Evaluation of alternative processing strategies', *Eng. Struct.*, vol. 45, pp. 372–384, Dec. 2012, doi: 10.1016/j.engstruct.2012.06.038.
[51] C. Moutinho, A. Cunha, and E. Caetano, 'Analysis and control of vibrations in a stress-ribbon footbridge', *Struct. Control Health Monit.*, vol. 18, no. 6, pp. 619–634, Oct. 2011, doi: 10.1002/stc.390.
[52] P. T. Brewick and A. W. Smyth, 'An investigation of the effects of traffic induced local dynamics on global damping estimates using operational modal analysis', *Mech. Syst. Signal Process.*, vol. 41, no. 1–2, pp. 433–453, Dec. 2013, doi: 10.1016/j.ymssp.2013.07.013.

[53] J.-H. Weng, C.-H. Loh, J. P. Lynch, K.-C. Lu, P.-Y. Lin, and Y. Wang, 'Output-only modal identification of a cable-stayed bridge using wireless monitoring systems', *Eng. Struct.*, vol. 30, no. 7, pp. 1820–1830, July 2008, doi: 10.1016/j.engstruct.2007.12.002.
[54] H. Hasani and F. Freddi, 'Operational Modal Analysis on Bridges: A Comprehensive Review', *Infrastructures*, vol. 8, no. 12, p. 172, Dec. 2023, doi: 10.3390/infrastructures8120172.
[55] W. H. Chen *et al.*, 'Theoretical and experimental modal analysis of the Guangzhou New TV Tower', *Eng. Struct.*, vol. 33, no. 12, pp. 3628–3646, Dec. 2011, doi: 10.1016/j.engstruct.2011.07.028.
[56] Y. Pan *et al.*, 'Ambient Vibration Testing of a Super Tall Building in Shanghai', in *Dynamics of Civil Structures, Volume 2*, 1st edn, New York: River Publishers, 2025, pp. 155–162. doi: 10.1007/978-3-319-29751-4_16.
[57] M. Amer, C. E. Ventura, N. Maroldt, J. R. Seume, and J. Wallaschek, 'Modal parameter estimation of turbomachinery in operation taking into account friction damping', *Mech. Syst. Signal Process.*, vol. 216, p. 111414, July 2024, doi: 10.1016/j.ymssp.2024.111414.
[58] J. Li, T. Bao, and C. E. Ventura, 'An automated operational modal analysis algorithm and its application to concrete dams', *Mech. Syst. Signal Process.*, vol. 168, p. 108707, Apr. 2022, doi: 10.1016/j.ymssp.2021.108707.
[59] J. Jasieńko, Ed., *Structural analysis of historical constructions: proceedings of the International Conference on Structural Analysis of Historical Constructions, SAHC 2012, 15-17 October 2012, Wrocław, Poland. Vol. 1*. Wrocław: Dolnośląskie Wydawnictwo Edukacyjne, 2012.
[60] F. Magalhães, A. Cunha, and E. Caetano, 'Vibration based structural health monitoring of an arch bridge: From automated OMA to damage detection', *Mech. Syst. Signal Process.*, vol. 28, pp. 212–228, Apr. 2012, doi: 10.1016/j.ymssp.2011.06.011.
[61] F. Magalhães, Á. Cunha, and E. Caetano, 'Online automatic identification of the modal parameters of a long span arch bridge', *Mech. Syst. Signal Process.*, vol. 23, no. 2, pp. 316–329, Feb. 2009, doi: 10.1016/j.ymssp.2008.05.003.
[62] E. Reynders, J. Houbrechts, and G. De Roeck, 'Fully automated (operational) modal analysis', *Mech. Syst. Signal Process.*, vol. 29, pp. 228–250, May 2012, doi: 10.1016/j.ymssp.2012.01.007.
[63] R. Brincker and C. E. Ventura, *Introduction to Operational Modal Analysis*, 1st edn. Wiley, 2015. doi: 10.1002/9781118535141.
[64] C. Rainieri and G. Fabbrocino, *Operational Modal Analysis of Civil Engineering Structures: An Introduction and Guide for Applications*. New York, NY: Springer New York, 2014. doi: 10.1007/978-1-4939-0767-0.
[65] C. Rainieri, 'ENGINEERING OF MATERIALS AND STRUCTURES'.
[66] F. Magalhães and Á. Cunha, 'Explaining operational modal analysis with data from an arch bridge', *Mech. Syst. Signal Process.*, vol. 25, no. 5, pp. 1431–1450, July 2011, doi: 10.1016/j.ymssp.2010.08.001.
[67] S. Gade, N. B. Møller, H. Herlufsen, and H. Konstantin-Hansen, 'Frequency Domain Techniques for Operational Modal Analysis'.
[68] R. Brincker, 'Understanding Stochastic Subspace Identification'.
[69] B. Peeters and G. De Roeck, 'Stochastic System Identification for Operational Modal Analysis: A Review', *J. Dyn. Syst. Meas. Control*, vol. 123, no. 4, pp. 659–667, Dec. 2001, doi: 10.1115/1.1410370.
[70] R. Brincker, L. Zhang, and P. Andersen, 'Modal identification of output-only systems using frequency domain decomposition', *Smart Mater. Struct.*, vol. 10, no. 3, pp. 441–445, June 2001, doi: 10.1088/0964-1726/10/3/303.
[71] B. Peeters and G. De Roeck, 'Reference based stochastic subspace identification in civil engineering', *Inverse Probl. Eng.*, vol. 8, no. 1, pp. 47–74, Feb. 2000, doi: 10.1080/174159700088027718.

[72] R. J. Allemang, 'The Modal Assurance Criterion – Twenty Years of Use and Abuse', *SOUND Vib.*, 2003.
[73] P. Vacher, B. Jacquier, and A. Bucharles, 'Extensions of the MAC criterion to complex modes'.
[74] M. Baruch, 'Optimization Procedure to Correct Stiffness and Flexibility Matrices Using Vibration Tests', *AIAA J.*, vol. 16, no. 11, pp. 1208–1210, Nov. 1978, doi: 10.2514/3.61032.
[75] A. BERMAN and E. NAGY, 'Improvement of a large dynamic analytical model using ground vibration test data', in *23rd Structures, Structural Dynamics and Materials Conference*, 0 vols, in Structures, Structural Dynamics, and Materials and Co-located Conferences. , American Institute of Aeronautics and Astronautics, 1982. doi: 10.2514/6.1982-743.
[76] J. E. Mottershead and M. I. Friswell, 'Model Updating In Structural Dynamics: A Survey', *J. Sound Vib.*, vol. 167, no. 2, pp. 347–375, Oct. 1993, doi: 10.1006/jsvi.1993.1340.
[77] M. I. Friswell, D. J. Inman, and D. F. Pilkey, 'Direct Updating of Damping and Stiffness Matrices'.
[78] S. V. Modak, T. K. Kundra, and B. C. Nakra, 'Comparative study of model updating methods using simulated experimental data', *Comput. Struct.*, vol. 80, no. 5–6, pp. 437–447, Mar. 2002, doi: 10.1016/S0045-7949(02)00017-2.
[79] J. E. Mottershead, M. Link, and M. I. Friswell, 'The sensitivity method in finite element model updating: A tutorial', *Mech. Syst. Signal Process.*, vol. 25, no. 7, pp. 2275–2296, Oct. 2011, doi: 10.1016/j.ymssp.2010.10.012.
[80] F. Magalhães, A. Cunha, and E. Caetano, 'Vibration based structural health monitoring of an arch bridge: From automated OMA to damage detection', *Mech. Syst. Signal Process.*, vol. 28, pp. 212–228, Apr. 2012, doi: 10.1016/j.ymssp.2011.06.011.
[81] A. Teughels and G. De Roeck, 'Structural damage identification of the highway bridge Z24 by FE model updating', *J. Sound Vib.*, vol. 278, no. 3, pp. 589–610, Dec. 2004, doi: 10.1016/j.jsv.2003.10.041.
[82] S. Pakzad and C. Juan, Eds, *Dynamics of Civil Structures, Volume 2: Proceedings of the 34th IMAC, A Conference and Exposition on Structural Dynamics 2016*. in Conference Proceedings of the Society for Experimental Mechanics Series. Cham: Springer International Publishing, 2016. doi: 10.1007/978-3-319-29751-4.
[83] F. Bianconi, G. P. Salachoris, F. Clementi, and S. Lenci, 'A Genetic Algorithm Procedure for the Automatic Updating of FEM Based on Ambient Vibration Tests', *Sensors*, vol. 20, no. 11, p. 3315, June 2020, doi: 10.3390/s20113315.
[84] Y. Feng, K. Yavuz, and C. Ventura, 'Finite Element Model Updating of Portage Creek Bridge', 2016, pp. 247–253. doi: 10.1007/978-3-319-29751-4_25.
[85] G. Lacanna, M. Betti, M. Ripepe, and G. Bartoli, 'Dynamic Identification as a Tool to Constrain Numerical Models for Structural Analysis of Historical Buildings', *Front. Built Environ.*, vol. 6, p. 40, Apr. 2020, doi: 10.3389/fbuil.2020.00040.
[86] B. Jaishi and W.-X. Ren, 'Structural Finite Element Model Updating Using Ambient Vibration Test Results', *J. Struct. Eng.*, vol. 131, no. 4, pp. 617–628, Apr. 2005, doi: 10.1061/(ASCE)0733-9445(2005)131:4(617).
[87] Q. Pu, Y. Hong, L. Chen, S. Yang, and X. Xu, 'Model updating–based damage detection of a concrete beam utilizing experimental damped frequency response functions', *Adv. Struct. Eng.*, vol. 22, no. 4, pp. 935–947, Mar. 2019, doi: 10.1177/1369433218789556.
[88] M. Sanayei, G. R. Imbaro, J. A. S. McClain, and L. C. Brown, 'Structural Model Updating Using Experimental Static Measurements', *J. Struct. Eng.*, vol. 123, no. 6, pp. 792–798, June 1997, doi: 10.1061/(ASCE)0733-9445(1997)123:6(792).
[89] H. Schlune, M. Plos, and K. Gylltoft, 'Improved bridge evaluation through finite element model updating using static and dynamic measurements', *Eng. Struct.*, vol. 31, no. 7, pp. 1477–1485, July 2009, doi: 10.1016/j.engstruct.2009.02.011.

[90] H. Wang, A. Li, and J. Li, 'Progressive finite element model calibration of a long-span suspension bridge based on ambient vibration and static measurements', *Eng. Struct.*, vol. 32, no. 9, pp. 2546–2556, Sept. 2010, doi: 10.1016/j.engstruct.2010.04.028.
[91] J. B. Liao, G. W. Tang, and F. Pan, 'Finite Element Model Updating of Existing T-Girder Bridge by Field Quasi-Static Generalized Influence Line', *Appl. Mech. Mater.*, vol. 226–228, pp. 1609–1613, Nov. 2012, doi: 10.4028/www.scientific.net/AMM.226-228.1609.
[92] C. Costa, D. Ribeiro, P. Jorge, R. Silva, A. Arêde, and R. Calçada, 'Calibration of the numerical model of a stone masonry railway bridge based on experimentally identified modal parameters', *Eng. Struct.*, vol. 123, pp. 354–371, Sept. 2016, doi: 10.1016/j.engstruct.2016.05.044.
[93] H. Tran-Ngoc, S. Khatir, G. De Roeck, T. Bui-Tien, L. Nguyen-Ngoc, and M. Abdel Wahab, 'Model Updating for Nam O Bridge Using Particle Swarm Optimization Algorithm and Genetic Algorithm', *Sensors*, vol. 18, no. 12, p. 4131, Nov. 2018, doi: 10.3390/s18124131.
[94] R. I. Levin and N. A. J. Lieven, 'DYNAMIC FINITE ELEMENT MODEL UPDATING USING SIMULATED ANNEALING AND GENETIC ALGORITHMS', *Mech. Syst. Signal Process.*, vol. 12, no. 1, pp. 91–120, Jan. 1998, doi: 10.1006/mssp.1996.0136.
[95] W.-X. Ren, S.-E. Fang, and M.-Y. Deng, 'Response Surface–Based Finite-Element-Model Updating Using Structural Static Responses', *J. Eng. Mech.*, vol. 137, no. 4, pp. 248–257, Apr. 2011, doi: 10.1061/(ASCE)EM.1943-7889.0000223.
[96] Y. Zhao, J. Zhang, D. Li, D. Zhou, and D. Xin, 'Finite Element Model Updating of Bridge Structures Based on Improved Response Surface Methods', *Struct. Control Health Monit.*, vol. 2023, pp. 1–16, Mar. 2023, doi: 10.1155/2023/2488951.
[97] I. Behmanesh, B. Moaveni, G. Lombaert, and C. Papadimitriou, 'Hierarchical Bayesian model updating for structural identification', *Mech. Syst. Signal Process.*, vol. 64–65, pp. 360–376, Dec. 2015, doi: 10.1016/j.ymssp.2015.03.026.
[98] P. Asadollahi, Y. Huang, and J. Li, 'Bayesian Finite Element Model Updating and Assessment of Cable-Stayed Bridges Using Wireless Sensor Data', *Sensors*, vol. 18, no. 9, p. 3057, Sept. 2018, doi: 10.3390/s18093057.
[99] M. Song, I. Behmanesh, B. Moaveni, and C. Papadimitriou, 'Modeling Error Estimation and Response Prediction of a 10-Story Building Model Through a Hierarchical Bayesian Model Updating Framework', *Front. Built Environ.*, vol. 5, p. 7, Jan. 2019, doi: 10.3389/fbuil.2019.00007.
[100] J. L. Beck and L. S. Katafygiotis, 'Updating Models and Their Uncertainties. I: Bayesian Statistical Framework', *J. Eng. Mech.*, vol. 124, no. 4, pp. 455–461, Apr. 1998, doi: 10.1061/(ASCE)0733-9399(1998)124:4(455).
[101] J. L. Beck, 'Bayesian system identification based on probability logic', *Struct. Control Health Monit.*, vol. 17, no. 7, pp. 825–847, Nov. 2010, doi: 10.1002/stc.424.
[102] L. S. Katafygiotis, C. Papadimitriou, and H.-F. Lam, 'A probabilistic approach to structural model updating', *Soil Dyn. Earthq. Eng.*, vol. 17, no. 7–8, pp. 495–507, Oct. 1998, doi: 10.1016/S0267-7261(98)00008-6.
[103] E. Simoen, G. De Roeck, and G. Lombaert, 'Dealing with uncertainty in model updating for damage assessment: A review', *Mech. Syst. Signal Process.*, vol. 56–57, pp. 123–149, May 2015, doi: 10.1016/j.ymssp.2014.11.001.
[104] D. Hester, K. Koo, Y. Xu, J. Brownjohn, and M. Bocian, 'Boundary condition focused finite element model updating for bridges', *Eng. Struct.*, vol. 198, p. 109514, Nov. 2019, doi: 10.1016/j.engstruct.2019.109514.
[105] G. Bartoli, M. Betti, L. Facchini, A. M. Marra, and S. Monchetti, 'Bayesian model updating of historic masonry towers through dynamic experimental data', *Procedia Eng.*, vol. 199, pp. 1258–1263, 2017, doi: 10.1016/j.proeng.2017.09.267.

[106] A. Belleri, B. Moaveni, and J. I. Restrepo, 'Damage assessment through structural identification of a three-story large-scale precast concrete structure', *Earthq. Eng. Struct. Dyn.*, vol. 43, no. 1, pp. 61–76, Jan. 2014, doi: 10.1002/eqe.2332.
[107] A. C. Altunişik, F. Y. Okur, A. F. Genç, M. Günaydin, and S. Adanur, 'Automated Model Updating of Historical Masonry Structures Based on Ambient Vibration Measurements', *J. Perform. Constr. Facil.*, vol. 32, no. 1, p. 04017126, Feb. 2018, doi: 10.1061/(ASCE)CF.1943-5509.0001108.
[108] S. Atamturktur and J. A. Laman, 'Finite element model correlation and calibration of historic masonry monuments: review', *Struct. Des. Tall Spec. Build.*, vol. 21, no. 2, pp. 96–113, Feb. 2012, doi: 10.1002/tal.577.
[109] A. Mehrjoo *et al.*, 'Recursive Bayesian estimation of wind load on a monopile-supported offshore wind turbine using output-only measurements', *Mech. Syst. Signal Process.*, vol. 224, p. 112183, Feb. 2025, doi: 10.1016/j.ymssp.2024.112183.
[110] B. Moaveni, *Physics-based and data-driven digital twinning of offshore wind turbines using sensor measurements*. 2025. doi: 10.1117/12.3057755.
[111] S. Ereiz, I. Duvnjak, and J. Fernando Jiménez-Alonso, 'Review of finite element model updating methods for structural applications', *Structures*, vol. 41, pp. 684–723, July 2022, doi: 10.1016/j.istruc.2022.05.041.
[112] M. Bartholomew-Biggs, *Nonlinear Optimization with Engineering Applications*, vol. 19. in Springer Optimization and Its Applications, vol. 19. Boston, MA: Springer US, 2008. doi: 10.1007/978-0-387-78723-7.
[113] J. Nocedal and S. J. Wright, *Numerical optimization*, 2nd ed. in Springer series in operations research. New York: Springer, 2006.
[114] R. (Roger) Fletcher, 'Practical methods of optimization'.
[115] A. Antoniou and W.-S. Lu, *Practical Optimization: Algorithms and Engineering Applications*. in Texts in Computer Science. New York, NY: Springer US, 2021. doi: 10.1007/978-1-0716-0843-2.
[116] X.-S. Yang, *Nature-inspired optimization algorithms*, First edition. Amsterdam ; Boston: Elsevier, 2014.
[117] M. di Prisco, M. Colombo, P. Martinelli, and D. Coronelli, 'The technical causes of the collapse of Annone overpass on SS.36 Le cause tecniche del crollo del cavalcavia di Annone'.
[118] T. Liu, Q. Zhang, T. Zordan, and B. Briseghella, 'Finite Element Model Updating of Canonica Bridge Using Experimental Modal Data and Genetic Algorithm', *Struct. Eng. Int.*, vol. 26, no. 1, pp. 27–36, Feb. 2016, doi: 10.2749/101686616X14480232444405.
[119] G. Piccardo, F. Tubino, and A. Luongo, 'Equivalent Timoshenko linear beam model for the static and dynamic analysis of tower buildings', *Appl. Math. Model.*, vol. 71, pp. 77–95, July 2019, doi: 10.1016/j.apm.2019.02.005.
[120] R. Rahgozar, A. R. Ahmadi, and Y. Sharifi, 'A simple mathematical model for approximate analysis of tall buildings', *Appl. Math. Model.*, vol. 34, no. 9, pp. 2437–2451, Sept. 2010, doi: 10.1016/j.apm.2009.11.009.
[121] A. Greco, I. Fiore, G. Occhipinti, S. Caddemi, D. Spina, and I. Caliò, 'An Equivalent Non-Uniform Beam-Like Model for Dynamic Analysis of Multi-Storey Irregular Buildings', *Appl. Sci.*, vol. 10, no. 9, p. 3212, May 2020, doi: 10.3390/app10093212.
[122] A. Greco, I. Fiore, S. Caddemi, I. Caliò, and G. Occhipinti, 'Inhomogeneous beam-like models for the dynamic analysis of multi-storey buildings', in *Advances in Engineering Materials, Structures and Systems: Innovations, Mechanics and Applications*, 1st edn, A. Zingoni, Ed., CRC Press, 2019, pp. 55–60. doi: 10.1201/9780429426506-9.
[123] E. Taciroglu, S. F. Ghahari, and F. Abazarsa, 'Efficient model updating of a multi-story frame and its foundation stiffness from earthquake records using a timoshenko beam model', *Soil Dyn. Earthq. Eng.*, vol. 92, pp. 25–35, Jan. 2017, doi: 10.1016/j.soildyn.2016.09.041.

[124] M. Gaetani d'Aragona, M. Polese, M. Di Ludovico, and A. Prota, 'Large scale loss assessment using stick-it model: A comparison with actual cost data', *Soil Dyn. Earthq. Eng.*, vol. 160, p. 107363, Sept. 2022, doi: 10.1016/j.soildyn.2022.107363.
[125] M. Gaetani d'Aragona, M. Polese, M. Di Ludovico, and A. Prota, 'The use of Stick-IT model for the prediction of direct economic losses', *Earthq. Eng. Struct. Dyn.*, vol. 50, no. 7, pp. 1884–1907, June 2021, doi: 10.1002/eqe.3429.
[126] M. Gaetani d'Aragona, M. Polese, and A. Prota, 'Stick-IT: A simplified model for rapid estimation of IDR and PFA for existing low-rise symmetric infilled RC building typologies', *Eng. Struct.*, vol. 223, p. 111182, Nov. 2020, doi: 10.1016/j.engstruct.2020.111182.
[127] C. Xiong, X. Lu, X. Lin, Z. Xu, and L. Ye, 'Parameter Determination and Damage Assessment for THA-Based Regional Seismic Damage Prediction of Multi-Story Buildings', *J. Earthq. Eng.*, vol. 21, no. 3, pp. 461–485, Apr. 2017, doi: 10.1080/13632469.2016.1160009.
[128] G. Bernagozzi, C. E. Ventura, S. Allahdadian, Y. Kaya, L. Landi, and P. P. Diotallevi, 'Application of modal flexibility-based deflections for damage diagnosis of a steel frame structure', *Procedia Eng.*, vol. 199, pp. 2026–2033, 2017, doi: 10.1016/j.proeng.2017.09.468.
[129] S. H. Sung, K. Y. Koo, and H. J. Jung, 'Modal flexibility-based damage detection of cantilever beam-type structures using baseline modification', *J. Sound Vib.*, vol. 333, no. 18, pp. 4123–4138, Sept. 2014, doi: 10.1016/j.jsv.2014.04.056.
[130] A. Zare Hosseinzadeh, G. Ghodrati Amiri, S. A. Seyed Razzaghi, K. Y. Koo, and S. H. Sung, 'Structural damage detection using sparse sensors installation by optimization procedure based on the modal flexibility matrix', *J. Sound Vib.*, vol. 381, pp. 65–82, Oct. 2016, doi: 10.1016/j.jsv.2016.06.037.

Software and Technical Documentation

[131] The MathWorks Inc. (2023). MATLAB – Version R2023a. Documentation and User's Guide. Natick, MA, USA.

[132] McKenna, F., Fenves, G.L., Scott, M.H. (2000–2023). OpenSees: Open System for Earthquake Engineering Simulation – User Manual. Pacific Earthquake Engineering Research Center, University of California, Berkeley, USA.

[133] ASDEA Software Technology (2023). STKO – Scientific ToolKit for OpenSees: User Manual. Pescara, Italy.

[134] MIDAS Information Technology Co., Ltd. (2023). Midas Gen – General Structure Design System: User Manual. Seongnam, South Korea.

[135] QGIS Development Team (2023). QGIS Geographic Information System – User Guide. Open Source Geospatial Foundation Project.

[136] De Roeck, G., Peeters, B., & Maeck, J. (2000). MACEC 3.4 - The MATLAB Toolbox for Experimental and Operational Modal Analysis. Department of Civil Engineering, KU Leuven.